TENSILE OPENING MODE FRACTURE TOUGHNESS MEASUREMENTS AND SIZE EFFECT INVESTIGATIONS WITH BRAZILIAN DISC TYPE ROCK SPECIMENS

A THESIS SUBMITTED TO
THE GRADUATE SCHOOL OF NATURAL AND APPLIED SCIENCES
OF
MIDDLE EAST TECHNICAL UNIVERSITY

BY

ELIFNAZ ŞAR

IN PARTIAL FULFILLMENT OF THE REQUIREMENTS
FOR
THE DEGREE OF MASTER OF SCIENCE
IN
MINING ENGINEERING

JANUARY 2020

Approval of the thesis:

TENSILE OPENING MODE FRACTURE TOUGHNESS MEASUREMENTS AND SIZE EFFECT INVESTIGATIONS WITH BRAZILIAN DISC TYPE ROCK SPECIMENS

submitted by **ELIFNAZ ŞAR** in partial fulfillment of the requirements for the degree of **Master of Science in Mining Engineering Department, Middle East Technical University** by,

Prof. Dr. Halil Kalıpçılar
Dean, Graduate School of **Natural and Applied Sciences**

Prof. Dr. N. Emre Altun
Head of Department, **Mining Engineering**

Prof. Dr. Levend Tutluoğlu
Supervisor, **Mining Engineering, METU**

Examining Committee Members:

Prof. Dr. Celal Karpuz
Mining Engineering Department, METU

Prof. Dr. Levend Tutluoğlu
Mining Engineering, METU

Assoc. Prof. Dr. Mehmet Ali Hindistan
Mining Engineering Department, HU

Date: 30.01.2020

I hereby declare that all information in this document has been obtained and presented in accordance with academic rules and ethical conduct. I also declare that, as required by these rules and conduct, I have fully cited and referenced all material and results that are not original to this work.

Name, Surname: Elifnaz Şar

Signature:

ABSTRACT

TENSILE OPENING MODE FRACTURE TOUGHNESS MEASUREMENTS AND SIZE EFFECT INVESTIGATIONS WITH BRAZILIAN DISC TYPE ROCK SPECIMENS

Şar, Elifnaz
Master of Science, Mining Engineering
Supervisor: Prof. Dr. Levend Tutluoğlu

January 2020, 176 pages

The flattened Brazilian disc (FBD) geometries were subjected to compressive loads at the loading ends. Tensile stresses were generated indirectly at the center of the disc specimens. Cracks were initiated, and they propagated stably to the onset of unstable fracture. Loads recorded at this stage were used in measuring the tensile opening mode fracture toughness. The specimen size effect on mode I fracture toughness of Gölbaşı andesite was investigated by changing specimen diameters. The boundary influence on fracture toughness was examined by machining flat compressive loading ends of various widths on specimens.

Numerical modeling was performed with the ABAQUS finite element program to compute mode I stress intensity factors of FBD geometries of various sizes. With the evaluation of numerical results, two different equations in terms of loading angle have been developed, one of which is used to calculate the critical dimensionless crack length and the other to determine the maximum dimensionless stress intensity factor.

For examining size effect phenomena for FBD geometry, the fracture toughness tests were carried out on Gölbaşı andesite specimens of different sizes. The specimen diameters were 54 mm, 75 mm, 100 mm, and 125 mm. The loading angles ranged from 16° to 42°. The thickness to diameter ratio t/D was kept constant at around 0.6 in all fracture toughness tests.

The average mode I fracture toughness values of Gölbaşı andesite were 2.03±0.20 MPa$\sqrt{m}$, 2.33±0.13 MPa$\sqrt{m}$, 2.85±0.16 MPa$\sqrt{m}$, and 3.26±0.39 MPa$\sqrt{m}$ for 54 mm, 75 mm, 100 mm and 125 mm diameters, respectively. The test results indicated that an increase in specimen diameter from 54 mm to 125 mm led to an approximately 60.6% $(3.26/2.03=1.606)$ increase in mode I fracture toughness of Gölbaşı andesite.

Keywords: Numerical Modeling, Mode I Fracture Toughness Testing, Flattened Brazilian Disc Method, Flattened Brazilian Disc Geometry, Size Effect

ÖZ

BREZİLYAN DİSKİ TİPİ KAYA NUMUNELERİNDE AÇILMA MODU ÇATLAK TOKLUĞUNUN BELİRLENMESİ VE BOYUT ETKİSİNİN ARAŞTIRILMASI

Şar, Elifnaz
Yüksek Lisans, Maden Mühendisliği
Tez Danışmanı: Prof. Dr. Levend Tutluoğlu

Ocak 2020, 176 sayfa

Düzleştirilmiş Brezilyan Disk geometrileri (DBD), yükleme uçlarından basma yüklerine maruz bırakıldı. Çekme gerilmelerinin disk numunelerinin merkezinde endirekt olarak gelişmesi sağlandı. Çatlaklar kontrollü bir şekilde oluşturulduktan sonra, çatlakların stabil ilerleme durumuna geçene kadar stabil olmayan çatlak ilerleme modunda yüklenmesi sağlandı. Bu aşamada kaydedilen yükler açılma modu çatlak tokluğu değerlerinin hesaplanması için kullanıldı. Numune büyüklüğünün Gölbaşı andezitinin mod I çatlak tokluğununa etkisi numune çapları değiştirilerek araştırıldı. Çatlak tokluğu üzerindeki sınır etkisi numunelerin düzleştirilmiş yükleme uçları farklı genişliklerde olacak şekilde işlenerek incelendi.

Çeşitli boyutlardaki DBD geometrilerinin mod I gerilme şiddeti faktörlerini hesaplamak için ABAQUS sonlu eleman programı ile sayısal modellemeler yapılmıştır. Nümerik sonuçların değerlendirilmesi ile yükleme açısı cinsinden iki farklı denklem geliştirilmiştir; biri kritik boyutsuz çatlak uzunluğunu hesaplamak için, diğeri ise maksimum boyutsuz gerilme yoğunluğu faktörünü belirlemek için kullanılır.

DBD geometrisi için boyut etkisini incelemek amacıyla, çatlak tokluğu testleri farklı boyutlardaki Gölbaşı andezit numuneleri üzerinde gerçekleştirilmiştir. Numune çapları 54 mm, 75 mm, 100 mm ve 125 mm olup; yükleme açıları 16° ila 42° arasında değişmektedir. Numunelerin kalınlık/çap oranı t/D tüm çatlak tokluğu testlerinde 0.6 civarında sabit tutulmuştur.

Gölbaşı andezitinin ortalama mod I çatlak tokluğu değerleri 54 mm, 75 mm, 100 mm ve 125 mm numune çapları için sırasıyla 2.03±0.20 MPa$\sqrt{m}$, 2.33±0.13 MPa$\sqrt{m}$, 2.85±0.16 MPa$\sqrt{m}$, 3.26±0.39 MPa$\sqrt{m}$ olarak bulunmuştur. Test sonuçları numune çapı arttıkça mod I çatlak tokluğunun da arttığını gösterdi.

Anahtar Kelimeler: Sayısal Modelleme, Mod I Çatlak Tokluğu Deneyi, Düzleştirilmiş Brazilyan Disk Yöntemi, Düzleştirilmiş Brazilyan Disk Geometrisi, Boyut Etkisi

To my family

ACKNOWLEDGMENTS

I would like first of all to extend my sincere gratitude and appreciation to my supervisor, Prof. Dr. Levend Tutluoğlu, for his illuminating and inspiring guidance, continuous support and encouragement throughout the present thesis.

I wish to express my special thanks to the examining committee members: Prof. Dr. Celal Karpuz and Assoc. Prof. Dr. Mehmet Ali Hindistan for their valuable contributions and comments.

I am very grateful to M.Sc Uğur Alkan for his help and for sharing his valuable knowledge. I would also like to thank Hakan Uysal for his help during laboratory work.

I must express my gratitude to Emel Torun, Sinem Durmaz, Ezgi Altay and Tuğçe Yıldırımer for being always with me. I want to thank M.Sc Tuğçe Tayfuner, M.Sc Raheel Bawani and METU Mining Engineering Department research assistants Kutay Emre Karadeniz, Alper Kırmacı, Doğukan Güner, Cengiz Kaydım, and Enver Yılmaz for their support and motivation.

I want to express my deepest appreciation to my mother, Selma Erdel, my father, Zeynal Şar, and my sister, Zeynep Şar, for their limitless love, reliance, and encouragement in my whole life. I also owe thanks to the rest of my family.

Finally, I feel deeply grateful to Burak Kahraman for his endless support, patience, and love.

TABLE OF CONTENTS

ABSTRACT v

ÖZ vii

ACKNOWLEDGMENTS x

TABLE OF CONTENTS xi

LIST OF TABLES xiv

LIST OF FIGURES xvi

LIST OF ABBREVIATIONS xxv

LIST OF SYMBOLS xxvi

CHAPTERS

1. INTRODUCTION 1

  1.1. Statement of The Problem 2

  1.2. Research Objectives 3

  1.3. Research Methodology 3

  1.4. Organization of Thesis 4

2. BASICS OF FRACTURE MECHANICS 5

  2.1. Literature Review 5

  2.2. Linear Elastic Fracture Mechanics (LEFM) 8

    2.2.1. Modes of Fracture 8

    2.2.2. Crack Tip Stress and Displacement Field 9

    2.2.3. Stress Intensity Factor 11

    2.2.4. The Relations between Energy Release Rate and Stress Intensity Factor 13

    2.2.5. Fracture Toughness 13

2.3. Elastic-Plastic Fracture Mechanics (EPFM) 14
2.3.1. Crack Tip Opening Displacement (CTOD) 15
2.3.2. *J*-integral 16
3. MODE I FRACTURE TOUGHNESS TESTING WITH DISC TYPE ROCK SPECIMENS 19
3.1. Mode I Fracture Toughness Testing Methods 19
3.1.1. Brazilian Disc Test 25
3.1.2. Flattened Brazilian Disc Test 27
3.1.2.1. Investigation of Loading Angle Effect on Test Validity 32
3.1.2.2. Tensile Strength Determination with the FBD Geometry 33
4. NUMERICAL MODELING OF FLATTENED BRAZILIAN DISC SPECIMEN 37
4.1. 2D FBD Modeling 37
4.2. Maximum Dimensionless SIF and Critical Crack Length Formulations 44
5. TESTING THE MECHANICAL PROPERTIES OF ANDESITE 53
5.1. Petrographic Analysis of Gölbaşı Andesite 54
5.2. Static Deformability Test 56
5.3. Indirect Tensile Test (Brazilian Test) 58
5.4. Comparison of Results of Different Researchers 61
6. MODE I FRACTURE TOUGHNESS TESTING WITH FBD GEOMETRY 63
6.1. Specimen Preparation 63
6.2. Fracture Toughness Testing Work 69
6.3. Detection of Critical Crack Length 73
6.4. Determination of Fracture Toughness 75

6.5. FBD Test Validity Conditions..76

6.6. Fracture Toughness Test Results of Andesite Rock.......................................80

6.6.1. FBD Specimens Having 54 mm Diameter 80

6.6.2. FBD Specimens Having 75 mm Diameter 81

6.6.3. FBD Specimens Having 100 mm Diameter 83

6.6.4. FBD Specimens Having 125 mm Diameter 85

7. RESULTS AND DISCUSSION..89

7.1. Specimen Diameter Effect on KIC..89

7.2. Loading Angle Effect on KIC 93

7.3. Evaluation of Test Results in terms of Stress Drop Variation........................97

7.4. Effect of Specimen Diameter and Loading Angle on Critical Crack Length..99

7.5. Stress Analysis for the Loading Angle Effect 101

7.6. Tensile Strength Comparison from Flattened Brazilian Disc Tests of Different Researchers...109

8. CONCLUSIONS AND RECOMMENDATIONS 113

REFERENCES...115

APPENDICES

A. FORCE-DISPLACEMENT CURVES OF FBD TESTS 123

B. EXPERIMENTALLY MEASURED CRITICAL CRACK LENGTHS OF TESTED SPECIMENS 151

LIST OF TABLES

TABLES

Table 2.1. Stress components for mode I loading 10

Table 2.2. Crack tip displacement solution for mode I... 11

Table 3.1. Fracture toughness testing methods on core-based specimens................. 20

Table 3.2. Average mode I fracture toughness values for some rock types determined by Brazilian disc geometry 27

Table 3.3. Average mode I fracture toughness values of some rock types determined by the flattened Brazilian disc geometry 31

Table 4.1. Dimensions of 2D FBD geometry 38

Table 4.2. Boundary Conditions of 2D FBD model... 41

Table 4.3. a, a/R and YI values for FBD geometry with $2\alpha = 20°$ 45

Table 5.1. Results of static deformability tests.. 58

Table 5.2. Results of Brazilian tests 61

Table 5.3. Material properties of andesite compiled from the literature 61

Table 6.1. 2α, $2L$, $YI\ max$, ΔP, $\Delta\sigma_a$, $Pmin$ and KIC values of FBD specimens having 54 mm diameter 80

Table 6.2. Critical crack lengths and critical dimensionless crack lengths for 54 mm diameter FBD specimens 81

Table 6.3. 2α, $2L$, $YI\ max$, ΔP, $\Delta\sigma_a$, $Pmin$ and KIC values of FBD specimens having 75 mm diameter 82

Table 6.4. Critical crack lengths and critical dimensionless crack lengths for 75 mm diameter FBD specimens 83

Table 6.5. 2α, $2L$, $YI\ max$, ΔP, $Pmin$, $\Delta\sigma_a$ and KIC values of FBD specimens having 100 mm diameter 84

Table 6.6. Critical crack lengths and critical dimensionless crack lengths for 100 mm diameter FBD specimens 85

Table 6.7. 2α, $2L$, $YI\ max$, ΔP, $Pmin$, $\Delta\sigma_a$ and KIC values of FBD specimens having 125 mm diameter......86
Table 6.8. Critical crack lengths and critical dimensionless crack lengths for 125 mm diameter FBD specimens......87
Table 7.1. Average mode I fracture toughness for each diameter group......91
Table 7.2. $KIC\ avg$ results of FBD specimens compiled from the literature......92
Table 7.3. $KIC\ avg$ values of FBD specimens having various diameters and loading angles......95
Table 7.4. Loading angle groups for samples with a diameter of 125 mm......96
Table 7.5. Dimensions of A10016s1 and A10038s2 specimens......102
Table 7.6. Correction coefficients calculated for four different approaches......111
Table 7.7. Tensile strength estimation from FBD tests......112
Table A.1. Flattened Brazilian disc specimens with D =54 mm......123
Table A.2. Flattened Brazilian disc specimens with D =75 mm......123
Table A.3. Flattened Brazilian disc specimens with D =100 mm......124
Table A.4. Flattened Brazilian disc specimens with D =125 mm......125

LIST OF FIGURES

FIGURES

Figure 2.1. Basic modes of fracture (Kanninen and Popelar, 1985)............................8
Figure 2.2. Crack tip stress field (Moustabchir et al., 2015) 9
Figure 2.3. Stress intensity factor calculation for different geometries (Wang, 1996) 12
Figure 2.4. Crack tip small scale yielding (Jin and Sun, 2012)..................................14
Figure 2.5. Crack tip opening displacement (Jin and Sun, 2012)..............................15
Figure 2.6. Arbitrary contours surrounding the crack tip (Brocks and Scheider, 2001) 16
Figure 3.1. Mode I fracture toughness tests with CSTBD, DC, CCNBD and MR methods..21
Figure 3.2. Mode I fracture toughness determination with BD, FBD, SCB and CNSCB methods..22
Figure 3.3. Geometries and loading conditions of CB, SECRBB, SNDB and SR specimens..23
Figure 3.4. Brazilian disc under diametral compression 25
Figure 3.5. Flattened Brazilian disc specimen and loading configuration 28
Figure 3.6. Flattened Brazilian disc specimen...29
Figure 4.1. Sketch of the 2D FBD geometry...38
Figure 4.2. Contour integral regions and seam crack in 2D body 39
Figure 4.3. Crack modeling and detailed view of contour integral region................40
Figure 4.4. Loading configuration and boundary conditions of FBD specimen 41
Figure 4.5. Fine meshing of the whole FBD body 42
Figure 4.6. Finite element grid generation for contour integral region 43
Figure 4.7. Deformed shape of FBD geometry in 2D 44

Figure 4.8. Variations of dimensionless stress intensity factor with the dimensionless crack length for 2α =20° 46
Figure 4.9. Variations of dimensionless stress intensity factor with the dimensionless crack length for 2α =0° 47
Figure 4.10. Relation between $YI\ max$ and 2α (in radians) 48
Figure 4.11. Curve fitting for $YI\ max$ vs 2α (in radians) 49
Figure 4.12. Relation between acn/R and 2α (in radians) 50
Figure 4.13. Curve fitting for acn/R and 2α (in radians) 51
Figure 5.1. Location of the quarry where andesite rocks are taken (Google Earth, 2020) 53
Figure 5.2. Thin section analysis for Gölbaşı andesite 54
Figure 5.3. Flow texture in Gölbaşı andesite 55
Figure 5.4. Static deformability test specimen with extensometers 56
Figure 5.5. Axial and diametric stress-strain curves of the sample A-SD-1 57
Figure 5.6. Brazilian disc test configuration 59
Figure 5.7. A typical force vs displacement curve of the sample A-BT-2 60
Figure 5.8. Failure pattern of Brazilian disc specimens 60
Figure 6.1. Rock coring machine 64
Figure 6.2. Thickness adjustment of specimen 65
Figure 6.3. Diametral line positioning with the goniometer 66
Figure 6.4. Reference lines drawn 67
Figure 6.5. Flattening top and bottom ends 68
Figure 6.6. Specimen labeling method 69
Figure 6.7. FBD specimen under compression 70
Figure 6.8. A typical valid force-displacement curve of FBD test on A10030s1 specimen 71
Figure 6.9. Loading procedure 72
Figure 6.10. Critical crack length formation at local minimum load 73

Figure 6.11. Experimental critical crack length measurement ($2ace$ =71.7 mm for A10022s2 specimen) 75
Figure 6.12. Crack formation and related force-displacement record of A12518s1 specimen 77
Figure 6.13. Crack formation and related force-displacement record of A12528s1 specimen 78
Figure 6.14. Crack formation and related force-displacement record of A12542s2 specimen 78
Figure 6.15. Invalid force-displacement curve due to the drastic fall in load 79
Figure 6.16. Invalid force-displacement curve due to the two-stage load drop 79
Figure 7.1. KIC values of FBD specimens having various diameters (Regardless of 2α) 90
Figure 7.2. Loading angle effect on KIC values 94
Figure 7.3. Variation of KIC values with loading angles for 125 mm diameter specimens 97
Figure 7.4. Stress drop versus specimen diameter 98
Figure 7.5. ac/R vs. 2α for FBD specimens having 54 mm diameter 99
Figure 7.6. ac/R vs. 2α for FBD specimens having 125 mm diameter 100
Figure 7.7. Geometric dimensions of A10016s1 and A10038s2 specimens 101
Figure 7.8. Von mises stress path for $2\alpha = 16°$ 103
Figure 7.9. Von mises stress path for $2\alpha = 38°$ 103
Figure 7.10. Von mises stress contours around the crack tip for $2\alpha = 16°$ 104
Figure 7.11. Von mises stress contours around the crack tip for $2\alpha = 38°$ 104
Figure 7.12. Comparison of Von mises stress values for $2\alpha = 16°$ and $2\alpha = 38°$ 105
Figure 7.13. Stress perpendicular to the crack plane for $2\alpha = 16°$ 106
Figure 7.14. Stress perpendicular to the crack plane for $2\alpha = 38°$ 106
Figure 7.15. Stress perpendicular to the crack plane around the crack tip for $2\alpha = 16°$ 107

Figure 7.16. Stress perpendicular to the crack plane around the crack tip for $2\alpha = 38°$ 107
Figure 7.17. Comparison of stress perpendicular to crack plane values for $2\alpha = 16°$ and $2\alpha = 38°$ 108
Figure A.1. Force versus displacement curve of A5418s1 specimen 125
Figure A.2. Force versus displacement curve of A5420s1 specimen 126
Figure A.3. Force versus displacement curve of A5420s2 specimen 126
Figure A.4. Force versus displacement curve of A5426s1 specimen 127
Figure A.5. Force versus displacement curve of A5426s2 specimen 127
Figure A.6. Force versus displacement curve of A5432s1 specimen 128
Figure A.7. Force versus displacement curve of A5432s2 specimen 128
Figure A.8. Force versus displacement curve of A5434s1 specimen 129
Figure A.9. Force versus displacement curve of A7518s1 specimen 129
Figure A.10. Force versus displacement curve of A7522s1 specimen 130
Figure A.11. Force versus displacement curve of A7522s2 specimen 130
Figure A.12. Force versus displacement curve of A7524s1 specimen 131
Figure A.13. Force versus displacement curve of A7524s2 specimen 131
Figure A.14. Force versus displacement curve of A7530s1 specimen 132
Figure A.15. Force versus displacement curve of A7530s2 specimen 132
Figure A.16. Force versus displacement curve of A7534s1 specimen 133
Figure A.17. Force versus displacement curve of A7536s1 specimen 133
Figure A.18. Force versus displacement curve of A7538s1 specimen 134
Figure A.19. Force versus displacement curve of A7538s2 specimen 134
Figure A.20. Force versus displacement curve of A10016s1 specimen 135
Figure A.21. Force versus displacement curve of A10019s1 specimen 135
Figure A.22. Force versus displacement curve of A10020s1 specimen 136
Figure A.23. Force versus displacement curve of A10022s1 specimen 136
Figure A.24. Force versus displacement curve of A10022s2 specimen 137
Figure A.25. Force versus displacement curve of A10024s1 specimen 137

Figure A.26. Force versus displacement curve of A10024s2 specimen 138
Figure A.27. Force versus displacement curve of A10026s1 specimen 138
Figure A.28. Force versus displacement curve of A10026s2 specimen 139
Figure A.29. Force versus displacement curve of A10028s1 specimen 139
Figure A.30. Force versus displacement curve of A10028s2 specimen 140
Figure A.31. Force versus displacement curve of A10030s1 specimen 140
Figure A.32. Force versus displacement curve of A10032s1 specimen 141
Figure A.33. Force versus displacement curve of A10034s1 specimen 141
Figure A.34. Force versus displacement curve of A10034s2 specimen 142
Figure A.35. Force versus displacement curve of A10036s1 specimen 142
Figure A.36. Force versus displacement curve of A10038s1 specimen 143
Figure A.37. Force versus displacement curve of A10038s2 specimen 143
Figure A.38. Force versus displacement curve of A12518s1 specimen 144
Figure A.39. Force versus displacement curve of A12520s1 specimen 144
Figure A.40. Force versus displacement curve of A12520s2 specimen 145
Figure A.41. Force versus displacement curve of A12524s1 specimen 145
Figure A.42. Force versus displacement curve of A12524s2 specimen 146
Figure A.43. Force versus displacement curve of A12528s1 specimen 146
Figure A.44. Force versus displacement curve of A12528s2 specimen 147
Figure A.45. Force versus displacement curve of A12534s1 specimen 147
Figure A.46. Force versus displacement curve of A12534s2 specimen 148
Figure A.47. Force versus displacement curve of A12536s1 specimen 148
Figure A.48. Force versus displacement curve of A12538s1 specimen 149
Figure A.49. Force versus displacement curve of A12538s2 specimen 149
Figure A.50. Force versus displacement curve of A12542s1 specimen 150
Figure A.51. Force versus displacement curve of A12542s2 specimen 150
Figure B.1. Critical crack length measurement of A5418s1 coded specimen ($2ace$ =43.9 mm) 151
Figure B.2. Critical crack length measurement of A5420s1 coded specimen ($2ace$ =41.6 mm) 152

Figure B.3. Critical crack length measurement of A5420s2 coded specimen ($2ace$ =42.1 mm) 152
Figure B.4. Critical crack length measurement of A5426s1 coded specimen ($2ace$ =38.0 mm) 153
Figure B.5. Critical crack length measurement of A5426s2 coded specimen ($2ace$ =38.5 mm) 153
Figure B.6. Critical crack length measurement of A5432s1 coded specimen ($2ace$ =34.8 mm) 154
Figure B.7. Critical crack length measurement of A5432s2 coded specimen ($2ace$ =36.1 mm) 154
Figure B.8. Critical crack length measurement of A5434s1 coded specimen ($2ace$ =32.7 mm) 155
Figure B.9. Critical crack length measurement of A7518s1 coded specimen $2ace$ =58.1 mm)...155
Figure B.10. Critical crack length measurement of A7522s1 coded specimen ($2ace$ =55.5 mm) 156
Figure B.11. Critical crack length measurement of A7522s2 coded specimen ($2ace$ =55.3 mm) 156
Figure B.12. Critical crack length measurement of A7524s1 coded specimen ($2ace$ =53.1 mm) 157
Figure B.13. Critical crack length measurement of A7524s2 coded specimen ($2ace$ =53.4 mm) 157
Figure B.14. Critical crack length measurement of A7530s1 coded specimen ($2ace$ =49.3 mm) 158
Figure B.15. Critical crack length measurement of A7530s2 coded specimen ($2ace$ =51.6 mm) 158
Figure B.16. Critical crack length measurement of A7534s1 coded specimen ($2ace$ =47.2 mm) 159

Figure B.17. Critical crack length measurement of A7536s1 coded specimen ($2ace$ =44.4 mm) 159

Figure B.18. Critical crack length measurement of A7538s1 coded specimen ($2ace$ =43.0 mm) 160

Figure B.19. Critical crack length measurement of A7538s2 coded specimen ($2ace$ =43.1 mm) 160

Figure B.20. Critical crack length measurement of A10016s1 coded specimen ($2ace$ =82.1 mm) 161

Figure B.21. Critical crack length measurement of A10019s1 coded specimen $2ace$ =75.7 mm) 161

Figure B.22. Critical crack length measurement of A10020s1 coded specimen ($2ace$ =74.8 mm) 162

Figure B.23. Critical crack length measurement of A10022s1 coded specimen ($2ace$ =72.6 mm) 162

Figure B.24. Critical crack length measurement of A10022s2 coded specimen ($2ace$ =73.7 mm) 163

Figure B.25. Critical crack length measurement of A10024s1 coded specimen ($2ace$ =72.6 mm) 163

Figure B.26. Critical crack length measurement of A10024s2 coded specimen ($2ace$ =73.4 mm) 164

Figure B.27. Critical crack length measurement of A10026s1 coded specimen ($2ace$ =69.2 mm) 164

Figure B.28. Critical crack length measurement of A10026s2 coded specimen ($2ace$ =71.4 mm) 165

Figure B.29. Critical crack length measurement of A10028s1 coded specimen $2ace$ =67.4 mm) 165

Figure B.30. Critical crack length measurement of A10028s2 coded specimen ($2ace$ =68.1 mm) 166

Figure B.31. Critical crack length measurement of A10030s1 coded specimen ($2ace$ =65.9 mm) 166
Figure B.32. Critical crack length measurement of A10032s1 coded specimen ($2ace$ =66.7 mm) 167
Figure B.33. Critical crack length measurement of A10034s1 coded specimen ($2ace$ =62.8 mm) 167
Figure B.34. Critical crack length measurement of A10034s2 coded specimen ($2ace$ =63.1 mm) 168
Figure B.35. Critical crack length measurement of A10036s1 coded specimen ($2ace$ =59.4 mm) 168
Figure B.36. Critical crack length measurement of A10038s1 coded specimen ($2ace$ =57.3 mm) 169
Figure B.37. Critical crack length measurement of A10038s2 coded specimen ($2ace$ =57.5 mm) 169
Figure B.38. Critical crack length measurement of A12518s1 coded specimen ($2ace$ =96.6 mm) 170
Figure B.39. Critical crack length measurement of A12520s1 coded specimen ($2ace$ =94.3 mm) 170
Figure B.40. Critical crack length measurement of A12520s2 coded specimen ($2ace$ =94.3 mm) 171
Figure B.41. Critical crack length measurement of A12524s1 coded specimen ($2ace$ =90.8 mm) 171
Figure B.42. Critical crack length measurement of A12524s2 coded specimen $2ace$ =87.8 mm)........172
Figure B.43. Critical crack length measurement of A12528s1 coded specimen ($2ace$ =83.1 mm) 172
Figure B.44. Critical crack length measurement of A12528s2 coded specimen ($2ace$ =84.3 mm) 173

Figure B.45. Critical crack length measurement of A12534s1 coded specimen ($2ace$ =76.4 mm) 173

Figure B.46. Critical crack length measurement of A12534s2 coded specimen ($2ace$ =76.6 mm) 174

Figure B.47. Critical crack length measurement of A12536s1 coded specimen ($2ace$ =74.5 mm) 174

Figure B.48. Critical crack length measurement of A12538s1 coded specimen ($2ace$ =71.7mm) 175

Figure B.49. Critical crack length measurement of A12538s2 coded specimen ($2ace$ =71.8 mm) 175

Figure B.50. Critical crack length measurement of A12542s1 coded specimen ($2ace$ =67.8 mm) 176

Figure B.51. Critical crack length measurement of A12542s2 coded specimen ($2ace$ =67.7 mm) 176

LIST OF ABBREVIATIONS

ABBREVIATIONS

2D : Two-dimensional
3D : Three-dimensional
ASTM : American Society for Testing and Materials
BD : Brazilian disc
BDT : Brazilian disc test
CB : Chevron bend
CCNBD : Cracked chevron notched Brazilian disc
CNSCB : Chevron notched semi-circular bending
CSTBD : Cracked straight through Brazilian disc
CTOD : Crack tip opening displacement
DC : Diametric compression
DOF : Degree of freedom
EPFM : Elastic-plastic fracture mechanics
FBD : Flattened Brazilian disc
GBD : Grooved Brazilian disc
ISRM : International Society for Rock Mechanics
LEFM : Linear elastic fracture mechanics
MR : Modified ring
SCB : Semi-circular bending
SECRBB : Straight edge cracked round bar bend
SIF : Stress intensity factor
SNDB : Straight-notched disc bending
SR : Short rod
TSI : Turkish Standards Institute
UCS : Uniaxial compressive strength

LIST OF SYMBOLS

SYMBOLS

a : Half of the crack length

a_c : Half of the critical crack length

$2a$: Crack length

$2a_c$: Critical crack length

$2a_{ce}$: Critical crack length determined from experimental results

$2a_{cn}$: Critical crack length computed from numerical modeling

a/R : Dimensionless crack length

a_c/R : Critical dimensionless crack length

a_{cn}/R : Critical dimensionless crack length computed from numerical modeling

a_{ce}/R : Critical dimensionless crack length acquired from the test results

A : Andesite

D : Specimen diameter

E : Young’s modulus (Elastic modulus)

G : Energy release rate

G_C : Critical energy release rate

G_I : Energy release rate for mode I

J : J-integral

k : Correction coefficient

K : Stress intensity factor

K_C : Fracture toughness

K_I : Mode I stress intensity factor

K_{II} : Mode II stress intensity factor

K_{III} : Mode III stress intensity factor

K_{IC} : Mode I fracture toughness

$K_{IC\ avg}$: Average mode I fracture toughness
L : Half of the flattened end width
$2L$: Flattened end width
P : Applied concentrated load
P_{max} : Local maximum load
P_{min} : Local minimum load
R : Specimen radius
S_{11} : Stress component in $x-$direction
S_{22} : Stress component in $y-$direction
t : Specimen thickness
Y_I : Mode I dimensionless stress intensity factor
$Y_{I\ max}$: Maximum mode I dimensionless stress intensity factor
θ : Polar coordinate
α : Half of the loading angle
2α : Loading angle
$2\alpha_{max}$: Maximum loading angle
$2\alpha_{min}$: Minimum loading angle
σ : Applied stress
σ_t : Tensile strength
ΔP : Load drop
$\Delta\sigma_a$: Stress drop
ε : Flattened Brazilian disc coefficient
μ : Shear modulus
τ : Shear stress
v : Poisson’s ratio

CHAPTER 1

INTRODUCTION

No material in nature can be considered as completely flawless and homogeneous. Pores, flaws, and defects are the structural impurities that can be observed by examination of the internal structure of a material. Under loading, these defects may cause important issues in engineering practice. For instance, in earth sciences, these issues are originated by some discontinuities such as faults, joints, and bedding planes. In addition to the conventional analyses, these discontinuity problems are suggested to be investigated, utilizing the principles of fracture mechanics.

Fractures and cracks have a significant influence on the failure behavior of the structures because they play a role as a stress concentrator, especially for brittle materials. In mining, geotechnical, and civil engineering practice, these impurities can cause abrupt and disastrous damages, which are catastrophic; therefore, they may cause an interruption in the whole activity. Pre-caution measures like defect design can be employed to ensure the structural stability of the system by applying the fundamentals of fracture mechanics.

Cracks as stress intensifiers in the materials have been studied for more than 100 years by fracture mechanics. How a crack originates and propagates by applied loads on rocks and other brittle materials such as concrete, mortars, etc. is the study of fracture mechanics. The critical load threshold is reached due to loading, the crack propagates unstably within the material and causes its cohesion lost through the cohesive zone. This critical point is called fracture toughness denoted as K_C of that material, and it is a mechanical property.

In the past, due to crack formation and growth, many catastrophic accidents have occurred, for example, the Liberty Fleet Ships failure, the Titanic accident, the Boston molasses disaster, and the Comet disaster can be given for fracture-related disasters. In order to prevent such accidents, fracture mechanics has been utilized for the design and integrity assessment of the engineering structures. The main objective of fracture mechanics in the disciplines, such as mechanical engineering and aerospace engineering, is to protect the structural element in local or the entire structure in global from the fracturing. On the other hand, in rock fracture mechanics, the main objective is to evaluate input energy for the new fracture surfaces to be created through the ligament.

1.1. Statement of The Problem

Hydraulic fracturing, rock excavations, rock cutting, rock bursts, and rock slope stability engineering require a comprehensive understanding of the rock fracture mechanism. A thorough understanding of fracture processes, including crack initiation and propagation, is based on a detailed understanding of mode I fracture toughness. Therefore, different methods have been developed to measure the mode I fracture toughness of rocks. The flattened Brazilian method (FBD) is one of those methods, and it is preferred due to its easiness of specimen preparation and practical loading configuration.

The mode I fracture toughness is declared to be a material property, so it is expected material in different sizes have almost the same fracture toughness. However, in the literature, there is an ongoing discussion as to whether mode I fracture toughness changes depending on sample size. Since the size effect phenomenon has been a controversial and unclear point, this issue should be investigated and clarified in an easy way.

In the previous studies, the loading angle range of the FBD geometry was narrow, and sample diameters were limited. In this study, it is planned to use FBD geometries with different combinations of diameters and loading angles, as well as using a wider loading angle range. The effect of varying specimen diameter and loading angle on mode I fracture toughness will be investigated with the FBD method.

1.2. Research Objectives

This study aims to measure the mode I fracture toughness of Gölbaşı andesite in a simple and convenient way.

The objectives of conducting this research are to investigate the specimen size effects on mode I fracture toughness with flattened Brazilian disc method, and to develop two new equations in terms of loading angle, one of which is used to calculate the critical dimensionless crack length and the other to determine the maximum dimensionless stress intensity factor.

1.3. Research Methodology

The methodology of this study covers two main parts that are numerical computation study and experimental study, and contains the following steps;

- Testing the conventional mechanical properties of andesite (such as elastic modulus E, Poisson's ratio v, uniaxial compressive strength UCS, and tensile strength σ_t)
- 2D modeling of flattened Brazilian disc geometries in different sizes to compute mode I stress intensity factor
- Studying the maximum mode I dimensionless stress intensity factor and loading angle relation numerically, and formulating this relation using the curve fitting program
- Numerical analysis of critical dimensionless crack length and loading angle relation, and developing a new formula for this relation
- Preparation of FBD samples
- Mode I fracture toughness testing work with FBD method using MTS 815 rock testing system
- Detection of experimental critical crack lengths and comparison with numerical results
- Investigating the size effect on mode I fracture toughness by changing specimen diameters

- Examining the boundary influence on mode I fracture toughness by changing loading angles
- Determination of average fracture toughness of Gölbaşı andesite for each diameter group and loading angle group
- 3D modeling of flattened Brazilian disc geometries for stress analysis
- Tensile strength determination with FBD geometry
- Evaluation and interpretation of test results

1.4. Organization of Thesis

This thesis comprises of eight chapters. Firstly, Chapter 1 covers the general information about the thesis and problem. In Chapter 2, fracture toughness, intensity factor, LEFM, and EPFM concepts, and literature review about fracture mechanics are described. Chapter 3 contains the mode I fracture toughness test methods applied using disc samples. The numerical modeling of 2D FBD geometries is presented in Chapter 4 to develop maximum mode I dimensionless stress intensity factor and critical dimensionless crack length formulas. Testing the mechanical properties of andesite is presented in Chapter 5, followed by details of the mode I fracture toughness experiments with the FBD method, and their results are given in Chapter 6. In Chapter 7, interpretation and evaluation of all test results are presented. In the last part, Chapter 8, conclusions, and recommendations for future research are given.

CHAPTER 2

BASICS OF FRACTURE MECHANICS

Fracture mechanics emerged in the early 1900s and developed as a new discipline in science and engineering in the following decades. In the first half of the 1900s, it proved itself as a new consideration in the design processes, since design must also be safe against the initiation and propagation of defects and cracks.

The developments and fundamentals of fracture mechanics are summarized in the following parts.

2.1. Literature Review

Kirsch (1898) employed a mathematical method to determine stress concentration around a circular hole in an infinite plate subjected to tensile stress. Like Kirsch's linear elastic solution, Inglis (1913) examined the elastic stress distribution with an elliptic hole. He deduced that the stress in the vicinity of the hole is directly proportional to the square root of the crack length and inversely proportional to the radius of curvature.

With the help of Inglis' solution, Griffith calculated fracture stress and total energy of an infinite plate containing an internal crack length of $2a$ under biaxial loading (Griffith, 1921; Griffith, 1924). Griffith's work on the brittle fracture of glass is known as the pioneering work of fracture mechanics because he proposed the energy balance approach, which is one of the two fundamental approaches to fracture mechanics. Griffith's approach is based on consideration of energy balance that required surface energy to create new surfaces is obtained from the liberated strain energy of a solid body when the crack propagates.

The term $\sigma\sqrt{a}$, which is the stress intensity factor for a crack in the infinite plate under stress, was introduced by Griffith as a constant value. Griffith (1924) also depicted the relationship between the fracture strength and crack size and gave the following expression for fracture stress calculations.

For plane strain;

$$\sigma_c = \sqrt{\frac{2E(1-\nu)^2\gamma}{\pi a}} \tag{2.1}$$

Where;

σ_c: Fracture stress (MPa)

E: Young's modulus (GPa)

ν: Poisson's ratio

γ: Specific surface energy (J/m^2 or N/m)

a: Crack length at the edge of the plate or half of the crack length in the interior of the plate

However, Sack (1946) and Munz and Fett (2015) put forward that Griffith gave the equation incorrectly for plane strain condition. For plane strain, the correct equation was given by:

$$\sigma_c = \sqrt{\frac{2E\gamma}{\pi(1-\nu)^2 a}} \tag{2.2}$$

Westergaard (1934) computed stress and displacement solution at the crack tip. Lyse and Steward (1935) experimentally confirmed Westergaard's stress solution and found a similar stress diagram. Then, Sack (1946) extended Griffith's energy balance approach to three-dimensions by calculation of strain and energy correction. Due to the Poisson effect, the results of the two studies were different. Williams (1957) verified Westergaard's solution and described stress and displacement distribution at the vicinity of the crack tip for any crack type and loading conditions.

Griffith's theory did not take into account the plastic deformation around the crack tip, so it cannot be applied to ductile materials. Irwin (1948) stated that the stored strain energy in ductile materials was consumed not only for creating new surfaces but also for the required energy for plastic deformation. He defined the critical energy release rate G_C to formulate a crack growth criterion. The energy release rate characterizes the total strain energy released per extension of crack. Irwin (1957) introduced three different fracture modes in the region at the crack tips: mode I (opening mode), mode II (sliding mode), and mode III (tearing mode). Irwin examined the stress state around the crack tip when LEFM prevails. He defined the magnitude of the local stress around this field as the stress intensity factor.

In the early 1960s, there was a growing interest in the application of elastic-plastic fracture mechanics, so elastic-plastic fracture parameters and analysis of crack tip plastic regions were developed. In order to determine the size of the plastic zone near the crack tip Irwin (1960) suggested a stress relaxation model. With the assumption of small-scale yielding, he calculated the adjusted stress intensity factor using an effective crack length that is the sum of actual crack length and half-length of the plastic zone. Dugdale (1960) determined the plastic zone size for both small-scale yielding and large-scale yielding assumption. Wells (1961) and (1963) established a crack growth criterion called crack tip opening displacement (CTOD) to analyze the plastic behavior of crack. CTOD can be determined with Irwin's model or Dugdale's model. Rice (1968) developed the J-integral concept that is defined as a path independent line integral that measures the stresses and strains on a path. He described J-integral as a way of determining the energy release rate and proposed a mathematical expression to determine the energy release rate for both linear elastic and elastic-plastic materials.

Linear elastic fracture mechanics (LEFM) and elastic-plastic fracture mechanics (EPFM) are basic theories of fracture. LEFM is applicable when plastic deformation is limited to an insignificant region near the crack tip. In other words, the size of the plastic region is smaller than the size of the crack. If the nonlinear behavior of the crack tip is not small enough, LEFM is usually not sufficient, and EPFM is used for large scale yield conditions. In LEFM, it is assumed that the material is both linear elastic and isotropic, whereas EFM is based on an assumption the material is elastic-plastic and isotropic.

2.2. Linear Elastic Fracture Mechanics (LEFM)

LEFM theory commonly studies the failure of brittle materials such as rock, glass, ceramic, and cast iron, caused by crack initiation and propagation. On the basis of LEFM, crack-tip stress and displacement field are analyzed by methods of the theory of elasticity. In LEFM, the size of the plastic zone near the crack tip is considerably smaller than the crack length, so the main assumption when adopting this theory is that non-linear effects are negligible.

2.2.1. Modes of Fracture

Modes of fracture are categorized according to crack tip loading. Cracks can deform in three fundamental fracture modes, as sketched in Figure 2.1.

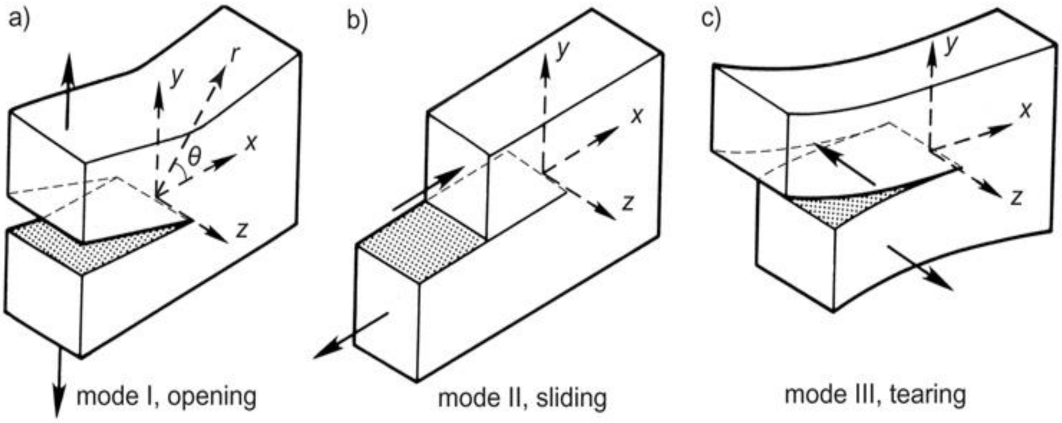

Figure 2.1. Basic modes of fracture (Kanninen and Popelar, 1985)

These three independent movements are recognized as mode I, mode II, and mode III, respectively. Mixed-mode loading is the simultaneous formation of two or all three basic modes. In mode I, also known as pure tension or opening mode, the direction of forces and crack plane displacements are perpendicular to the crack planes. The crack extension is in the crack plane direction. Brittle materials are considerably weaker under tension, so mode I is the most significant failure mode type. Mode II is also called sliding or shear mode, and it is characterized by crack surfaces slide over each other. Applied forces and crack plane displacements are parallel to the crack plane. In mode III, out of plane shearing or tearing mode, the force and crack surface displacements are parallel to the front-line of the crack.

2.2.2. Crack Tip Stress and Displacement Field

The crack tip of linear elastic materials can be subjected to opening, shearing, tearing, or mixed-mode loading. Stress fields ahead of the crack tip are expressed as a function of polar coordinates (r,θ) or Cartesian coordinates (x,y) and stress intensity factor for mode I, mode II and mode III. Stress components of the crack tip in terms of both polar and rectangular coordinates are schematically illustrated in Figure 2.2.

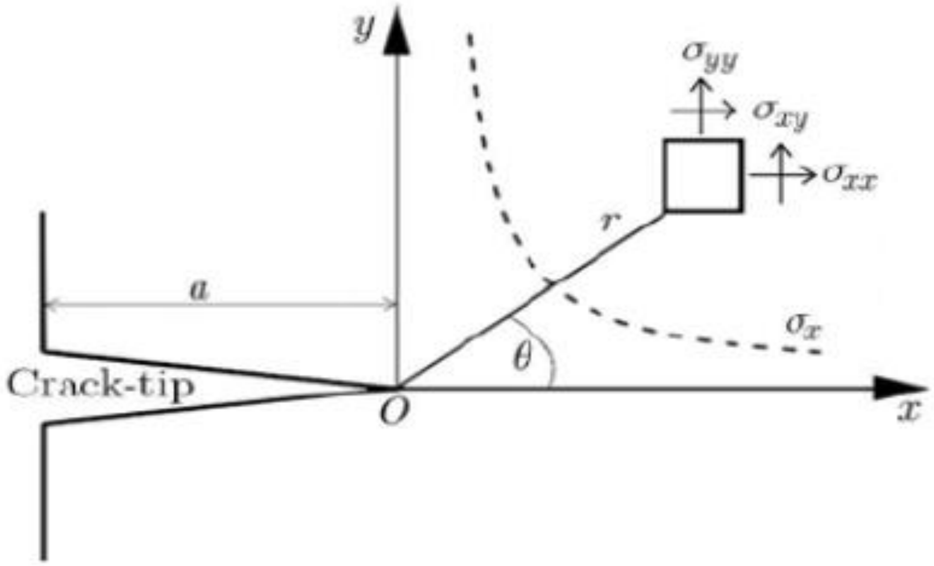

Figure 2.2. Crack tip stress field (Moustabchir et al., 2015)

The stress field in the region at the crack tip produces stress singularity. The decrease in radial distance measured from the crack tip leads to an increase in stress values, and crack causes infinite stress at r =0. Stress components at the immediate vicinity of the crack tip have an inverse square root singularity, and it means $\propto \frac{1}{\sqrt{r}}$.

General analytical solutions of stress and displacement at the crack tip for mode I are represented in Table 2.1 and Table 2.2, respectively.

Table 2.1. *Stress components for mode I loading*

Mode I	
σ_{xx}	$= \frac{K_I}{\sqrt{2\pi r}} \cos(\frac{\theta}{2}) \left[1 - \sin(\frac{\theta}{2})\sin(\frac{3\theta}{2})\right]$
σ_{yy}	$= \frac{K_I}{\sqrt{2\pi r}} \cos(\frac{\theta}{2}) \left[1 + \sin(\frac{\theta}{2})\sin(\frac{3\theta}{2})\right]$
σ_{zz}	$= \begin{cases} 0 \text{ for plane stress} \\ v(\sigma_{xx} + \sigma_{yy}) \text{ for plane strain} \end{cases}$
τ_{xy}	$= \frac{K_I}{\sqrt{2\pi r}} \cos(\frac{\theta}{2}) \sin(\frac{\theta}{2}) \cos(\frac{3\theta}{2})$
τ_{yz}	$= 0$
τ_{xz}	$= 0$

Table 2.2. *Crack tip displacement solution for mode I*

Mode I	
u_x	$= \begin{cases} \dfrac{K_I}{2\mu}\sqrt{\dfrac{r}{2\pi}}\cos(\dfrac{\theta}{2})\left[\kappa - 1 + 2\sin^2(\dfrac{\theta}{2})\right] \\ \dfrac{1+v}{4\pi E}K_I\sqrt{2\pi r}\left[(2\kappa - 1)\cos(\dfrac{\theta}{2}) - \cos(\dfrac{3\theta}{2})\right] \end{cases}$
u_y	$= \begin{cases} \dfrac{K_I}{2\mu}\sqrt{\dfrac{r}{2\pi}}\sin(\dfrac{\theta}{2})\left[\kappa + 1 - 2\cos^2(\dfrac{\theta}{2})\right] \\ \dfrac{1+v}{4\pi E}K_I\sqrt{2\pi r}\left[(2\kappa + 1)\sin(\dfrac{\theta}{2}) - \sin(\dfrac{3\theta}{2})\right] \end{cases}$
u_z	$= 0$

where μ is shear modulus and κ is a parameter that varies depending on whether the condition is plane stress or plane strain.

$$\kappa = \begin{cases} \dfrac{3-v}{1+v} \text{ for plane stress} \\ 3 - 4v \text{ for plane strain} \end{cases} \tag{2.3}$$

2.2.3. Stress Intensity Factor

In LEFM, there are two basic approaches: Griffith’s energy balance theory and Irwin’s crack tip stress field analysis. Based on the LEFM assumption, Irwin (1957) developed the stress intensity factor, and this parameter is one of the most useful and fundamental approaches for engineering practice. Stress intensity factor gives the grade of stress concentration around the crack tip and measures the intensities of the singular stress field. The stress intensity factor is abbreviated SIF and denoted as K. The magnitude of applied stress, the length, and location of the crack, the geometry of the component, and the loading conditions are effective in the calculation of SIF. The general form of the stress intensity factor in mode I loading is given in Equation 2.4.

$$K_I = \sigma\sqrt{\pi\, a}\, f\left(\frac{a}{W}\right) \tag{2.4}$$

K_I: Stress intensity factor corresponding to the opening mode of fracture (MPa$\sqrt{\text{m}}$)

σ: Applied stress to the component (MPa)

a: Crack length (m)

$f\left(\frac{a}{W}\right)$: Dimensionless function which depends on crack and specimen geometry

W: Specimen width (m)

Stress intensity factor formulas for several well-known geometries are given in Figure 2.3.

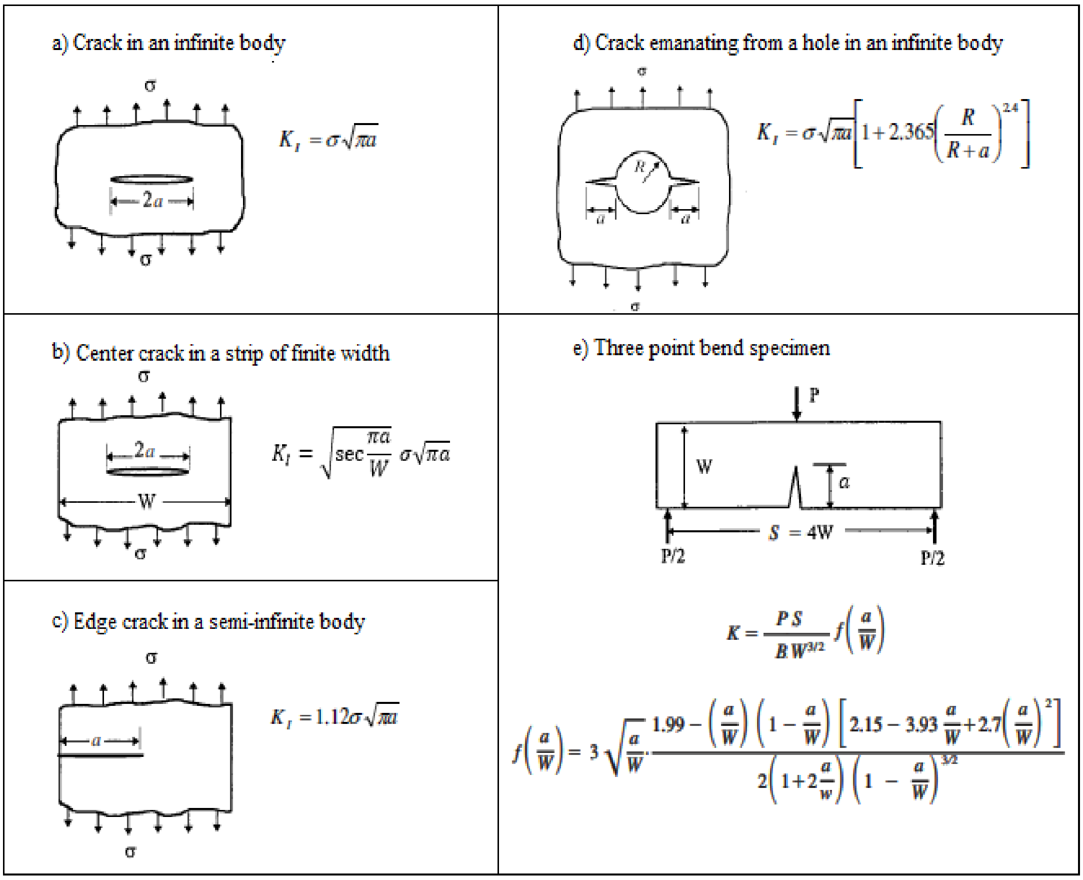

Figure 2.3. Stress intensity factor calculation for different geometries (Wang, 1996)

2.2.4. The Relations between Energy Release Rate and Stress Intensity Factor

The energy release rate G is introduced by Irwin (1957) is expressed as the amount of energy dissipated by fracture during unit crack extension. For brittle materials, the value at which G is equal to 2γ is called a critical energy release rate or crack resistance force G_C. When the strain energy released from the material is equal to or greater than the surface energy required to form new surfaces, the crack can propagate. This criterion is the global failure criterion derived from Griffith's energy balance approach. The local fracture criterion is expressed in terms of the stress intensity factor obtained from the crack tip stress field. The relationship between the energy release rate and stress intensity factor in mode I loading is defined in the following equations.

For plane stress;

$$G_I = \frac{{K_I}^2}{2\mu(1+v)} = \frac{{K_I}^2}{E} \tag{2.5}$$

For plane strain;

$$G_I = \frac{(1-v)}{2\mu}{K_I}^2 = \frac{(1-v^2)}{E}{K_I}^2 \tag{2.6}$$

where G_I is the energy release rate for mode I (MPa.m or J/m^2), E is Young's modulus (MPa), v is Poisson's ratio, K_I is mode I stress intensity factor (MPa$\sqrt{\mathrm{m}}$) and μ is shear modulus calculated by Equation 2.7.

$$\mu = \frac{E}{2(1+v)} \tag{2.7}$$

2.2.5. Fracture Toughness

Irwin (1957) established a local crack growth criterion indicating that when stress intensity factor attains a critical value, crack extension occurs. The critical value of the stress intensity factor is called fracture toughness and denoted by K_C. This parameter signifies the resistance of the materials to crack growth.

Theoretically, fracture toughness is assumed to be a material constant and measured by using standard specimens. However, intrinsic factors such as composition and microstructure of the material and extrinsic factors like the geometry of the test specimen, loading rate, and loading type have an influence on the fracture toughness of the material (Obaraa et al., 2017).

2.3. Elastic-Plastic Fracture Mechanics (EPFM)

Theoretically, the linear elastic fracture mechanics assumes that the elastic stress around the crack tip reaches infinite value when the distance measured from the crack tip approaches zero. However, in reality, stresses remain finite, and plastic yielding occurs in the vicinity of the crack tip if elastic stresses reach a critical level. LEFM can only be applied once the size of the plastic region in the vicinity of the crack tip is negligible compared to the crack length. This situation is referred to as small scale yielding. In Figure 2.4, the plastic deformation region around the crack tip is confined in the *K*-dominance zone of the LEFM. *K*-field zone is dominant around the crack tip, and it has inverse square root singular stresses.

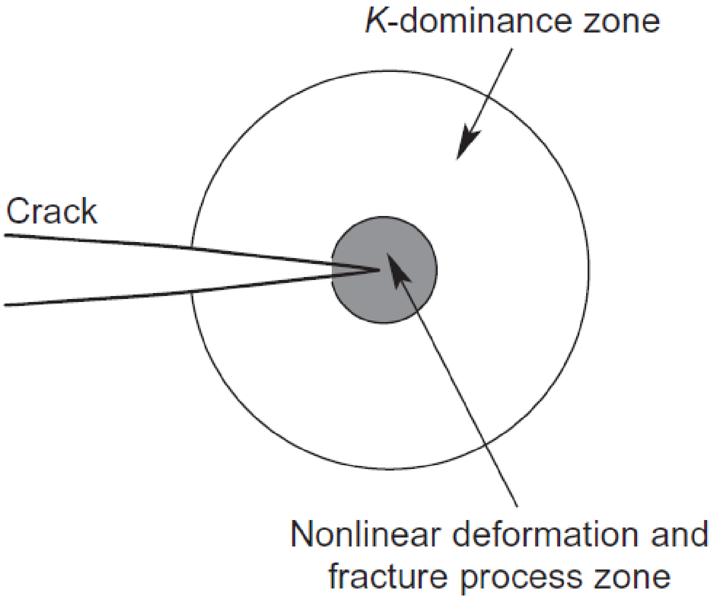

Figure 2.4. Crack tip small scale yielding (Jin and Sun, 2012)

When the nonlinear deformation region around the crack tip is not small enough, and thus small-scale yielding cannot be assumed, elastic-plastic fracture mechanics is applicable to analyze the behavior of crack tip fields. EPFM assumes that material exhibits nonlinear behavior, and large-scale yielding conditions are satisfied. Under large scale yielding conditions, the size of the plastic region is larger than the crack length. Crack tip opening displacement and J integral are fracture parameters generally used for the analysis of plastic behavior of the crack.

2.3.1. Crack Tip Opening Displacement (CTOD)

Wells (1961) and (1963) proposed crack tip opening displacement methods as fracture parameters for crack initiation and propagation in ductile materials. This criterion states that the initial sharp crack tip is blunted by plastic deformation at the crack tip. Otherwise, there will be stress singularity at the vicinity of the crack tip. The crack tip displacement at the original crack tip and CTOD at 90° line intersections are illustrated in Figure 2.5. The crack tip opening displacement is denoted by δ and experimentally determined. The critical value of CTOD is used to measure fracture toughness of materials exhibit elastic-plastic behavior.

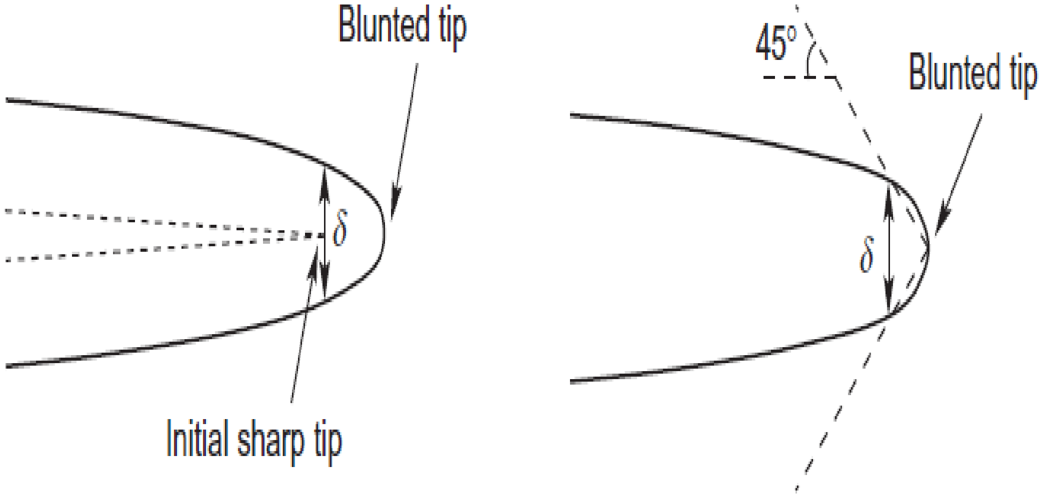

Figure 2.5. Crack tip opening displacement (Jin and Sun, 2012)

2.3.2. *J*-integral

In elastic-plastic fracture mechanics, the behavior of the crack can be described by J-integral. Rice (1968) established the J-integral theory (J for James Rice) based on the energy release rate concept. The J-integral was the way of calculating the strain energy release rate. Rice evaluated J-integral for both small-scale yielding and large-scale yielding conditions. He stated that the J-integral theory was applicable to both linear elastic and elastic-plastic materials. In Figure 2.6, integral is evaluated starting from the lower crack surface and continuing along to the contour Γ.

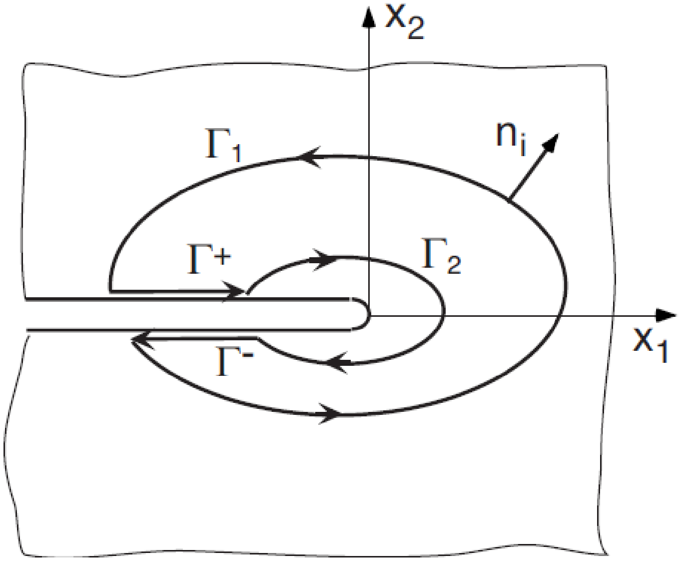

Figure 2.6. Arbitrary contours surrounding the crack tip (Brocks and Scheider, 2001)

For small-scale yielding, J represents the reduction in potential energy per unit crack growth and can be described in Equation 2.8. This means that J is identical to G in linear elasticity so that J can be used in the fracture criteria of LEFM instead of G.

$$G = J = \int_{\Gamma} \left(W dy - T_i \frac{\partial u_i}{\partial x} d\Gamma \right) = \int_{\Gamma} \left(W dn_1 - \sigma_{ij} \frac{\partial u_i}{\partial x} n_j \right) \qquad (2.8)$$

Where;

Γ: Integration path surrounding the crack tip

σ_{ij}: Stress tensor

ε_{ij}: Strain tensor

n_j: x_2 component of unit outward vector which is normal to the contour Γ

T_i: Traction vector $T_i = \sigma_{ij} n_j$

W: Strain energy density that is the stored elastic energy per unit of volume $W = \int_{\Gamma}^{\varepsilon_{ij}} \sigma_{ij}\, d\varepsilon_{ij}$

u_i: x_1 component of the displacement vector

$d\Gamma$: Element of arc on Γ contour

For mode I, under small scale yielding conditions, the relation between J and K for the plane strain deformation field is given in Equation 2.9.

$$J_I = G_I = \frac{(1 - v^2)}{E} {K_I}^2 \tag{2.9}$$

In Chapter 4, it will be seen that J-integral is the major output of the numerical modeling work to estimate the mode I SIFs of various geometries.

CHAPTER 3

MODE I FRACTURE TOUGHNESS TESTING WITH DISC TYPE ROCK SPECIMENS

Fracture toughness tests are commonly performed on core-based specimens such as discs and cylinders since rock cores can be easily obtained in pieces from the boreholes of site investigation.

The opening mode is a critical type of failure mode for brittle materials such as rock, ceramic, concrete, and glass. Brittle materials tend to be weak in tension. The fracture can be due to the propagation of an already existing crack under tension.

In the past, a wide variety of specimen types and methods have been developed to measure the mode I fracture toughness of rock. The simplest method among tensile opening fracture toughness measurement methods is always preferred. Easy to prepare samples, practical loading configuration, and the method whose test results are directly interpreted, provides a significant advantage over other tensile opening fracture toughness measurement methods.

3.1. Mode I Fracture Toughness Testing Methods

Mode I fracture toughness testing methods on core-based specimens can be divided into three categories, namely compression, tension, and bending, according to loading conditions. These methods are listed in Table 3.1.

Table 3.1. *Fracture toughness testing methods on core-based specimens*

	Loading Methods		
	Compressive	Tensile	Bending
Testing Methods	❖ Cracked straight through Brazilian disc (CSTBD) ❖ Cracked chevron notched Brazilian disc (CCNBD) ❖ Diametric compression (DC) ❖ Modified ring (MR) ❖ Brazilian disc (BD) ❖ Flattened Brazilian disc (FBD)	❖ Short Rod (SR)	❖ Straight edge cracked round bar bending (SECRBB) ❖ Chevron notched semi-circular bending (CNSCB) ❖ Semi-circular bending (SCB) ❖ Chevron bend (CB) ❖ Straight Notched Disk Bending (SNDB)

The analytical formulas used to calculate the mode I fracture toughness of the various geometries, and loading conditions are given in Figure 3.1, Figure 3.2, and Figure 3.3, respectively.

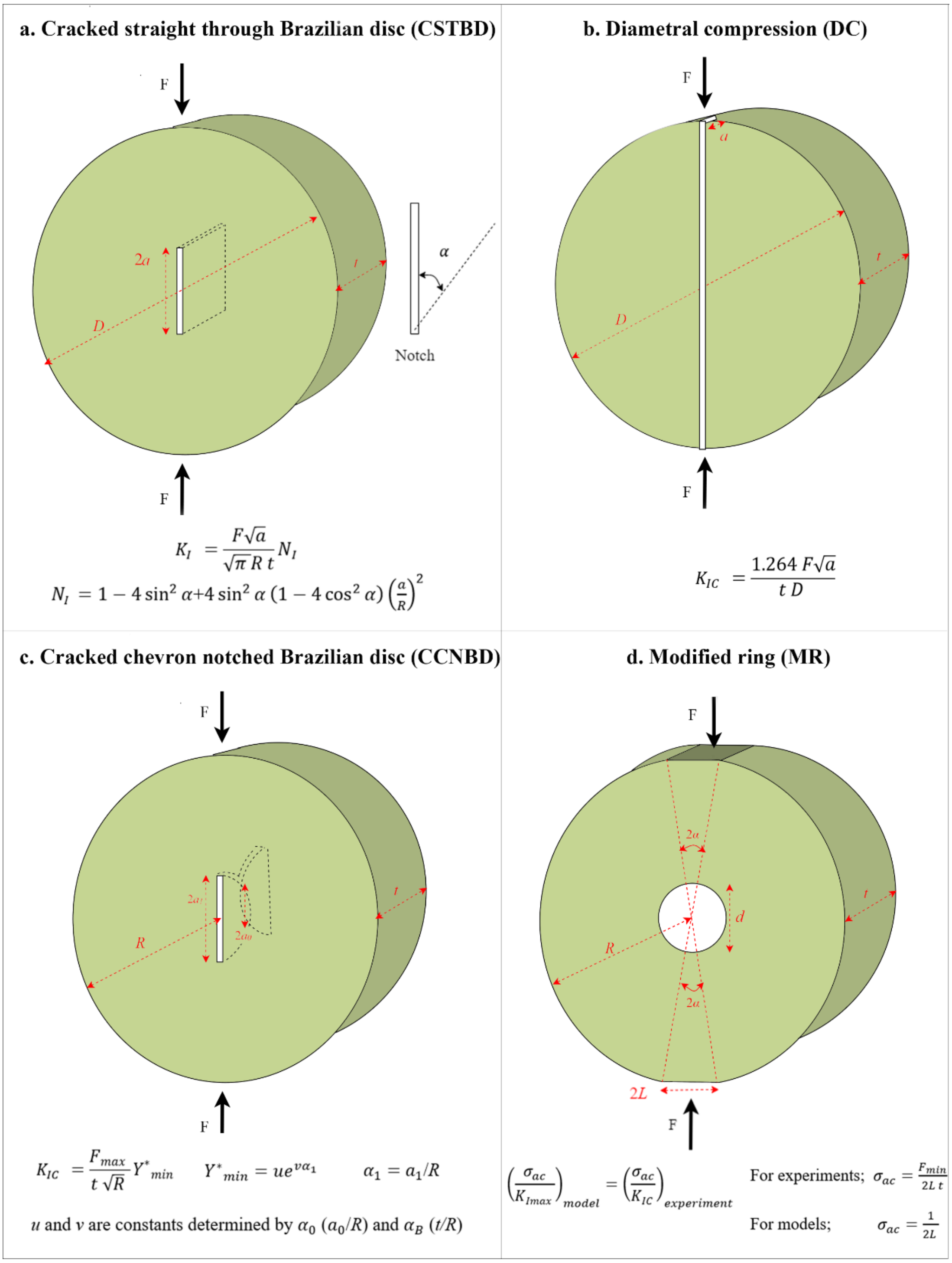

a. Cracked straight through Brazilian disc (CSTBD)

$$K_I = \frac{F\sqrt{a}}{\sqrt{\pi}\,R\,t} N_I$$

$$N_I = 1 - 4\sin^2\alpha + 4\sin^2\alpha\,(1 - 4\cos^2\alpha)\left(\frac{a}{R}\right)^2$$

b. Diametral compression (DC)

$$K_{IC} = \frac{1.264\,F\sqrt{a}}{t\,D}$$

c. Cracked chevron notched Brazilian disc (CCNBD)

$$K_{IC} = \frac{F_{max}}{t\,\sqrt{R}} Y^*{}_{min} \qquad Y^*{}_{min} = ue^{v\alpha_1} \qquad \alpha_1 = a_1/R$$

u and v are constants determined by α_0 (a_0/R) and α_B (t/R)

d. Modified ring (MR)

$$\left(\frac{\sigma_{ac}}{K_{Imax}}\right)_{model} = \left(\frac{\sigma_{ac}}{K_{IC}}\right)_{experiment}$$

For experiments; $\sigma_{ac} = \frac{F_{min}}{2L\,t}$

For models; $\sigma_{ac} = \frac{1}{2L}$

Figure 3.1. Mode I fracture toughness tests with CSTBD, DC, CCNBD and MR methods

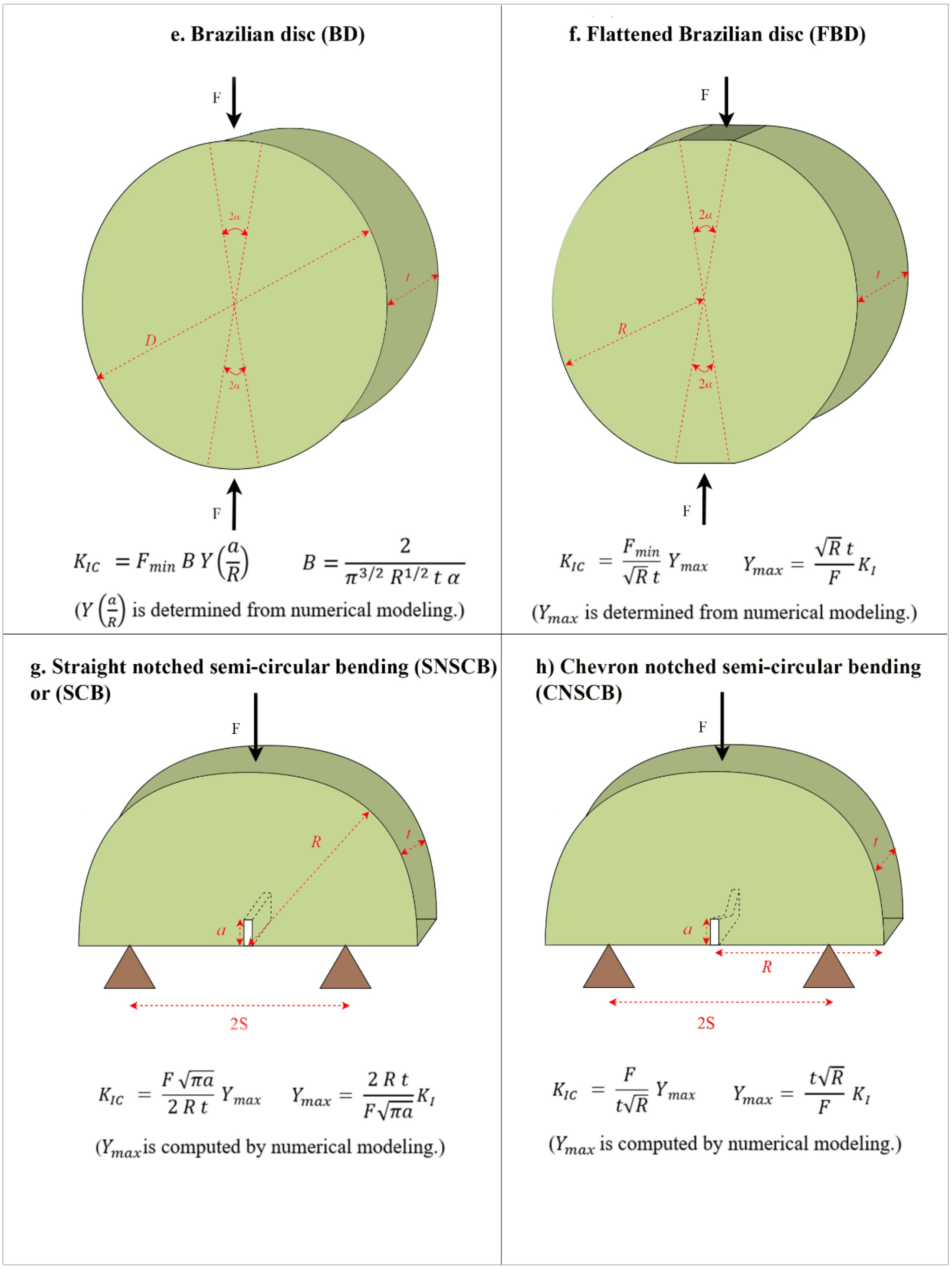

e. Brazilian disc (BD)

$$K_{IC} = F_{min}\, B\, Y\left(\frac{a}{R}\right) \qquad B = \frac{2}{\pi^{3/2}\, R^{1/2}\, t\, \alpha}$$

($Y\left(\frac{a}{R}\right)$ is determined from numerical modeling.)

f. Flattened Brazilian disc (FBD)

$$K_{IC} = \frac{F_{min}}{\sqrt{R}\, t}\, Y_{max} \qquad Y_{max} = \frac{\sqrt{R}\, t}{F} K_I$$

(Y_{max} is determined from numerical modeling.)

g. Straight notched semi-circular bending (SNSCB) or (SCB)

$$K_{IC} = \frac{F\sqrt{\pi a}}{2\, R\, t}\, Y_{max} \qquad Y_{max} = \frac{2\, R\, t}{F\sqrt{\pi a}} K_I$$

($Y_{max}$is computed by numerical modeling.)

h) Chevron notched semi-circular bending (CNSCB)

$$K_{IC} = \frac{F}{t\sqrt{R}}\, Y_{max} \qquad Y_{max} = \frac{t\sqrt{R}}{F}\, K_I$$

(Y_{max} is computed by numerical modeling.)

Figure 3.2. Mode I fracture toughness determination with BD, FBD, SCB and CNSCB methods

i. Chevron bend (CB)

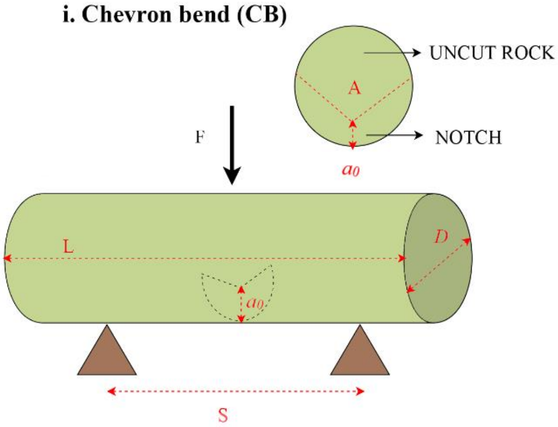

For level 1 testing;

$$K_{IC} = \frac{A\,F_{max}}{D^{1.5}}$$

$$A = \left[1.835 + 7.15\frac{a_0}{D} + 9.85\left(\frac{a_0}{D}\right)^2\right]\frac{S}{D}$$

For level 2 testing;

$$K_{IC}^{c} = \sqrt{\frac{1+p}{1-p}}\,K_{IC}$$

(p is calculated by considering Load-CMOD curves.)

j. Straight edge cracked round bar bending (SECRBB)

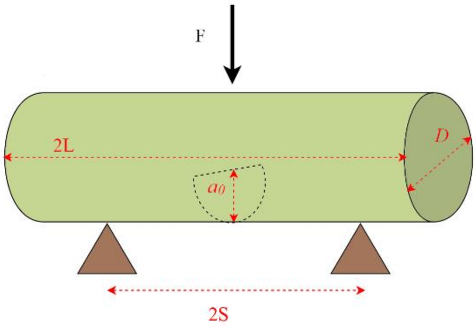

$$K_{IC} = 0.25\left(\frac{2S}{D}\right)\left(\frac{F}{D^{1.5}}\right)\times Y_1^{'}$$

$$Y_1^{'} = \frac{2\left(\frac{D}{2S}\right)\left[450.8531\left[\frac{1}{3.33}\left(\frac{2S}{D}\right)\right]^2\left(\frac{a}{D}\right)^{1.5}\right]^{0.5}}{\left[\left(\frac{a}{D}\right)-\left(\frac{a}{D}\right)^2\right]^{0.25}}$$

k. Straight notched disk bending (SNDB)

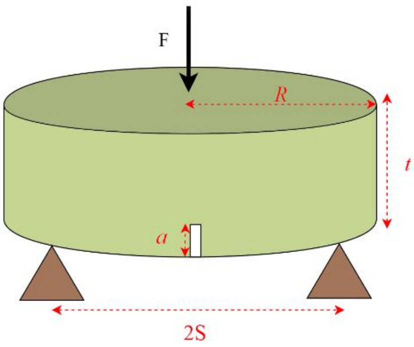

$$K_{IC} = \frac{F\sqrt{\pi a}}{2\,D\,t}\,Y_{max}$$

$$Y_{max} = \frac{2\,D\,t}{F\sqrt{\pi a}}\,K_I$$

(Y_{max} is computed by numerical modeling.)

l. Short rod (SR)

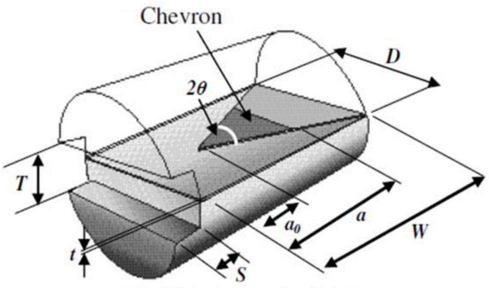

(Modified from Alkılıçgil, 2010)

For level 1 testing;

$$C_K = \left(1 - \frac{0.6\Delta W}{D} + \frac{1.4\Delta a_0}{D} - 0.01\Delta\theta\right)$$

If $0.99 < C_K < 1.01$ $\quad K_{IC} = 24.0F_{max}/D^{1.5}$

Otherwise $\quad K_{IC} = C_K\,24.0F_{max}/D^{1.5}$

For level 2 testing;

$$K_{IC}^{c} = \sqrt{\frac{1+p}{1-p}}\,K_{IC}$$

(p is calculated by considering Load-CMOD curves.)

Figure 3.3. Geometries and loading conditions of CB, SECRBB, SNDB and SR specimens

International Society for Rock Mechanics (ISRM) recommended several suggested methods for determining the fracture toughness of rocks with core specimens. These were short rod (SR) method (Ouchterlony, 1988), chevron bend (CB) method (Ouchterlony, 1988), cracked chevron notched Brazilian disc (CCNBD) method (Fowell et al., 1995) and semi-circular bending (SCB) method (Ulusay, 2016). Some of these suggested methods have some difficulties and limitations. For instance, CB and SR tests are more complex than other methods because they consist of two levels: level 1 requiring only maximum load measurement and level 2 requiring continuous measurement of load and displacement. The main disadvantage of the SR method is that specimen preparation is more complicated than the other methods.

Fowell and Xu (1993) recommended the CCNBD method to overcome these problems. They proposed that CCNBD showed higher tolerance to specimen machining errors and had the most straightforward testing procedure among the suggested methods. On the other hand, there are some dimensional restrictions for the CCNBD test to be valid. In addition to geometrical constraints, it is difficult to machine the chevron notch because there should be proper slit alignment on both surfaces of the specimen.

Chong and Kuruppu (1984) developed the SCB method to measure fracture toughness of rocks and other materials. Many researchers preferred this method due to ease of machining the straight notch, simplicity of the set-up, and testing procedure. It should be noted that CB and SCB tests require the loading fixtures as in all bending type loading configurations, so the specimen must be properly aligned in regard to the loading fixture.

Compared to the methods proposed by ISRM, the Brazilian disc method and flattened Brazilian disc method are an easy and convenient way to the measurement of mode I fracture toughness. Fracture toughness determination with Brazilian disc test and flattened Brazilian disc test are summarized in the following parts.

3.1.1. Brazilian Disc Test

In general, the Brazilian disc is used for the determination of the tensile strength of rock. Guo et al. (1993) proposed a Brazilian test for the measurement of rock fracture toughness due to its simplicity and convenience. This technique was inspirational to many subsequent works in fracture toughness determination. The Brazilian disc specimen under uniformly distributed radial loads is schematically shown in Figure 3.4.

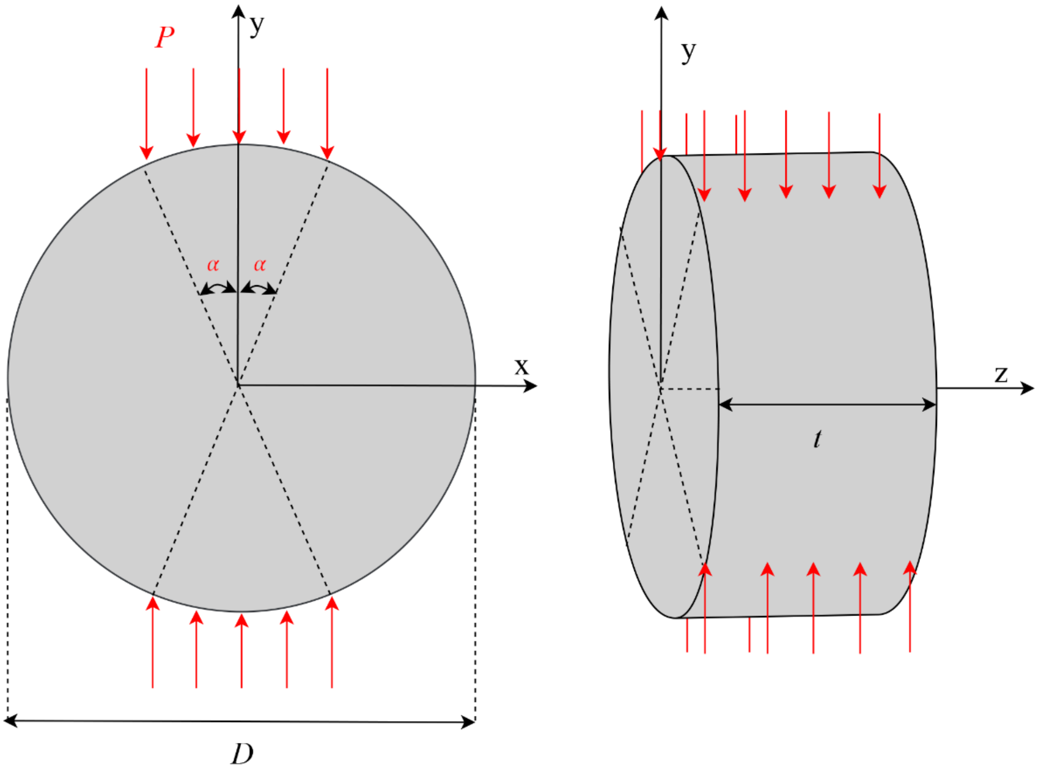

Figure 3.4. Brazilian disc under diametral compression

Guo et al. (1993) investigated the crack propagation behavior of Brazilian disc analytically and experimentally. They established a relationship between dimensionless stress intensity factor $Y\left(\frac{a}{R}\right)$ and dimensionless crack length $\frac{a}{R}$. Dimensionless stress intensity factor values for different loading angles in increments of 5° from 5° to 50° were given from the results of numerical computations. After numerical computation of $Y\left(\frac{a}{R}\right)$, the opening mode fracture toughness can be given as in Equation 3.1 below.

$$K_{IC} = P_{min}\, B\, Y\left(\frac{a}{R}\right) \tag{3.1}$$

Where;

K_{IC} : Mode I fracture toughness (MPa$\sqrt{\text{m}}$)

P_{min}: Local minimum load determined from testing (MN)

B: Constant which depends on the geometry of the specimen and loading conditions

$$B = \frac{2}{\sqrt{\pi^3}\,\sqrt{R}\; t\; \alpha} \tag{3.2}$$

R: Disc radius (m)

t: Disc thickness (m)

α: Half of the loading angle (radians)

a: Half of the crack length (m)

$Y\left(\frac{a}{R}\right)$: Dimensionless stress intensity factor computed from numerical modeling

$\frac{a}{R}$: Dimensionless crack length

To estimate rock fracture toughness, they conducted Brazilian tests on six different types of rocks. The core specimens had 54 mm diameter and 27 mm thickness. The contact angle 2α between the steel jaws and the specimen was 10°. The average values of mode I fracture toughness for some rock types determined by Brazilian disc geometry are given in Table 3.2.

Table 3.2. *Average mode I fracture toughness values for some rock types determined by Brazilian disc geometry*

Rock Type	Description	$K_{IC\,avg}$ (MPa$\sqrt{m}$)	Source
Sandstone	-	0.67±0.05	Guo et al. (1993)
Limestone	White	1.38±0.20	Guo et al. (1993)
Limestone	Grey	1.58±0.16	Guo et al. (1993)
Marble	Fine-grained	1.00±0.07	Guo et al. (1993)
Marble	Coarse-grained	1.12±0.19	Guo et al. (1993)
Basalt	-	3.01±0.49	Guo et al. (1993)

Zhao et al. (1994) detected some problems in the study of Guo et al. (1993). Instead of the notch, Guo et al. (1993) assumed that a central crack occurred during the test, but the crack was not actually initiated at the center of the disc for loading angle $2\alpha = 10°$. Another problem was the effect of secondary crack, starting from the loading jaw. They argued that the secondary crack affects the quality of the central crack. Besides, Guo et al. (1993) derived the analytical expressions of SIF for a central crack in an infinite plate, which means that the crack length is very small relative to the radius of the plate. They calculated the dimensionless crack length $\frac{a}{R}$ as approximately 0.8 for $2\alpha = 10°$. Zhao et al. (1994) claimed that Guo et al.'s SIF expression could lead to inaccurate results.

3.1.2. Flattened Brazilian Disc Test

Wang and Xing (1999) put forward that there were identifiable shortcomings and drawbacks in the Brazilian disc test. The main shortcoming in Guo et al.'s work involved the issue of central crack initiation. Guo et al. (1993) assumed that the crack initiation starts at the center of the specimen, but they did not take into account that the loading angle may affect the location of the crack initiation, and they chose an arbitrary loading angle. Another important shortcoming was the inconsistent SIF results due to the wrong domain selection for the analytical solution of the problem. The main drawback was associated with the difficulty of arc loading. The stress distribution on the arc is not always uniform, and it is difficult to determine the loading angle accurately.

Wang and Xing (1999) proposed a new technique called the flattened Brazilian disc (FBD) to overcome all these problems when testing the fracture toughness of rocks. The flattened Brazilian disc is schematically shown in Figure 3.5.

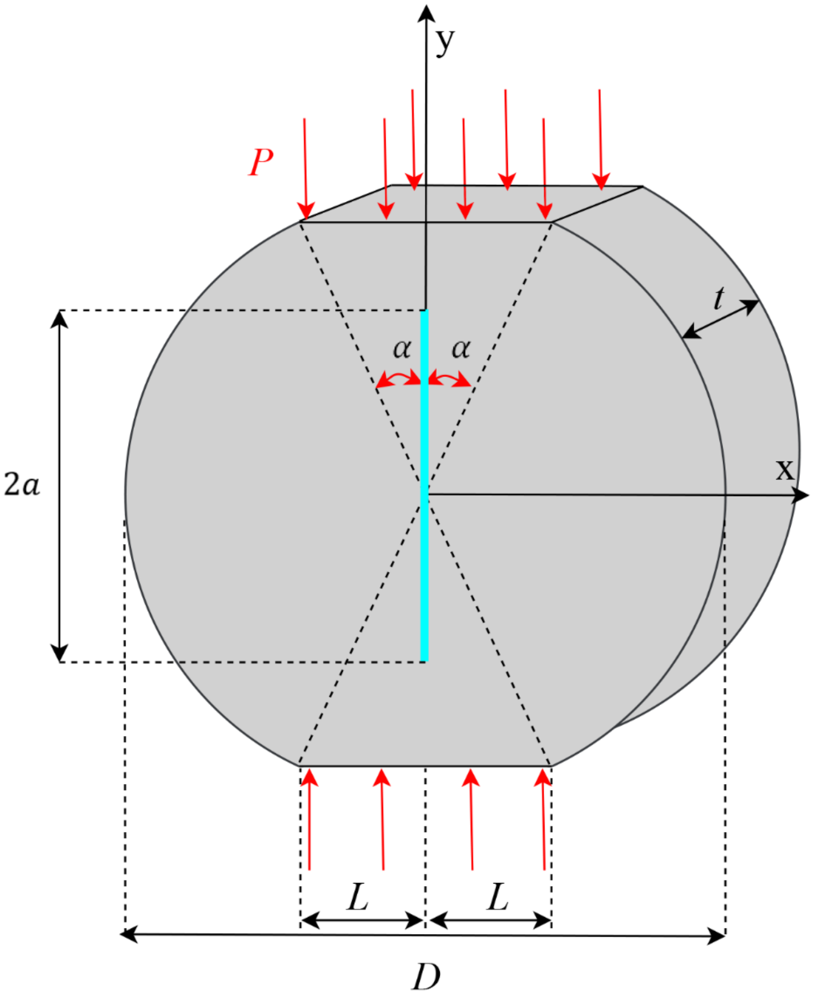

Figure 3.5. Flattened Brazilian disc specimen and loading configuration

The blue line ($2a$) represents the length of the crack generating automatically during the fracture toughness test, 2α illustrates the loading angle and $2L$ shows the flattened end width of the specimen.

The flattened Brazilian disc (FBD) technique, in principle, is similar to the work of Guo et al. (1993), but this is the modified version of the Brazilian disc geometry to ensure the central crack initiation. The flattened Brazilian disc was designed by introducing the two parallel flat loading ends in the specimen to reduce the stress concentration of the loading region by spreading the load more uniformly.

In Figure 3.6, the areas to be cut in the FBD sample are white. The vertical length of the section to be cut above and below the sample is determined separately as $R - R\cos\alpha$. The half of the flattened end width (L) is $R\sin\alpha$.

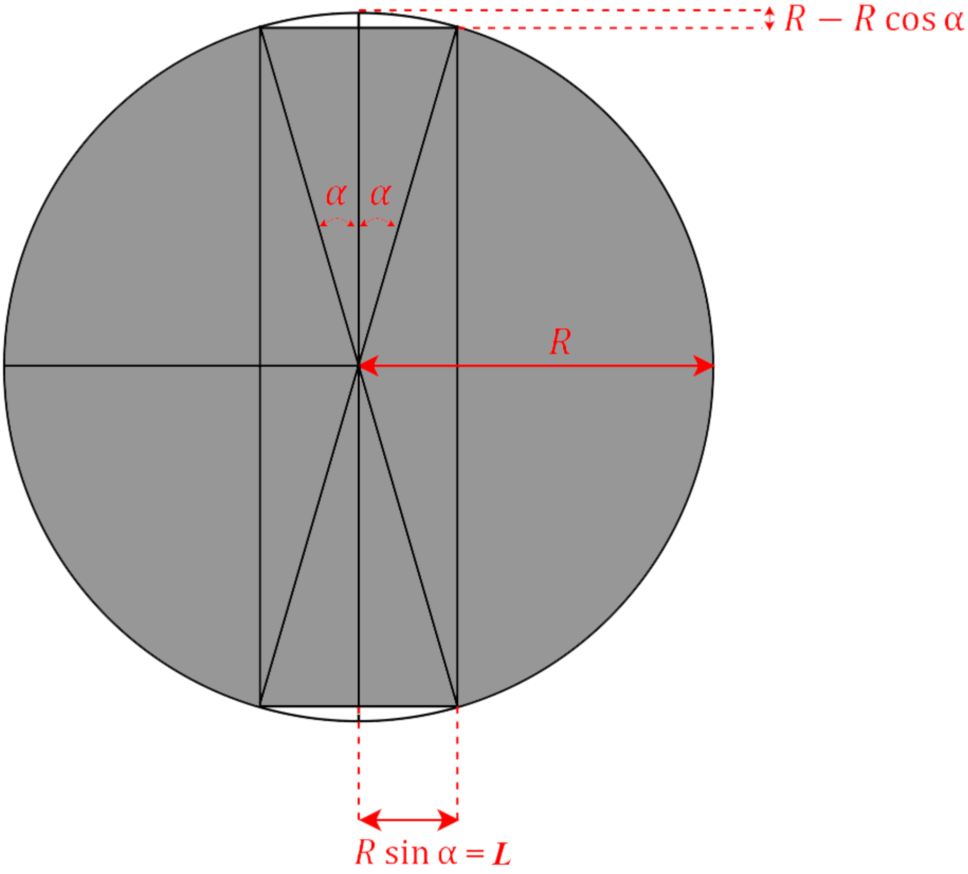

Figure 3.6. Flattened Brazilian disc specimen

Wang and Xing (1999) established Equation 3.3 for the calculation of fracture toughness.

$$K_{IC} = \frac{P_{min}\, Y_{I\,max}}{\sqrt{R}\, t} \tag{3.3}$$

Where;

K_{IC} : Mode fracture toughness (MPa$\sqrt{\text{m}}$)

P_{min}: Local minimum load determined from the load-displacement test record (MN)

Y_I : Maximum mode I dimensionless SIF computed from numerical modeling

R: Disc radius (m)

t: Disc thickness (m)

Wang et al. (2004) conducted the conceptually identical work, utilizing the same method. They utilized a finite element program to compute the SIFs and proposed the analytical formulas for the measurement of three material parameters from the FBD geometry: the elastic modulus, tensile strength, and fracture toughness. Wang and Wu (2004) determined the fracture toughness of two marbles with the FBD method. They interpreted the criteria for the validity of the FBD test according to the crack initiation location and load-displacement record. Kaklis et al. (2005) carried out the numerical computations of FBD geometry for two different loading cases: with and without flat loading platens. A more realistic simulation of the experiments were the models of FBD geometry using flat platens because the contact between the flat platen of the testing machine and the flat end of the specimen was considered.

In recent years, significant progress has been made in the fracture toughness determination with FBD specimen. Khavari and Heidari (2016) conducted numerical and experimental studies to determine the effect of loading angle on the location of crack initiation in FBD. They conducted both 2D and 3D numerical analysis for different loading angles and employed the FBD test to calculate the fracture toughness of marble. Liu et al. (2016) investigated the effect of temperature on fracture toughness of FBD granite and marble specimens. The temperature was varied in the range of 25 °C to 1000 °C. According to the test results, the fracture toughness of marble and granite decreased gradually as the temperature increased. Marble was much more affected by temperature than granite due to the structural properties and mineral compositions. Mahanta et al. (2017) attempted to investigate the influence of strain rates on the fracture toughness of sandstone. For examination of strain rate effects, FBD specimens having 20 and 30 loading angles were chosen, and the strain rates ranged from 10^{-5} to 10^{-2} s^{-1}. Test results showed that the increase in strain rate causes an increase in fracture toughness of sandstone.

The average fracture toughness values of some rocks determined by the FBD method are listed in Table 3.3 prepared from the literature.

Table 3.3. *Average mode I fracture toughness values of some rock types determined by the flattened Brazilian disc geometry*

Rock Type	Description or Location	2α (°)	$K_{IC\ avg}$ (MPa$\sqrt{m}$)	Source
Limestone	Chongqing	30	1.25	(Wang and Xing, 1999)
Marble	Type A	20 and 30	0.97	Wang and Wu (2004)
Marble	Type B	20 and 30	1.60	Wang and Wu (2004)
Marble	Iran	30	1.95	Khavari and Heidari (2016)
Granite	China	20	1.73*	Liu et al. (2016)
Marble	China	20	0.99*	Liu et al. (2016)

(* symbol represents the average fracture toughness of rock calculated for different temperatures.)

The advantages of the FBD test specimen are summarized below;

- The convenient and simple method
- Easy specimen preparation
- No require any crack or notch
- No need any complicated and extra equipment
- Easy identification of local minimum load from the record
- No need crack length measurement for fracture toughness calculation
- Uniformly distributed load on flattened areas

3.1.2.1.Investigation of Loading Angle Effect on Test Validity

Researchers attempted to find the appropriate loading angle that guarantees the crack initiation at the center of the disc and prevents the occurrence of undesirable secondary cracks at some points like flat end sharp edges and corners of the specimen. Wang and Xing (1999) stated that for the Brazilian disk specimen, the loading angle 2α should be greater than 19.5° to guarantee the central crack initiation, which is a prerequisite for the validity of this test. This critical loading angle must be greater than or equal to 20° for a valid test using the FBD configuration (Wang et al., 2004; Wang and Wu, 2004; Elghazel et al., 2015). Kaklis et al. (2005) modeled FBD geometry numerically with and without loading platens to investigate the friction coefficient between platen and FBD specimen. They suggested that the loading angle should be at least 2α =20° for a valid test without flat loading platens and 15° using flat loading platens. The loading angle of FBD specimen geometry was investigated through experiments and finite element analysis, and it was recommended to be 20°-30° (Huang et al., 2015).

According to the 3D numerical work of Lin et al. (2015), the central crack initiation of the FBD depends on both loading angle and thickness to radius ratio. The recommended loading angle and thickness to radius ratio were 24° and 0.5, respectively. To obtain more accurate results, Lin et al. (2016) conducted tests again to investigate the effect of the loading angle, thickness to radius ratio, and Poisson's ratio on central crack initiation. Based on the numerical results recommended t/R ratio was between 0.5 and 0.8. For ν =0.15, 0.20, 0.25, 0.30 and 0.35, they suggested loading angles of $2\alpha \geq$20°, $2\alpha \geq$20°, $2\alpha \geq$24°, $2\alpha \geq$24°, and $2\alpha \geq$26°, respectively. Khavari and Heidari (2016) determined the optimal loading angle as $2\alpha =$30° by utilizing both numerical and experimental methods. Wang and Cao (2016) defined the flattened Brazilian disc coefficient ε as $(R - R\cos\alpha)/R$, and ε must be less than or equal to 0.035 to guarantee the accuracy of the FBD test. In other words, 2α should not exceed 30°.

Wang et al. (2017) introduced a new method called Grooved Brazilian disc (GBD) to improve the BD method and performed BD, FBD, and GBD tests for observation of crack initiation location. Laboratory tests had shown that all FBD specimens were successful, and the central crack initiation was satisfied by applying a 20° loading angle. However, Mahanta et al. (2017) put forward that FBD specimen having a 20° loading angle overestimated the fracture toughness of sandstone, so they preferred 30° for estimation of fracture toughness.

Wu et al. (2018) made a visual presentation of crack initiation in FBD and BD marble disc using the discrete element method reflecting the heterogeneity of the rock. According to the FBD simulation for $2\alpha =$20°, the crack initiated at the center of the FBD and spread towards the loading ends, but a small number of microcracks occurred at the same time near the loading ends. Therefore, the assumption of crack initiation at the center of FBD was satisfied, and the maximum tensile strength occurred at the center. On the contrary, due to the high-stress concentration of the loading region, the cracks first initiated near the loading ends of BD.

3.1.2.2.Tensile Strength Determination with the FBD Geometry

In order to calculate the tensile strength of concrete, Liang and Tao (2014) carried out tests on FBD and BD specimens. They observed that the force-displacement curves of BD and FBD specimens were consistent with each other. They deduced from the tests that the average tensile strength of the BD group was approximately 49% smaller than the average value of the FBD group. Lin et al. (2015) mainly focused on the stress distribution of the flattened Brazilian disc. They analyzed the effect of loading angle and thickness to radius ratio on the stress distribution of the FBD. They determined the most appropriate FBD geometry and considered the influence of Poisson's ratio on the tensile strength. They established a 3D tensile strength formula for the special case of 2α =24° and t/R =0.5. Shin and Kim (2015) conducted a numerical study to determine the stress state of the FBD geometry under diametral compression, and the stresses at important locations were compared with analytical solutions of arc loaded and point loaded disc specimens. Based on finite element analysis, it was deduced that the maximum tensile stress along both the x and y-axis was obtained at the center of the FBD specimen. As the loading angle increases, the maximum tensile stress at the center decreases.

In 2016, a modified formula for the FBD specimen was proposed, taking into account the 3D geometric parameters and material parameters such as loading angle, t/R ratio, and Poisson's ratio (Lin et al., 2016). The new tensile strength formula using the FBD geometry depended on both the loading angle and Poisson's ratio. Similarly, Wang and Cao (2016) generated the empirical tensile strength formula using FBD geometry. They used the flattened Brazilian disc coefficient expressed as $(R - R\,cos\,\alpha)/R$. The influence of the flattened Brazilian disc coefficient on the FBD has been researched through numerical simulation. The findings of numerical simulation showed that the high coefficient leads to the deviation of the crack initiation location. Liu et al. (2016) determined the tensile strength of FBD marble and granite specimens for different temperatures. Test results showed that the tensile strength of the two rocks progressively decreased with increasing temperature values. Mazel et al. (2016) examined the stress and strain distribution of FBD and BD under the diametral compression experimentally and numerically. The results of both numerical simulation and laboratory tests showed that maximum tensile stress and strain were located at the center of the FBD specimen, but this was not the case for BD specimen. They stated that BD geometry had a tendency to underestimate the tensile strength.

Mahanta et al. (2017) conducted an experimental study of strain sensitivity to fracture toughness and tensile strength using FBD sandstone specimens. The experimental results indicated that as the strain rate increased, the tensile strength of material also increased. Unlike Mazel et al. (2016), Mahanta et al. (2017) claimed that the Brazilian disk test tended to overestimate the tensile strength of rock. Hence, the FBD method was more reliable for tensile strength estimation of rock.

The flattened Brazilian disk can be used not only in the static tensile test but also in the dynamic tensile test. Wang et al. (2009) measured the dynamic tensile strength of marble using the flattened Brazilian disc. The dynamic tensile strength of marble was around 22-27 MPa, but the corresponding static value was 5 MPa. Similarly, Chen et al. (2013) utilized the FBD method for determining the dynamic tensile stress-strain curve of polymer-bonded explosives.

CHAPTER 4

NUMERICAL MODELING OF FLATTENED BRAZILIAN DISC SPECIMEN

Before the mode I fracture toughness tests, FBD specimens were modeled with various loading angles to compute mode I stress intensity factors. The stress and fracture analyses were performed by utilizing commercial finite element package ABAQUS software. 2D simulations were carried out in the numerical study. 2D plane strain modeling was preferred for formula generation due to its less computation time. Stress intensity factor results were compared to the results of previous work.

The main purpose of modeling work is to develop two different equations by numerical analysis. The first equation is to be used in determining maximum mode I dimensionless SIF ($Y_{I\,max}$) for FBD geometries having different loading angles. $Y_{I\,max}$ is used for calculation of mode I fracture toughness of andesite samples used in testing work. In this part, crack lengths are varied from small lengths to larger lengths to identify the maximum point yielding $Y_{I\,max}$. The crack length at that point is named as numerically computed critical dimensionless crack length. The second equation is for calculating numerical critical dimensionless crack lengths in terms of the loading angle. Approximately 270 2D models were analyzed. The equations developed were valid with loading angles ranging from 0.03 radians (2°) to 0.87 radians (50°). A curve fitting program of wide functional coverage was employed to generate these equations.

4.1. 2D FBD Modeling

To understand the stress state of flattened Brazilian disc geometries and determine the mode I stress intensity factor, FBD geometries were modeled in 2D plane strain condition. 2D modeling was preferred because the computational time is considerably less than the 3D case. For all 2D FBD models, the diameter was taken as 75 mm, and the loading angle 2α was ranged between 2° and 50°. The elastic input properties were the results of the static deformability tests on andesite. As measured in the experimental work, the elastic modulus and Poisson's ratio of the specimen models were input as 31.9 GPa and 0.10, respectively. A sketch of example FBD geometry with a loading angle of 38° is illustrated in Figure 4.1. Related dimensions are given in Table 4.1. The half of the crack length (a) is 21.50 mm for this particular example.

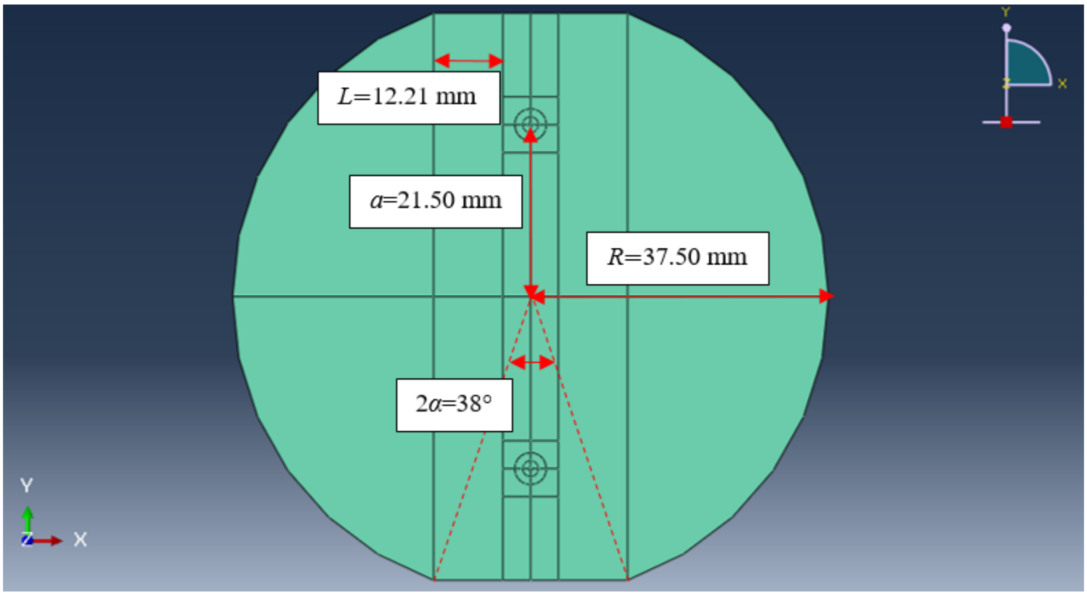

Figure 4.1. Sketch of the 2D FBD geometry

Table 4.1. *Dimensions of 2D FBD geometry*

Parameters	Values
Specimen radius, R	37.5 mm
Loading angle, 2α	38°
Half of the crack length, a	21.50 mm
Half of the flattened end width, L	12.21 mm

A sharp crack is modeled using seam geometry to investigate singular behavior at the crack tip. Figure 4.2 shows the seam crack that was embedded in the center of the plate. The seam crack has zero thickness.

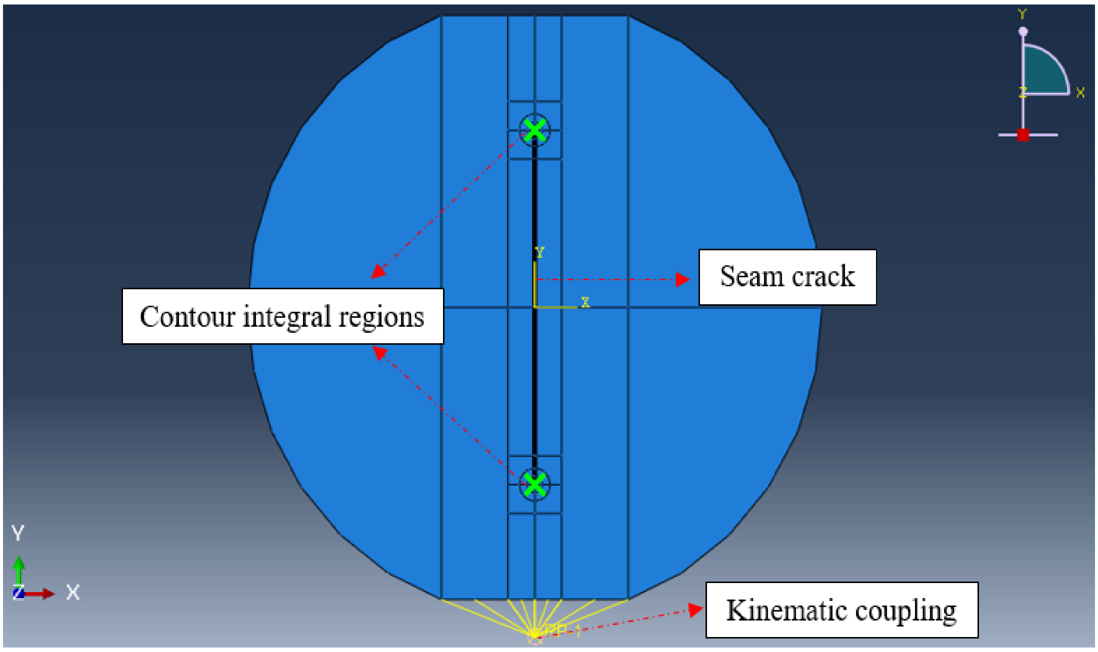

Figure 4.2. Contour integral regions and seam crack in 2D body

The stress intensity factor is calculated in the contour integral region. A detailed view of the contour integral regions is shown in Figure 4.3. The size of the innermost, middle and the outermost contour integral radius is set as 0.25, 1, and 2 mm, respectively. The edge length of the smallest square surrounding the contour integral region is set as 7 mm. To define the location of the crack in the 2D model, the crack tip and the crack front are selected, as shown in Figure 4.3. The crack front is the area surrounding the crack tip to the first contour integral circle. Then, the crack extension direction is imposed by specifying the q vector.

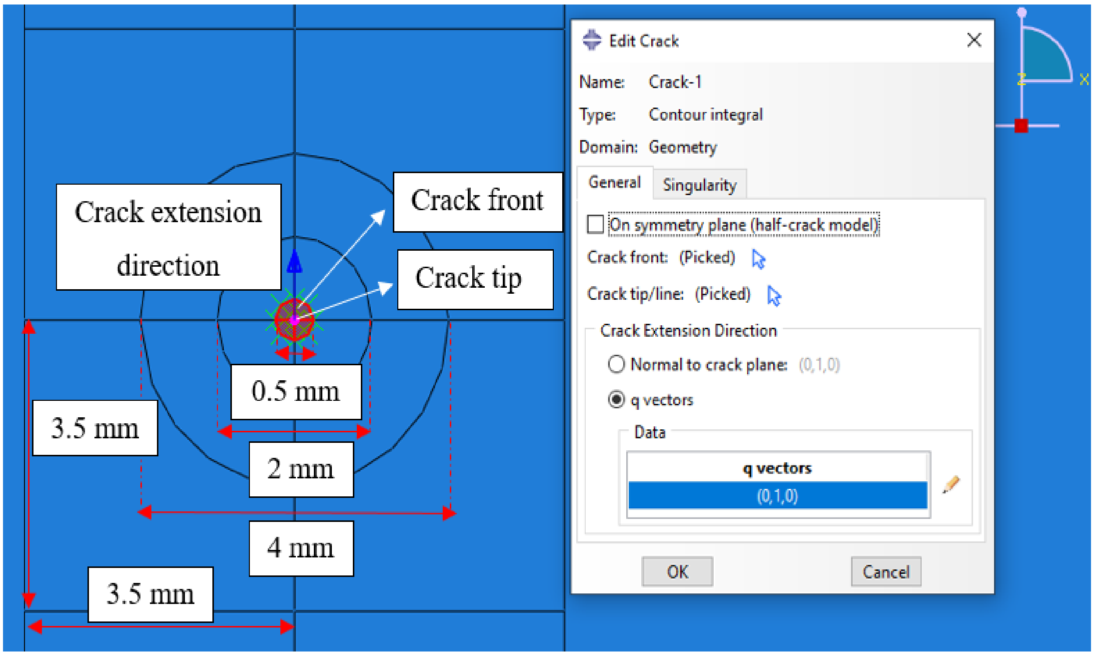

Name: Crack-1
Type: Contour integral
Domain: Geometry
☐ On symmetry plane (half-crack model)
Crack front: (Picked)
Crack tip/line: (Picked)
Crack Extension Direction
○ Normal to crack plane: (0,1,0)
● q vectors
Data

q vectors
(0,1,0)

Figure 4.3. Crack modeling and detailed view of contour integral region

Due to the large stress concentration, the stress field is singular around the crack tip. Linear elastic fracture mechanics assumes that stress state at the crack tip has an inverse square-root singularity ($\frac{1}{\sqrt{r}}$).

The boundary conditions for this model are listed in Table 4.2 and illustrated in Figure 4.4. The upper flattened length was fixed in the y-direction. The fixed displacement and rotation degrees of freedom (DOF) are given for each boundary condition. The midpoint of upper flattened length was fixed in the x-direction. The lower flattened length and the reference point were fixed in the x-direction and free to move in the y-direction. The model cannot rotate out of the plane for all boundary conditions ($u_{R3} = 0$).

Table 4.2. *Boundary Conditions of 2D FBD model*

Boundary Condition	Application Area	Fixed DOF
BC 1	The upper flattened length	u_2, u_{R3}
BC 2	The midpoint of upper flattened length	u_1, u_{R3}
BC 3	The lower flattened length	u_1, u_{R3}
BC 4	The reference point	u_1, u_{R3}

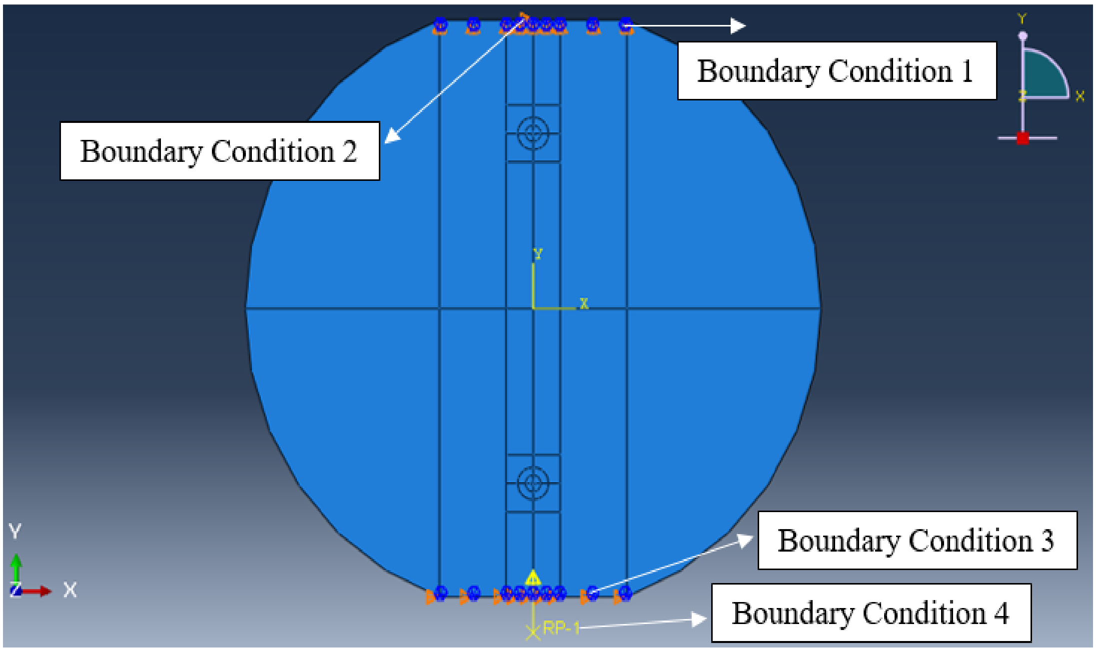

Figure 4.4. Loading configuration and boundary conditions of FBD specimen

The compressive load transfer requires the use of a reference point below the lower flat boundary of the disc. Applied vertical load is distributed along the flat bottom boundary. A concentrated load of 1 kN in the y-direction is applied to the lower flattened end length of the specimen via a reference point (Figure 4.4).

The next step is meshing. The finite element mesh is supposed to be more refined around the critical regions, such as contour integral regions. Due to the high-stress gradients around the crack tip, a larger number of elements are used in this region. The total number of elements is approximately 100000. The element type is selected as the eight-node plane strain element (CPE8R) throughout the entire specimen. An example fine mesh constructed for the FBD geometry is illustrated in Figure 4.5.

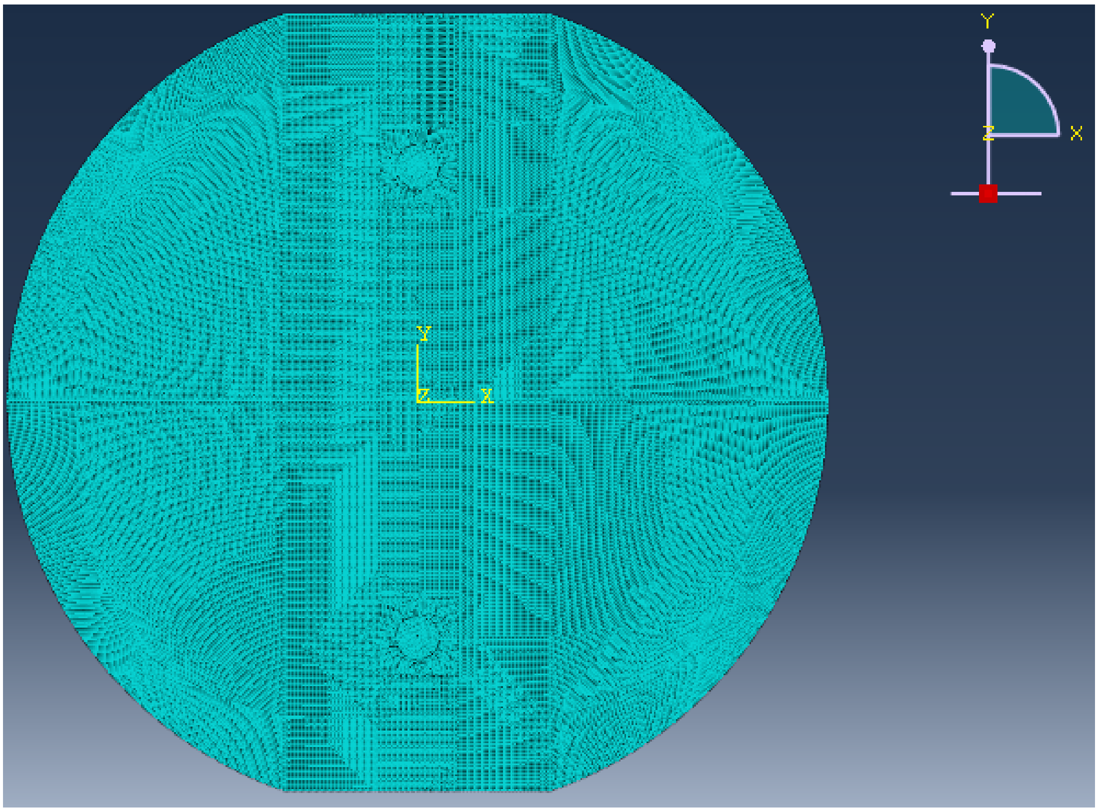

Figure 4.5. Fine meshing of the whole FBD body

The mesh focus around the crack tip is illustrated in Figure 4.6. Sweep mesh is constructed around the crack tip while the remaining part is assigned as structured meshes.

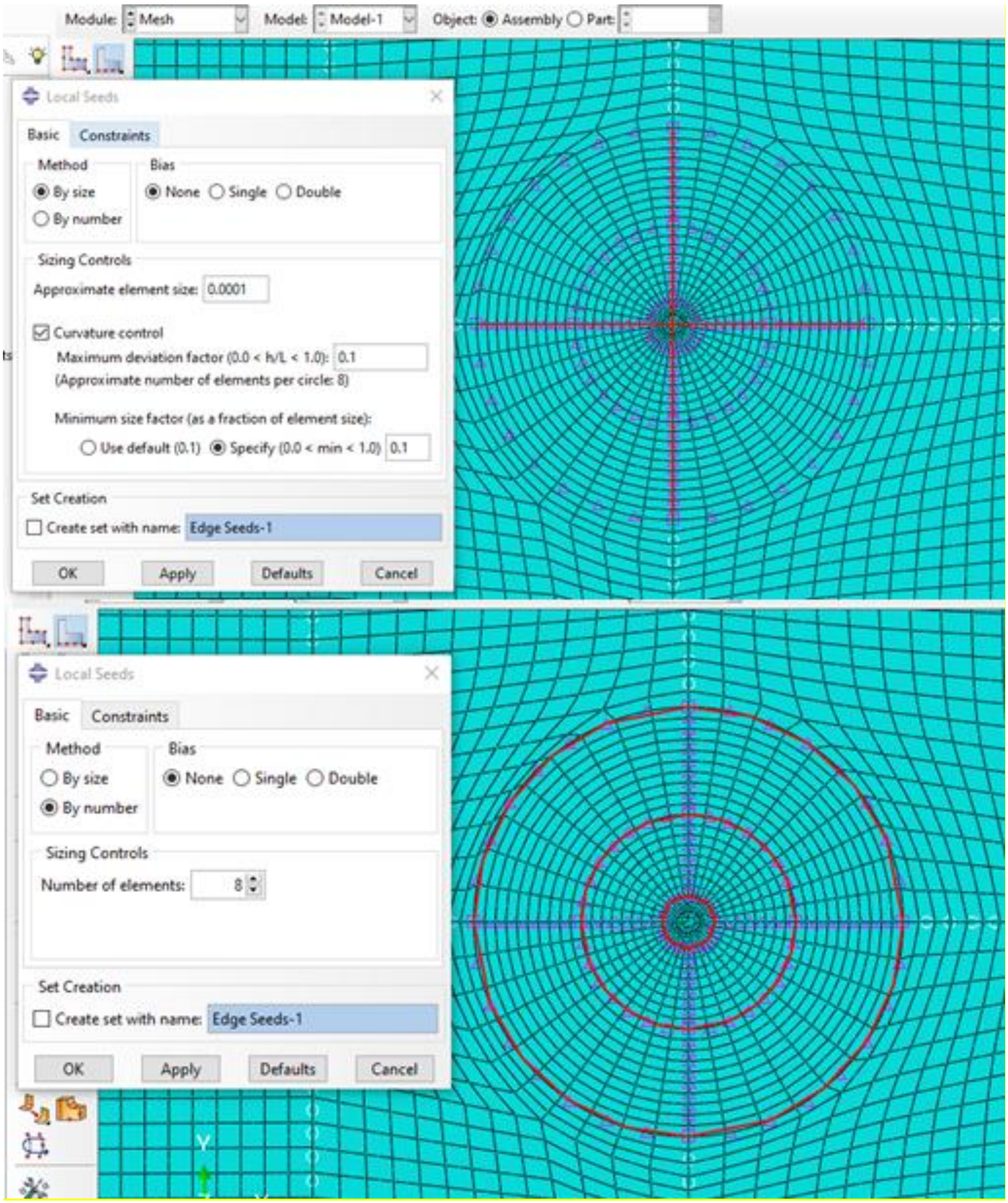
Module: Mesh
Model: Model-1
Object: ● Assembly ○ Part:

Local Seeds

Method: ● By size ○ By number
Bias: ● None ○ Single ○ Double
Sizing Controls
Approximate element size: 0.0001
☑ Curvature control
Maximum deviation factor (0.0 < h/L < 1.0): 0.1
(Approximate number of elements per circle: 8)
Minimum size factor (as a fraction of element size):
○ Use default (0.1) ● Specify (0.0 < min < 1.0) 0.1
Set Creation
☐ Create set with name: Edge Seeds-1

Local Seeds

Method: ○ By size ● By number
Bias: ● None ○ Single ○ Double
Sizing Controls
Number of elements: 8
Set Creation
☐ Create set with name: Edge Seeds-1

Figure 4.6. Finite element grid generation for contour integral region

Contour integrals were calculated for layers of elements around the crack tip. To compute the first contour integral, the crack front and one layer of elements surrounding the crack front were used. The number of contours in the contour integral region was selected as 19 for all FBD models. The innermost contour radius was 0.25 mm, and the outermost contour integral radius was 2 mm.

In Figure 4.7, in order to prove that model body deforms in a mechanically expected fashion, a typical deformed FBD geometry is illustrated in 2D. Open crack is clearly seen in the figure.

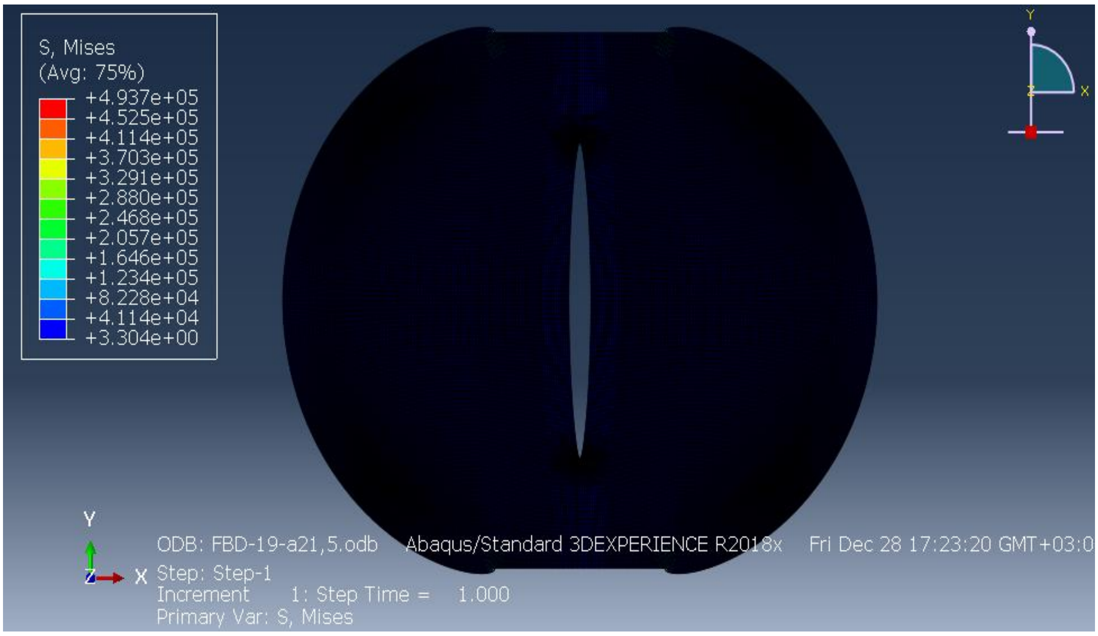

Figure 4.7. Deformed shape of FBD geometry in 2D

4.2. Maximum Dimensionless SIF and Critical Crack Length Formulations

The mode I stress intensity factor was computed first for the determination of both maximum mode I dimensionless SIF ($Y_{I\,max}$) and numerical critical crack lengths ($2a_{cn}$) at different loading angles.

To compute the mode I stress intensity factor values K_I, the FBD geometries having a 75 mm diameter were constructed in 2D by utilizing ABAQUS software. In 2D numerical modeling, t and P were selected as 1 m and 1 kN, respectively. K_I values computed from the numerical work were converted into Y_I using Equation 4.1. For catching the turning point corresponding to $Y_{I\,max}$, the crack length was increased step by step. FBD numerical models were created based on different dimensionless crack lengths (a/R).

$$Y_I = \frac{K_I \sqrt{R}\, t}{P} \tag{4.1}$$

In Equation 4.1, Y_I represents the maximum mode I dimensionless SIF, K_I is the mode I stress intensity factor, and P is the applied load. R represents the radius of the specimen and t is the thickness of the sample.

An example $Y_{I\,max}$ computation of FBD geometry with D =75 mm and 2α =20° is given below. Some example data points of dimensionless crack lengths (a/R) and mode I dimensionless stress intensity factors (Y_I) for the FBD model are listed in Table 4.3.

Table 4.3. *a, a/R and Y_I values for FBD geometry with* $2\alpha = 20°$

a (mm)	a/R	K_I (Pa$\sqrt{m}$)	Y_I	a (mm)	a/R	K_I (Pa$\sqrt{m}$)	Y_I
5.00	0.13	1021.57	0.1978	26.50	0.71	3330.25	0.6449
7.50	0.20	1286.11	0.2491	26.75	0.71	3343.40	0.6474
10.00	0.27	1540.45	0.2983	27.00	0.72	3354.53	0.6496
12.50	0.33	1799.69	0.3485	27.25	0.73	3363.28	0.6513
15.00	0.40	2071.18	0.4011	27.50	0.73	3369.52	0.6525
17.50	0.47	2357.37	0.4565	27.75	0.74	3373.05	0.6532
20.00	0.53	2655.32	0.5142	**28.00**	**0.75**	**3373.51**	**0.6533**
22.50	0.60	2952.70	0.5718	28.25	0.75	3370.73	0.6527
25.00	0.67	3216.95	0.6230	29.00	0.77	3339.49	0.6467
25.50	0.68	3260.25	0.6313	30.00	0.80	3231.69	0.6258
26.00	0.69	3298.35	0.6387	33.00	0.88	2226.72	0.4312

To better visualize data, Y_I versus a/R curve for 2α =20° is created in Figure 4.8. It can be seen from the graph that each red point represents the specimen that is modeled for different crack lengths in ABAQUS.

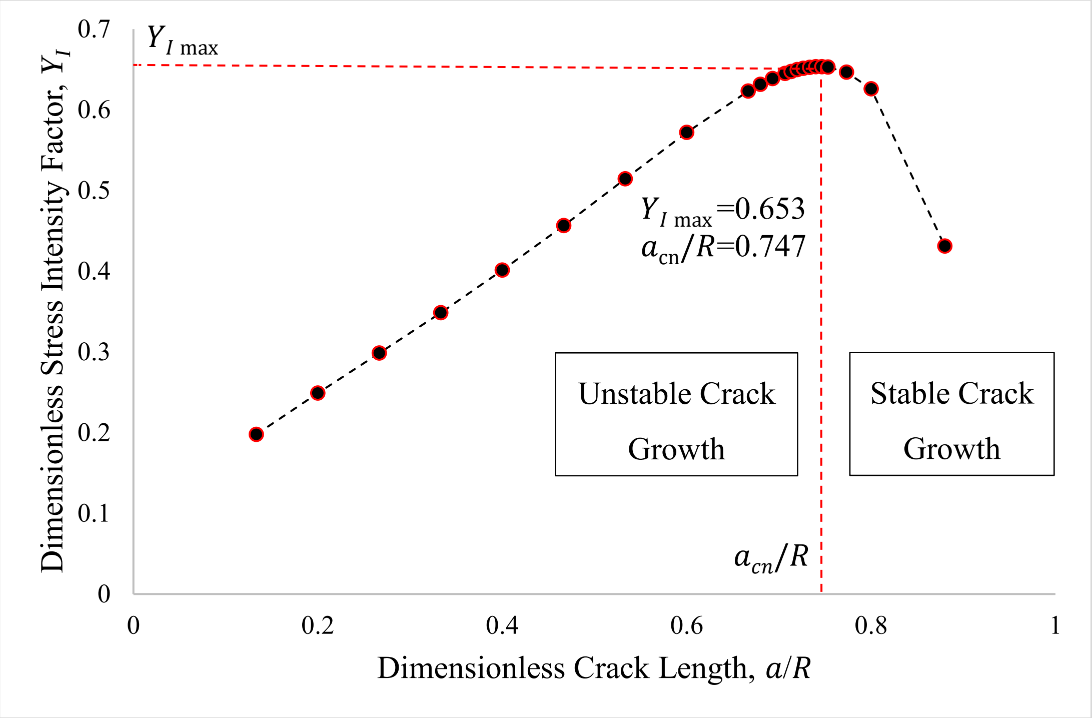

Figure 4.8. Variations of dimensionless stress intensity factor with the dimensionless crack length for 2α =20°

The trend of Y_I versus a/R is similar to the shape of a bell: the trend rises to the maximum value, and then falls. The Y_I versus a/R curve is divided into two typical regions: unstable crack growth and stable crack growth. In the first region of the curve corresponding to the unstable crack propagation, the value of Y_I increases with the crack length up to the point of the $Y_{I\,max}$. The reason why this region is called the unstable crack propagation is that the crack will continue to propagate even if the load is kept constant. In the second region of the curve, after $Y_{I\,max}$ has been achieved, Y_I decreases progressively with the increase in crack length. The second region corresponds to the stable crack propagation because additional load must be applied to the specimen for further crack extension. If the load applied to the sample is not increased, the crack growth will stop. The turning point of the curve that shows the behavior first ascending and then descending is between unstable and stable crack propagation region. This critical point gives the maximum mode I dimensionless stress intensity factor ($Y_{I\,max}$) and corresponding critical dimensionless crack length computed from numerical modeling (a_{cn}/R). $Y_{I\,max}$ is essential for mode I fracture toughness measurement, since it will be used in the formula for the fracture toughness tests. As obtained from Figure 4.8, $Y_{I\,max}$ is 0.653 and a_{cn}/R is 0.747 for this particular example modeling work when 2α =20°.

Figure 4.9 illustrates the variations of dimensionless stress intensity factor with the dimensionless crack length for 2α =0°. This is the simulation of the common regular Brazilian disk test. $Y_{I\,max}$ cannot be determined for 2α =0°, because $Y_{I\,max}$ vs. a/R does not show ascending-maximum-decreasing behavior as in other loading angles.

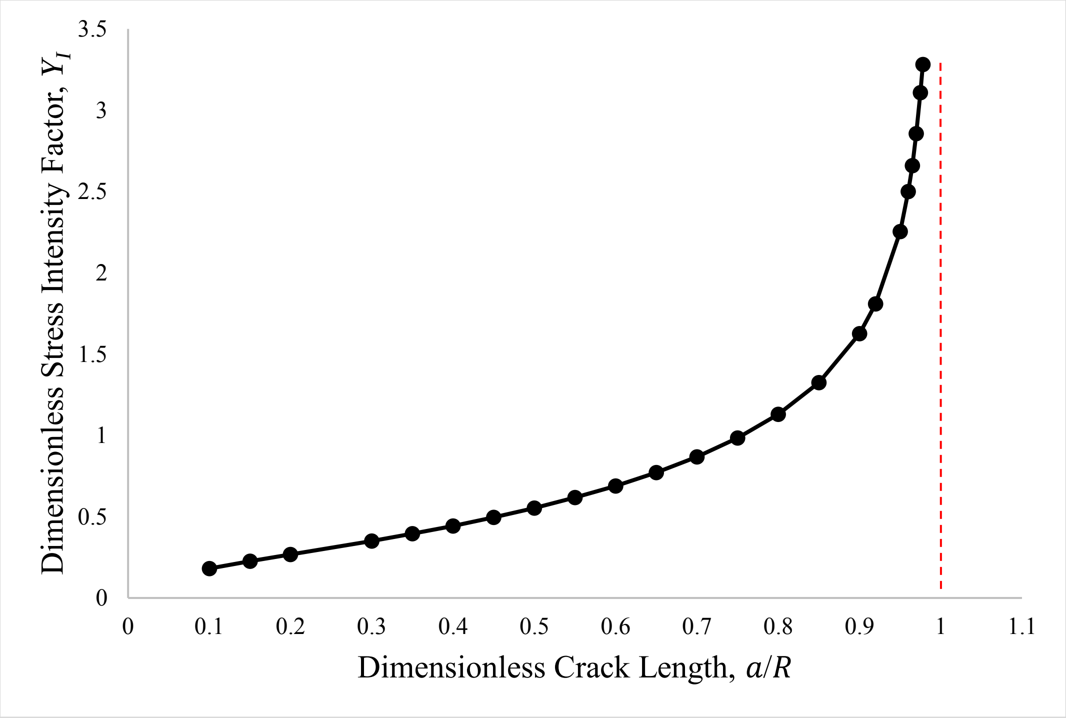

Figure 4.9. Variations of dimensionless stress intensity factor with the dimensionless crack length for 2α =0°

$Y_{I\,max}$ values were calculated from 0.03 radians (2°) to 0.87 radians (50°) with increments of 0.03 radians for different 2α.

The relation between $Y_{I\,max}$ and 2α is shown in Figure 4.10. $Y_{I\,max}$ values show a decreasing trend with increasing loading angle, as shown in Figure 4.10.

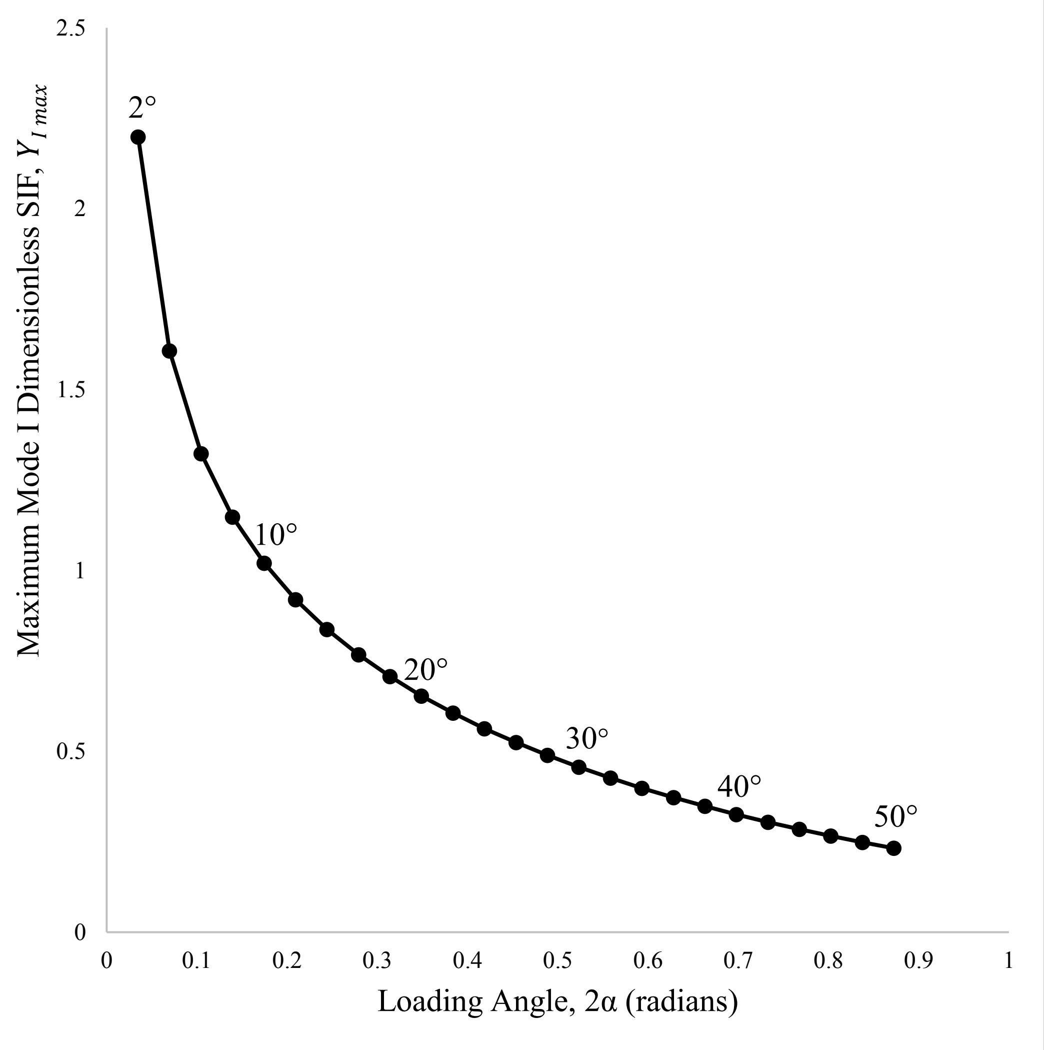

Figure 4.10. Relation between $Y_{I\,max}$ and 2α (in radians)

From the results of these computations, a new formula was established for estimating the maximum dimensionless mode I SIF ($Y_{I\,max}$). New expression corresponded to the use of a larger number of data points for the FBD specimen geometry model. A curve fitting and data processing program was utilized to plot a curve that matches data points and to find the most appropriate equations of fitting work. (Figure 4.11).

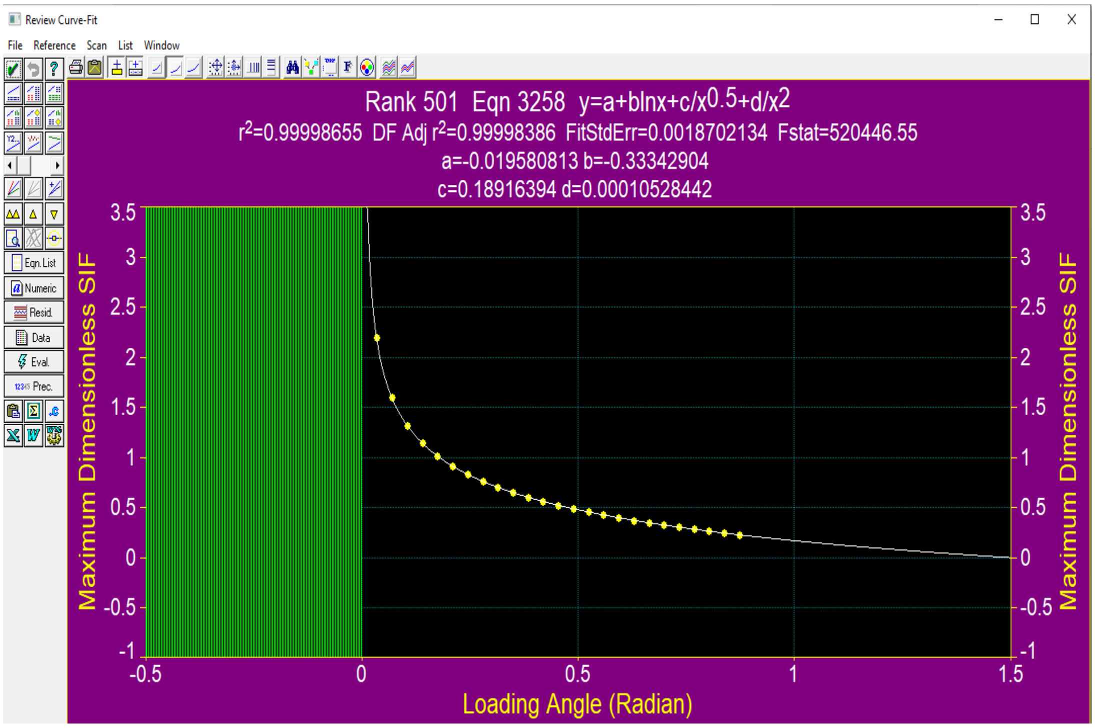

```
Rank 501  Eqn 3258  y=a+blnx+c/x0.5+d/x2
r2=0.99998655  DF Adj r2=0.99998386  FitStdErr=0.0018702134  Fstat=520446.55
a=-0.019580813 b=-0.33342904
c=0.18916394 d=0.00010528442
```

Figure 4.11. Curve fitting for $Y_{I\,max}$ vs 2α (in radians)

$Y_{I\,max}$ can be calculated in terms of 2α by the following equation:

$$Y_{I\,max} = -0.0196 - 0.3334\ln(2\alpha) + \frac{0.1892}{(2\alpha)^{0.5}} + \frac{0.0001}{(2\alpha)^{2}} \qquad (4.2)$$

Where;

$Y_{I\,max}$: Maximum dimensionless stress intensity factor for mode I

2α: Loading angle (radians)

The proposed equation in this study has a high-quality fitting with a high coefficient of determination (R^2 =0.99998), indicating that it is more appropriate than the possible equations and represents the data in the best way. Equation 4.2 applies to the determination of the maximum dimensionless stress intensity factor of FBD models with loading angles greater than 0°.

Dimensionless critical crack lengths (a_{cn}/R) corresponding to maximum dimensionless stress intensity factors ($Y_{I\,max}$) were computed for 0.03 radians (2°) to 0.87 radians (50°) loading angle range. The relation between a_{cn}/R and 2α (radians) is shown in Figure 4.12. a_{cn}/R and 2α are inversely proportional to each other. a_{cn}/R decreases with increasing 2α.

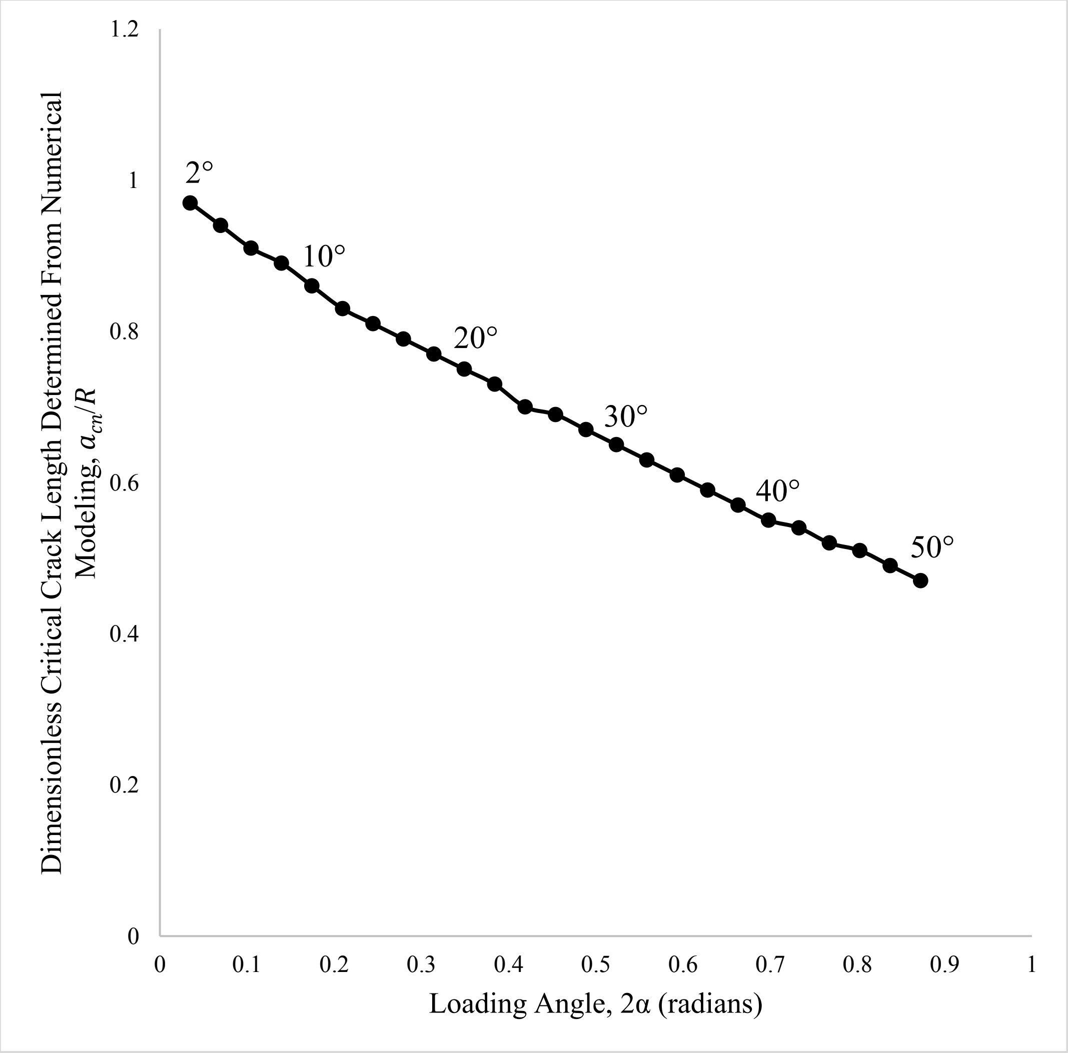

Figure 4.12. Relation between a_{cn}/R and 2α (in radians)

Figure 4.13 shows the best curve fit for a_{cn}/R and 2α data provided by the curve fitting and data processing program. To calculate a_{cn}/R, the new logarithmic equation is proposed below. The coefficient of determination is 0.9995, and it is demonstrated that all points pass through the curve.

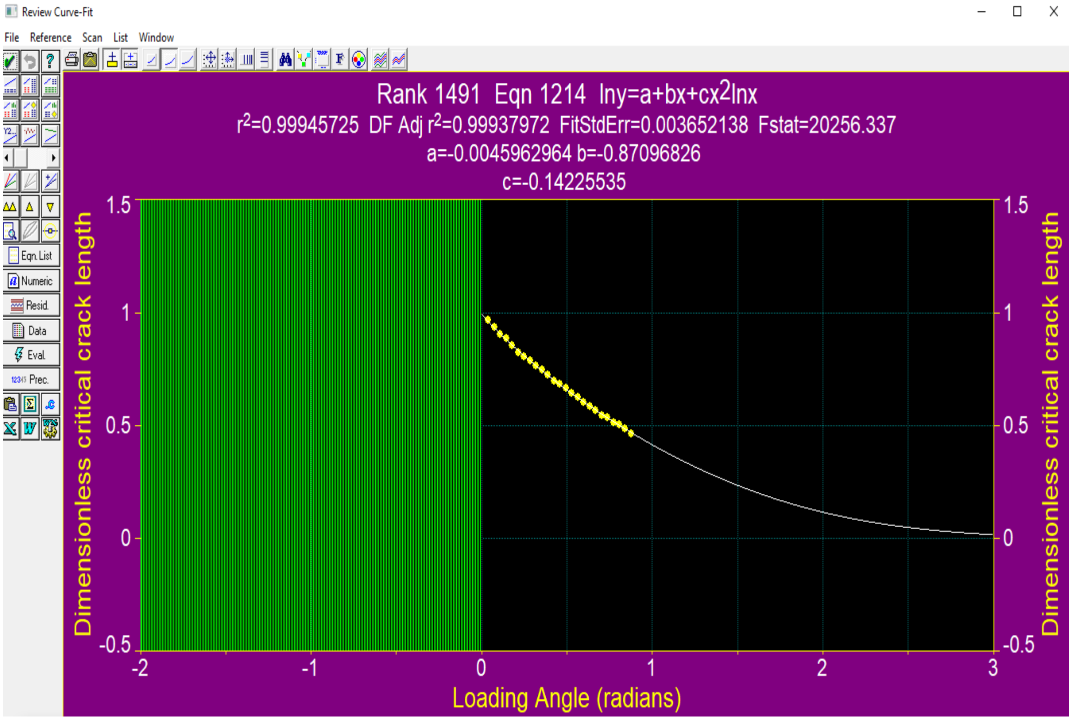

```
Rank 1491  Eqn 1214  lny=a+bx+cx2lnx
r2=0.99945725  DF Adj r2=0.99937972  FitStdErr=0.003652138  Fstat=20256.337
a=-0.0045962964 b=-0.87096826
c=-0.14225535
```

Figure 4.13. Curve fitting for a_{cn}/R and 2α (in radians)

$$a_{cn}/R = e^{-0.0046-0.8710\times(2\alpha)-0.1423\times(2\alpha)^2\times\ln(2\alpha)} \tag{4.3}$$

Where;

a_{cn}/R: Dimensionless critical crack length determined from numerical modeling

2α: Loading angle (radians)

It is noted that Equation 4.3 is applicable from 0.03 radians (2°) to 0.87 radians (50°). When selecting the best-fit equation, the restraint that a_{cn} should be less than or equal to R is considered. For the lower limit case 2α =0.03 radians (2°), a_{cn}/R is 0.97.

Similar work was conducted by Özdoğan (2017) and Keles and Tutluoglu (2011) to derive two parametric equations. However, comprehensive numerical modeling was not conducted to cover more data points, especially for geometries with smaller loading angles. In order to assess the quality of the equations proposed here, $Y_{I\,max}$ and a_{cn}/R values were compared with previous studies.

The average $Y_{I\,max}$ difference between the present work and Keles and Tutluoğlu's numerical study is around 2.1%. In the comparison between the present work and Özdoğan's numerical study shows a negligible difference at around 0.2%. The maximum differences were observed at the loading angles less than or equal to 10°. As a result of this comparative study, there was no considerable difference between the computed $Y_{I\,max}$ values.

The average a_{cn}/R difference was around 3.0% between this work, and Keles and Tutluoglu's work. This study and Özdoğan's numerical study were compatible, and the a_{cn}/R difference was approximately 0.6%.

CHAPTER 5

TESTING THE MECHANICAL PROPERTIES OF ANDESITE

Before examining the fracture behavior of grey colored Gölbaşı andesite, petrographic analysis was conducted. Then, some important mechanical behaviors were ascertained by performing static deformability and indirect tensile tests. The elastic modulus E, Poisson's ratio v, and uniaxial compressive strength UCS were acquired from the static deformability tests. Tensile strength σ_t was determined from the Brazilian test.

All tests were conducted on andesite core samples according to ASTM or ISRM standards. For all tests, the MTS 815 rock mechanics testing system was used. The specimen preparation and tests were carried out at the Rock Mechanics Laboratory of Mining Engineering Department, METU. The location of the andesite rock taken from a quarry nearby Ankara Gölbaşı is given in Figure 5.1.

Figure 5.1. Location of the quarry where andesite rocks are taken (Google Earth, 2020)

5.1. Petrographic Analysis of Gölbaşı Andesite

A thin section of Gölbaşı andesite was prepared to examine a detailed description of the texture and the optical characteristic of minerals. The petrographic analysis was carried out at Geological Engineering Department in METU. The thin section of Gölbaşı andesite was given in Figure 5.2.

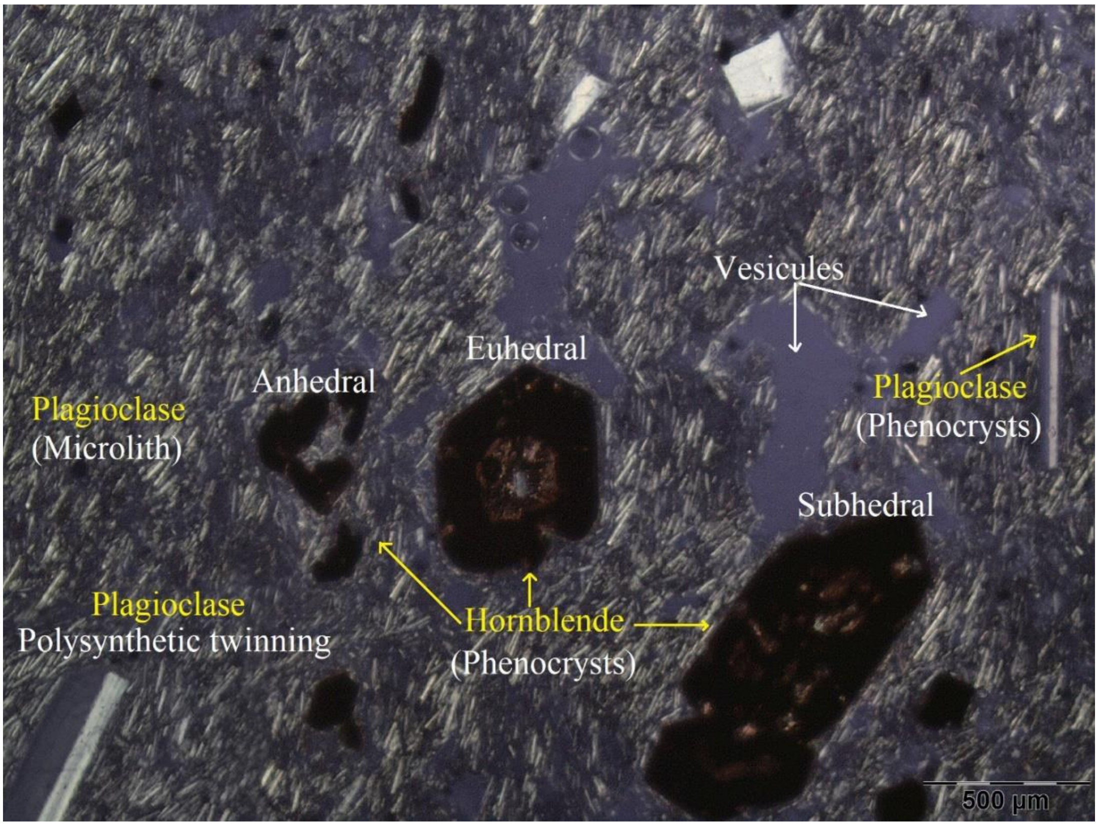

Figure 5.2. Thin section analysis for Gölbaşı andesite

The name of the sample is porphyritic andesite because the sample includes both coarse and fine-grained texture. The sample contains hornblende and plagioclase minerals as phenocrysts can be seen in Figure 5.2. The hornblende minerals are euhedral shape, which shows well developed hexagonal geometry as well as subhedral and anhedral shape. Hornblende minerals are also in dark brownish color since the alteration gives rise to an increase in opacity. The characteristic textures can be observable in the analyzer in a microscope for the plagioclase crystals, which are polysynthetic twinning and zonation. The groundmass is composed mainly of microlith minerals, which are small scale crystallized plagioclase minerals.

When the entire thin section is examined, the two most distinguishable texture can be observed. One of them is a vesicular texture. The other and the most prominent texture in the sample is flow texture observable for both hornblende and plagioclase crystals. It shows a lineation direction from the top right to the bottom left can be seen in Figure 5.3.

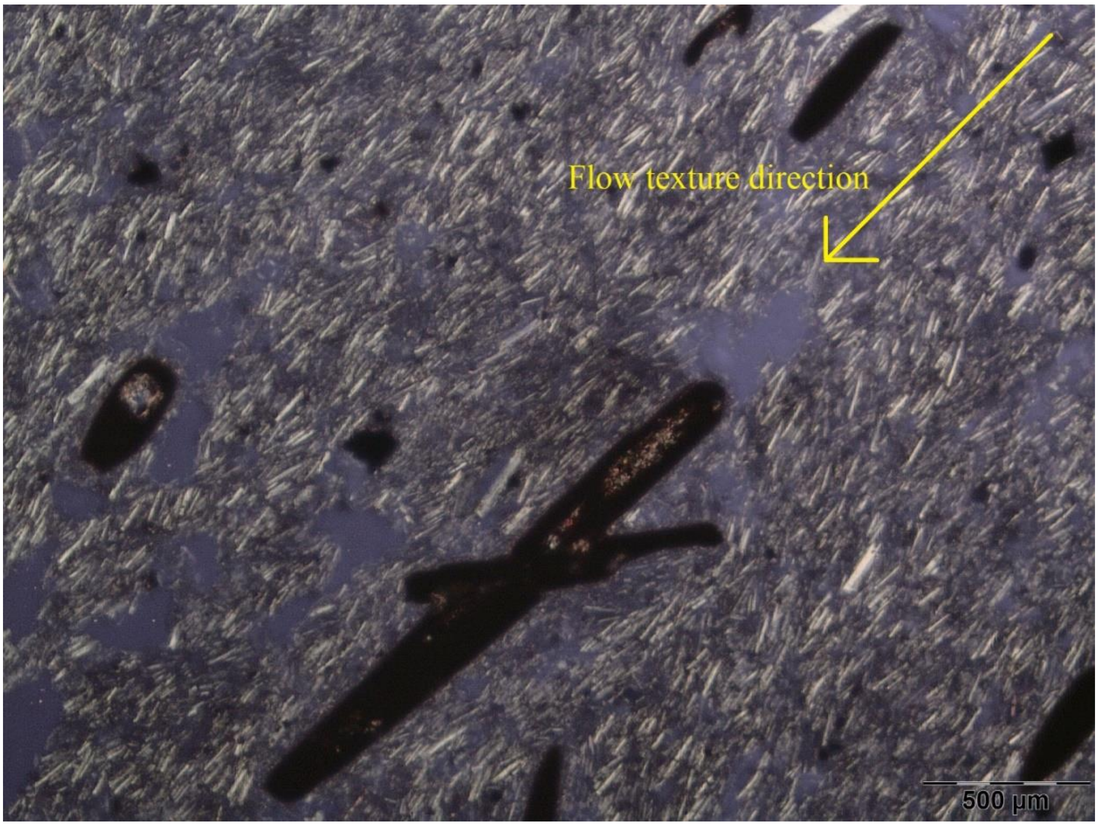

Figure 5.3. Flow texture in Gölbaşı andesite

Whether the direction of these flows is parallel or perpendicular to the loading direction of the sample affects the mechanical test results of andesite. As a result, the mechanical properties of andesites from different locations around Ankara may show large variations in the testing work of a number of researchers.

5.2. Static Deformability Test

In order to measure Young’s modulus, Poisson’s ratio, and uniaxial compressive strength of Gölbaşı andesite, the static deformability test is performed. The test is designed in general for the classification and characterization of rock.

ASTM and TSI have proposed the ideal geometry for the UCS of the test specimen as the length to diameter ratio of 2-2.5 (ASTM D7012-14, 2014; TS 699, 1987). Three NX type andesite core specimens having approximately 54 mm diameter and 130 mm thickness were prepared to satisfy the proposed length to diameter ratio.

Tests were conducted under compression by MTS 815 rock testing machine with a displacement-controlled rate of 0.0005 mm/s so that yield occurred within 15-20 minutes. During the test, the axial and circumferential deformations were recorded for each increment of load. Two extensometers were attached to the specimen to measure both axial and circumferential displacements under compression (Figure 5.4).

Figure 5.4. Static deformability test specimen with extensometers

Figure 5.5 shows the typical plot of axial stress versus diametric and axial strains. Such curves demonstrate the characteristic behavior of rock materials from zero to ultimate stress. The modulus of elasticity can be determined from the slope of the straight-line portion of the stress-axial strain curve, which is at a fixed percentage of UCS. The Poisson's ratio can be calculated by dividing the slope of the stress-axial strain curve by the negative of the slope of the stress-diametral strain curve.

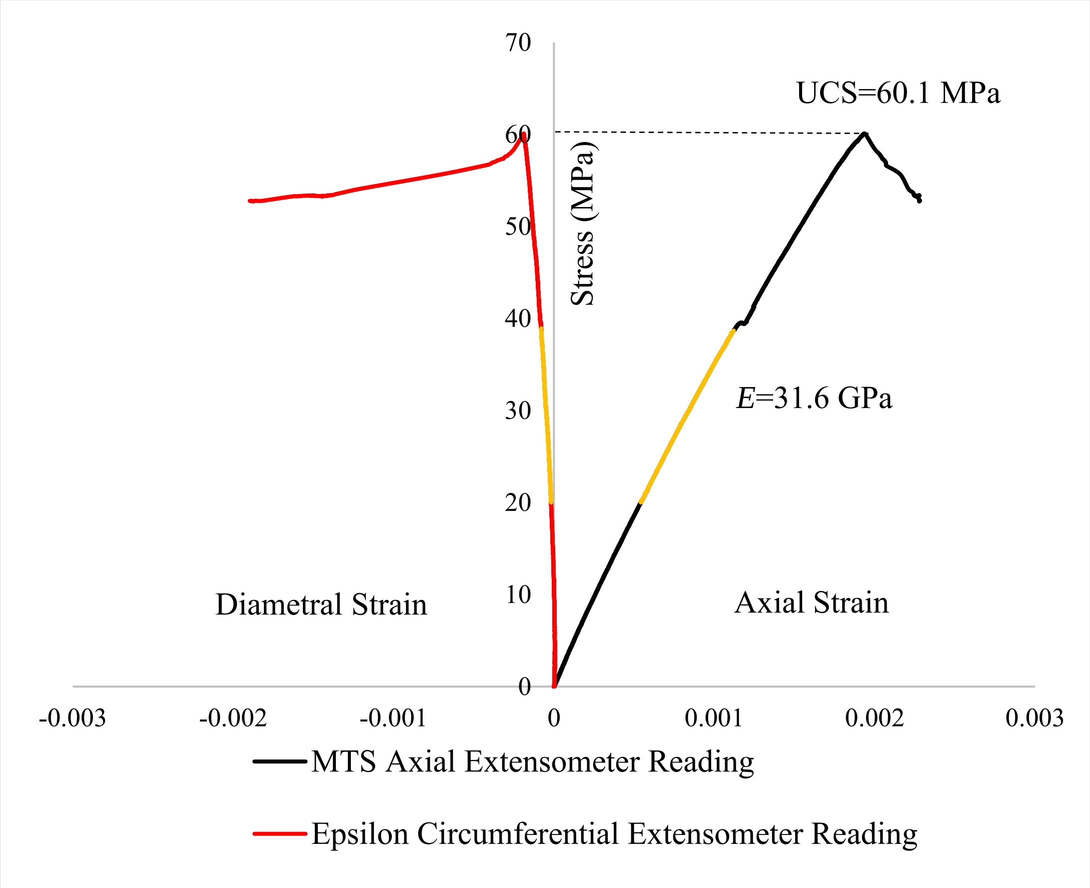

Figure 5.5. Axial and diametric stress-strain curves of the sample A-SD-1

The static deformability test results are given in Table 5.1. As seen from Table 5.1, the average failure load, elastic modulus, Poisson's ratio, and uniaxial compressive strength are found to be 144.6±4.2 kN, 31.9±0.4 GPa, 0.10±0.02, and 61.8±1.8 MPa, respectively.

Table 5.1. *Results of static deformability tests*

Specimen	Failure Load (kN)	Elastic Modulus (GPa)	Poisson's Ratio	Uniaxial Compressive Strength (MPa)
A-SD-1	140.5	31.6	0.10	60.1
A-SD-2	148.9	31.9	0.08	63.7
A-SD-3	144.3	32.4	0.11	61.7
Average±STD	144.6±4.2	31.9±0.4	0.10±0.02	61.8±1.8

5.3. Indirect Tensile Test (Brazilian Test)

International Society for Rock Mechanics and American Society for Testing and Materials suggested the Brazilian disc test method for determining the indirect tensile strength of brittle material such as rock, concrete, and rock-like materials (ASTM D3967–95a, 2008; ISRM, 1978). Thanks to the ease of sample preparation and simple testing method, the Brazilian disc test has become an extensively used test method in rock mechanics.

The Brazilian tests were performed for determining the tensile strength of Gölbaşı andesite. ASTM recommended the thickness diameter ratio t/D between 0.2 and 0.75 (ASTM D3967–95a, 2008). The disc specimens with a diameter of about 54 mm and thicknesses of about 33 mm will satisfy this criterion. Three andesite disc specimens were subjected to constantly increasing compressive loads. The compressive load induced tensile stress perpendicular to the loading axis. The disc specimen was loaded using two opposing curved jaws, as seen in Figure 5.6. Line loading leads to stress concentrations at the loading ends of the specimen, and the curved loading jaws reduce the contact stresses on the test specimen. Experiments were conducted utilizing MTS 815 rock testing machine with a displacement-controlled rate of 0.001 mm/s. Failure in the Brazilian disc specimens occurred within 5 to 10 minutes.

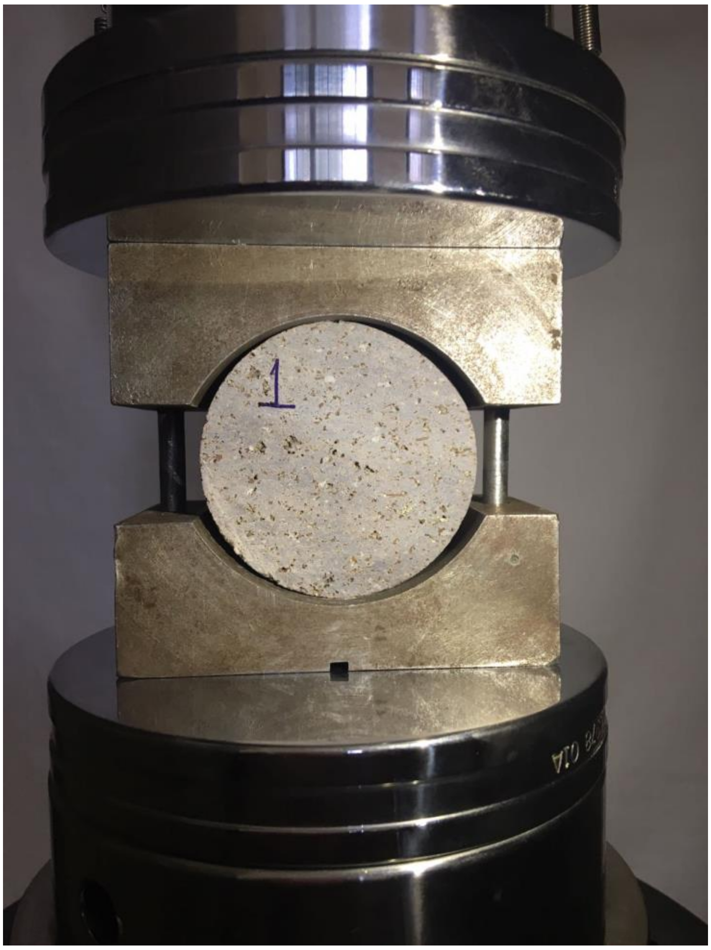

Figure 5.6. Brazilian disc test configuration

A typical force-displacement curve is plotted for the A-BT-2 coded specimen in Figure 5.7, and the tensile strength of andesite is calculated using P_{max}. This curve has both P_{max} and P_{min} values and shows a similar trend as the FBD test curve. The use of curved jaw at the loading ends reduces stress concentration by imposing an average loading angle of about 10° (ISRM, 1978). Similarly, two flat surfaces are introduced in the FBD specimen for the same purpose.

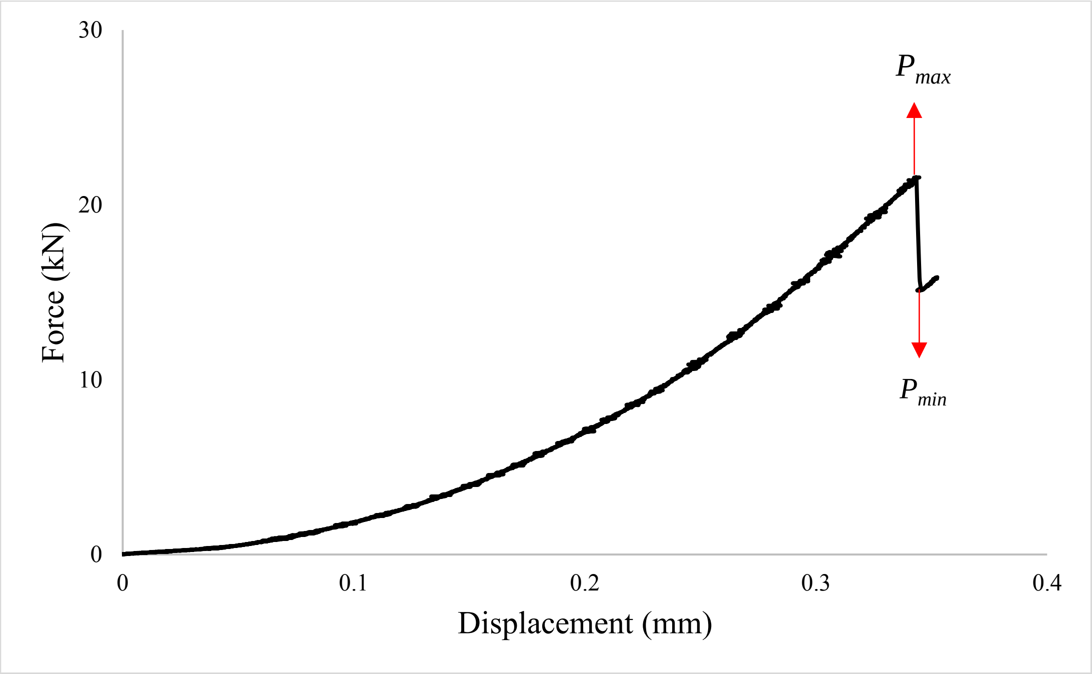

Figure 5.7. A typical force vs displacement curve of the sample A-BT-2

The fractured Brazilian disc specimens after the test are shown in Figure 5.8. The formation of crack through the vertical diameter of the specimen can be seen in Figure 5.8.

Figure 5.8. Failure pattern of Brazilian disc specimens

The peak loads and tensile strengths of andesite are given in Table 5.2. According to Table 5.2, the average peak load and the tensile strength of BD andesite specimens with the curved platens are 20.50±0.99 kN and 7.18±0.20 MPa, respectively.

Table 5.2. *Results of Brazilian tests*

Specimen	Peak Load (kN)	Tensile Strength (MPa)
A-BT-1	20.28	7.17
A-BT-2	21.59	7.39
A-BT-3	19.64	6.99
Average±STD	20.50±0.99	7.18±0.20

5.4. Comparison of Results of Different Researchers

Static deformability and indirect tensile test results of andesite compiled from the literature were given in Table 5.3.

Table 5.3. *Material properties of andesite compiled from the literature*

Source	Elastic Modulus (GPa)	Poisson's Ratio	UCS (MPa)	Tensile Strength (MPa)
Keles and Tutluoglu (2011)	12.3±0.1	0.15±0.01	82.8±4.1	7.00±0.67
Karakaş (2011)	18.1±4.1	0.15±0.06	69.9±14.8	10.19±1.04
Alkan (2015)	12.3±0.5	0.12±0.05	58.6±0.8	3.37±0.22
Özdoğan (2017)	21.9±1.3	0.15±0.01	84.7±7.1	9.57±1.78
Present Work	31.9±0.4	0.10±0.02	61.8±1.8	7.18±0.20

The results show that there are significant differences in the mechanical properties of andesite. Andesite includes heterogenous populations of crystals, and mineral heterogeneity causes a wide variation in the mechanical properties. The orientation between the flow texture direction and applied force affects the test results of andesite.

CHAPTER 6

MODE I FRACTURE TOUGHNESS TESTING WITH FBD GEOMETRY

To understand the key factors in the design of specimens for mode I fracture toughness determination, it would be more useful to use a configuration as simple as possible. Fracture toughness measurement with the flattened Brazilian disc (FBD) specimen is a convenient and simple method. This method does not require any complicated specimen preparation procedure and extra equipment for load-displacement measurement. Core specimens available from the site investigation can be readily adopted for fracture toughness testing. Specimen preparation is relatively easier than other fracture toughness methods since pre-cracking and notching are not required before testing.

This chapter presents a detailed description of the flattened Brazilian disc specimen preparation procedure, testing work with FBD specimen, experimental critical crack length measurement procedure, and conditions for the validity of FBD test results.

FBD tests were conducted on grey colored Gölbaşı andesite specimens of varying diameter and loading angle to verify whether the mode I fracture toughness varies with the specimen size. The tests were performed on the specimen groups of four diameters, which were 54 mm, 75 mm, 100 mm, and 125 mm. Loading angles were varied within the individual diameter groups. The lowest and highest loading angle were 16° and 42°, respectively. A total of 51 FBD specimens were tested. In all of the fracture toughness tests, MTS Model 815 rock mechanics test system was used.

6.1. Specimen Preparation

Rock fracture toughness tests are susceptible to specimen size and shape. The machining precision of the disc and the reliability of the instruments have a major impact on test results. Therefore, specimen preparation is a crucial step in FBD testing.

After the size reduction of large blocks into appropriate segments, large blocks were cored with a rock coring machine (Figure 6.1). The cores were about 54, 75, 100, and 125 mm in diameter.

Figure 6.1. Rock coring machine

A rotary saw was used to cut discs to the desired thickness, and the flat surfaces of the specimen were machined by polishing. Polishing is necessary since the specimen was not cut with a precision saw, and the ends of the specimen should be smooth and flat. The milling machine with the diamond milling cutter was used for thickness adjustment and creating flat and smooth surfaces (Figure 6.2). The ends of the specimen must be parallel to each other. This requirement can be met by properly positioning the core samples in the milling machine for thickness adjustment. ASTM D3967–95a (2008) suggested thickness to diameter ratio (t/D) between 0.2 and 0.75 for the Brazilian disc specimen. The thickness to diameter ratio of the FBD test specimen was selected as 0.6. The thickness of specimens having 54, 75, 100, and 125 mm diameter was reduced to approximately 32 mm, 45 mm, 60 mm, and 75 mm, respectively.

Figure 6.2. Thickness adjustment of specimen

Specimens were selected by visual observation, based on grain size and shape, without a series of samples based on defects such as pores and cracks. Specimens containing voids and visible large cracks were eliminated. The center of the disc is located and marked following the diametral line drawn (Figure 6.3).

Figure 6.3. Diametral line positioning with the goniometer

The reference lines are drawn, as shown in Figure 6.4. $R\sin\alpha$ portion represents the half-flattened end at upper and lower boundaries of the FBD geometry. The vertical length of the section to be cut above and below the specimen is calculated separately as $R - R\cos\alpha$, and these sections were marked on the sample. These lines are used as reference lines for properly positioning the specimen in the milling machine and constructing the parallel flat surfaces.

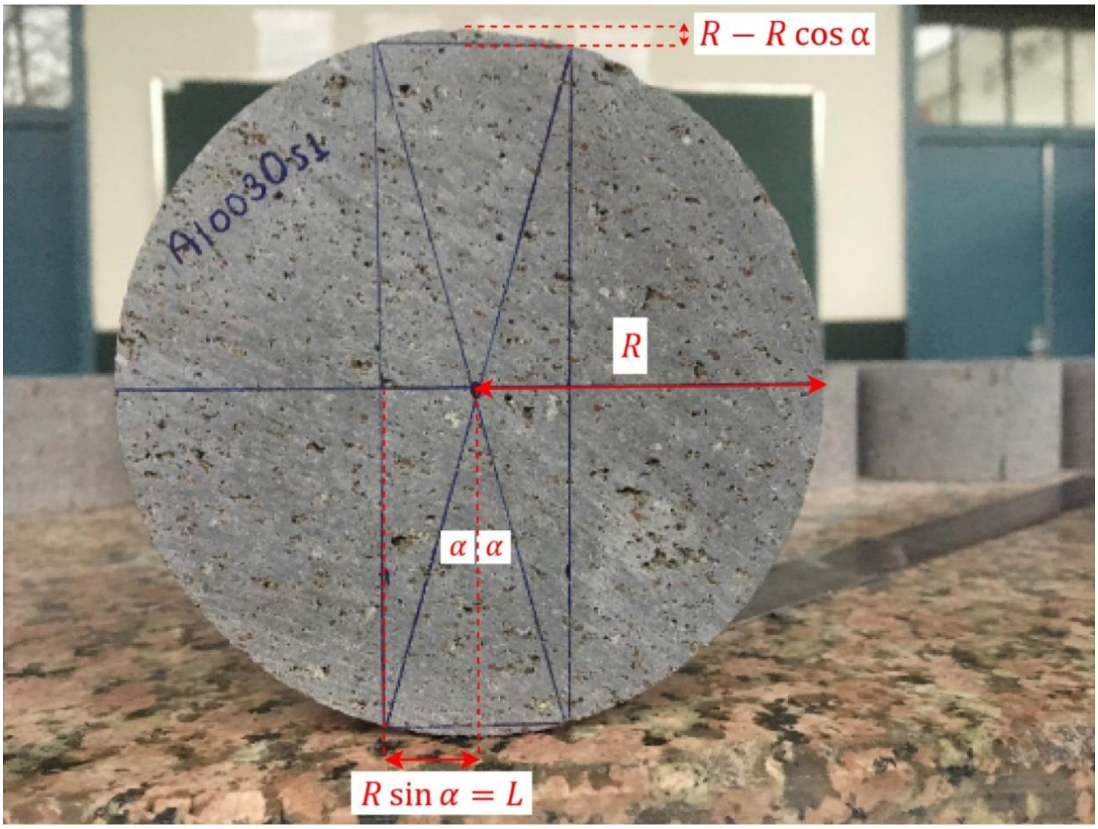

Figure 6.4. Reference lines drawn

The core sample was placed axially in the milling machine, as illustrated in Figure 6.5. To ensure the flatness and parallelism of the flattened ends, the screws were tightened to prevent movement of the specimen. The top and bottom ends of the specimen were machined and flattened according to the desired loading angle.

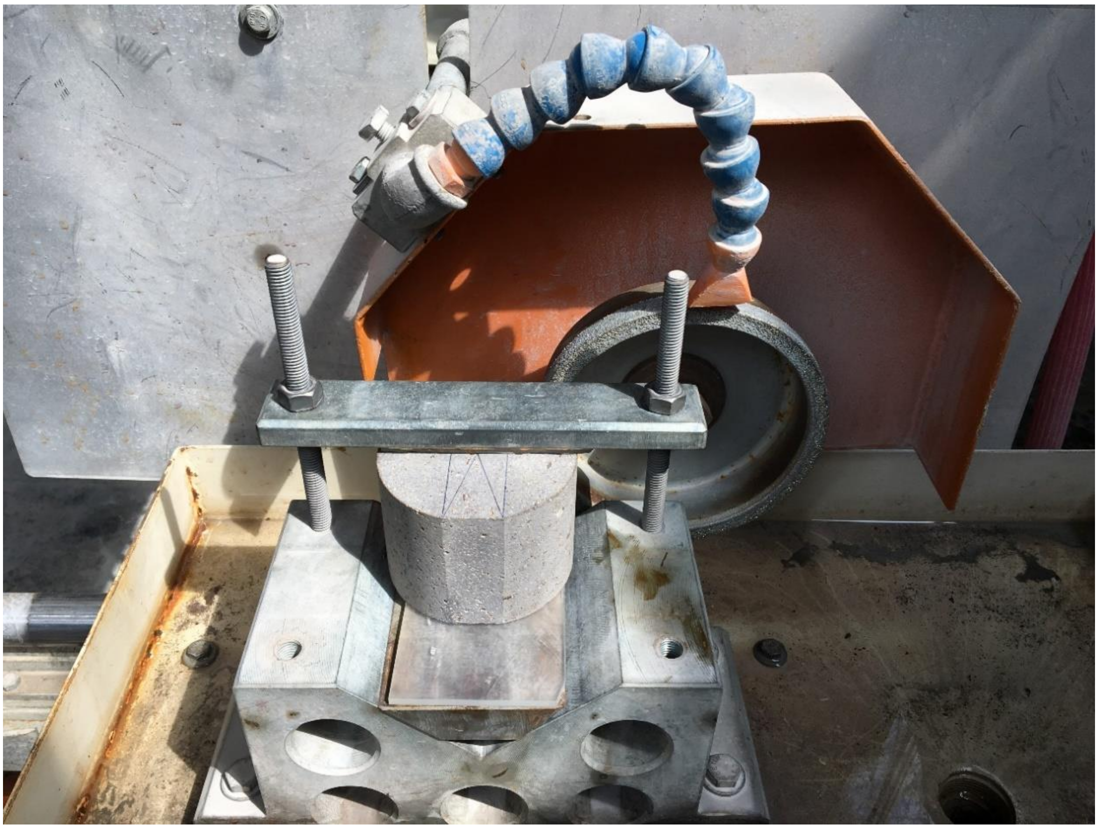

Figure 6.5. Flattening top and bottom ends

Specimens are labeled before testing. Labeling provides coding involving information regarding the specimen category and group. Each specimen is assigned a code, and the specimen labeling rule is illustrated in Figure 6.6. In specimen labeling A indicates andesite used in the tests, 100 (or 54, or 75 or 125) represents the core diameter, 24 shows the loading angle ranging from 16° to 42°, and s1 (or s2, or s3) signifies the sample number in a certain category.

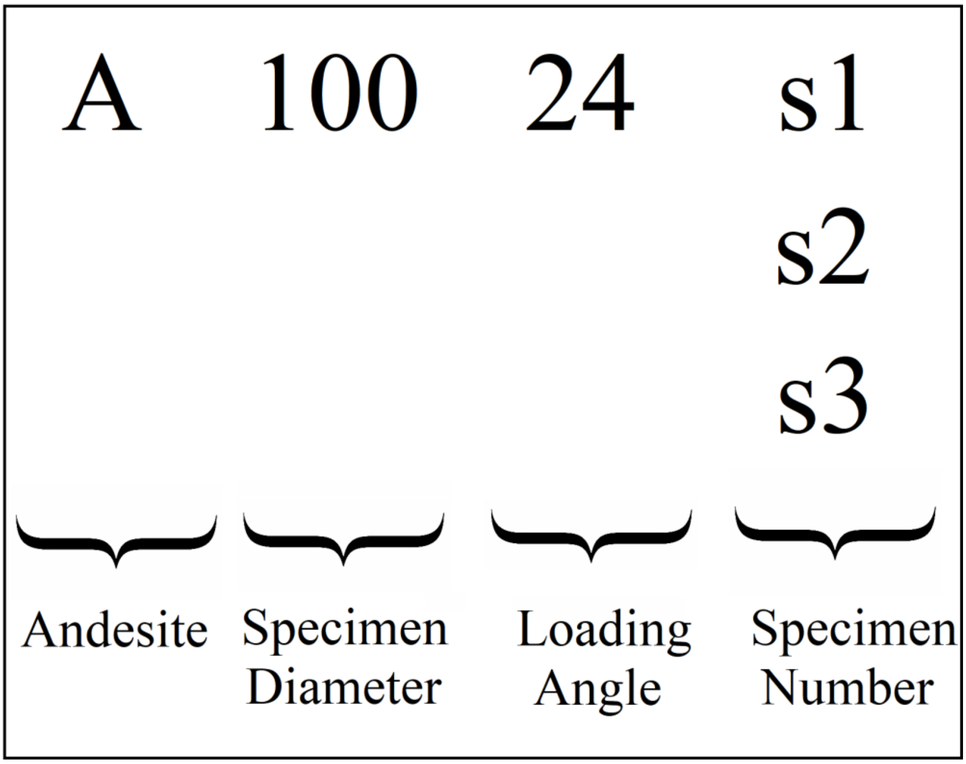

Figure 6.6. Specimen labeling method

6.2. Fracture Toughness Testing Work

After the flattening process of the top and bottom edges of Brazilian discs was completed and the flatness and parallelism of both surfaces of the specimens were ensured, the specimen dimensions (t and D) were measured and noted. Then, testing was conducted under compression by the servo-hydraulic MTS 815 testing system. The test specimen was positioned between the top and bottom loading platens. Flattened Brazilian disc specimen under the platens of the servo-controlled loading frame is shown in Figure 6.7. The FBD specimen was subjected to a continuously increasing compressive load, and displacement-controlled loading was applied to the specimen. During the test, the local minimum load (P_{min}) was recorded to be used in the computation of fracture toughness.

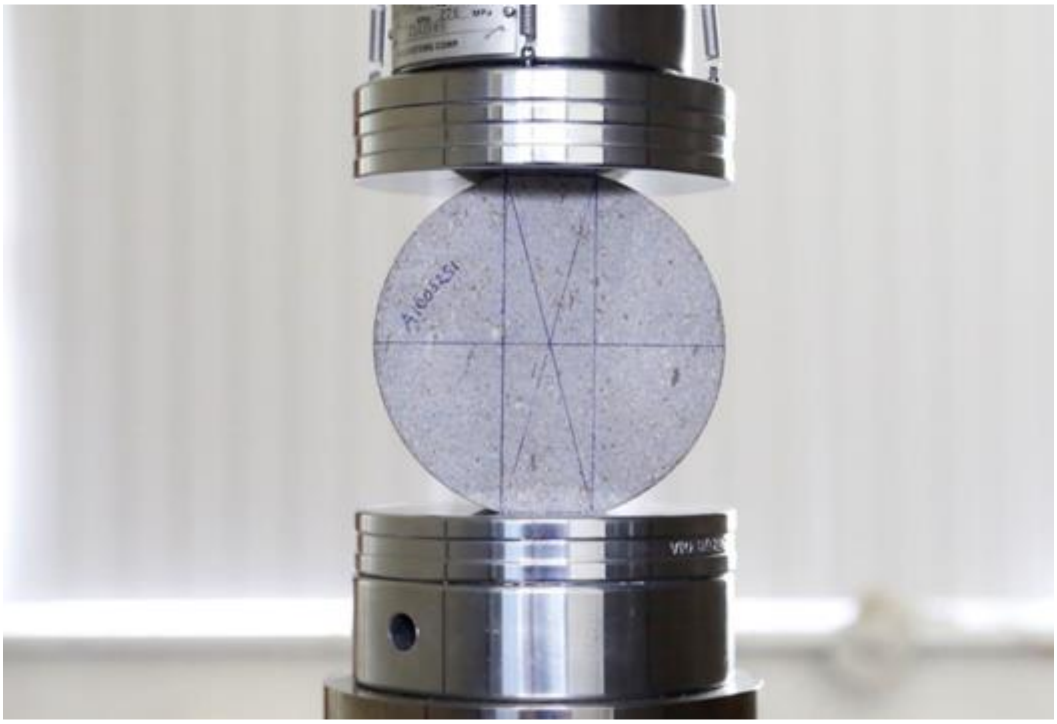

Figure 6.7. FBD specimen under compression

A typical force versus displacement curve of the flattened Brazilian disc specimen is shown in Figure 6.8. The rest of the force-displacement curves are presented in Appendix A.

The process of fracture can be described in three stages as can be seen in Figure 6.8. At first, the specimen behaves nonlinearly, possibly due to the compression of existing porosity and voids. In the first region up to the local maximum load (P_{max}), the specimen has a linear behavior that represents the elastic deformation of the specimen. At the peak load, a tensile crack initiates at the center of the specimen. Tensile strength calculation can be done using maximum load P_{max} based on the FBD method.

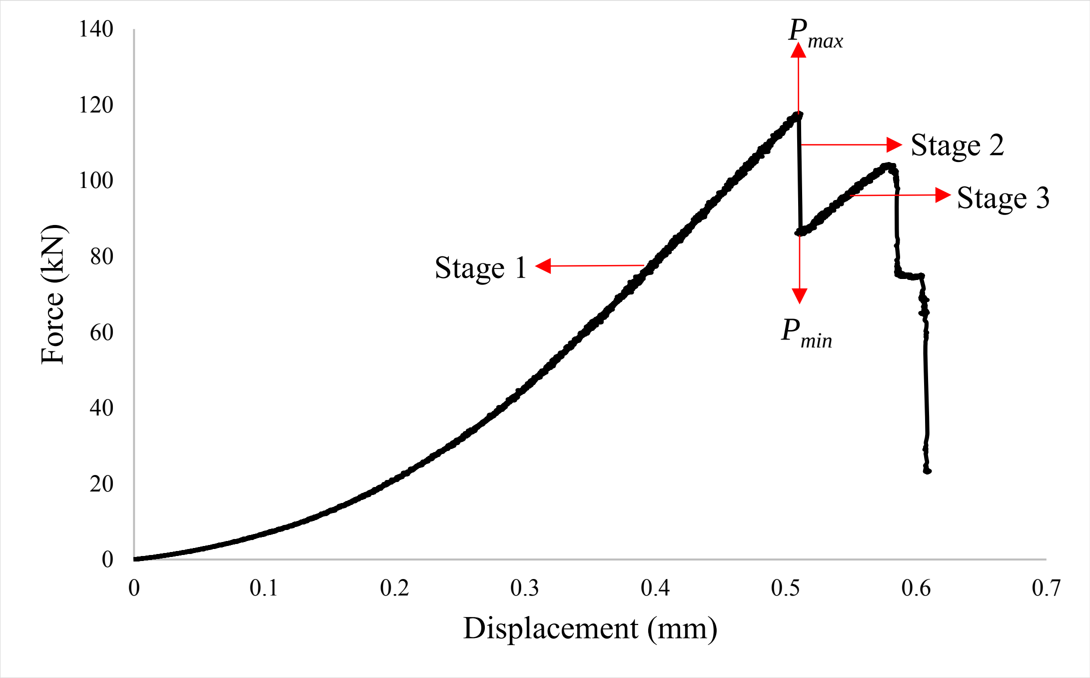

Figure 6.8. A typical valid force-displacement curve of FBD test on A10030s1 specimen

The second stage corresponding to the load drop from local maximum load (P_{max}) to local minimum load (P_{min}) represents the unstable crack propagation. The crack develops unstably along the centerline until the load drops to the local minimum load. P_{min} is selected as the critical point, and it is used in the formula for computing the fracture toughness. P_{min} separates the unstable and stable regions and corresponds to the critical crack length a_{cn}/R. The determination of the critical crack length has been explained in detail in section 6.3. The difference between the first peak point P_{max} and local minimum load P_{min} is named as load drop (ΔP), and the division of the load drop by the flattened end area is defined as stress drop ($\Delta\sigma_a$).

Finally, at the third stage, the load starts to increase for further crack propagation. This stage corresponds to the stable crack propagation because the crack develops with the increase in load. Secondary cracks develop with further load increase, and the curve fluctuates.

The loading procedure is a code written in the function generator part of the MTS FlexTest controller console, and it is called procedure. The loading procedure of FBD specimens is presented in Figure 6.9. The procedure begins with a high rate of loading (0.4 µm/sec) and continues until the first load limit detector. Then, the intermediate rate loading stage starts at a displacement rate of 0.2 µm/sec. The step of the intermediate loading rate continues until the second load limit detector. Finally, the low loading rate (0.1 µm/sec) carries on until the failure of the specimen. The reason for a slow rate choice at this stage is to detect the a_{cn} and the load drop clearly. Since the specimens to be tested have different diameters and loading angles, the load-displacement curve behaviors are different. Therefore, a common procedure was prepared for all specimens. The loading speed should be quite slow to guarantee the observation of load drop and experimental crack length clearly and precisely. At the low loading rate stage, there is sufficient time to photograph the experimental critical crack length. The gradual change in the loading rate saves time in experiments. Even with this procedure, the experiments for large diameter specimen take about 1.5 hours.

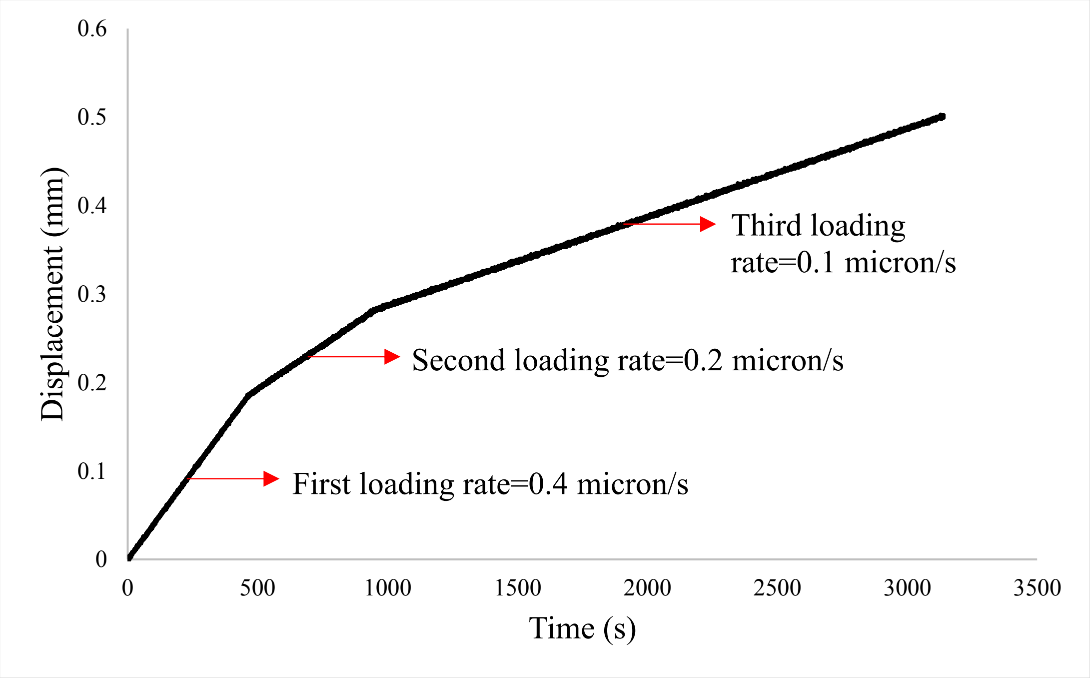

Figure 6.9. Loading procedure

To investigate the size effect on K_{IC}, the mode I fracture toughness tests were conducted on four different diameters, which are 54 mm, 75 mm, 100 mm, and 125 mm. The loading angle was varied between 16° and 42° to investigate the loading angle effect.

6.3. Detection of Critical Crack Length

A typical cracked specimen photo during load drop detection in the load-displacement graph is shown in Figure 6.10.

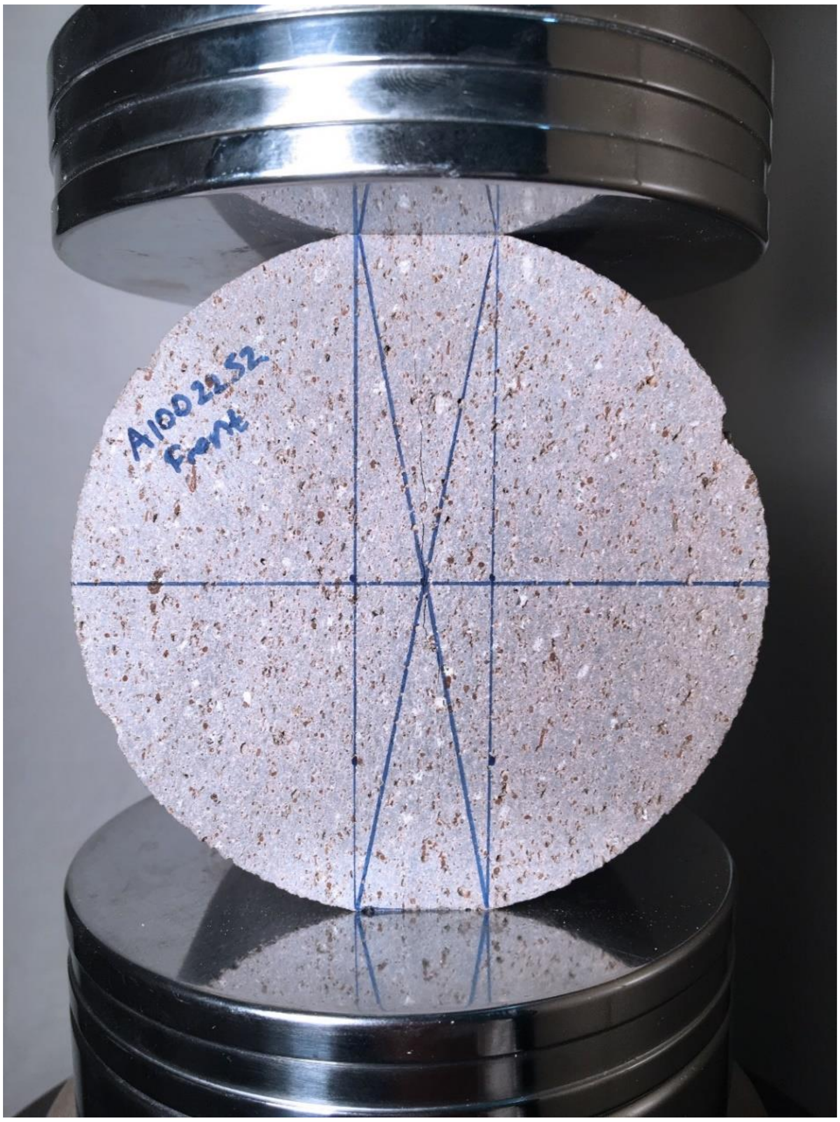

Figure 6.10. Critical crack length formation at local minimum load

The size of the experimental critical crack length is measured by the following procedure:

- The loading rate is set to 0.1 µm/sec to see the crack initiation and unstable crack propagation.
- When a load drop is detected in the force versus displacement graph, the cracks formed on both surfaces of the sample are photographed.
- Using Adobe Photoshop software, the photo is scaled to its actual size of the specimen.
- A horizontal guideline is added directly above the diametral line of the specimen.
- If necessary, the sample is rotated or cropped.
- The measurement scale is adjusted to the actual dimensions of the sample.
- A line with the ruler tool is drawn to measure linear distance between the start and endpoints of the initial crack. The crack length scaled according to the actual size of the sample is measured.

An example of experimental critical crack length measurement by utilizing Adobe Photoshop software is represented in Figure 6.11. The crack initiated at the center of the FBD specimen as expected and propagated to the flattened loading ends with minimum deviation from the expected path. Experimentally determined critical crack length photographs for all FBD specimens are shown in Appendix B.

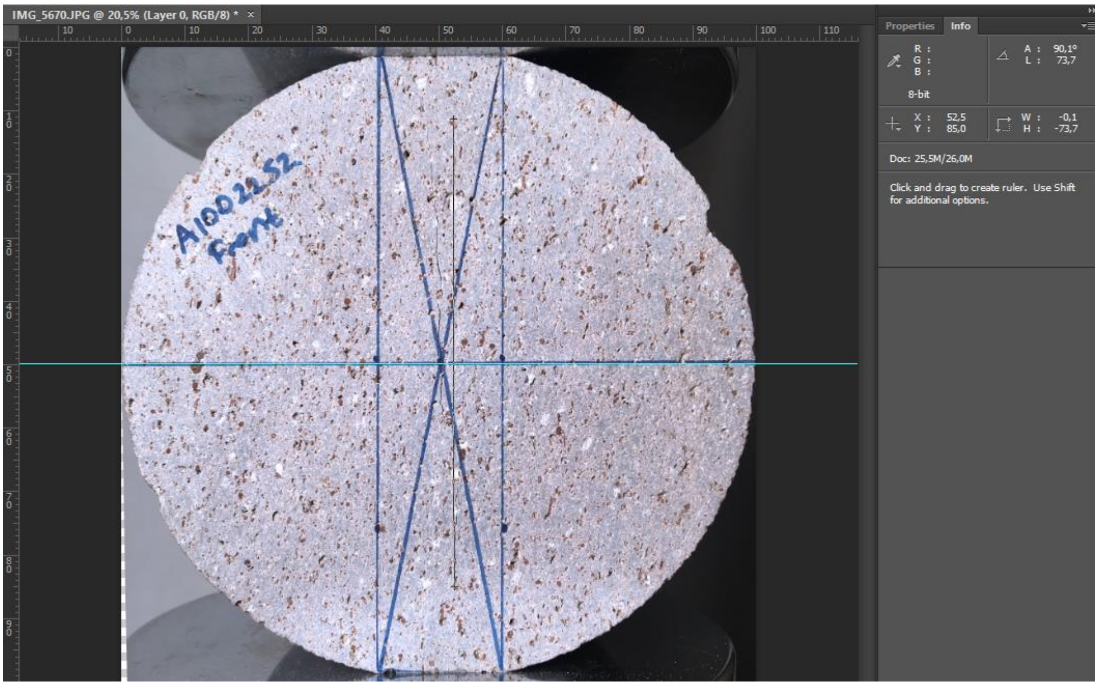

R :
G :
B :
8-bit
A : 90,1°
L : 73,7
X : 52,5
Y : 85,0
W : -0,1
H : -73,7
Doc: 25,5M/26,0M

Click and drag to create ruler. Use Shift for additional options.

Figure 6.11. Experimental critical crack length measurement ($2a_{ce}$ =71.7 mm for A10022s2 specimen)

6.4. Determination of Fracture Toughness

The mode I fracture toughness with the flattened Brazilian disc specimen is calculated using Equation 6.1 (Wang and Xing, 1999).

$$K_{IC} = \frac{P_{min}\, Y_{I\,max}}{\sqrt{R}\, t} \tag{6.1}$$

where K_{IC} is mode I fracture toughness (MPa$\sqrt{\text{m}}$), P_{min} is the local minimum load of the load-displacement test record (MN), $Y_{I\,max}$ represents maximum mode I dimensionless SIF computed from numerical modeling, R signifies disc radius (m), and t is disc thickness (m). The maximum dimensionless stress intensity factor for mode I ($Y_{I\,max}$) in Equation 6.1 is computed as described in Equation 6.2.

$$Y_{I\,max} = \frac{K_{I\,max}\sqrt{R}\, t}{P} \tag{6.2}$$

In Equation 6.2, $K_{I\,max}$ is the mode I maximum stress intensity factor. For loading angle between 0.03 radian (2°) and 0.87 radian (50°), $Y_{I\,max}$ can be calculated using Equation 6.3.

$$Y_{I\,max} = -0.0196 - 0.3334\ln(2\alpha) + \frac{0.1892}{(2\alpha)^{0.5}} + \frac{0.0001}{(2\alpha)^{2}} \qquad (6.3)$$

Where 2α is the loading angle in radians.

An example computation is presented in the steps below for the sample A10022s2.

- $Y_{I\,max}$ value computed by numerical modeling work is 0.61 for 2α =20°.
- The thickness and diameter of the disc are 60.68 mm and 100 mm, respectively.
- The local minimum load (P_{min}) is determined from the load-displacement test record. P_{min} is detected as 66.29 kN for the A10022s2 specimen.
- The mode I fracture toughness is calculated by using Equation 6.1.

$$K_{IC} = \frac{(66.29 \times 10^{-3}\mathrm{MN}) \times 0.61}{\sqrt{(50 \times 10^{-3}\mathrm{m})} \times (60.68 \times 10^{-3}\ \mathrm{m})} = 2.98\ \mathrm{MPa}\sqrt{m}$$

6.5. FBD Test Validity Conditions

In the literature, the validity conditions of the FBD test have been extensively investigated theoretically, numerically, and experimentally. Two essential indicators of the validity of FBD tests are the crack initiation at the FBD specimen center and clear load drop in the force-displacement curve.

Wang and Wu (2004) defined the validity criteria for the FBD test, which depends on the shape of the load versus displacement record. They described the fracture process by load descending and then ascending behavior and stated that the ascending load should not exceed the preceding maximum load for the test validity (Figure 6.12). They claimed that when the peak value of the loading force was higher than the initial maximum load level, the secondary crack played the leading role instead of the primary crack, and the test will become invalid. However, Wu et al. (2018) argued that different rocks have different post-peak characteristics, and only the shape of the force-displacement curve cannot determine the validity of the test. They evaluated the validity of the FBD test by investigating whether the failure was caused by the central primary crack. They identified two conditions for the validity of the test: the central crack initiation and failure caused by the primary crack. Once these conditions were met, the test will still be valid even if the second peak was larger than the first peak. Besides, not all secondary cracks cause an invalid test. The secondary crack may occur following the complete development of the primary crack, as was the case in the load-displacement record of Figure 6.12.

The crack formations and related force-displacement records of FBD specimens with a loading angle of $2\alpha = 18°$, $2\alpha = 28°$, and $2\alpha = 42°$ are given in Figure 6.12, Figure 6.13, and Figure 6.14, respectively. The clear load drop was observed on the force-displacement plot of these three FBD specimens. As seen in Figure 6.13, the crack initiated at the center of A12528s1 coded FBD specimen and propagated toward the flat ends. For A12518s1 and A12542s2 specimens, however, the crack initiation location deviated from the center of the specimen. The crack initiation location may be affected by loading angle, material inhomogeneity, and distribution of voids, causing stress intensifications.

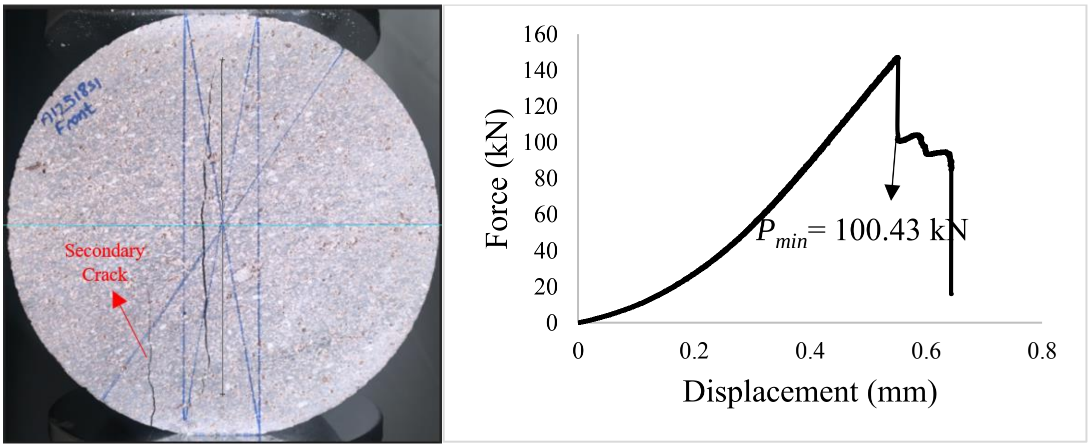

Figure 6.12. Crack formation and related force-displacement record of A12518s1 specimen

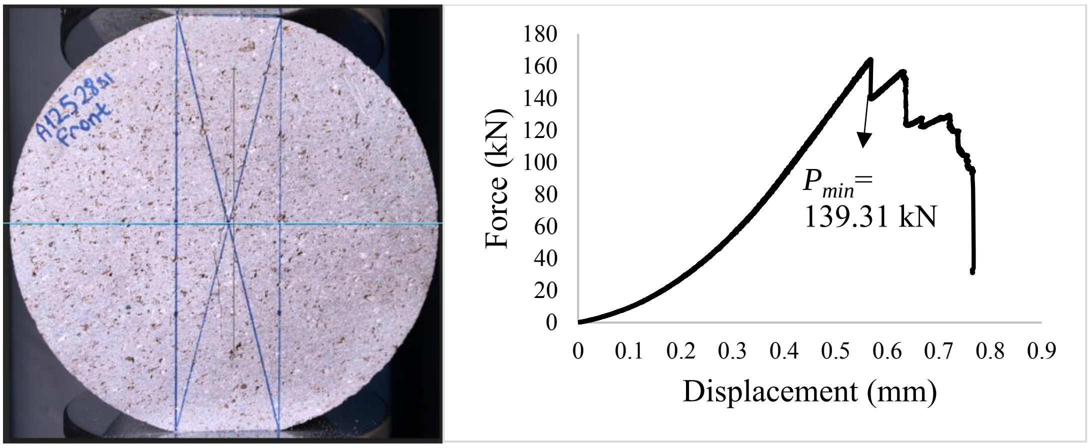

Figure 6.13. Crack formation and related force-displacement record of A12528s1 specimen

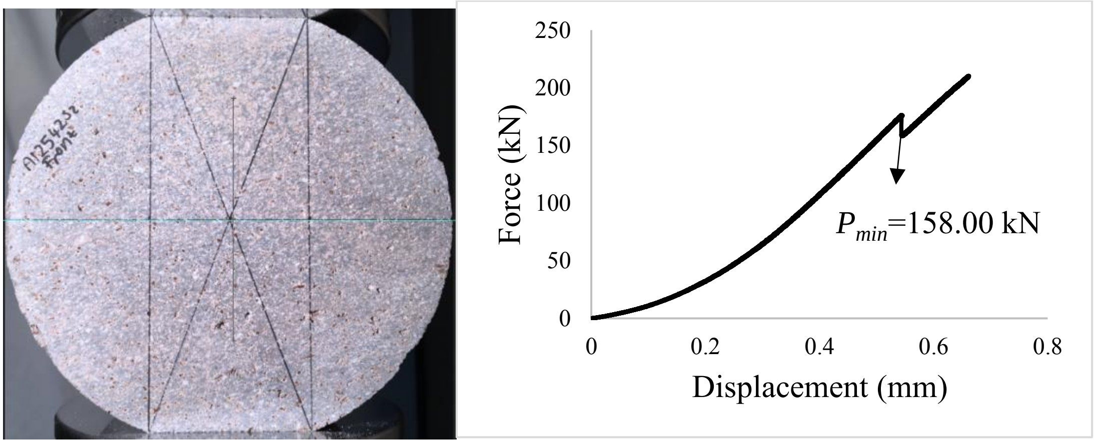

Figure 6.14. Crack formation and related force-displacement record of A12542s2 specimen

The predicted load drop and the subsequent load increase, which is the specific characteristic of the FBD test, was not observed in all tests due to some reasons. Figure 6.15 shows an example of an invalid test due to the sharp load drop. As seen in Figure 6.15, there was a drastic fall in load, and the load did not increase again. It demonstrated that the test was unstable, and the load could not evenly distribute on non-parallel flattened surfaces.

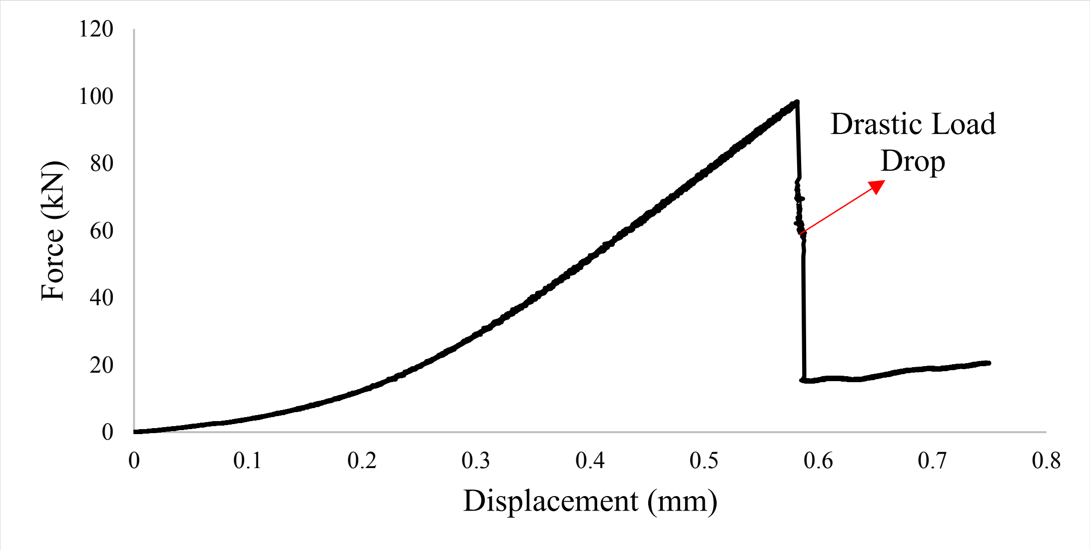

Figure 6.15. Invalid force-displacement curve due to the drastic fall in load

Another type of invalid test due to the two-stage load drop is given in Figure 6.16. The force-displacement curve indicates, following the first crack, another load drop occurs without an increase in load. This two-stage load drop is due to the formation of secondary cracks without the development of the first crack. The secondary crack leads to the failure of the FBD specimen. Therefore, the clear load drop cannot be detected from the curve.

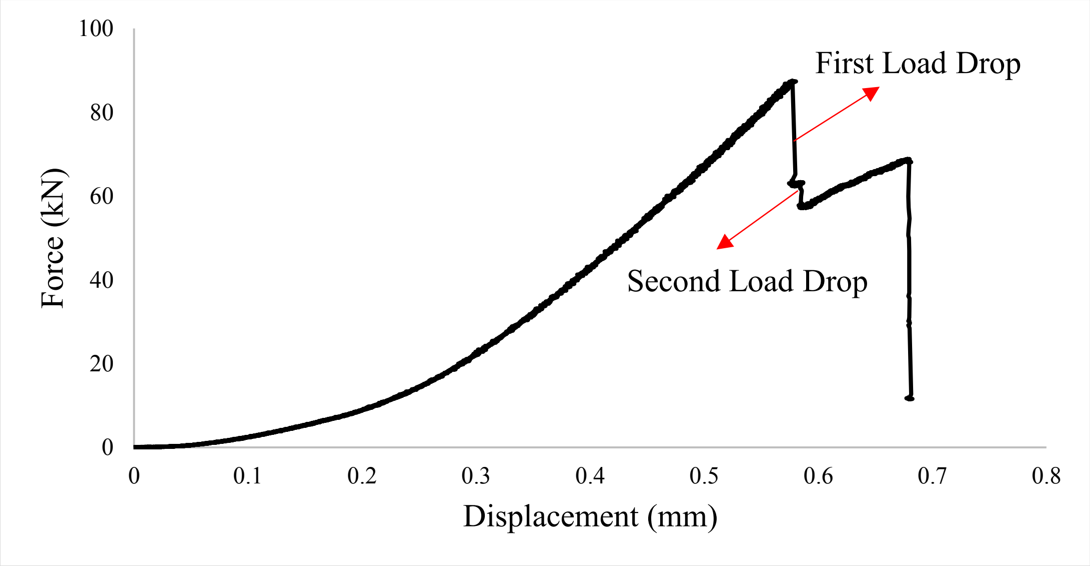

Figure 6.16. Invalid force-displacement curve due to the two-stage load drop

6.6. Fracture Toughness Test Results of Andesite Rock

Results are presented as tables for 54 mm, 75 mm, 100 mm and 125 mm diameter groups. In the tables, the loading angle (2α), flattened end width ($2L$), maximum mode I dimensionless stress intensity factor ($Y_{I\,max}$), load drop (ΔP), local minimum load (P_{min}), stress drop ($\Delta\sigma_a$) and mode I fracture toughness (K_{IC}) are presented.

6.6.1. FBD Specimens Having 54 mm Diameter

The FBD andesite test specimens were prepared with a 54 mm diameter, approximately 32 mm thickness, and five different loading angles. Eight mode I fracture toughness tests were performed, and local minimum loads were recorded during the tests. P_{min}, $Y_{I\,max}$, t and R were used for computation of mode I fracture toughness of andesite core samples of 54 mm. 2α, $2L$, $Y_{I\,max}$, ΔP, P_{min}, $\Delta\sigma_a$ and K_{IC} values are tabulated in Table 6.1.

Table 6.1. 2α, $2L$, $Y_{I\,max}$, ΔP, $\Delta\sigma_a$, P_{min} and K_{IC} values of FBD specimens having 54 mm diameter

Specimen	2α (°)	$2L$ (mm)	$Y_{I\,max}$	ΔP (kN)	$\Delta\sigma_a$ (MPa)	P_{min} (kN)	K_{IC} (MPa$\sqrt{m}$)
A5418s1	18	8.5	0.71	13.37	49.71	13.48	1.83
A5420s1	20	9.4	0.65	8.49	28.31	18.43	2.28
A5420s2	20	9.4	0.65	7.48	25.79	15.71	2.01
A5426s1	26	12.2	0.52	5.43	14.18	23.51	2.36
A5426s2	26	12.2	0.52	6.20	15.91	20.68	2.04
A5432s1	32	14.9	0.43	6.70	13.34	26.57	2.06
A5432s2	32	14.9	0.43	5.74	11.86	22.62	1.82
A5434s1	34	15.8	0.40	4.15	8.47	23.72	1.86
Average±STD							2.03±0.20

As can be seen from Table 6.1, the average mode I fracture toughness of eight FBD specimens having a 54 mm diameter is found as 2.03±0.20 MPa$\sqrt{m}$ for the loading angle range of 18° and 34°. ΔP values vary from 4.15 kN to 13.37 kN, and $\Delta\sigma_a$ values vary from 8.47 kN to 49.71 kN.

For various loading angles critical crack lengths ($2a_c$), critical dimensionless crack lengths (a_c/R) are given in Table 6.2.

Table 6.2. *Critical crack lengths and critical dimensionless crack lengths for 54 mm diameter FBD specimens*

Specimen	$2a_{cn}$ (mm)	$2a_{ce}$ (mm)	a_{cn}/R	a_{ce}/R
A5418s1	41.6	43.9	0.77	0.81
A5420s1	40.5	41.6	0.75	0.77
A5420s2	40.5	42.1	0.75	0.78
A5426s1	37.3	38.0	0.69	0.70
A5426s2	37.3	38.5	0.69	0.71
A5432s1	34.0	34.8	0.63	0.64
A5432s2	34.0	36.1	0.63	0.67
A5434s1	32.9	32.7	0.61	0.61
Average±STD			0.69±0.06	0.71±0.07

6.6.2. FBD Specimens Having 75 mm Diameter

The mode I fracture toughness experiments were carried out on the FBD specimens having 75 mm diameter and approximately 45 mm thickness. The flattened end widths of specimens were adjusted between 11.73 mm and 24.42 mm, which corresponds to the loading angles between 18° and 38°. 2α, $2L$, $Y_{I\,max}$, ΔP, P_{min}, $\Delta\sigma_a$ and K_{IC} values of 75 mm diameter FBD specimens were listed in Table 6.3. The average mode I fracture toughness value acquired from eleven FBD tests was obtained as 2.33±0.13 MPa$\sqrt{m}$. P_{min} values changed between 30.50 kN and 58.23 kN.

Table 6.3. 2α, $2L$, $Y_{I\,max}$, ΔP, $\Delta\sigma_a$, P_{min} and K_{IC} *values of FBD specimens having 75 mm diameter*

Specimen	2α (°)	$2L$ (mm)	$Y_{I\,max}$	ΔP (kN)	$\Delta\sigma_a$ (MPa)	P_{min} (kN)	K_{IC} (MPa$\sqrt{m}$)
A7518s1	18	11.7	0.71	20.44	38.29	30.91	2.49
A7522s1	22	14.3	0.61	22.24	34.29	30.50	2.12
A7522s2	22	14.3	0.61	9.60	14.65	35.48	2.44
A7524s1	24	15.6	0.56	10.74	15.27	37.91	2.43
A7524s2	24	15.6	0.56	16.07	22.93	38.09	2.45
A7530s1	30	19.4	0.46	13.02	14.66	43.74	2.27
A7530s2	30	19.4	0.46	9.74	10.97	46.62	2.42
A7534s1	34	21.9	0.40	6.79	6.83	50.69	2.31
A7536s1	36	23.2	0.37	5.96	5.77	49.17	2.11
A7538s1	38	24.4	0.35	5.76	5.18	58.23	2.31
A7538s2	38	24.4	0.35	6.99	6.27	57.58	2.28
			Average±STD				2.33±0.13

$2a_c$ and a_c/R values for FBD specimens having a 75 mm diameter are listed in Table 6.4.

Table 6.4. *Critical crack lengths and critical dimensionless crack lengths for 75 mm diameter FBD specimens*

Specimen	$2a_{cn}$ (mm)	$2a_{ce}$ (mm)	a_{cn}/R	a_{ce}/R
A7518s1	57.8	58.1	0.77	0.77
A7522s1	54.8	55.5	0.73	0.74
A7522s2	54.8	55.3	0.73	0.74
A7524s1	52.5	53.1	0.70	0.71
A7524s2	52.5	53.4	0.70	0.71
A7530s1	48.8	49.3	0.65	0.66
A7530s2	48.8	51.6	0.65	0.69
A7534s1	45.8	47.2	0.61	0.63
A7536s1	44.3	44.4	0.59	0.59
A7538s1	42.8	43.0	0.57	0.57
A7538s2	42.8	43.1	0.57	0.57
Average±STD			0.66±0.07	0.67±0.07

6.6.3. FBD Specimens Having 100 mm Diameter

Eighteen FBD specimens having 100 mm diameter were prepared with a thickness of around 60 mm, and the loading angles were set between 16° and 38°. $2L$ values of prepared specimens were between 13.92 mm and 32.56 mm. 2α, $2L$, $Y_{I\,max}$, ΔP, P_{min}, $\Delta\sigma_a$ and K_{IC}values are tabulated in Table 6.5. The average mode I fracture toughness calculated for eighteen FBD specimens having a 100 mm diameter is found as 2.85±0.16 MPa$\sqrt{m}$.

Table 6.5. 2α, $2L$, $Y_{I\,max}$, *ΔP, P_{min}, $\Delta\sigma_a$ and K_{IC} values of FBD specimens having 100 mm diameter*

Specimen	2α (°)	$2L$ (mm)	$Y_{I\,max}$	ΔP (kN)	$\Delta\sigma_a$ (MPa)	P_{min} (kN)	K_{IC} (MPa$\sqrt{m}$)
A10016s1	16	13.9	0.77	50.53	60.86	49.71	2.87
A10019s1	19	16.5	0.68	32.98	32.72	61.26	3.05
A10020s1	20	17.4	0.65	13.41	12.85	55.61	2.69
A10022s1	22	19.1	0.61	12.25	10.61	56.79	2.56
A10022s2	22	19.1	0.61	19.53	16.87	66.29	2.98
A10024s1	24	20.8	0.56	24.34	19.40	67.94	2.82
A10024s2	24	20.8	0.56	14.62	11.72	67.30	2.81
A10026s1	26	22.5	0.52	15.39	11.33	72.19	2.78
A10026s2	26	22.5	0.52	14.80	10.89	74.56	2.87
A10028s1	28	24.2	0.49	11.27	7.74	77.15	2.81
A10028s2	28	24.2	0.49	10.53	7.19	86.22	3.12
A10030s1	30	25.9	0.46	32.16	20.36	85.73	2.89
A10032s1	32	27.6	0.43	13.91	8.33	92.29	2.93
A10034s1	34	29.2	0.40	9.15	5.18	85.16	2.52
A10034s2	34	29.2	0.40	15.65	8.84	100.83	2.98
A10036s1	36	30.9	0.37	12.63	6.90	98.82	2.76
A10038s1	38	32.6	0.35	10.92	5.50	117.69	3.02
A10038s2	38	32.6	0.35	11.40	5.83	108.16	2.82
Average±STD							2.85±0.16

$2a_c$ and a_c/R values computed from numerical modeling and obtained from test results are listed in Table 6.6.

Table 6.6. *Critical crack lengths and critical dimensionless crack lengths for 100 mm diameter FBD specimens*

Specimen	$2a_{cn}$ (mm)	$2a_{ce}$ (mm)	a_{cn}/R	a_{ce}/R
A10016s1	79.0	82.1	0.79	0.82
A10019s1	76.0	75.7	0.76	0.76
A10020s1	75.0	74.8	0.75	0.75
A10022s1	73.0	72.6	0.73	0.73
A10022s2	73.0	73.7	0.73	0.74
A10024s1	70.0	72.6	0.70	0.73
A10024s2	70.0	73.4	0.70	0.73
A10026s1	69.0	69.2	0.69	0.69
A10026s2	69.0	71.4	0.69	0.71
A10028s1	67.0	67.4	0.67	0.67
A10028s2	67.0	68.1	0.67	0.68
A10030s1	65.0	65.9	0.65	0.66
A10032s1	63.0	66.7	0.63	0.67
A10034s1	61.0	62.8	0.61	0.63
A10034s2	61.0	63.1	0.61	0.63
A10036s1	59.0	59.4	0.59	0.59
A10038s1	57.0	57.3	0.57	0.57
A10038s2	57.0	57.5	0.57	0.58
Average±STD			0.67±0.07	0.69±0.07

6.6.4. FBD Specimens Having 125 mm Diameter

Fourteen FBD specimens having 125 mm diameter and 75 mm thickness were prepared and tested. The flattened end widths were held between 19.55 mm and 44.80 mm. The loading angles conforming to the $2L$ values were between 18° and 42°. 2α, $2L$, $Y_{I\,max}$, ΔP, P_{min}, $\Delta\sigma_a$ and K_{IC} values are presented in Table 6.7. The average mode

I fracture toughness of fourteen FBD specimens having 125 mm diameter is determined as 3.26±0.39 MPa$\sqrt{m}$.

Table 6.7. 2α, $2L$, $Y_{I\,max}$, *ΔP, P_{min}, $\Delta\sigma_a$ and K_{IC} values of FBD specimens having 125 mm diameter*

Specimen	2α (°)	$2L$ (mm)	$Y_{I\,max}$	ΔP (kN)	$\Delta\sigma_a$ (MPa)	P_{min} (kN)	K_{IC} (MPa$\sqrt{m}$)
A12518s1	18	19.6	0.71	46.86	31.77	100.43	3.78
A12520s1	20	21.7	0.65	38.12	23.41	106.46	3.69
A12520s2	20	21.7	0.65	31.36	19.41	103.06	3.60
A12524s1	24	26.0	0.56	26.98	14.03	108.35	3.28
A12524s2	24	26.0	0.56	29.42	15.07	120.38	3.59
A12528s1	28	30.2	0.49	25.02	11.09	139.31	3.66
A12528s2	28	30.2	0.49	21.54	9.38	116.21	3.00
A12534s1	34	36.6	0.40	19.65	7.10	159.06	3.36
A12534s2	34	36.6	0.40	18.98	6.88	158.41	3.36
A12536s1	36	38.6	0.37	22.71	7.86	165.17	3.27
A12538s1	38	40.7	0.35	15.24	4.96	149.29	2.77
A12538s2	38	40.7	0.35	18.85	6.15	155.42	2.89
A12542s1	42	44.8	0.30	16.45	4.95	169.30	2.74
A12542s1	42	44.8	0.30	18.32	5.63	158.00	2.61
Average±STD							3.26±0.39

Specimen preparation and testing of 125 mm diameter are easier than other diameters. As the flattened ends can be easily machined to the desired dimensions, the number of invalid tests is less, and the success rate of tests is much higher compared to the smaller diameters.

For FBD specimens with a diameter of 125 mm, $2a_c$ and a_c/R values are tabulated in Table 6.8.

Table 6.8. *Critical crack lengths and critical dimensionless crack lengths for 125 mm diameter FBD specimens*

Specimen	$2a_{cn}$ (mm)	$2a_{ce}$ (mm)	a_{cn}/R	a_{ce}/R
A12518s1	96.3	96.6	0.77	0.77
A12520s1	93.8	94.3	0.75	0.75
A12520s2	93.8	94.3	0.75	0.75
A12524s1	87.5	90.8	0.70	0.73
A12524s2	87.5	87.8	0.70	0.70
A12528s1	83.8	83.1	0.67	0.66
A12528s2	83.8	84.3	0.67	0.67
A12534s1	76.3	76.4	0.61	0.61
A12534s2	76.3	76.6	0.61	0.61
A12536s1	73.8	74.5	0.59	0.60
A12538s1	71.3	71.7	0.57	0.57
A12538s2	71.3	71.8	0.57	0.57
A12542s1	67.5	67.8	0.54	0.54
A12542s2	67.5	67.7	0.54	0.54
Average±STD			0.65±0.08	0.65±0.08

CHAPTER 7

RESULTS AND DISCUSSION

The fracture toughness test results of flattened Brazilian disc andesite specimens for various diameters and loading angles are used to examine specimen diameter and loading angle effect on mode I fracture toughness. This section includes the evaluation of test results in terms of the stress drop and critical crack length variations and 3D stress analysis for the loading angle effect. Tensile strength comparison from FBD tests of different researchers is also presented in this section.

In order to determine how the loading angles and specimen diameters affect the mode I fracture toughness test results, FBD test specimens having different diameters and loading angles were used. FBD andesite specimens were prepared for four different diameters that are 54 mm, 75 mm, 100 mm, and 125 mm. A total of 51 experiments were performed by changing the loading angle range from 16° to 42°, corresponding to the dimensionless vertical distance ($y_i/R = \cos\alpha$) between the center and flat boundary as 0.99 and 0.93.

7.1. Specimen Diameter Effect on K_{IC}

A graphical representation of K_{IC} values of all fifty-one FBD andesite specimens having various diameters and loading angles are given in Figure 7.1. The blue dots signify K_{IC} values of each FBD specimen, while orange dots characterize $K_{IC\,avg}$ values of each diameter regardless of 2α. The trend curve and fitted equation are generated for $K_{IC\,avg}$ values. The trend curve of average values is the third-order polynomial function with $R^2 = 1$. It is clear that the specimen diameter has a great effect on K_{IC} values because $K_{IC\,avg}$ values increase as specimen diameter increases.

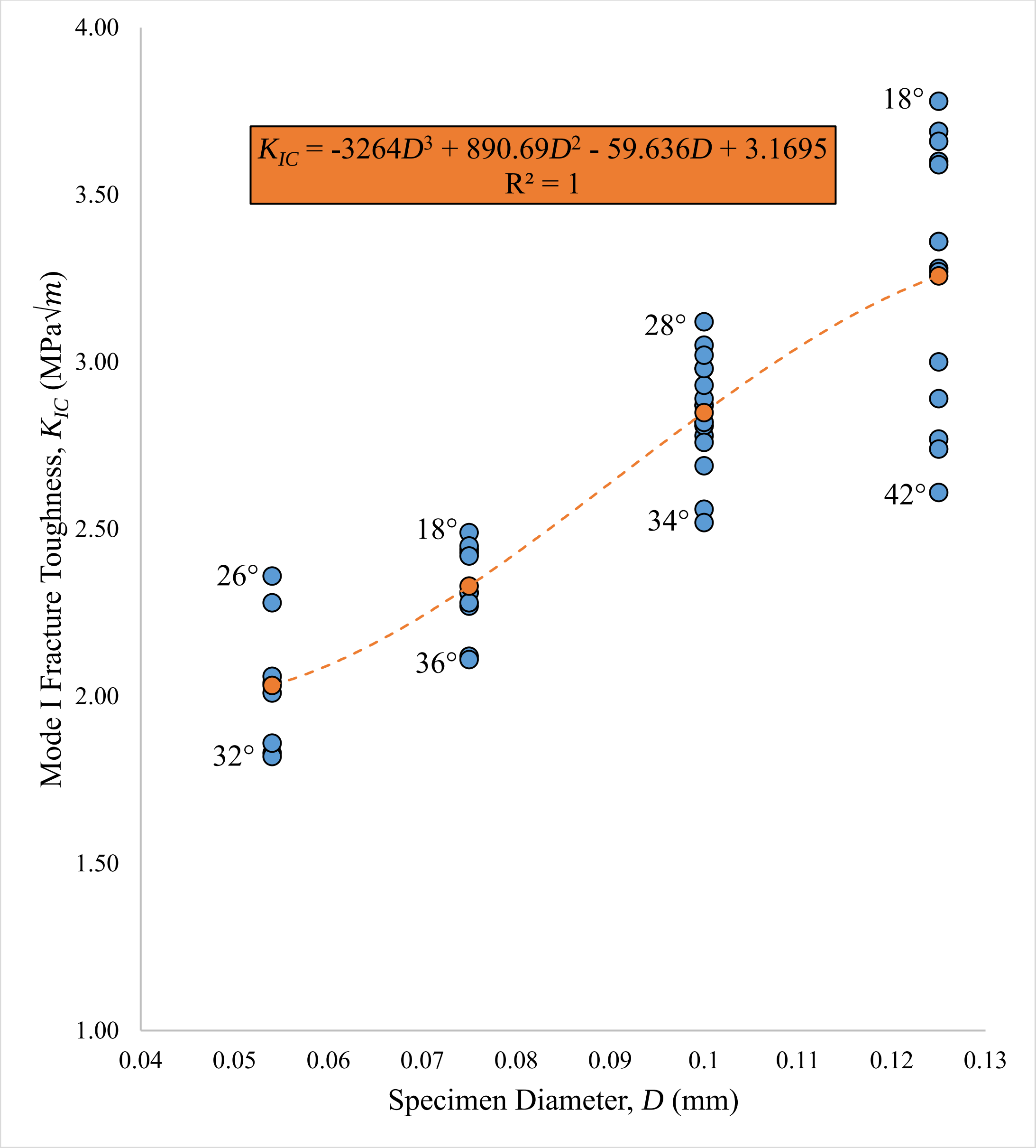

Figure 7.1. K_{IC} values of FBD specimens having various diameters (Regardless of 2α)

The local maximum point of third-order polynomial function can be determined by taking the first derivative of the function and equating it to zero. The mode I fracture toughness calculated at the peak point of the curve is believed to represent size-independent fracture toughness. After the diameter of the specimen increases up to local maximum value of the curve, K_{IC} is seen to tend to the constant size-independent K_{IC}. According to Figure 7.1, the size-independent fracture toughness of andesite is estimated as 3.32 MPa$\sqrt{m}$ for FBD specimens having approximately 140 mm in diameter.

Mode I fracture toughness values are grouped for four different diameters to examine the variation of mode I fracture toughness K_{IC} with the specimen diameter. The average mode I fracture toughness values for each diameter group of andesite are listed in Table 7.1.

Table 7.1. *Average mode I fracture toughness for each diameter group*

Diameter (mm)	Number of Specimens	Average Mode I Fracture Toughness (MPa$\sqrt{m}$)
54	8	2.03±0.20
75	11	2.33±0.13
100	18	2.85±0.16
125	14	3.26±0.39

According to Table 7.1, $K_{IC\,avg}$ values of andesite regardless of 2α are obtained as 2.03±0.20 MPa$\sqrt{m}$ (eight tests), 2.33±0.13 MPa$\sqrt{m}$ (eleven tests), 2.85±0.16 MPa$\sqrt{m}$ (eighteen tests), 3.26±0.39 MPa$\sqrt{m}$ (fourteen tests) for specimen having 54 mm, 75 mm, 100 mm and 125 mm diameters, respectively.

The mechanical properties of different materials used in the FBD tests and $K_{IC\,avg}$ results for different diameters and loading angles compiled from the literature are given in Table 7.2.

Table 7.2. $K_{IC\ avg}$ *results of FBD specimens compiled from the literature*

Material	UCS (MPa)	σ_t (MPa)	D (mm)	$2\alpha_{min}$ and $2\alpha_{max}$	Number of Tests	$K_{IC\ avg}$ (MPa$\sqrt{m}$)	Source
Andesite	82.8±4.1	7.0±0.7	54	16°-38°	17	1.76±0.37	Keles & Tutluoglu (2011)
			75	15°-36°	12	1.92±0.42	
			100	15°-39°	11	2.61±0.88	
Andesite	84.7±7.1	9.6±1.8	75	25°-28°	3	2.58±0.34	Özdoğan (2017)
			100	26°-28°	6	3.34±0.15	
Andesite	61.8±1.8	7.2±0.2	54	18°-34°	8	2.03±0.20	Present Work
			75	18°-38°	11	2.33±0.13	
			100	16°-38°	18	2.85±0.16	
			125	18°-42°	14	3.26±0.39	
Shotcrete (7 days cured)	39.4±0.7	4.1±0.2	75	24-30	10	0.99±0.06	Yoncacı (2019)
			100	22°-28°	10	1.13±0.06	
			120	22°-28°	10	1.21±0.05	
			140	22°-28°	15	1.30±0.06	
			160	22°-28°	15	1.37±0.05	
			180	22°-28°	10	1.42±0.06	
			200	20°-22°	10	1.49±0.03	
Shotcrete (7 days cured)	26.6±3.0	4.0±0.4	100	22°	5	0.93±0.11	Tayfuner (2019)
			120	22°	6	0.98±0.11	
			140	22°	5	1.06±0.09	
			160	22°	5	1.18±0.07	
			180	22°	5	1.43±0.04	
			200	22°	4	1.46±0.09	

For FBD specimens having 75 mm and 100 mm diameter, the size effect on K_{IC} of andesite was found to be approximately 36% (2.61/1.92=1.36) by Keles and Tutluoglu (2011) and 29% (3.34/2.58=1.29) by Özdoğan (2017). In this study, the size effect is observed at about 22% (2.85/2.33=1.22) for the same diameter groups of 75 mm and 100 mm. The size effect is about 61% (3.26/2.03=1.61) for tests involving all diameters from 54 mm to 125 mm. These test results indicate specimen size has a definite effect on K_{IC} test results.

$K_{IC\ avg}$ values of concrete were determined for specimens with diameters ranging from 75 mm to 200 mm in the study of Yoncacı (2019), and 100 mm to 200 mm in the study of Tayfuner (2019). In both, a tendency to size-independent K_{IC} was observed for a specimen diameter around 200 mm that were large enough sizes to achieve the purpose. Here, it was not possible to go over a specimen diameter of 125 mm due to the limited coring equipment.

7.2. Loading Angle Effect on K_{IC}

All results investigating the effect of loading angle on K_{IC} are plotted in Figure 7.2.

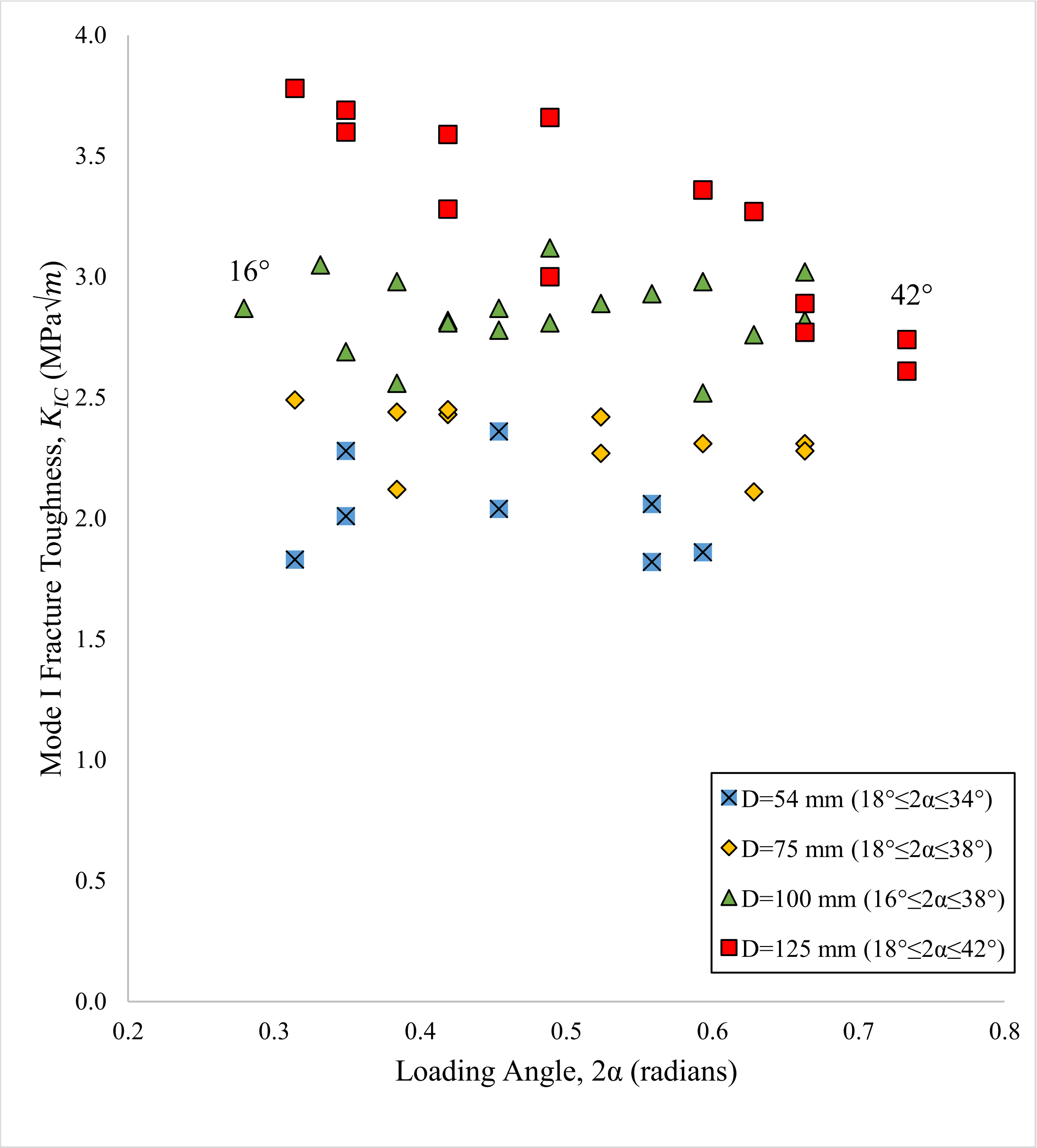

Figure 7.2. Loading angle effect on K_{IC} values

Results show too wide a scatter. In the machining and grinding process, it is difficult to adjust perfectly to the targeted value. There might be deviations within ±1°. Therefore, grouping the average K_{IC} values of FBD tests in a number of loading angle ranges for various diameters can be useful in the interpretation of results. The results are summarized in Table 7.3. The number of tests for different specimen diameter groups and loading angle ranges of each group are given in Table 7.3. To investigate the loading angle effect on K_{IC}, three different loading angle ranges are created: 16°-22°, 24°-30°, and 32°-38°.

Table 7.3. $K_{IC\ avg}$ *values of FBD specimens having various diameters and loading angles*

D (mm)	$2\alpha_{avg}$ (°)	$2\alpha_{min}$ and $2\alpha_{max}$ (°)	Number of tests	$K_{IC\ avg}$ (MPa$\sqrt{m}$)	Total number of tests	$K_{IC\ avg}$ (MPa$\sqrt{m}$)
54	19±1	18-20	3	2.04±0.23	8	2.03±0.20
	26±0	26	2	2.20±0.23		
	33±1	32-34	3	1.91±0.13		
75	21±2	18-22	3	2.35±0.20	11	2.33±0.13
	27±3	24-30	4	2.39±0.08		
	37±2	34-38	4	2.25±0.10		
100	20±2	16-22	5	2.83±0.20	18	2.85±0.16
	27±2	24-30	7	2.87±0.12		
	35±2	32-38	6	2.84±0.18		
125	19±1	18-20	3	3.69±0.09	14	3.26±0.39
	26±2	24-28	4	3.38±0.30		
	38±3	34-42	7	3.00±0.32		

According to Table 7.3, the variation of K_{IC} values with the loading angle is clearly observed only for the 125 mm diameter group. $K_{IC\ avg}$ of FBD andesite specimens having 125 mm diameter for 16°-22° loading angle group is 3.69±0.09 MPa$\sqrt{m}$, while for 32°-42° loading angle group, $K_{IC\ avg}$ is 3.00±0.32 MPa$\sqrt{m}$. $K_{IC\ avg}$ values of the largest diameter group (D =125mm) converge to $K_{IC\ avg}$ values of 100 mm diameter group at greater loading angles.

To examine the effect of loading angle on K_{IC} in more detail, four different loading angle groups are created in the largest diameter group of 125 mm. The loading angle group ranges, the average loading angle of each group, and the corresponding $K_{IC\ avg}$ results are given in Table 7.4.

Table 7.4. *Loading angle groups for samples with a diameter of 125 mm*

Loading Angle Group (°)	$2\alpha_{avg}$ (°)	Number of Tests	$K_{IC\ avg}$ (MPa$\sqrt{m}$)
18-20	19±1	3	3.69±0.09
24-28	26±2	4	3.38±0.30
34-36	35±1	3	3.33±0.05
38-42	40±2	4	2.75±0.12

According to Table 7.4, for samples with a diameter of 125 mm, the average fracture toughness corresponding to the largest loading angle group (38°-42°) is approximately 25% less than the average fracture toughness corresponding to the smallest loading angle group (18°-20°).

K_{IC} versus 2α for samples with a diameter of 125 mm is plotted in Figure 7.3. As seen in Figure 7.3, K_{IC} decreases with an increasing loading angle. A second-degree polynomial fit with R^2 =0.76 represents all data points.

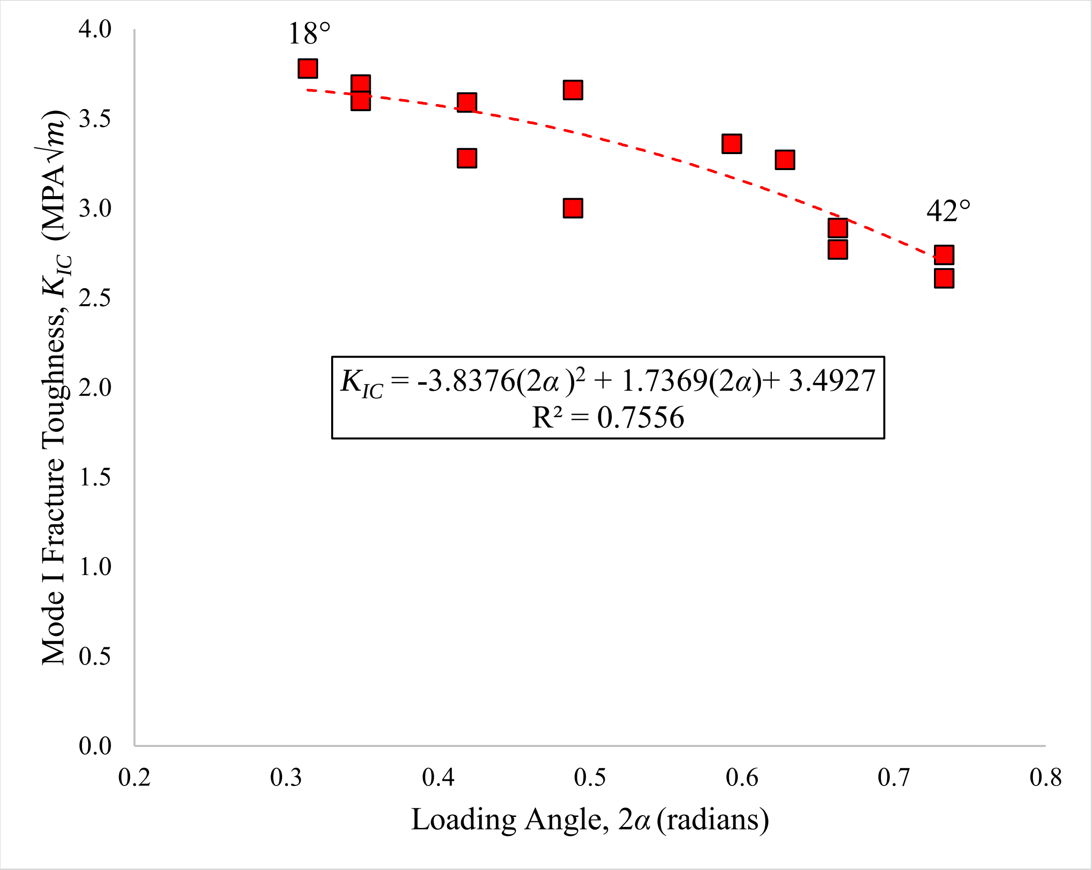

Figure 7.3. Variation of K_{IC} values with loading angles for 125 mm diameter specimens

Second-degree polynomial expression gives a maximum value of K_{IC} =3.69 MPa$\sqrt{m}$ at a loading angle of 2α =0.226 (≅ 13°). In the size effect part, K_{IC} is estimated as 3.32 MPa$\sqrt{m}$. The estimate here is about 11% higher. The reason for this difference is attributed to the complex mineralogical structure and its heterogeneity for Gölbaşı andesite. Gölbaşı andesite shows great variations in mechanical properties, depending on the location of sample blocks picked.

7.3. Evaluation of Test Results in terms of Stress Drop Variation

The stress drop ($\Delta\sigma_a$) is described by dividing the load drop (ΔP=$P_{max} - P_{min}$) by the flattened end area ($2L \times t$) where the load is applied. The stress drop is directly proportional to ΔP and inversely proportional to the $2L$ and t. The variation of stress drop according to the specimen diameters are plotted in Figure 7.4. Each blue dot represents the individual test results, while orange dots indicate the average stress drop values of each diameter group.

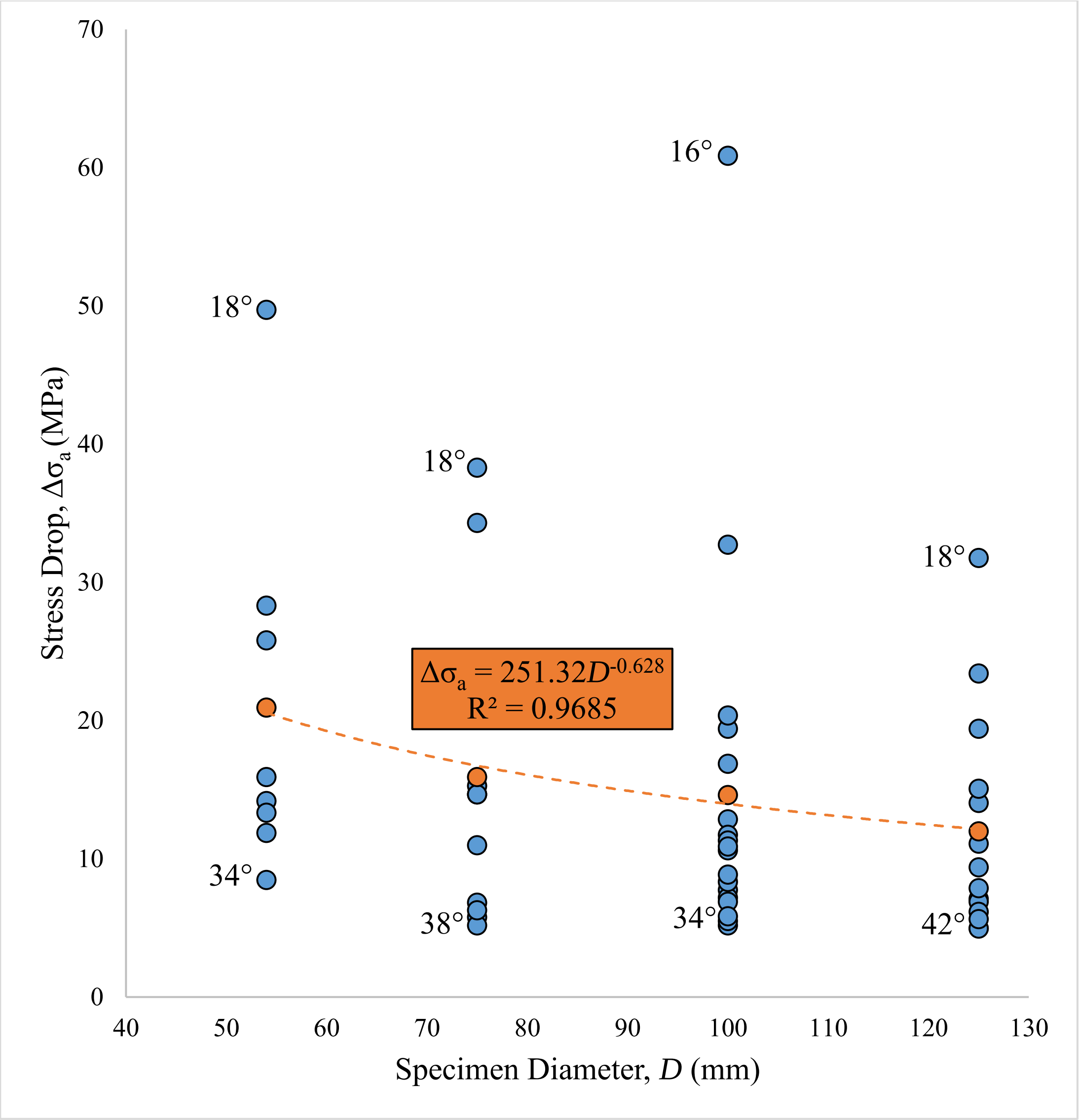

Figure 7.4. Stress drop versus specimen diameter

The average stress drop values are characterized by the power curve showing a best-fit through the data points. It is inferred from experimental results that variation in stress drop shows a decreasing trend with the increase in the specimen diameters. As the specimen diameter decreases, the flattened end area where the load is applied decreases, and the load drop decreases. The flattened area decreases more than ΔP, so an increasing tendency in stress drop is observed with decreasing diameter. $\Delta\sigma_a$ is also affected by the loading angle. As the loading angle decreases, $\Delta\sigma_a$ increases. The explanation for the load drop concept is based on the internal structure of the andesite samples. Cracks in larger specimens propagate longer through more representative paths regarding the distribution of minerals and matrix.

7.4. Effect of Specimen Diameter and Loading Angle on Critical Crack Length

The comparison of critical dimensionless crack lengths determined from numerical and experimental data for the smallest (D =54 mm) and the largest diameter samples (D =125 mm) is given in Figure 7.5 and Figure 7.6, respectively. Orange squares symbolize different test results, while blue diamond marks denote numerical model results.

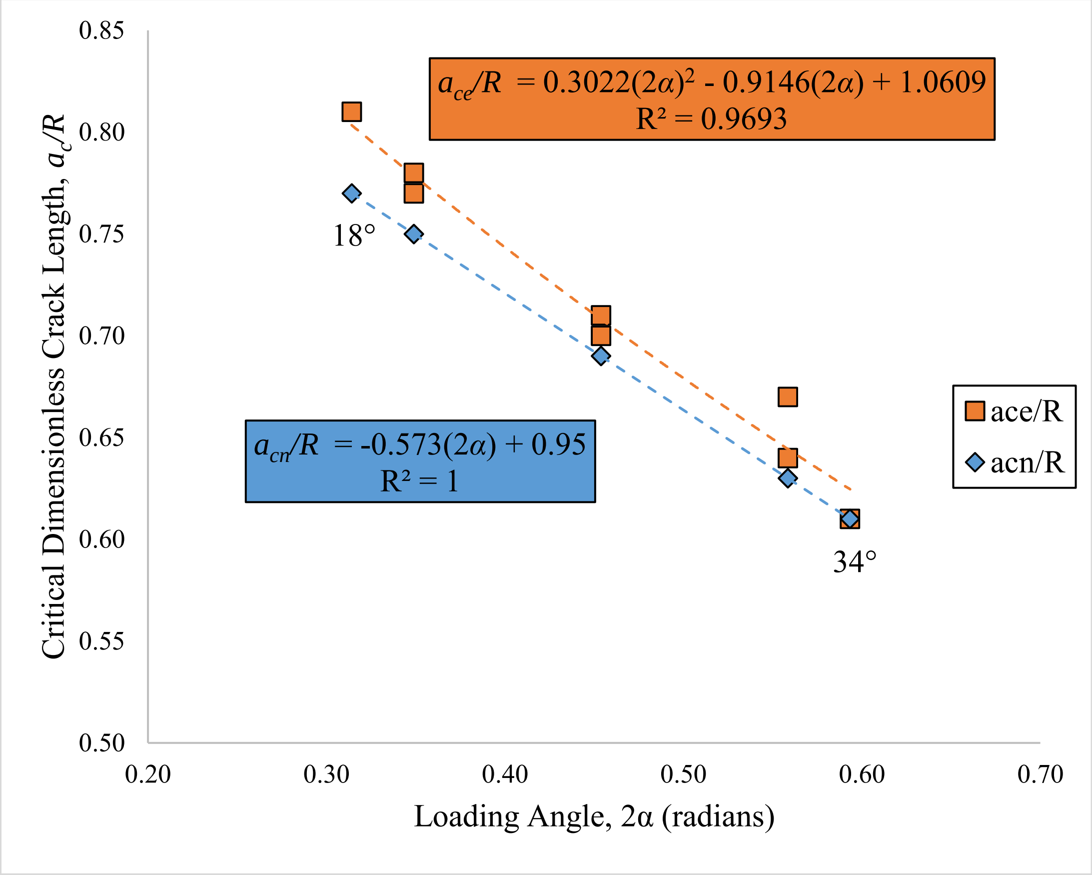

Figure 7.5. a_c/R vs. 2α for FBD specimens having 54 mm diameter

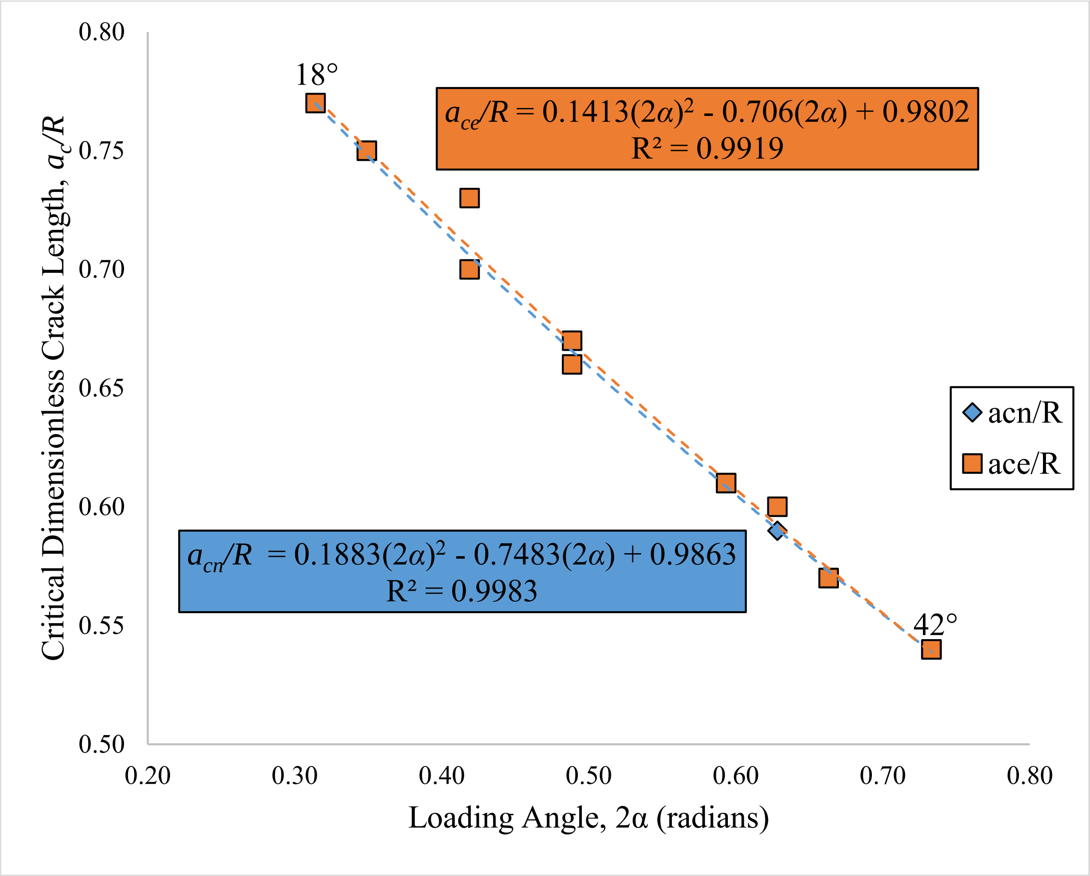

Figure 7.6. a_c/R vs. 2α for FBD specimens having 125 mm diameter

From Figures 7.5, it is clear that for 54 mm diameter specimens having smaller loading angles, there is more difference between critical dimensionless crack lengths computed from numerical modeling (a_{cn}/R) and critical dimensionless crack lengths acquired from the test results (a_{ce}/R). Except for a few examples, there are no significant differences between a_{ce}/R and a_{cn}/R for greater loading angles. For 125 mm diameter specimens, a_c/R ratios are almost equal for the same loading angles, as seen in Figure 7.6. The trend lines of a_{ce}/R and a_{cn}/R ratios nearly coincide with each other. It can be said that the specimen diameter increases, the difference between a_{ce}/R and a_{cn}/R decreases. One reason might be that it is more difficult to adjust the flattened ends of the specimen to the desired width for smaller specimens. But the real reason again is related to the propagation of cracks in more representative internal matrices for larger samples.

7.5. Stress Analysis for the Loading Angle Effect

The loading angle effect on K_{IC}, as observed in the previous section, was analyzed here by 3D modeling simulating some real FBD tests. In order to compute the mode I stress intensity factor and conduct stress analysis with more realistic simulation, three-dimensional numerical models of FBD geometries were generated. FBD geometries with the minimum (16°) and maximum (38°) loading angles in the 100 mm diameter group were sketched in Figure 7.7. Mechanical properties of andesite (E and ν) were obtained from static deformability tests, and these values were used as input parameters of the ABAQUS models. E and ν were 31.9 GPa and 0.10, respectively.

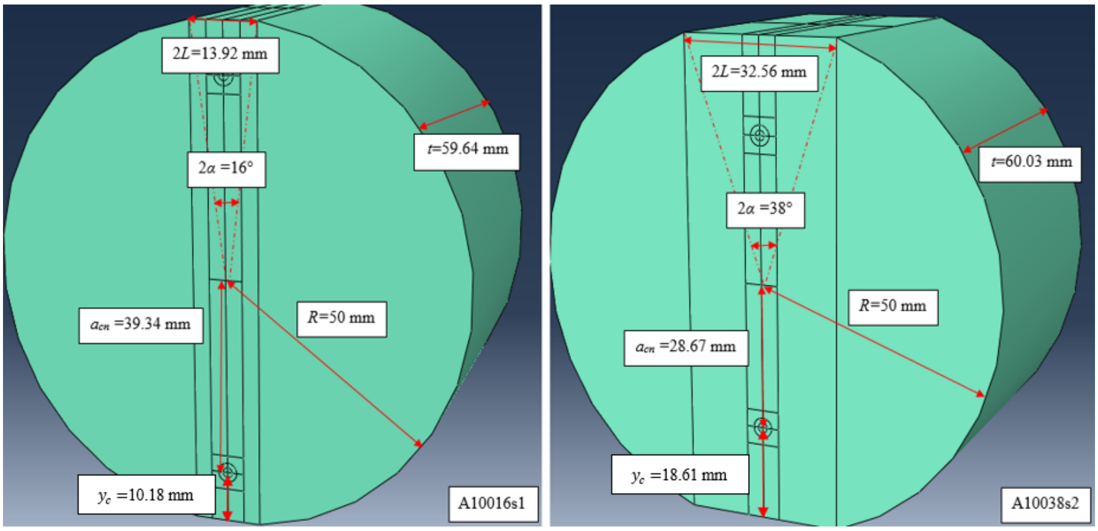

Figure 7.7. Geometric dimensions of A10016s1 and A10038s2 specimens

The dimensions of A10016s1 and A10038s2 specimens were given in Table 7.5.

Table 7.5. *Dimensions of A10016s1 and A10038s2 specimens*

Parameters	Specimen Code	
	A10016s1	A10038s2
Specimen thickness, t	59.6 mm	60.0 mm
Loading angle, 2α	16°	38°
Flattened end width, $2L$	13.92 mm	32.56 mm
Half of the critical crack length, a_{cn}	39.34 mm	28.67 mm
Distance from crack tip to flat end, y_c	10.18 mm	18.61 mm

The ratio of $y_c/2L$ is the critical parameter controlling the intensity of the boundary influence issue. The small ratio causes an increase in the intensity of the boundary influence issue. The $y_c/2L$ ratios for $2\alpha = 16°$ and $2\alpha = 38°$ were found approximately as 0.73 and 0.57, respectively. The results showed that the FBD geometry with $2\alpha = 38°$ suffered from the boundary influence issue.

P_{min} values obtained from a couple of the FBD tests were directly applied to the models for a particular loading angle. For specimens having 16° and 38° loading angles, P_{min} values were taken as 49.71 kN and 108.16 kN, respectively.

Von Mises stress is proportional to the squares of the principal stress differences and does not mean yielding occurs in tension. Von Mises stress is essential in the sense that it is expressed in terms of $\sqrt{J_2}$, which is the strongest or the most dominant parameter in all yield functions or yield criteria. To examine the Von Mises stresses, stress paths were assigned for $2\alpha = 16°$ and $2\alpha = 38°$, as seen in Figure 7.8 and Figure 7.9, respectively. These paths started from the upper crack tip and extended to the upper flattened end of the FBD samples.

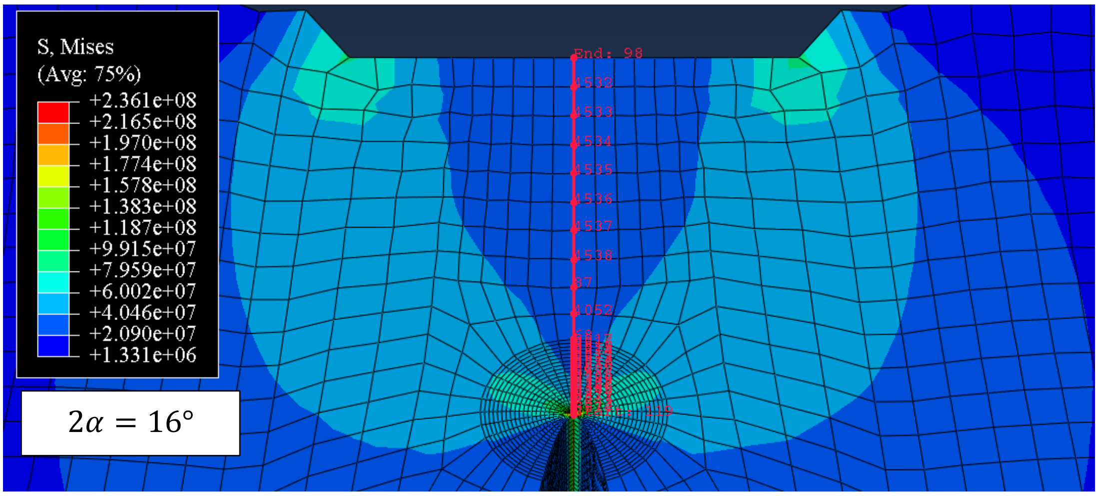

Figure 7.8. Von mises stress path for $2\alpha = 16°$

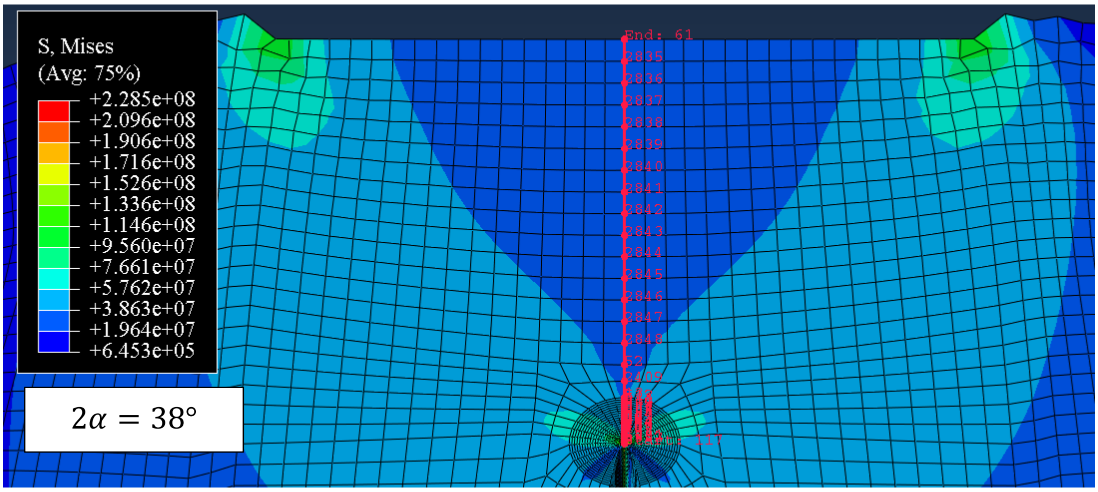

Figure 7.9. Von mises stress path for $2\alpha = 38°$

High-stress concentrations observed at the corners of flat loading end and crack front of FBD specimen geometry were shown in Figure 7.8 and Figure 7.9. Tensile stresses were indirectly evolved in the FBD specimen subjected to compressive loads at the flat loading ends. The maximum Von Mises stress was located at the crack tip for both loading angles, as can be seen in Figure 7.10 and Figure 7.11.

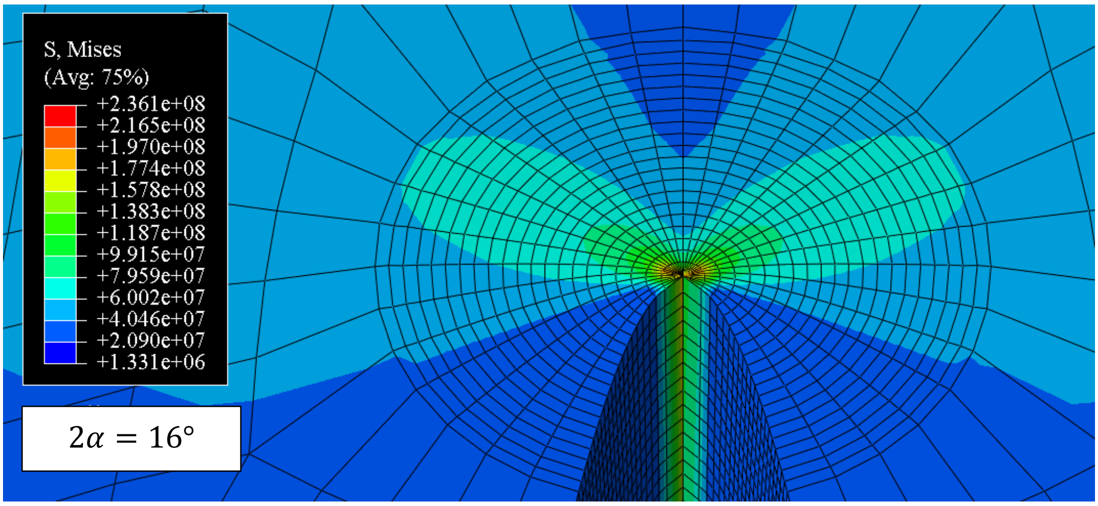

Figure 7.10. Von mises stress contours around the crack tip for $2\alpha = 16°$

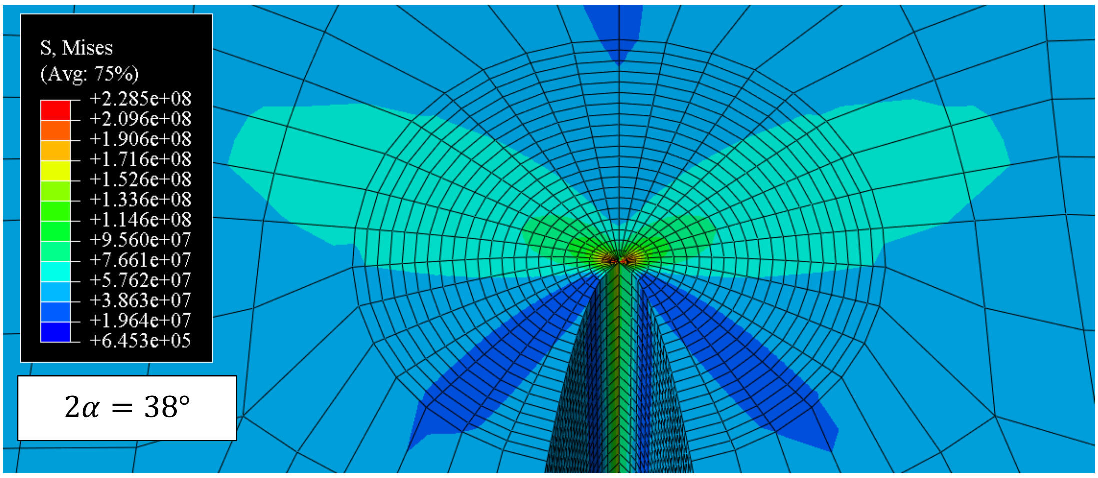

Figure 7.11. Von mises stress contours around the crack tip for $2\alpha = 38°$

Stress distribution analysis was conducted by creating the stress paths for $2\alpha = 16°$, and $2\alpha = 38°$. Von mises stress values for both loading angles were compared to clarify the presence of the loading angle effect. The graphical illustration of stress distribution along these paths was given in Figure 7.12. As can be seen from Figure 7.12, the maximum values of Von Mises stress for both loading angles were located at the crack tip. The stress values from the crack tip to the flattened end first decreased sharply and then remained constant at around 27 MPa and 35 MPa for $2\alpha = 16°$ and

$2\alpha = 38°$, respectively. From d/a_c=0.16 to 0.26, the average stress values for $2\alpha = 38°$ were approximately 30% higher than the average stress values for $2\alpha = 16°$.

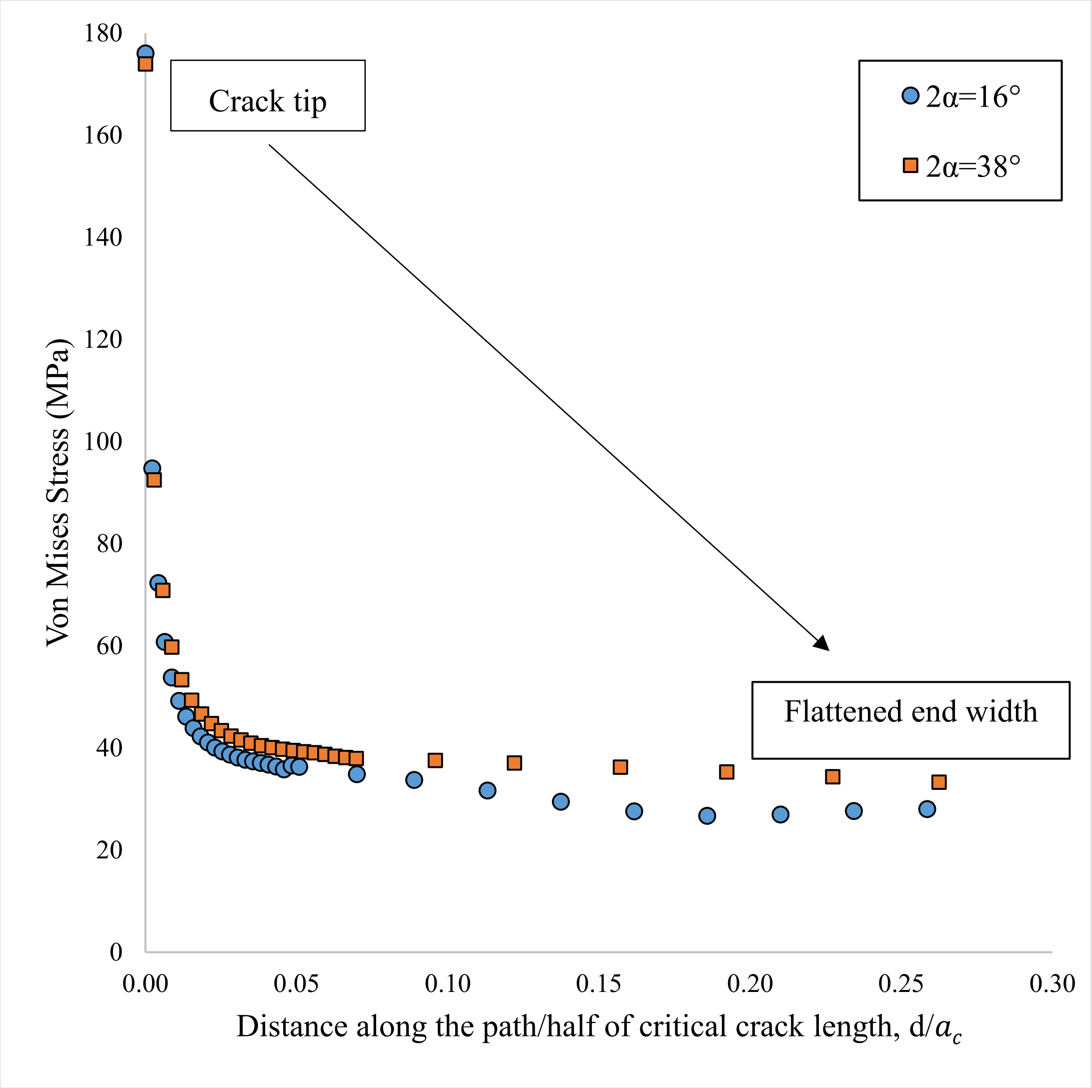

Figure 7.12. Comparison of Von mises stress values for $2\alpha = 16°$ and $2\alpha = 38°$

The stress paths were created for examining the stress perpendicular to the crack plane values from the crack tip to the upper flattened end width. Figure 7.13 and Figure 7.14 shows the stress paths and stress contours for $2\alpha = 16°$ and $2\alpha = 38°$.

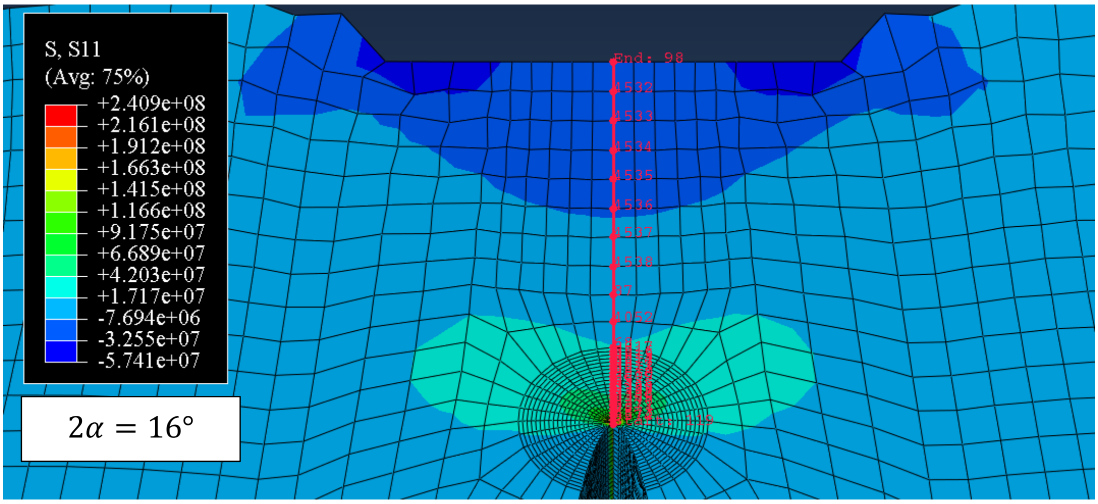

Figure 7.13. Stress perpendicular to the crack plane for $2\alpha = 16°$

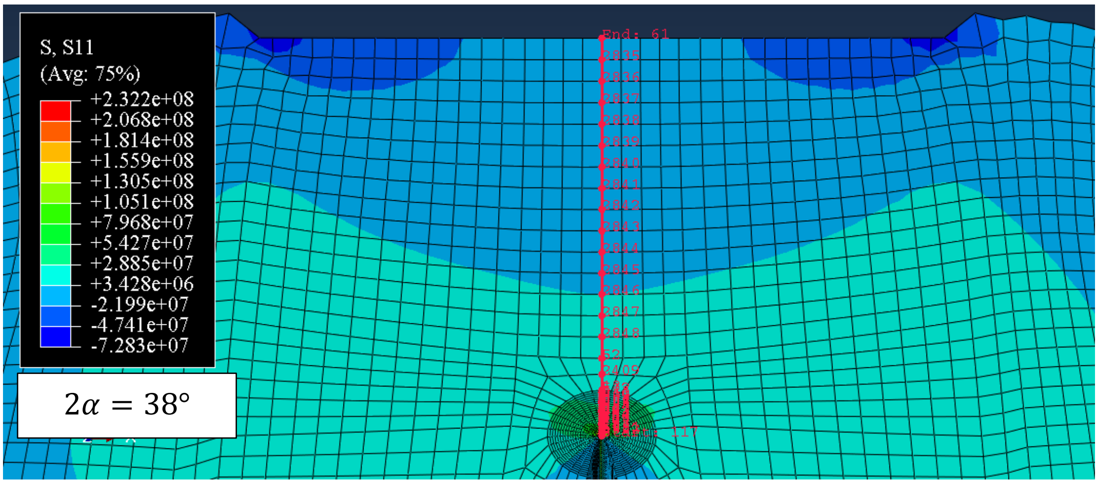

Figure 7.14. Stress perpendicular to the crack plane for $2\alpha = 38°$

Stress values perpendicular to the crack plane at the vicinity of the crack tip for both loading angles $2\alpha = 16°$ and $2\alpha = 38°$ are shown in Figure 7.15 and Figure 7.16, respectively. The maximum σ_{xx} values for both loading angles are located at the crack tip.

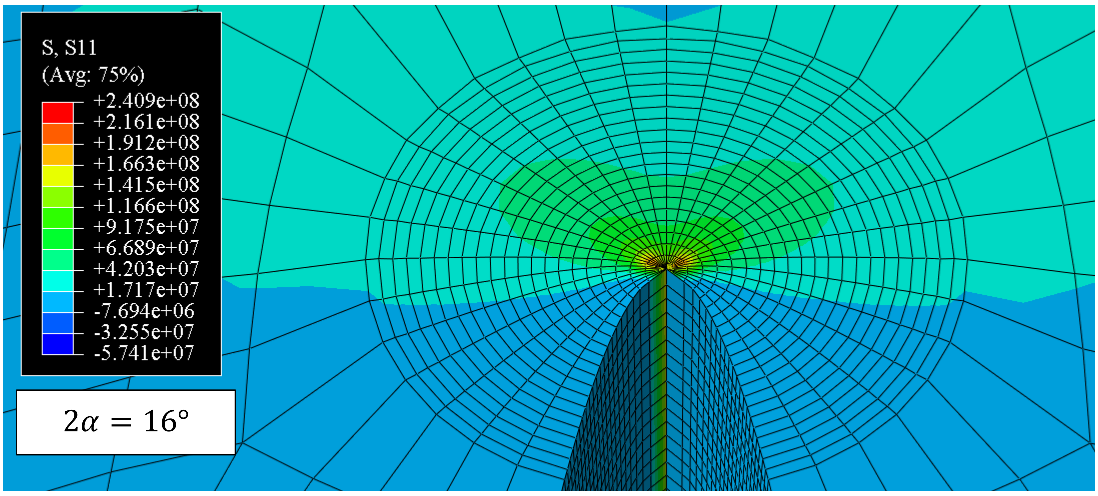

Figure 7.15. Stress perpendicular to the crack plane around the crack tip for $2\alpha = 16°$

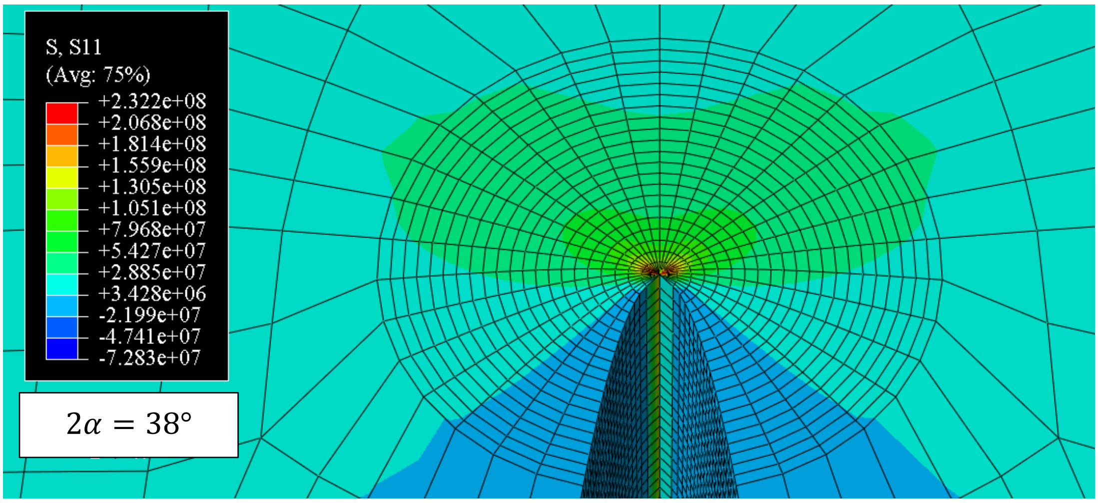

Figure 7.16. Stress perpendicular to the crack plane around the crack tip for $2\alpha = 38°$

The stress perpendicular to the crack plane values at the vicinity of the crack tip were compared. The stress values along the paths for $2\alpha = 16°$ and $2\alpha = 38°$ were plotted in Figure 7.17. The stress curves were intersected by the average tensile strength of andesite acquired from the indirect tensile strength tests to estimate the size of possible plastic zone near the crack tip. The average tensile strength was 7.18±0.20 MPa.

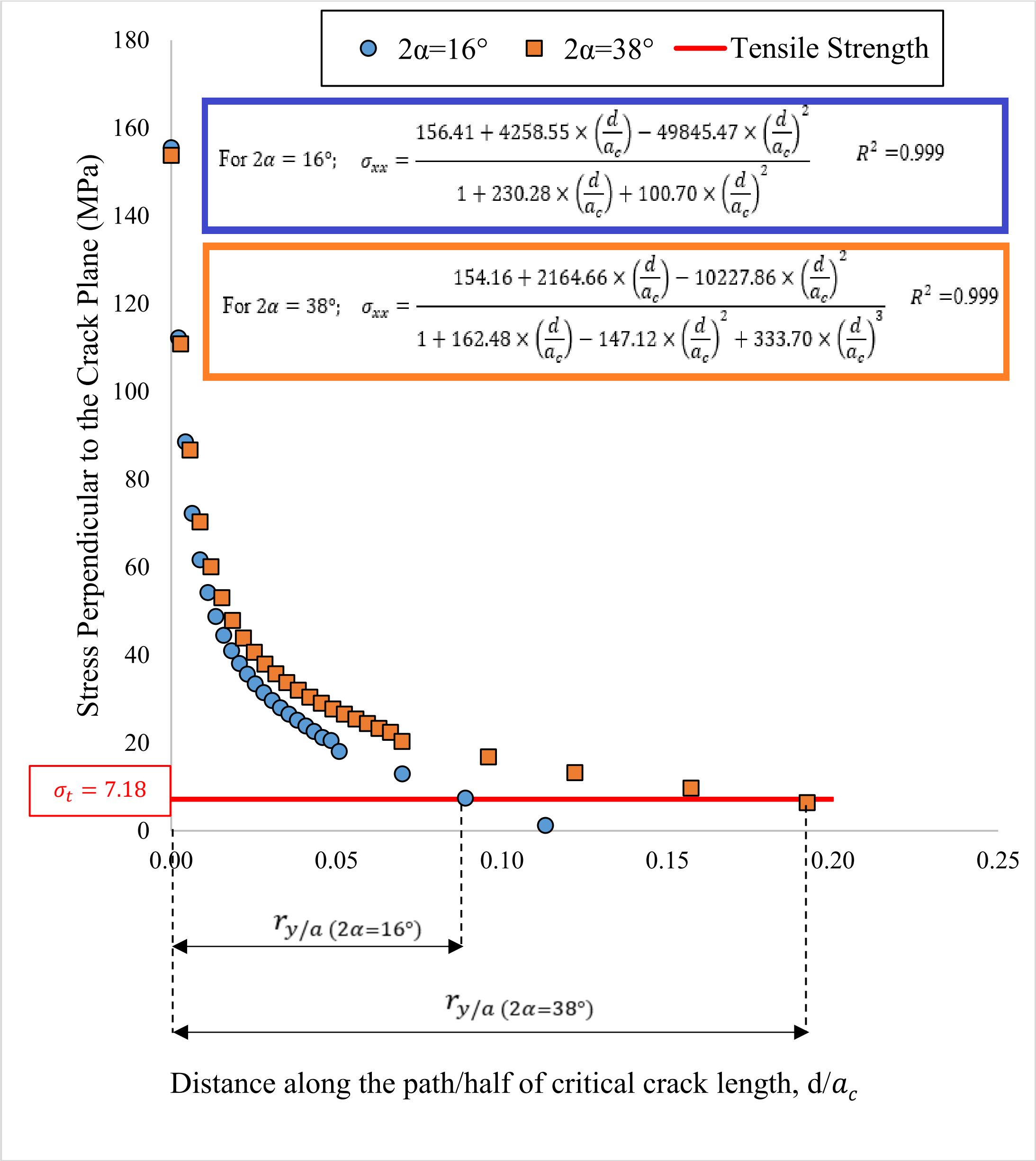

Figure 7.17. Comparison of stress perpendicular to crack plane values for $2\alpha = 16°$ and $2\alpha = 38°$

Using TableCurve2D program, Equation 7.1 and Equation 7.2 were developed for $2\alpha = 16°$ and $2\alpha = 38°$, respectively. Both equations have a high coefficient of determination R^2 =0.999.

For $2\alpha = 16°$;

$$\sigma_{xx} = \frac{156.41 + 4258.55 \times \left(\frac{d}{a_c}\right) - 49845.47 \times \left(\frac{d}{a_c}\right)^2}{1 + 230.28 \times \left(\frac{d}{a_c}\right) + 100.70 \times \left(\frac{d}{a_c}\right)^2} \tag{7.1}$$

For $2\alpha = 38°$;

$$\sigma_{xx} = \frac{154.16 + 2164.66 \times \left(\frac{d}{a_c}\right) - 10227.86 \times \left(\frac{d}{a_c}\right)^2}{1 + 162.48 \times \left(\frac{d}{a_c}\right) - 147.12 \times \left(\frac{d}{a_c}\right)^2 + 333.70 \times \left(\frac{d}{a_c}\right)^3} \tag{7.2}$$

As can be seen from Figure 7.17, the size of the plastic zone was approximately 0.09 ($r_{y/a\,(2\alpha=16°)}$) for $2\alpha = 16°$ and 0.19 ($r_{y/a\,(2\alpha=38°)}$) for $2\alpha = 38°$. The FBD geometry with loading angle $2\alpha = 16°$ had a possible fracture process zone of about 53% smaller than the FBD geometry with loading angle $2\alpha = 38°$. It indicates that as the loading angle of FBD geometry decreases, the size of the possible yielded zone in the vicinity of the crack tip becomes smaller.

7.6. Tensile Strength Comparison from Flattened Brazilian Disc Tests of Different Researchers

It is possible to determine the tensile strength of andesite from the FBD tests. The tensile strength can be calculated easily by using the local maximum load (P_{max}) from the FBD test load-displacement graph. Wang et al. (2004) proposed the following expressions for calculating tensile strength with FBD geometry.

$$\sigma_t = k\frac{2\,P_{max}}{\pi\,D\,t} \tag{7.3}$$

$$k = \frac{\left(2\cos^3\alpha + \cos\alpha + \frac{\sin\alpha}{\alpha}\right)^2}{8\left(\cos\alpha + \frac{\sin\alpha}{\alpha}\right)}\frac{\alpha}{\sin\alpha} \tag{7.4}$$

Where k is defined as the correction coefficient, and α is half of the loading angle in radians. For conventional Brazilian disc ($2\alpha = 0°$), k is equal to 1.

Similarly, Keles and Tutluoglu (2011) established the following expression for the calculation of correction coefficient k. Equation 7.5 is valid for 2α between 15° and 60°.

$$k = 0.83\,(\cos\alpha) + 0.15 \tag{7.5}$$

Lin et al. (2016) conducted similar work and established a 3D tensile strength formula considering both the loading angle and Poisson's ratio effect. The modified correction coefficient formula for the flattened Brazilian disc test is given below.

$$k = 1.027 + 0.108v - 0.014\alpha \tag{7.6}$$

It should be noted that the unit of α is the degree in Equation 7.6. According to static deformability test results, the average Poisson's ratio of andesite is taken as 0.10.

Wang and Cao (2016) established the following empirical formula for tensile strength calculation by utilizing the flattened Brazilian disc test.

$$k = 0.9993\exp(-11.65\varepsilon) \tag{7.7}$$

Instead of the loading angle, they introduced a new term called the FBD coefficient (ε) that is calculated as described in Equation 7.8. The FBD coefficient should be less than or equal to 0.035 ($\varepsilon \leq 0.035$), corresponding to $2\alpha \leq 30°$. Therefore, the correction coefficient in Wang and Cao's approach was not calculated for loading angles greater than 30°.

$$\varepsilon = \frac{R - R\cos\alpha}{R} \tag{7.8}$$

To determine the tensile strength of andesite with FBD geometry, the correction coefficients are calculated using Equation 7.4, 7.5, 7.6, and 7.7. Table 7.6 shows the correction coefficient values.

Table 7.6. *Correction coefficients calculated for four different approaches*

2α (°)	k_{W}	$k_{\mathrm{K\&T}}$	k_{L}	$k_{\mathrm{W\&C}}$
16	0.974	0.972	0.926	0.892
18	0.968	0.970	0.912	0.866
20	0.960	0.967	0.898	0.837
22	0.952	0.965	0.884	0.807
24	0.943	0.962	0.870	0.775
26	0.934	0.959	0.856	0.741
28	0.924	0.955	0.842	0.707
30	0.913	0.952	0.828	0.672
32	0.902	0.948	0.814	-
34	0.890	0.944	0.800	-
36	0.878	0.939	0.786	-
38	0.865	0.935	0.772	-
40	0.851	0.930	0.758	-
42	0.838	0.925	0.744	-

(k_{W}, $k_{\mathrm{K\&T}}$, k_{L}, and $k_{\mathrm{W\&C}}$ represent the correction coefficient of Wang et al. (2004), Keles and Tutluoglu (2011), Lin et al. (2016), and Wang and Cao (2016), respectively.)

The tensile strengths were computed separately for each sample using the correction coefficients obtained from Equation 7.4, 7.5, 7.6, and 7.7, and relevant FBD test results. Then, the average tensile strength values of each diameter group were calculated regardless of 2α by four different methods. The results were listed in Table 7.7.

Table 7.7. *Tensile strength estimation from FBD tests*

D (mm)	$\sigma_{\mathrm{t\,W}}$ (MPa)	$\sigma_{\mathrm{t\,K\&T}}$ (MPa)	$\sigma_{\mathrm{t\,L}}$ (MPa)	$\sigma_{\mathrm{t\,W\&C}}$ (MPa)
54	9.52±0.60	9.80±0.71	8.74±0.52	7.93±0.56
75	9.42±0.68	9.81±0.92	8.58±0.54	7.44±0.60
100	9.41±1.36	9.77±1.59	8.60±1.17	7.28±1.03
125	9.90±0.82	10.40±1.12	8.99±0.65	7.72±0.68

($\sigma_{\mathrm{t\,W}}$, $\sigma_{\mathrm{t\,K\&T}}$, $\sigma_{\mathrm{t\,L}}$ and $\sigma_{\mathrm{t\,W\&C}}$ represent the calculated tensile strength using approaches of Wang et al. (2004), Keles and Tutluoglu (2011), Lin et al. (2016), and Wang and Cao (2016), respectively.)

The highest average tensile strengths were obtained for Keles and Tutluoglu's approach, and these results are in agreement with the results of Wang et al.'s (2004). However, the average tensile strength of andesite was found to be 7.18±0.20 MPa by conventional Brazilian disc test using steel jaws. Among the tensile strength estimation methods by the FBD test, Wang and Cao's (2016) approach gave the closest results to real tensile strength. The average tensile strength calculated using the approach of Wang and Cao (2016) was approximately 8% higher than the average tensile strength of andesite acquired from the BD tests.

CHAPTER 8

CONCLUSIONS AND RECOMMENDATIONS

The following conclusions are drawn from the numerical study and experimental results.

- Two new numerical computational formulas, considering the loading angle (2α), were derived, one of which is used to calculate the numerically computed critical dimensionless crack length (a_{cn}/R) and the other to determine the maximum dimensionless stress intensity factor ($Y_{I\,max}$). These equations were valid for the loading angles in the range of 0.03 radians (2°) to 0.87 radians (50°). New expressions corresponded to the use of a larger number of modeling data points for the FBD specimen geometry model compared to the studies of Keles and Tutluoğlu (2011) and Özdoğan (2017).
- $2a_{cn}$ and $Y_{I\,max}$ formulas are not applicable to the Brazilian disc geometry of zero loading angle, which is for 2α =0°. In such a case, $Y_{I\,max}$ cannot be determined from $Y_{I\,max}$-a/R curve, which does not show ascending-maximum-descending behavior. This statement is confirmed by performing the Brazilian disc test without steel loading platens. During the Brazilian disc test, the load suddenly dropped, and the specimen was split into two identical pieces without any crack initiation-stable propagation phase was observed. Therefore, the local minimum load corresponding $Y_{I\,max}$ could not be detected from the test record.
- Both specimen diameter and loading angle have a significant influence on the mode I fracture toughness of andesite. An increase in specimen diameter from 54 mm to 125 mm led to an approximately 61% (3.26/2.03=1.606) increase in mode I fracture toughness of Gölbaşı andesite.

- The loading angle effect on tensile opening fracture toughness was only observed in 125 mm diameter FBD samples.
- The size-independent fracture toughness of andesite is estimated as 3.32 MPa$\sqrt{m}$ for FBD specimens having approximately 140 mm in diameter.
- As the diameter of FBD specimens increased from 54 mm to 125 mm, the diameter group average stress drop decreased around 43% (from 20.94±13.48 MPa to 11.98±8.03 MPa). The stress drop was also influenced by the loading angle, and as the loading angle increased, the stress drop decreased for each diameter group. The explanation of the concept of the load drop is based on the internal structure of the andesite samples. Cracks in larger samples spread for a longer period of time in more representative ways related to the distribution of minerals and matrix.
- The difference between the critical dimensionless crack lengths computed from numerical modeling (a_{cn}/R) and the critical dimensionless crack lengths acquired from the test results (a_{ce}/R) was the least for 125 mm diameter FBD samples. Therefore, FBD tests carried out on larger specimens were believed to yield more reliable results. The reason concerns the spread of cracks in more representative internal matrices for larger samples.
- Stress analysis was conducted to observe the loading angle effect on K_{IC} and estimate the size of the possible plastic zone near the crack tip. The size of the plastic zone value for $2\alpha = 16°$ was approximately 53% smaller than the FBD geometry with loading angle $2\alpha = 38°$.

Some recommendations for future research are below.

- It is suggested to repeat this work with a sample diameter larger than 125 mm.
- The thickness diameter ratios can be varied to examine the effect of thickness on mode I fracture toughness.
- Future studies should perform mode I fracture toughness testing on various rock types such as sedimentary rocks in petroleum engineering and hydrofracturing since mode I fracture toughness has broad application areas.

REFERENCES

A.A.Wells. (1961). “Unstable crack propagation in metals: cleavage and fast fracture.” *Proceedings of the Crack Propagation Symposium*.

Alkan, U. (2015). Investigation of fracture toughness with four point asymmetric bending on rectangular rock specimens. Ankara

ASTM D3967–95a. (2008). Standard test method for splitting tensile strength of intact rock core specimens. *ASTM International, West Conshohocken, PA,* (Reapproved), 20–23.

ASTM D7012-14. (2014). Standard Test Method for Compressive Strength and Elastic Moduli of Intact Rock Core Specimens under Varying States of Stress and Temperatures, ASTM International, West Conshohocken, PA. *ASTM International, West Conshohocken, PA*, (February), 4–11.

Brocks, W., & Scheider, I. (2001). Numerical Aspects of the Path-Dependence of the J-Integral in Incremental Plasticity How to Calculate Reliable J-Values in FE Analyses. *International Journal of Fatigue*, (October), 1–33.

Chen, R., Dai, F., Qin, J., & Lu, F. (2013). Flattened Brazilian Disc Method for Determining the Dynamic Tensile Stress-Strain Curve of Low Strength Brittle Solids. *Experimental Mechanics*, *53*(7), 1153–1159.

Chong, K. P., & Kuruppu, M. D. (1984). New specimen for fracture toughness determination for rock and other materials. *International Journal of Fracture*, *26*(2).

Dugdale, D. S. (1960). Yielding of steel sheets containing slits. *Journal of the Mechanics and Physics of Solids*, *8*(2), 100–104.

Elghazel, A., Taktak, R., & Bouaziz, J. (2015). Determination of elastic modulus, tensile strength and fracture toughness of bioceramics using the flattened

Brazilian disc specimen: analytical and numerical results. *Ceramics International*, *41*(9), 12340–12348.

Fowell, R. J., & Xu, C. (1993). The cracked chevron notched Brazilian disc test-geometrical considerations for practical rock fracture toughness measurement. *International Journal of Rock Mechanics and Mining Sciences And*, *30*(7), 821–824.

Fowell, R. J., Hudson, J. A., Xu, C., Chen, J. F., & Zhao, X. (1995, January 1). Suggested method for determining mode I fracture toughness using Cracked Chevron Notched Brazilian Disc (CCNBD) specimens. *International Journal of Rock Mechanics and Mining Sciences And*.

G.R. Irwin (1960) Plastic Zone Near a Crack Tip and Fracture Toughness, Sagamore Ordnance Material Conference, pp. 63–78.

Google Earth. (2020, February 13). Retrieved from https://earth.google.com/web/search/Yurtbeyi,+G%c3%b6lba%c5%9f%c4%b1+Andezit,+15+Ada,+G%c3%b6lba%c5%9f%c4%b1%2fAnkara,+T%c3%bcrkiye/@39.7708753,32.8749478,1253.53035959a,1728.73575813d,35y,0h,0t,0r/data=CigiJgokCQtGw_FW40NAEVnYaLYz4UNAGY_AAkjSckBAIZxi0pLW

Griffith, A. A. (1921). The Phenomena of Rupture and Flow in Solids. Philosophical Transactions of the Royal Society A: Mathematical, Physical and Engineering Sciences, 221(582-593), 163–198.

Griffith, A.A. (1924). The Theory of Rupture, Proc. of First Int. Cong. Appl. Mech., pp. 53-64.

Guo, H., Aziz, N. I., & Schmidt, L. C. (1993). Rock fracture-toughness determination by the Brazilian test. *Engineering Geology*, *33*(3), 177–188.

Huang, Y. G., Wang, L. G., Lu, Y. L., Chen, J. R., & Zhang, J. H. (2015). Semi-analytical and Numerical Studies on the Flattened Brazilian Splitting Test

Used for Measuring the Indirect Tensile Strength of Rocks. *Rock Mechanics and Rock Engineering*, *48*(5), 1849–1866.

Inglis, C. E. (1913) “Stresses in a plate due to the presence of cracks and sharp comers.” *T. Inst. Naval Architects,* 55, 219-241.

Irwin, G. R. (1948), Fracturing of metals, Am. Soc. Metals, Cleveland, p. 147.

Irwin, G. R. (1957). Analysis of Stresses and Strains Near the End of a Crack Traversing a Plate. *Journal of Applied Mechanics*.

ISRM (1978) Suggested Methods for Determining Tensile Strength of Rock Materials Part 2: Suggested Method for determining indirect tensile strength by the Brazil Test. International Journal of Rock Mechanics and Mining Sciences, 15, 99-103.

Jin, Z., & Sun, C. T. (2012). *Fracture Mechanics*. *Fracture Mechanics*. Elsevier Inc.

Kaklis, K. N., Agioutantis, Z., Sarris, E., & Pateli, A. (2005). A theoretical and numerical study of discs with flat edges. *5th GRACM International Congress on Computational Mechanics* (pp. 437-443). Limassol: GRACM.

Kanninen, M. F., & Popelar, C. H. (1985). *Advanced fracture mechanics*. New York, NY: Oxford University Press.

Karakaş, S. (2011). Shear mode rock fracture toughness determination with a circular plate type specimen under three-point bending. Ankara

Keles, C., & Tutluoglu, L. (2011). Investigation of proper specimen geometry for mode I fracture toughness testing with flattened Brazilian disc method. *International Journal of Fracture*, *169*(1), 61–75.

Khavari, P., & Heidari, M. (2016). Numerical and experimental studies on the effect of loading angle on the validity of flattened Brazilian disc test. *Journal of Geology and Mining Research*, *8*(1), 1–12.

Kirsch, G. (1898). *Die Theorie der Elastizität und die Bedürfnisse der Festigkeitslehre*. Berlin: Springer.

Liang, P., & Tao, J. L. (2014). The contrast of concrete Brazilian and flattened Brazilian disc specimen under quasi static diametral compression tests. In *Applied Mechanics and Materials* (Vol. 507, pp. 263–268).

Lin, H., Xiong, W., & Yan, Q. (2016). Modified formula for the tensile strength as obtained by the flattened Brazilian disk test. *Rock Mechanics and Rock Engineering*, *49*(4), 1579–1586.

Lin, H., Xiong, W., Xiong, Z., & Gong, F. (2015). Three-dimensional effects in a flattened Brazilian disk test. *International Journal of Rock Mechanics and Mining Sciences*, *74*, 10–14.

Liu, S., Xu, J., Wang, P., & Fang, X. (2016). Research on Fracture Toughness of Flattened Brazilian Disc Specimen after High Temperature. *High Temperature Materials and Processes*, *35*(1), 81–87.

Lyse, I., & Steward, D. M. (1935). *Discussion of the paper by Professor Westergaard: "Stresses at a crack, size of the crack and the bending of reinforced concrete"*.

Mahanta, B., Sirdesai, N., Singh, T. N., & Ranjith, P. G. (2017). Experimental Study of Strain Rate Sensitivity to Fracture Toughness of Rock using Flattened Brazilian Disc. In *Procedia Engineering* (Vol. 191, pp. 256–262). Elsevier Ltd.

Mazel, V., Guerard, S., Croquelois, B., Kopp, J. B., Girardot, J., Diarra, H., … Tchoreloff, P. (2016). Reevaluation of the diametral compression test for tablets using the flattened disc geometry. *International Journal of Pharmaceutics*, *513*(1–2), 669–677.

Moustabchir, H., Arbaoui, J., Zitouni, A., Hariri, S., & Dmytrakh, I. (2015). Numerical analysis of stress intensity factor and T-stress in pipeline of steel P264GH submitted to loading conditions. *Journal of Theoretical and Applied Mechanics*, *53*(3), 665–672.

Munz, D., & Fett, T. (2015). *Karlsruher Institut für Technologie (KIT).* Retrieved from publikationen.bibliothek: https://publikationen.bibliothek.kit.edu/1000049444

Obara, Y., Kataoka, M., & Jeong, S. S. (2017). Fracture toughness of rock. In *4th ISRM Young Scholars Symposium on Rock Mechanics, YSS 2017* (Vol. 2017-May, pp. 5–8). International Society for Rock Mechanics.

Ouchterlony, F. (1988). *Suggested methods for determining the fracture toughness of rock*. Oxford: Pergamon.

Özdoğan, C. (2017). Pure tensile fracture modelling and toughness measurements on brazilian discs of andesite and marble. Ankara

Rice, J. R. (1968). *A path independent integral and the approximate analysis of strain concentration by notches and cracks*. New York, NY: ASME.

Sack, R. A. (1946). Extension of Griffith's theory of rupture to three dimensions. *Proceedings of the Physical Society*, *58*(6), 729–736.

Shin, H., & Kim, J. B. (2015). Correction functions to determine the stress state of a flattened disk specimen in diametral testing with reference to analytical solutions for circular specimens. *International Journal of Precision Engineering and Manufacturing*, *16*(13), 2699–2707.

Tayfuner, T. (2019). Mode I fracture toughness and tensile strength investigation on molded shotcrete brazilian specimen. Ankara

TS 699 (1987) Tabii Yapı Taşları Muayene ve Deney Metotları. Turkish Standards Institution, Ankara

Ulusay, R. (2016). *ISRM suggested methods for rock characterization, testing and monitoring: 2007-2014*. Place of publication not identified: SPRINGER INTERNATIONAL PU.

Wang, C. H. (1996). *Introduction to fracture mechanics*. Melbourne, Vic.: DSTO Aeronautical and Maritime Research Laboratory.

Wang, M., & Cao, P. (2016). Numerical analysis of flattened brazilian disc test based on the cusp catastrophe theory. *Mathematical Problems in Engineering*, *2016*.

Wang, Q. Z., & Wu, L. Z. (2004). The flattened Brazilian disc specimen used for determining elastic modulus, tensile strength and fracture toughness of brittle rocks: Experimental results. *International Journal of Rock Mechanics and Mining Sciences*, *41*(SUPPL. 1).

Wang, Q. Z., & Xing, L. (1999). Determination of fracture toughness KIC by using the flattened Brazilian disk specimen for rocks. *Engineering Fracture Mechanics*, *64*(2), 193–201.

Wang, Q. Z., Jia, X. M., Kou, S. Q., Zhang, Z. X., & Lindqvist, P. A. (2004). The flattened Brazilian disc specimen used for testing elastic modulus, tensile strength and fracture toughness of brittle rocks: Analytical and numerical results. *International Journal of Rock Mechanics and Mining Sciences*, *41*(2), 245–253.

Wang, Q. Z., Li, L., Wu, L. Z., & Huang, R. Q. (2017). Improved Brazilian test specimen: From flattened Brazilian disc to grooved Brazilian disc. In *51st US Rock Mechanics / Geomechanics Symposium 2017* (Vol. 5, pp. 3669–3676). American Rock Mechanics Association (ARMA).

Wang, Q. Z., Li, W., & Xie, H. P. (2009). Dynamic split tensile test of Flattened Brazilian Disc of rock with SHPB setup. *Mechanics of Materials*, *41*(3), 252–260.

Wells, A. A. (1963). Application of fracture mechanics at and beyond general yielding. *British Welding Journal*, *10*(11), 563–570.

Westergaard, H. (1934). Stresses at a crack, size of the crack and the bending of reinforced concrete. Prov. American Concrete Institute, Vol. 30, 93-102.

Williams, M. L. (1957). On stress distribution at base of stationary crack. *American Society of Mechanical Engineers-Transactions-Journal of Applied Mechanics*, *24*(1), 109–114.

Wu, S., Ma, J., Cheng, Y., Xu, M., & Huang, X. (2018). Numerical analysis of the flattened Brazilian test: Failure process, recommended geometric parameters and loading conditions. *Engineering Fracture Mechanics*, *204*, 288–305.

Yoncacı, S. (2019). Investigation of fracture toughness on flattened brazilian disc type molded shotcrete specimens. Ankara

Zhao, X. L., Fowell, R. J., Roegiers, J. C., & Xu, C. (1994). Rock fracture-toughness determination by the Brazilian test, by H. Guo, N.I. Aziz, L.C. Schmidt. *Engineering Geology*, *38*(1–2), 181–184.

APPENDICES

A. FORCE-DISPLACEMENT CURVES OF FBD TESTS

Table A.1. *Flattened Brazilian disc specimens with* D *=54 mm*

Figure	Specimen Code	t (m)	2α (°)	$Y_{I\,max}$	P_{min} (kN)	K_{IC} (MPa$\sqrt{m}$)
Figure A.1.	A5418s1	0.0318	18	0.71	13.48	1.83
Figure A.2.	A5420s1	0.0320	20	0.65	18.43	2.28
Figure A.3.	A5420s2	0.0309	20	0.65	15.71	2.01
Figure A.4.	A5426s1	0.0315	26	0.52	23.51	2.36
Figure A.5.	A5426s2	0.0321	26	0.52	20.68	2.04
Figure A.6.	A5432s1	0.0338	32	0.43	26.57	2.06
Figure A.7.	A5432s2	0.0325	32	0.43	22.62	1.82
Figure A.8.	A5434s1	0.0310	34	0.4	23.72	1.86

Table A.2. *Flattened Brazilian disc specimens with* D *=75 mm*

Figure	Specimen Code	t (m)	2α (°)	$Y_{I\,max}$	P_{min} (kN)	K_{IC} (MPa$\sqrt{m}$)
Figure A.9.	A7518s1	0.0455	18	0.71	30.91	2.49
Figure A.10.	A7522s1	0.0453	22	0.61	30.50	2.12
Figure A.11.	A7522s2	0.0458	22	0.61	35.48	2.44
Figure A.12.	A7524s1	0.0451	24	0.56	37.91	2.43
Figure A.13.	A7524s2	0.0450	24	0.56	38.09	2.45
Figure A.14.	A7530s1	0.0458	30	0.46	43.74	2.27
Figure A.15.	A7530s2	0.0458	30	0.46	46.62	2.42
Figure A.16.	A7534s1	0.0453	34	0.40	50.69	2.31
Figure A.17.	A7536s1	0.0445	36	0.37	49.17	2.11
Figure A.18.	A7538s1	0.0456	38	0.35	58.23	2.31
Figure A.19.	A7538s2	0.0456	38	0.35	57.58	2.28

Table A.3. *Flattened Brazilian disc specimens with* D *=100 mm*

Figure	Specimen Code	t (m)	2α (°)	$Y_{I\,max}$	P_{min} (kN)	K_{IC} (MPa$\sqrt{m}$)
Figure A.20.	A10016s1	0.0596	16	49.71	49.71	2.87
Figure A.21.	A10019s1	0.0611	19	61.26	61.26	3.05
Figure A.22.	A10020s1	0.0601	20	55.61	55.61	2.69
Figure A.23.	A10022s1	0.0605	22	56.79	56.79	2.56
Figure A.24.	A10022s2	0.0607	22	66.29	66.29	2.98
Figure A.25.	A10024s1	0.0603	24	67.94	67.94	2.82
Figure A.26.	A10024s2	0.0600	24	67.30	67.30	2.81
Figure A.27.	A10026s1	0.0604	26	72.19	72.19	2.78
Figure A.28.	A10026s2	0.0604	26	74.56	74.56	2.87
Figure A.29.	A10028s1	0.0602	28	77.15	77.15	2.81
Figure A.30.	A10028s2	0.0606	28	86.22	86.22	3.12
Figure A.31.	A10030s1	0.0610	30	85.73	85.73	2.89
Figure A.32.	A10032s1	0.0606	32	92.29	92.29	2.93
Figure A.33.	A10034s1	0.0605	34	85.16	85.16	2.52
Figure A.34.	A10034s2	0.0605	34	100.83	100.83	2.98
Figure A.35.	A10036s1	0.0592	36	98.82	98.82	2.76
Figure A.36.	A10038s1	0.0610	38	117.69	117.69	3.02
Figure A.37.	A10038s2	0.0600	38	108.16	108.16	2.82

Table A.4. *Flattened Brazilian disc specimens with* D *=125 mm*

Figure	Specimen Code	t (m)	2α (°)	$Y_{I\,max}$	P_{min} (kN)	K_{IC} (MPa$\sqrt{m}$)
Figure A.38.	A12518s1	0.0755	18	0.71	100.43	3.78
Figure A.39.	A12520s1	0.0750	20	0.65	106.46	3.69
Figure A.40.	A12520s2	0.0744	20	0.65	103.06	3.60
Figure A.41.	A12524s1	0.0740	24	0.56	108.35	3.28
Figure A.42.	A12524s2	0.0751	24	0.56	120.38	3.59
Figure A.43.	A12528s1	0.0746	28	0.49	139.31	3.66
Figure A.44.	A12528s2	0.0759	28	0.49	116.21	3.00
Figure A.45.	A12534s1	0.0757	34	0.40	159.06	3.36
Figure A.46.	A12534s2	0.0754	34	0.40	158.41	3.36
Figure A.47.	A12536s1	0.0748	36	0.37	165.17	3.27
Figure A.48.	A12538s1	0.0755	38	0.35	149.29	2.77
Figure A.49.	A12538s2	0.0753	38	0.35	155.42	2.89
Figure A.50.	A12542s1	0.0741	42	0.30	169.30	2.74
Figure A.51.	A12542s1	0.0726	42	0.30	158.00	2.61

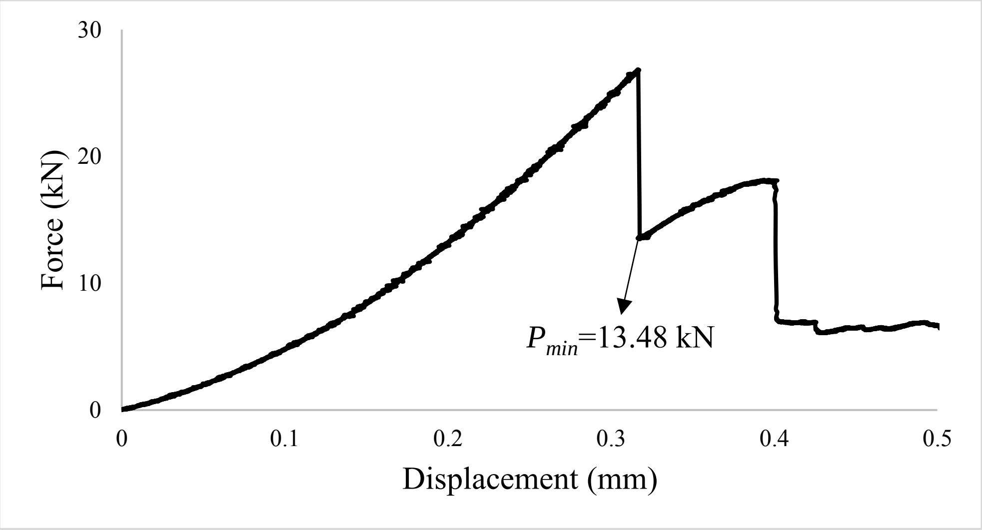

Figure A.1. Force versus displacement curve of A5418s1 specimen

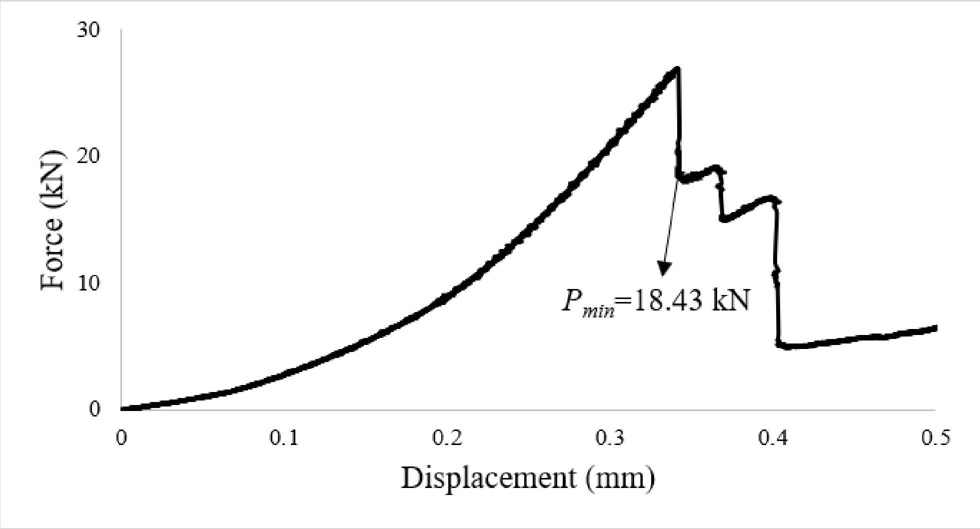

Figure A.2. Force versus displacement curve of A5420s1 specimen

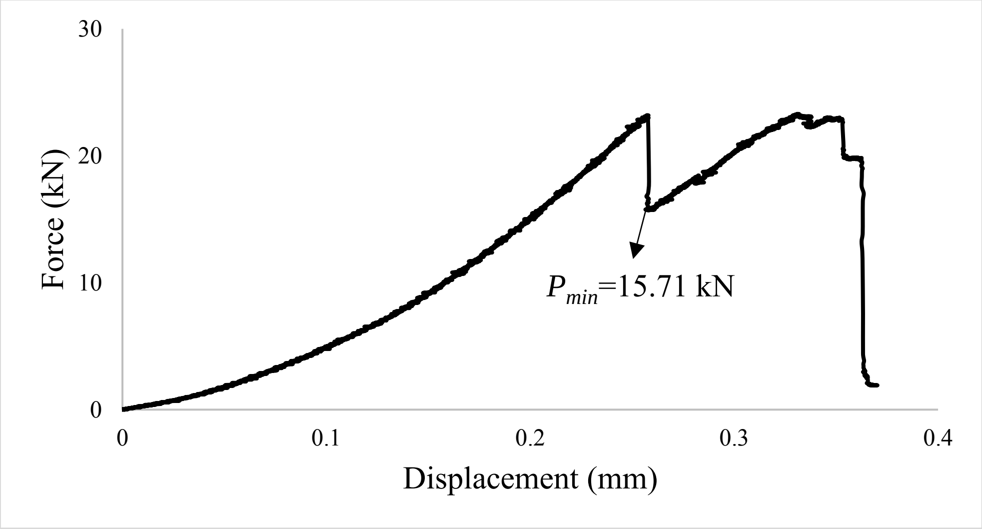

Figure A.3. Force versus displacement curve of A5420s2 specimen

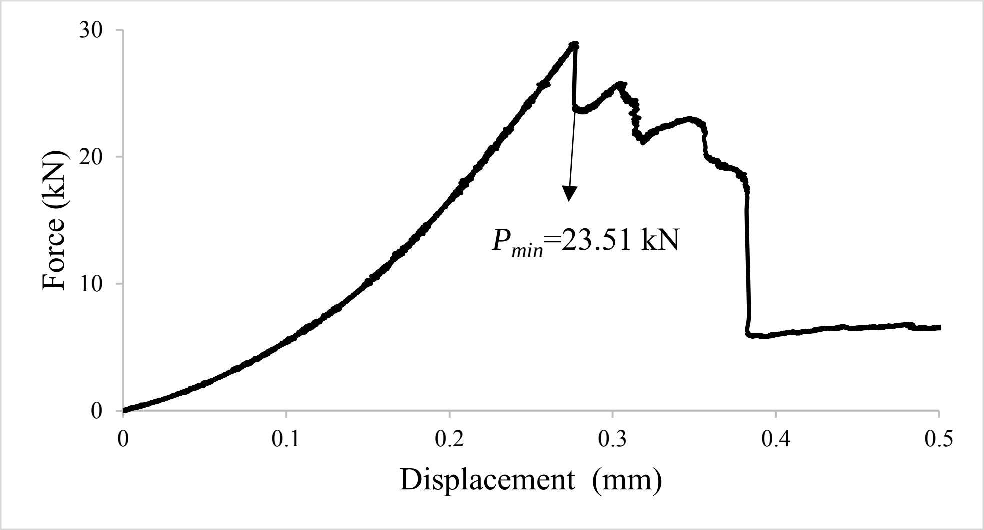

Figure A.4. Force versus displacement curve of A5426s1 specimen

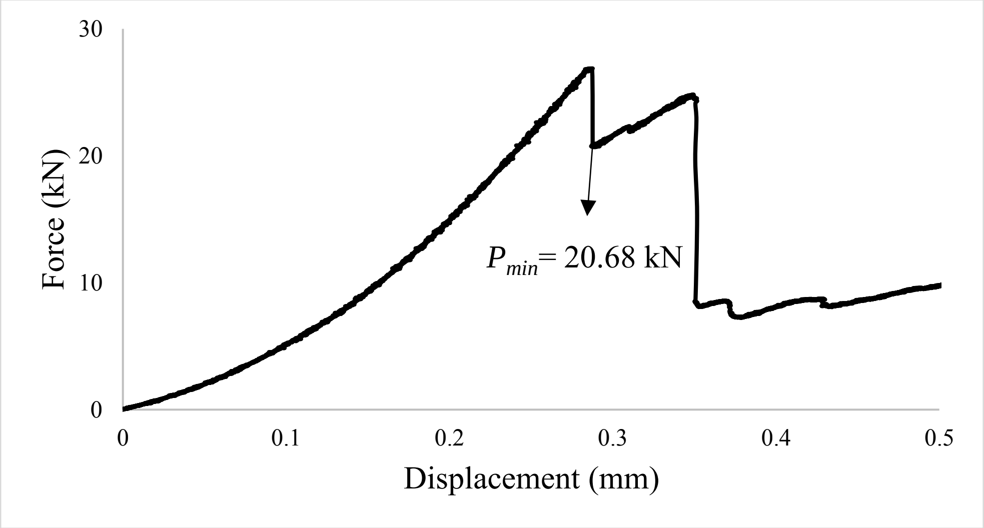

Figure A.5. Force versus displacement curve of A5426s2 specimen

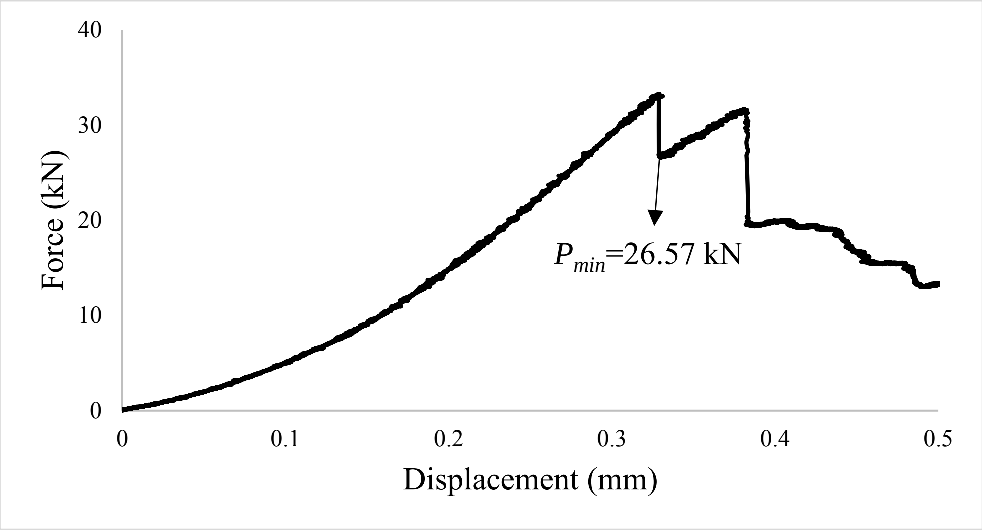

Figure A.6. Force versus displacement curve of A5432s1 specimen

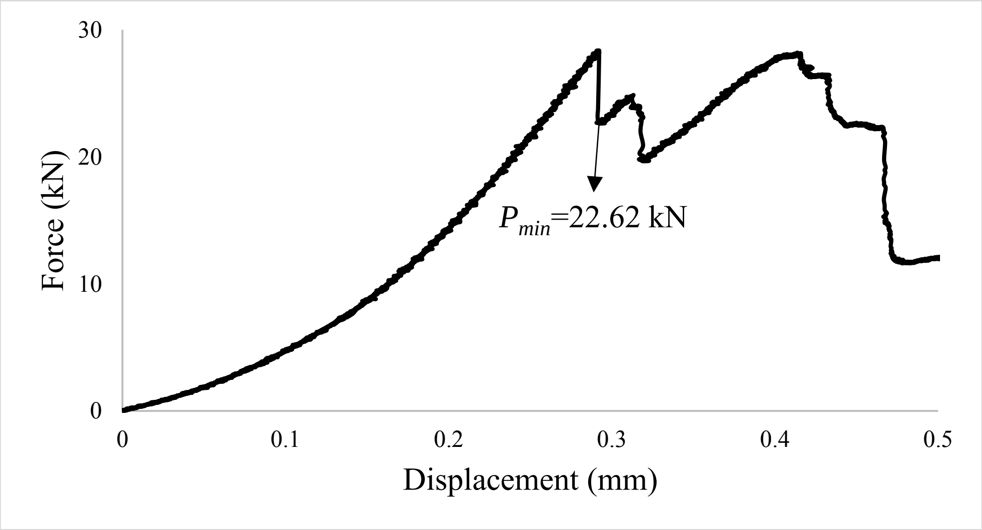

*Figure A.7.*Force versus displacement curve of A5432s2 specimen

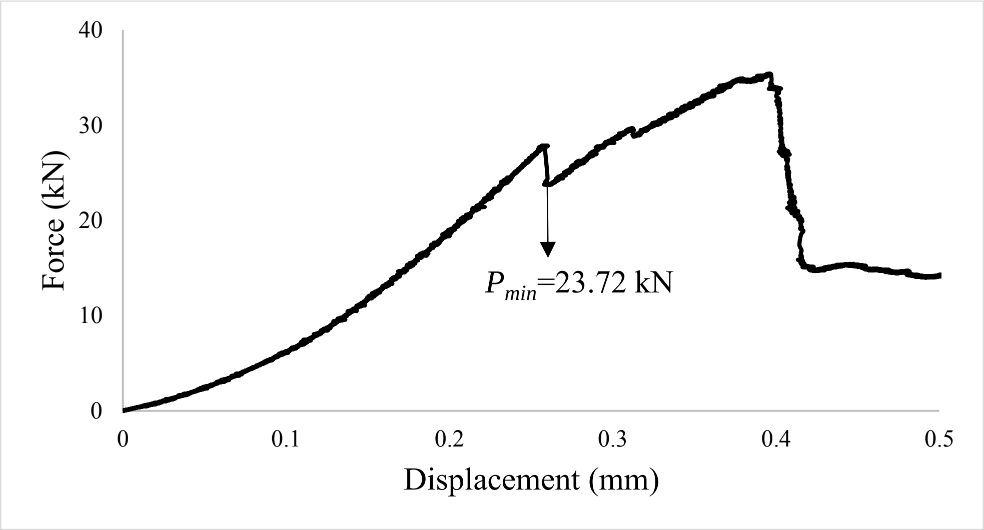

Figure A.8. Force versus displacement curve of A5434s1 specimen

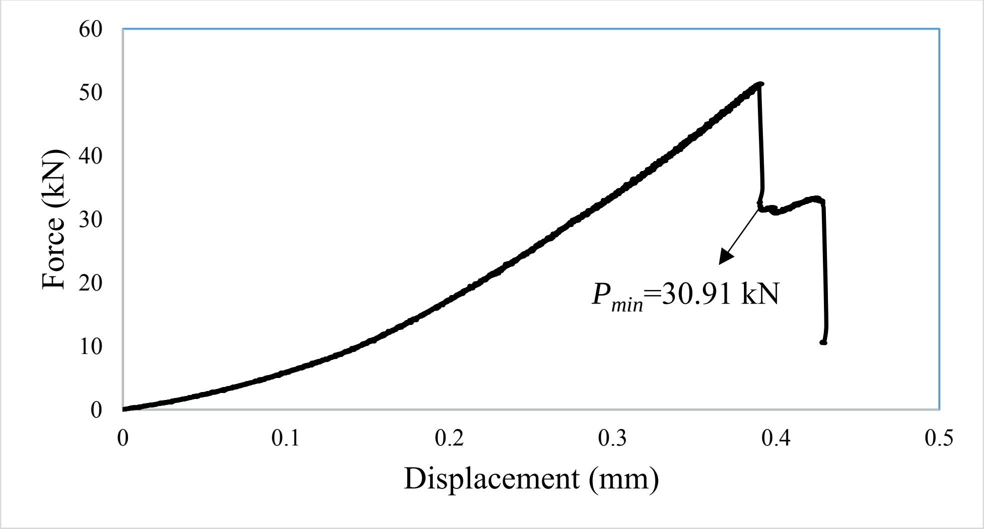

Figure A.9. Force versus displacement curve of A7518s1 specimen

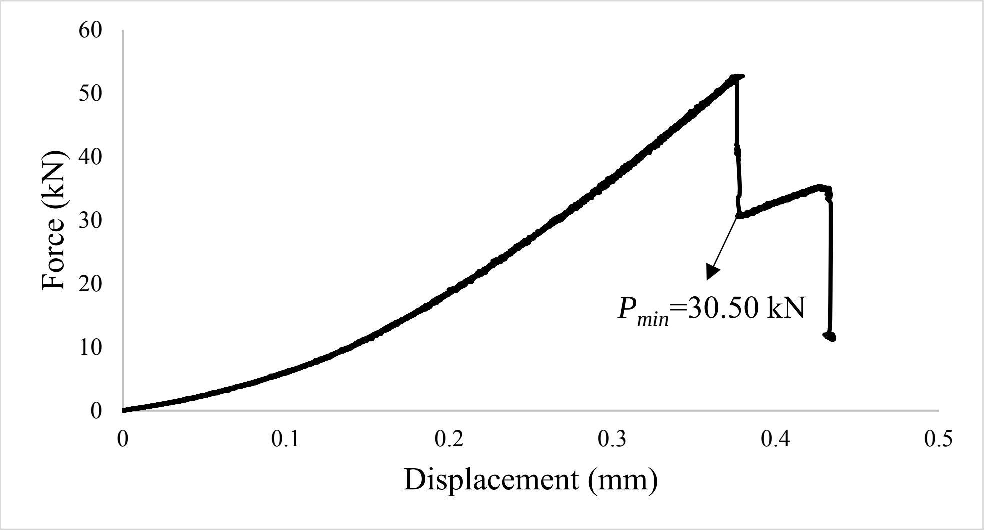

Figure A.10. Force versus displacement curve of A7522s1 specimen

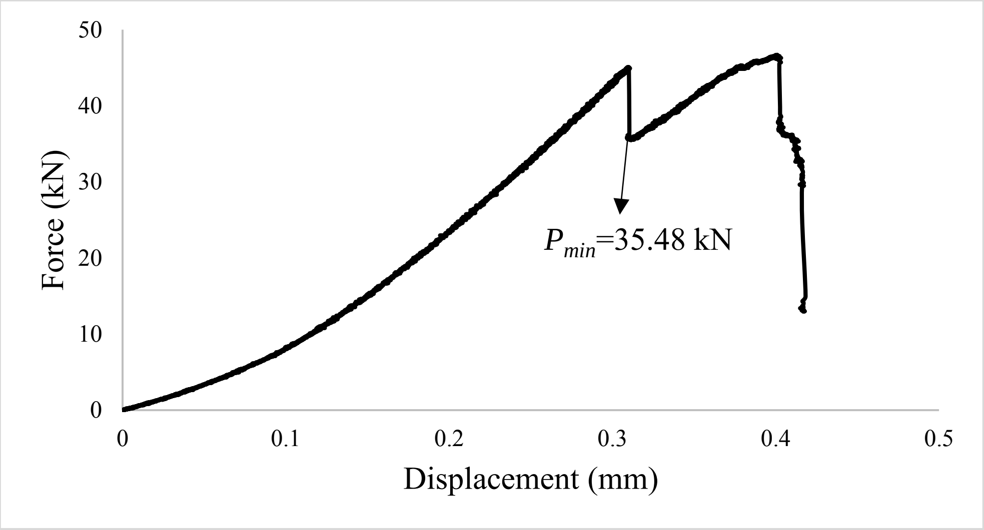

Figure A.11. Force versus displacement curve of A7522s2 specimen

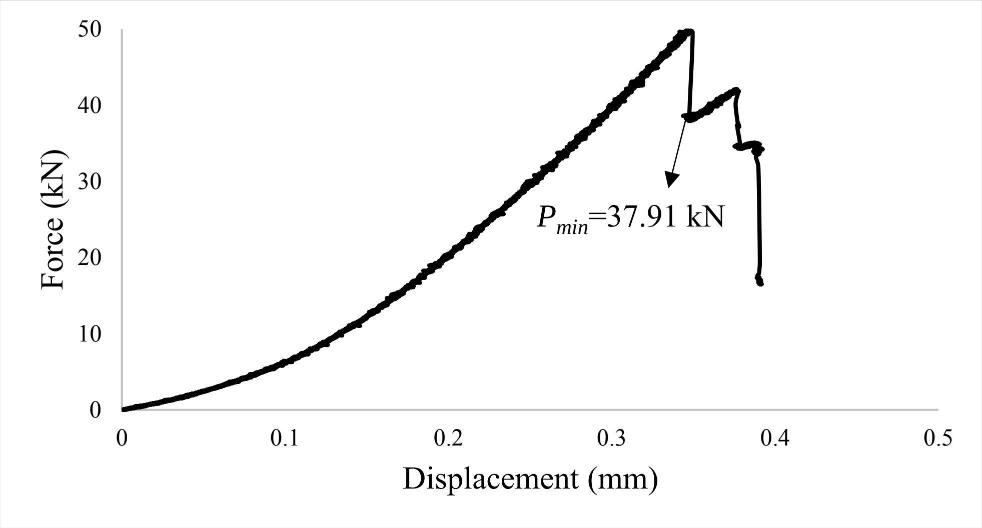

Figure A.12. Force versus displacement curve of A7524s1 specimen

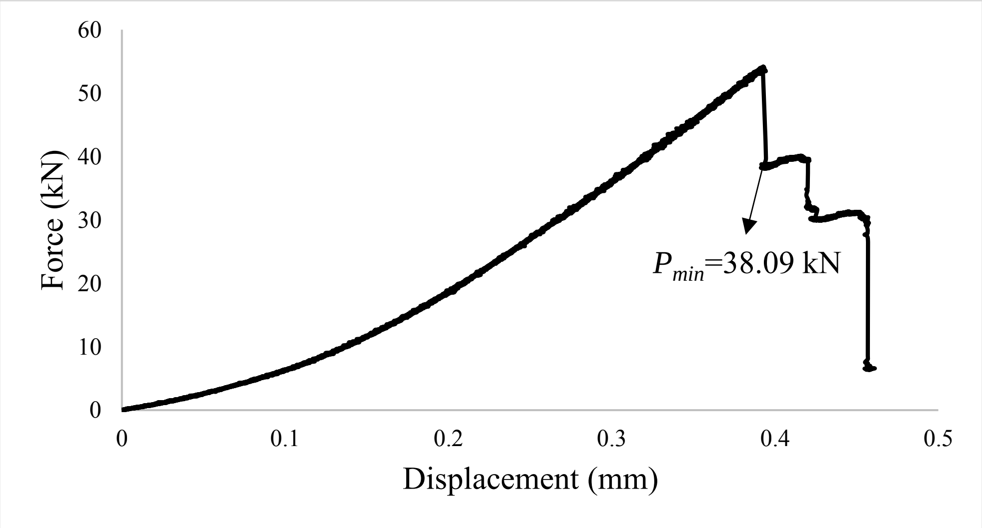

Figure A.13. Force versus displacement curve of A7524s2 specimen

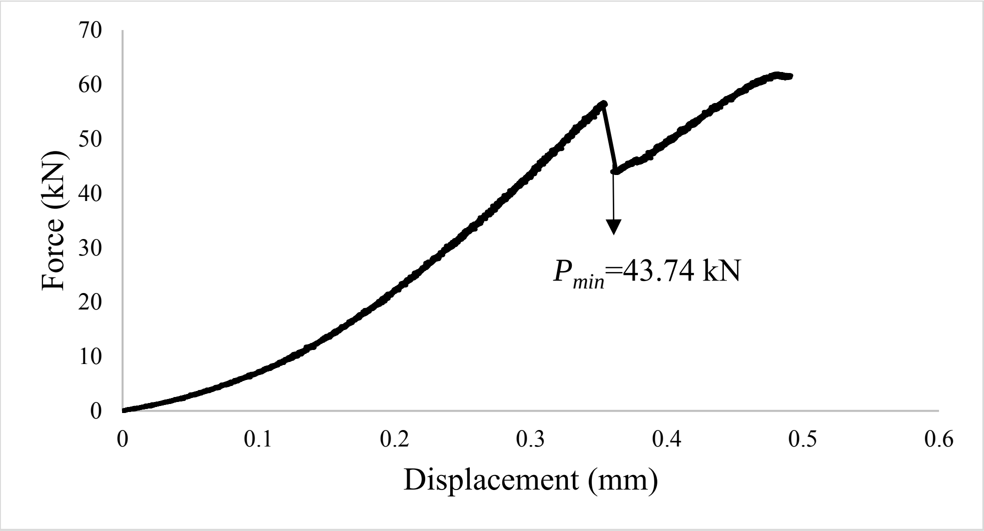

Figure A.14. Force versus displacement curve of A7530s1 specimen

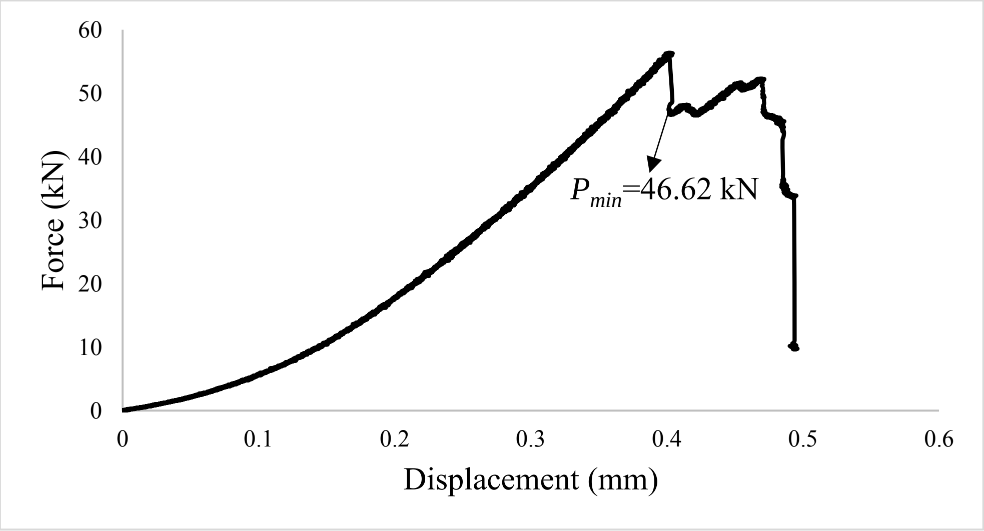

Figure A.15. Force versus displacement curve of A7530s2 specimen

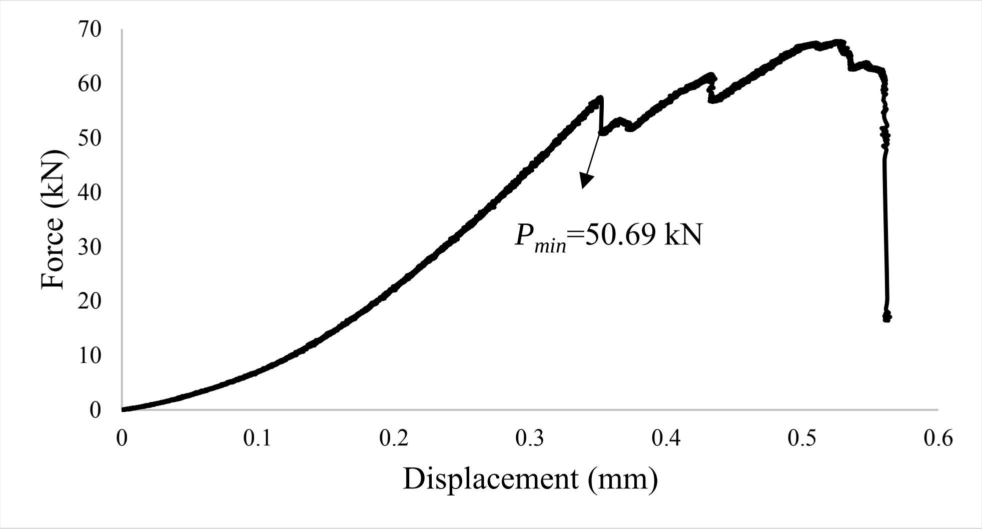

Figure A.16. Force versus displacement curve of A7534s1 specimen

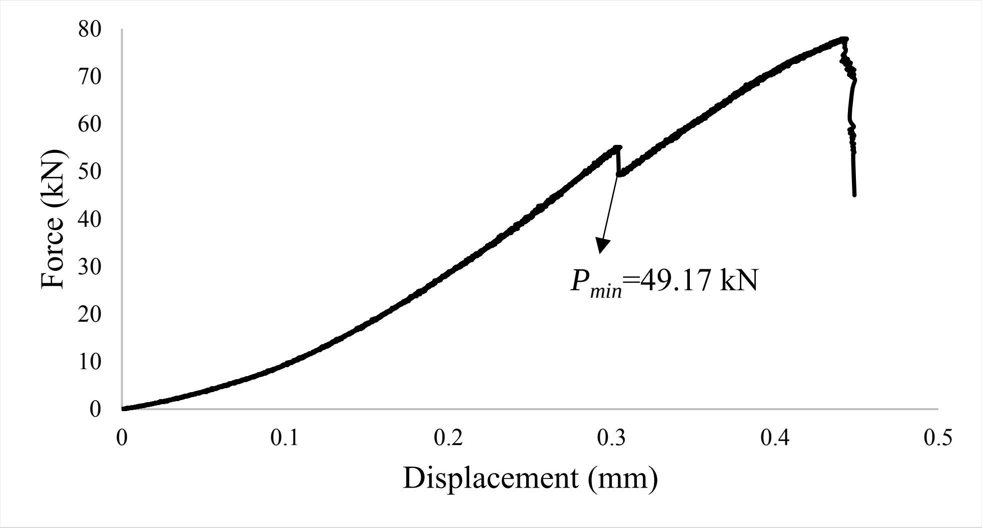

Figure A.17. Force versus displacement curve of A7536s1 specimen

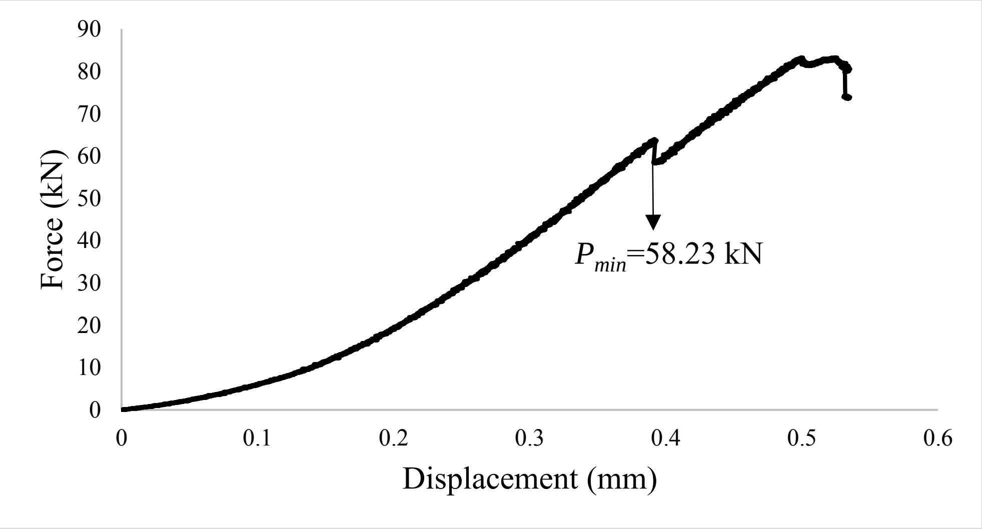

Figure A.18. Force versus displacement curve of A7538s1 specimen

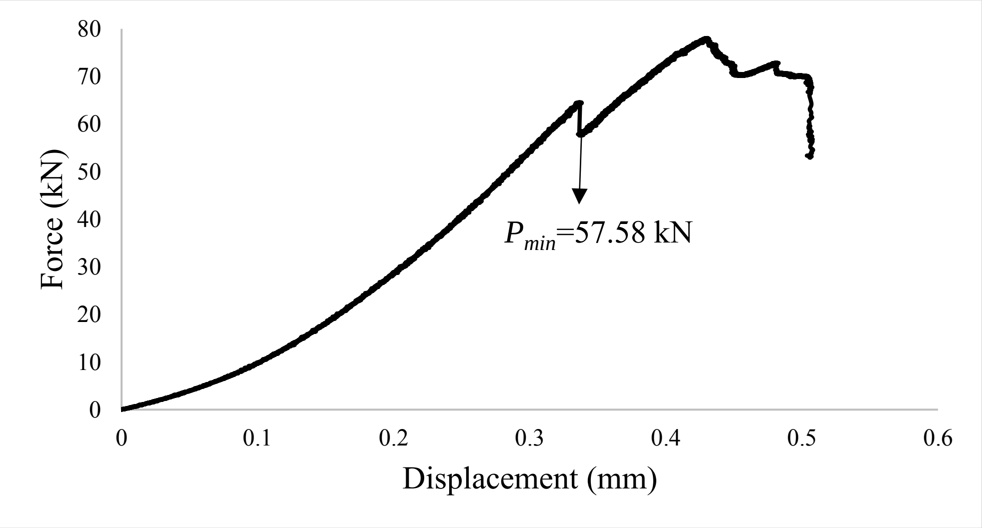

Figure A.19. Force versus displacement curve of A7538s2 specimen

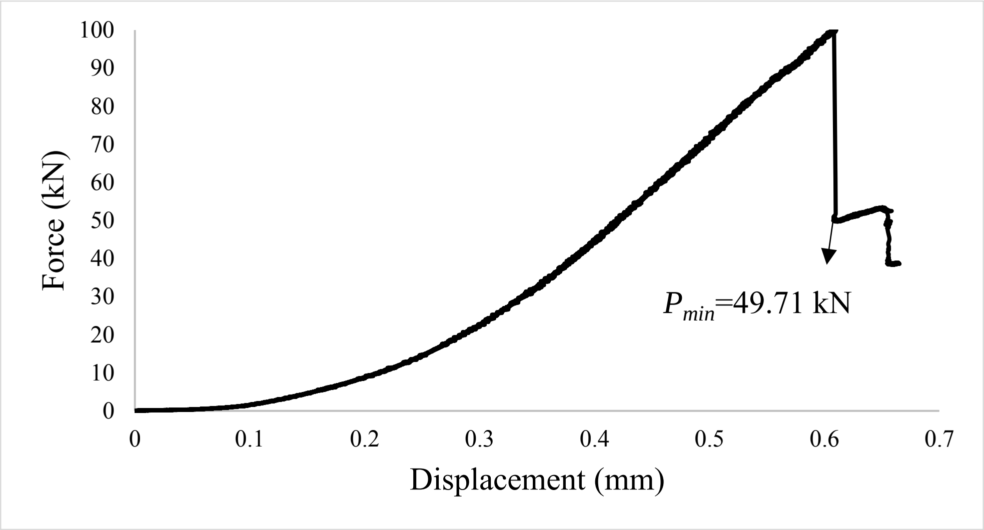

Figure A.20. Force versus displacement curve of A10016s1 specimen

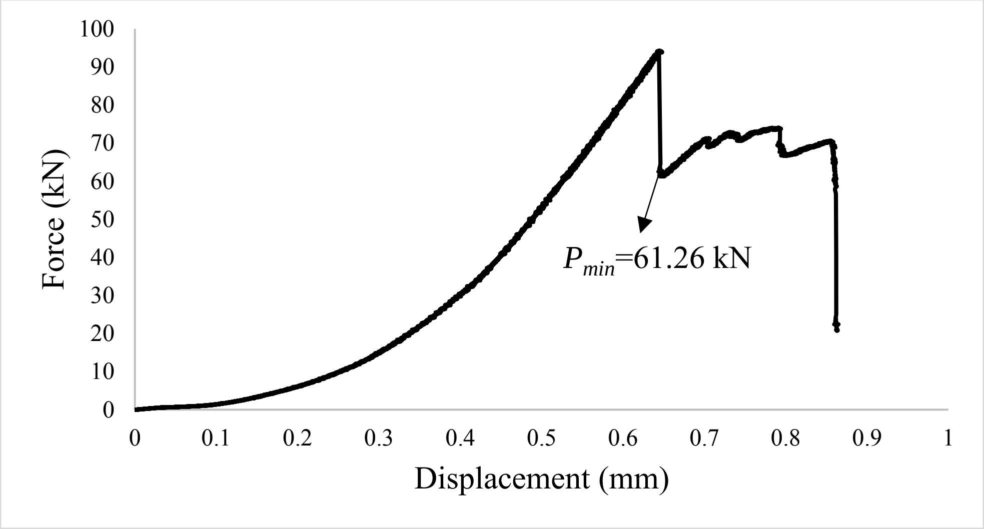

Figure A.21. Force versus displacement curve of A10019s1 specimen

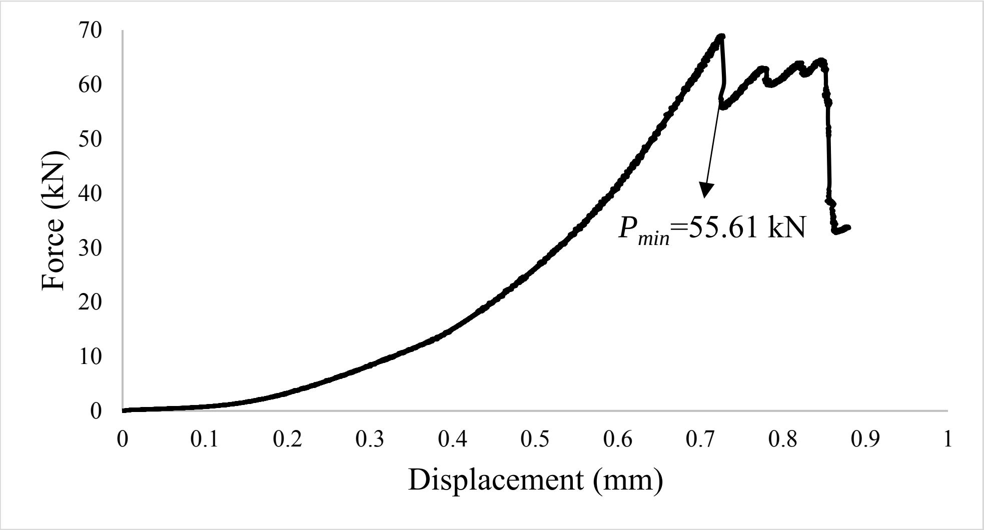

Figure A.22. Force versus displacement curve of A10020s1 specimen

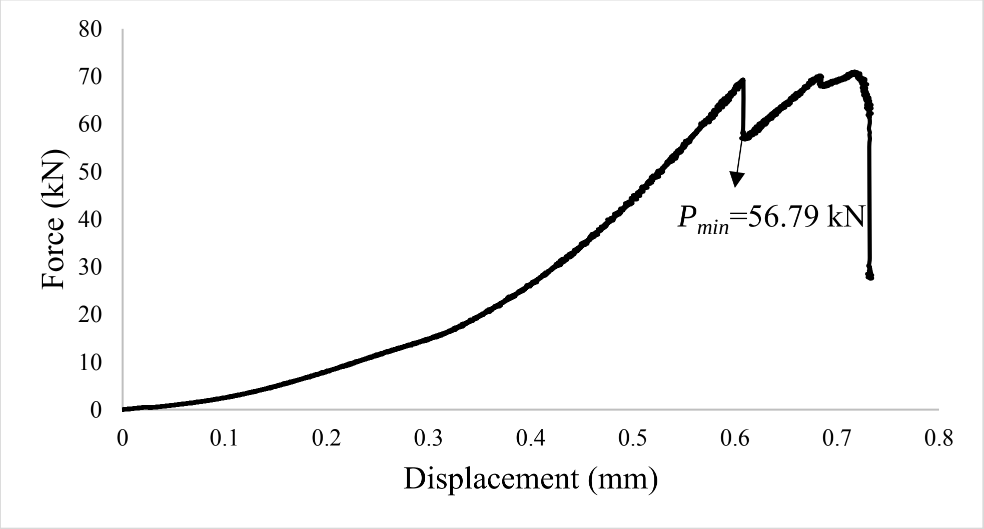

Figure A.23. Force versus displacement curve of A10022s1 specimen

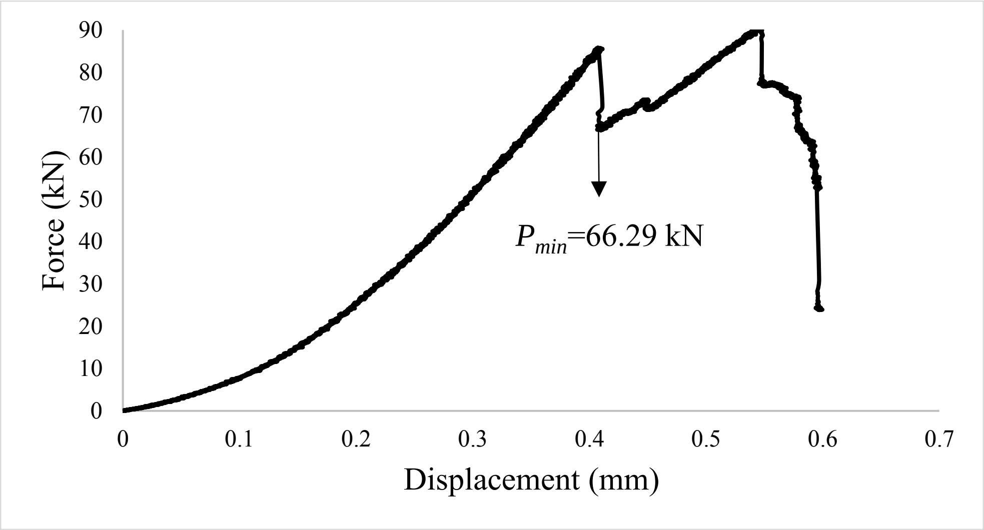

Figure A.24. Force versus displacement curve of A10022s2 specimen

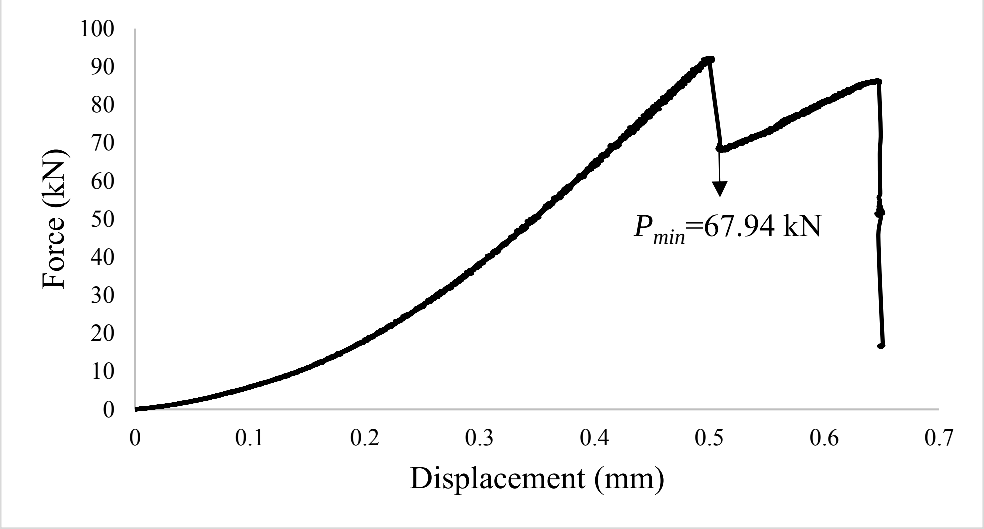

Figure A.25. Force versus displacement curve of A10024s1 specimen

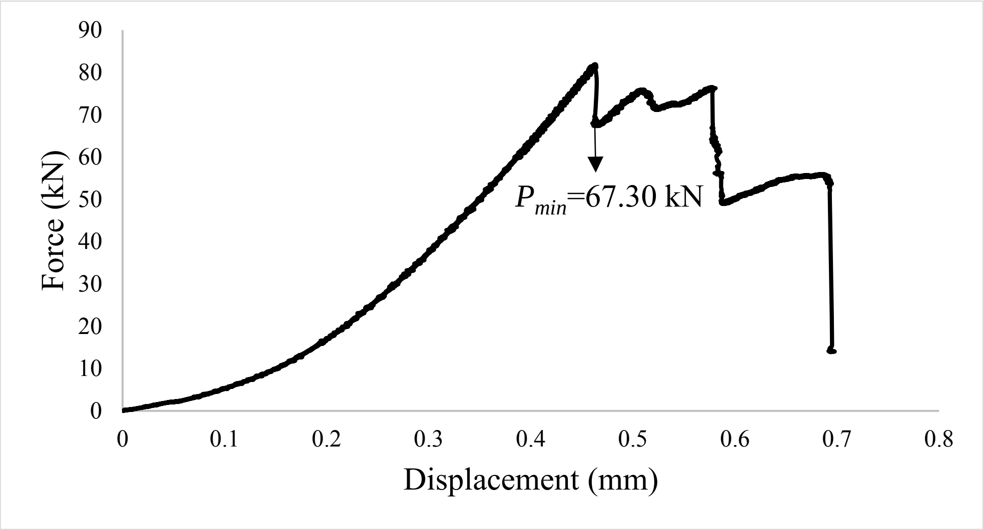

Figure A.26. Force versus displacement curve of A10024s2 specimen

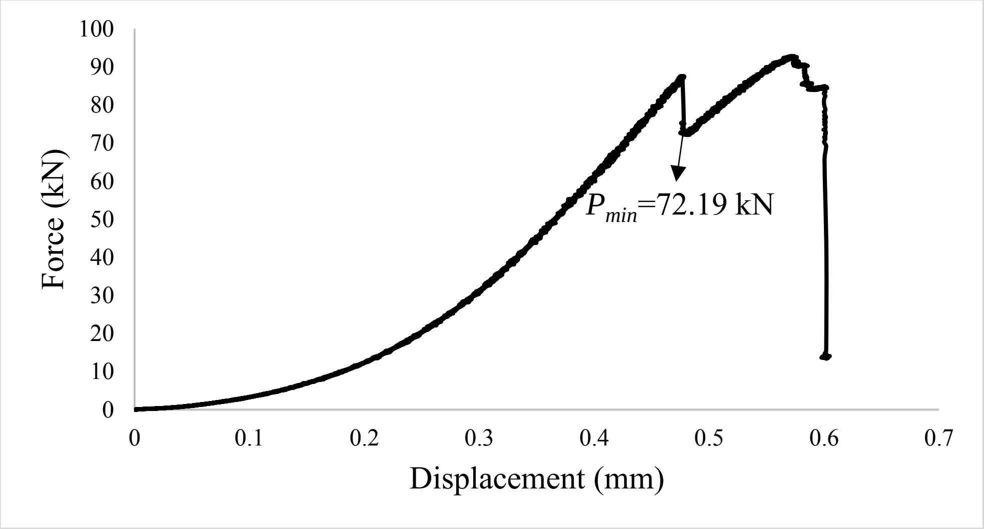

Figure A.27. Force versus displacement curve of A10026s1 specimen

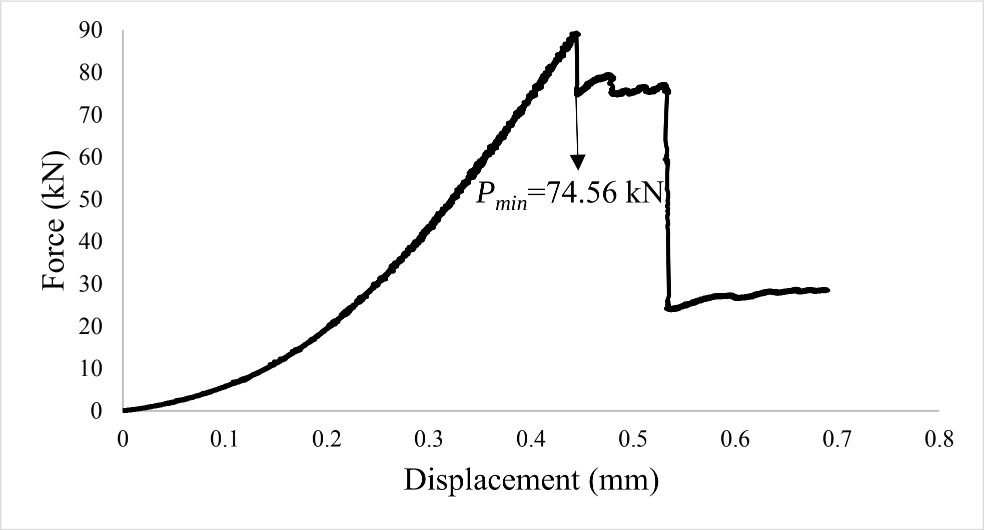

Figure A.28. Force versus displacement curve of A10026s2 specimen

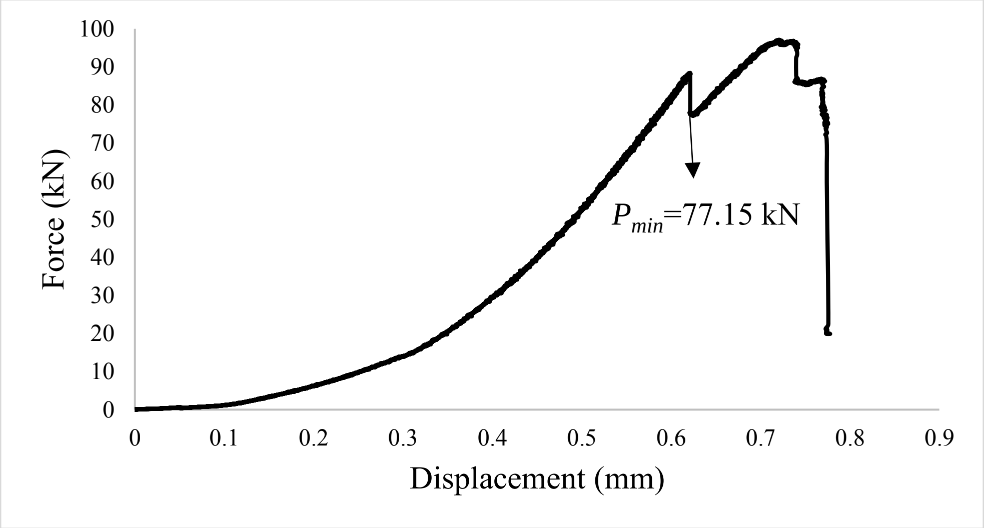

Figure A.29. Force versus displacement curve of A10028s1 specimen

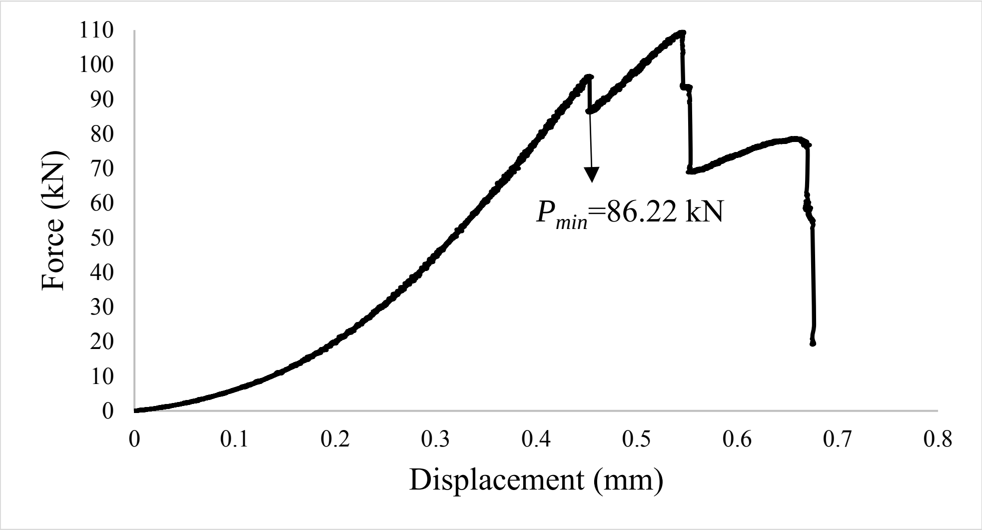

Figure A.30. Force versus displacement curve of A10028s2 specimen

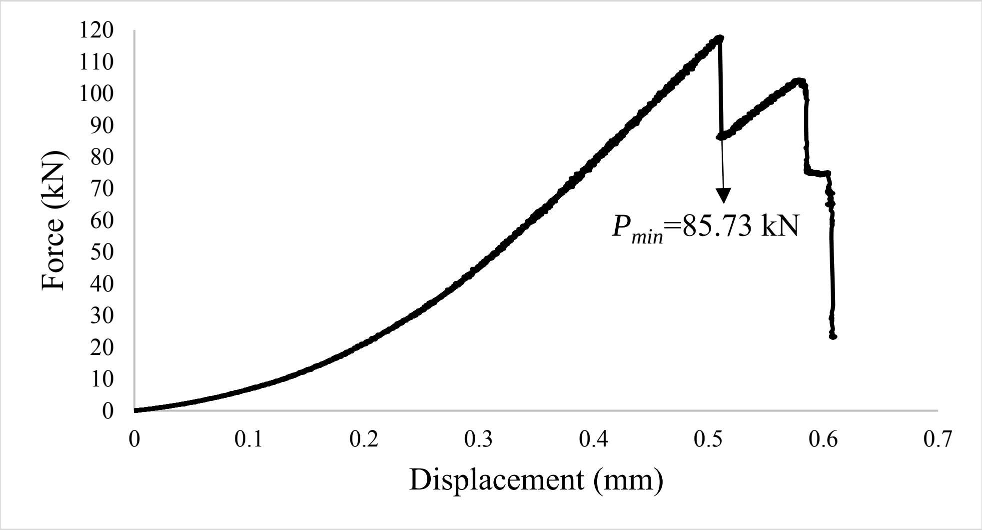

Figure A.31. Force versus displacement curve of A10030s1 specimen

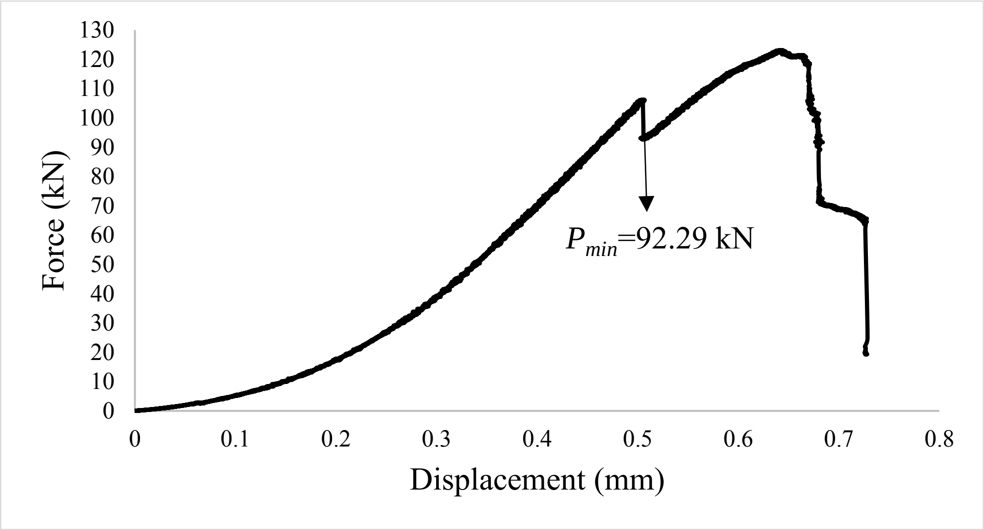

Figure A.32. Force versus displacement curve of A10032s1 specimen

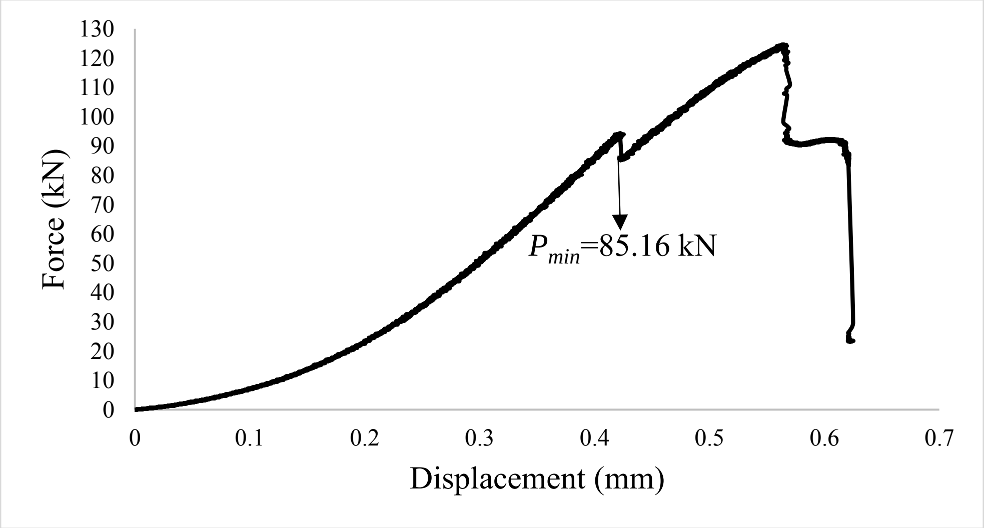

Figure A.33. Force versus displacement curve of A10034s1 specimen

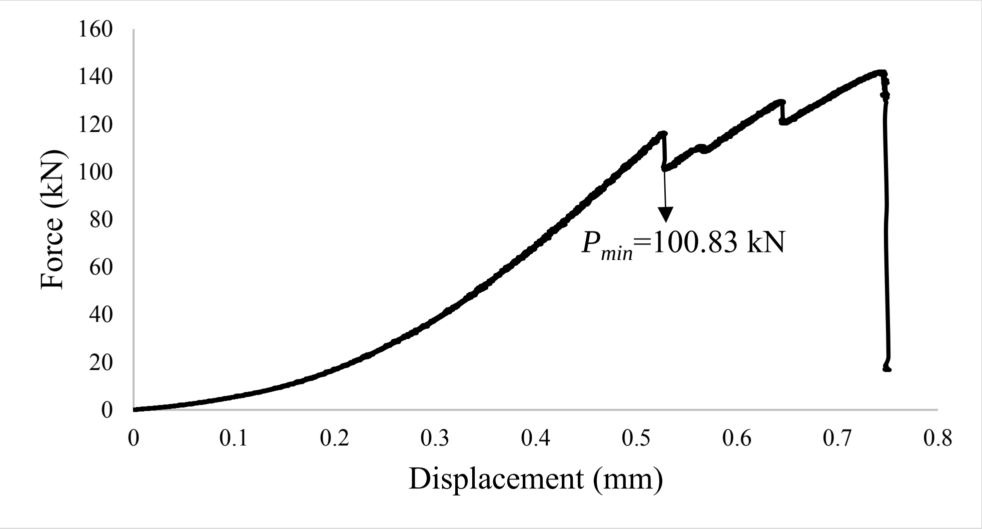

Figure A.34. Force versus displacement curve of A10034s2 specimen

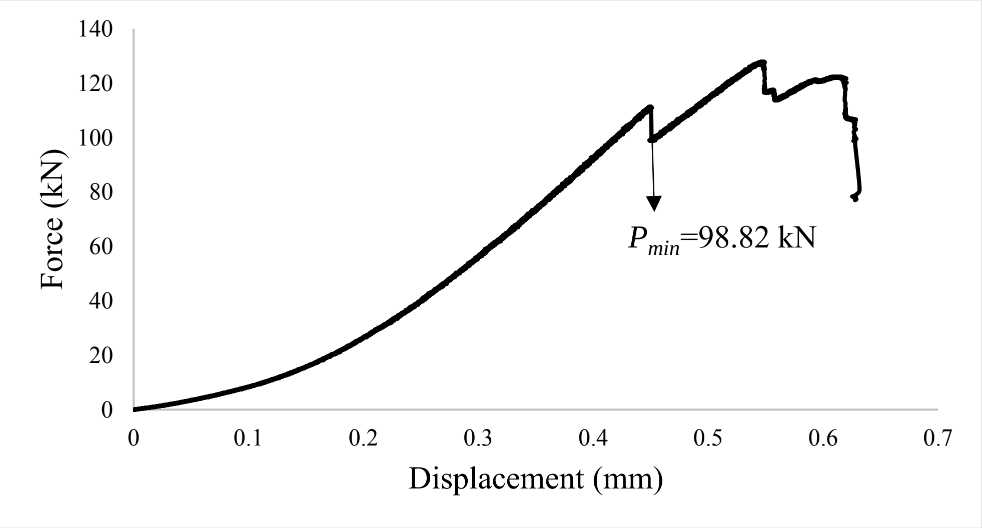

Figure A.35. Force versus displacement curve of A10036s1 specimen

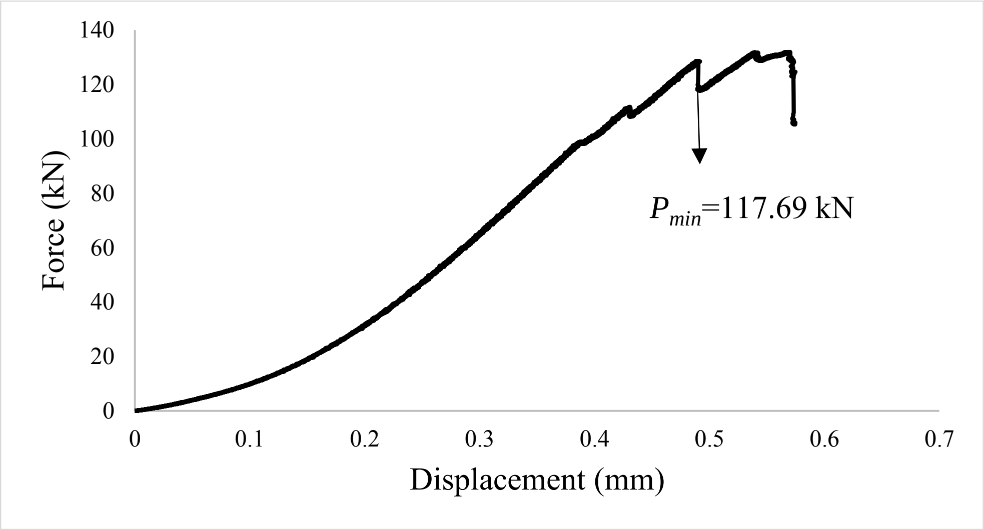

Figure A.36. Force versus displacement curve of A10038s1 specimen

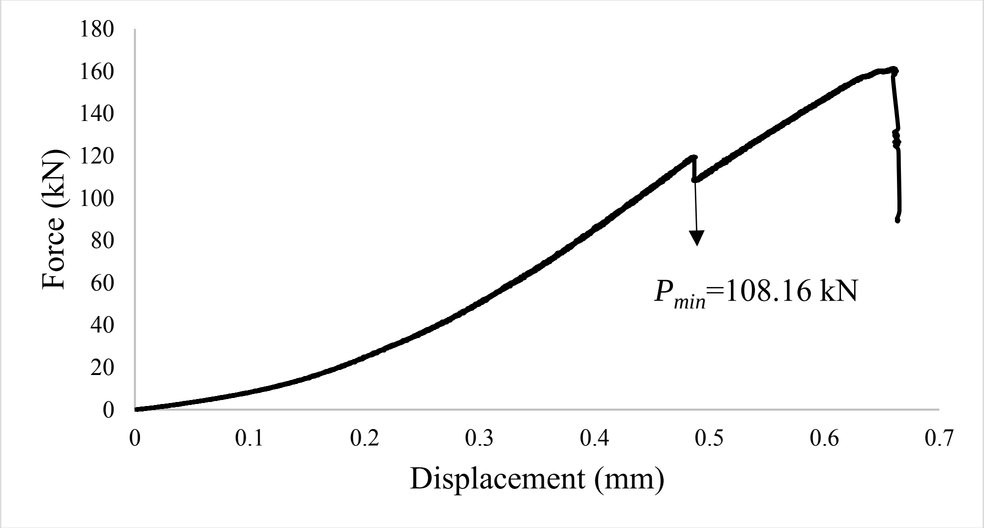

Figure A.37. Force versus displacement curve of A10038s2 specimen

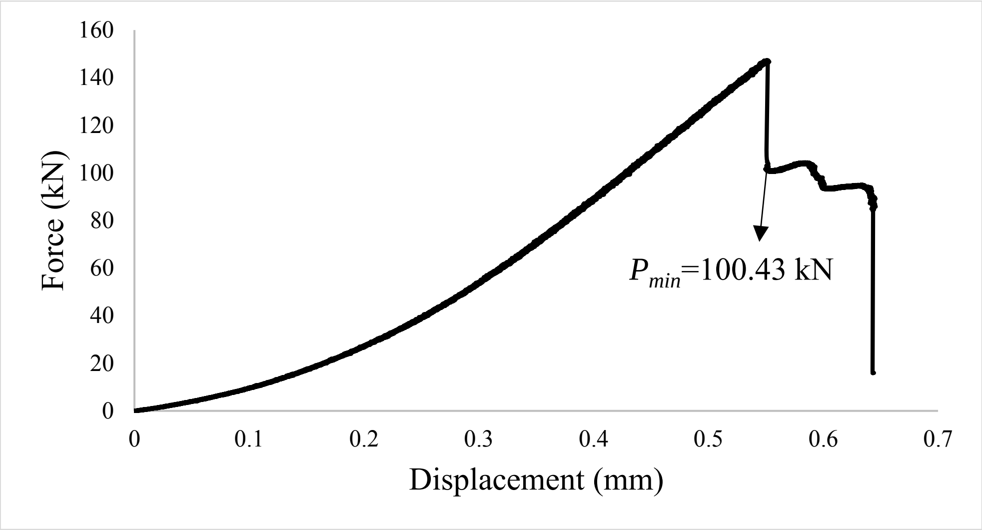

Figure A.38. Force versus displacement curve of A12518s1 specimen

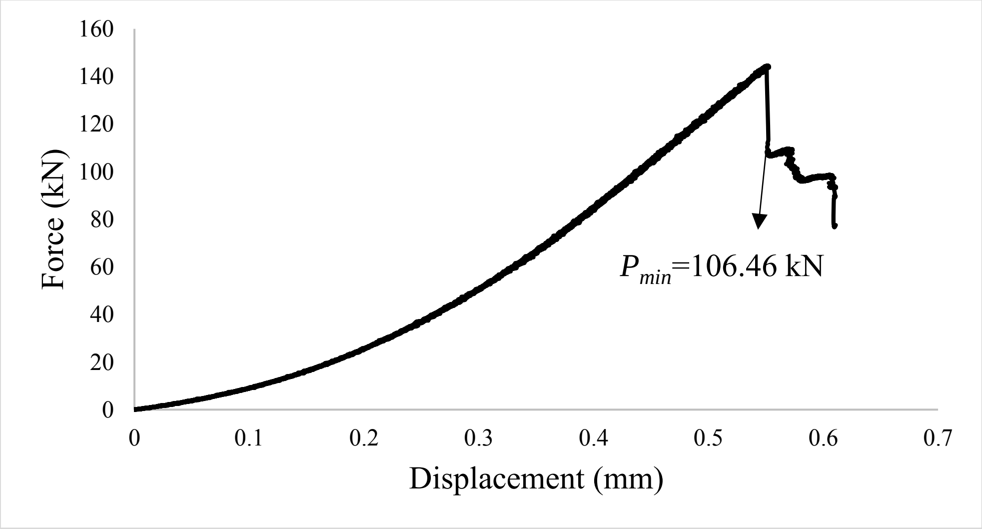

Figure A.39. Force versus displacement curve of A12520s1 specimen

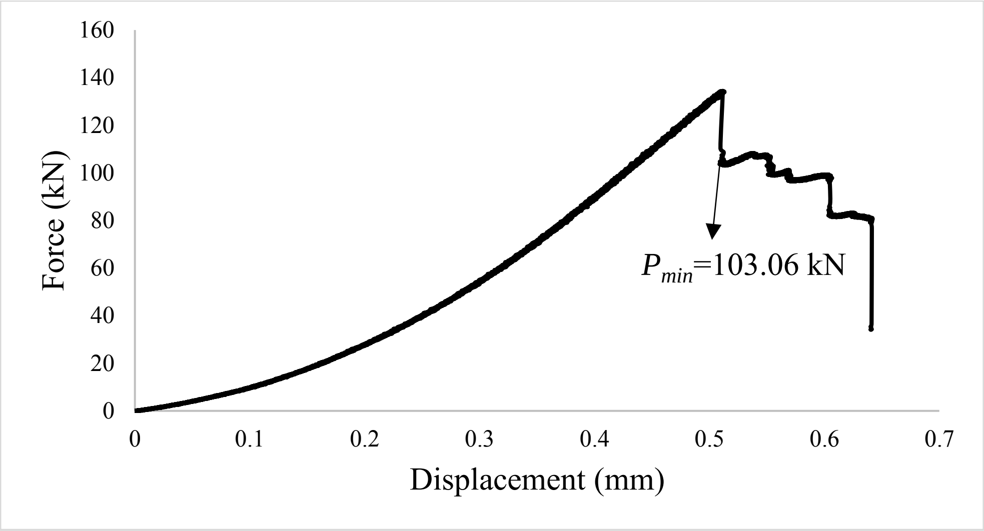

Figure A.40. Force versus displacement curve of A12520s2 specimen

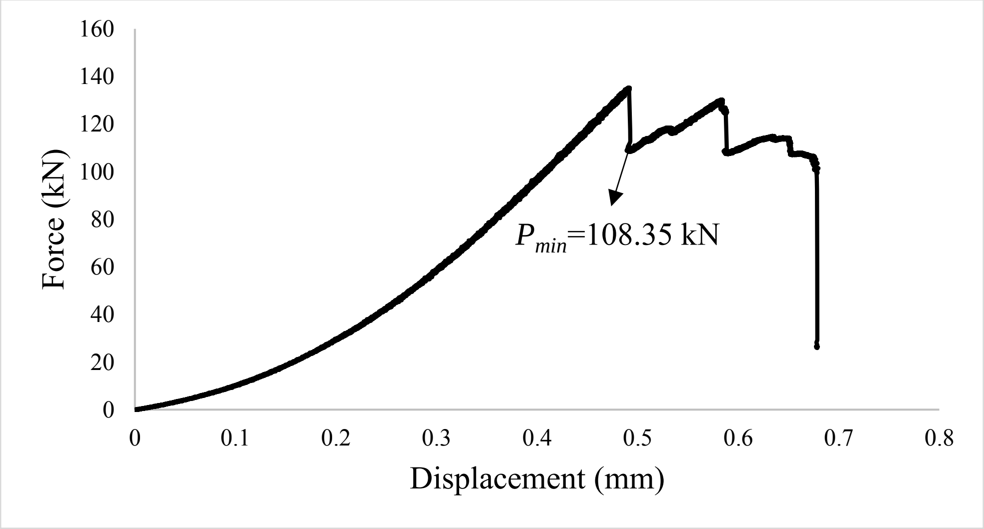

Figure A.41. Force versus displacement curve of A12524s1 specimen

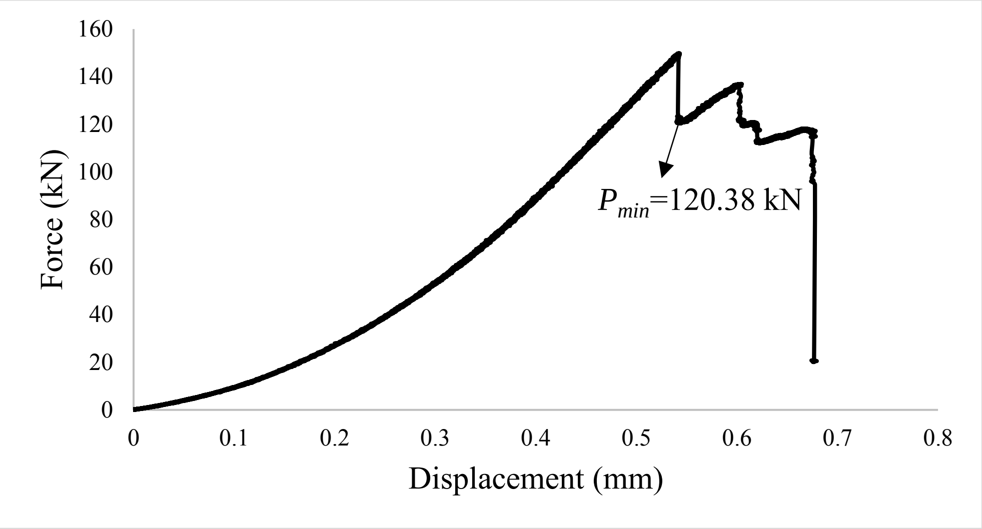

Figure A.42. Force versus displacement curve of A12524s2 specimen

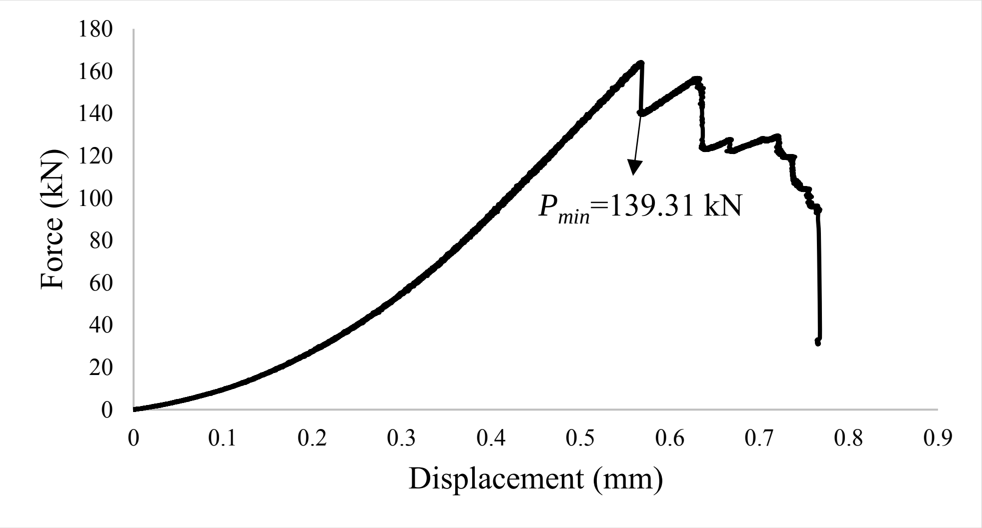

Figure A.43. Force versus displacement curve of A12528s1 specimen

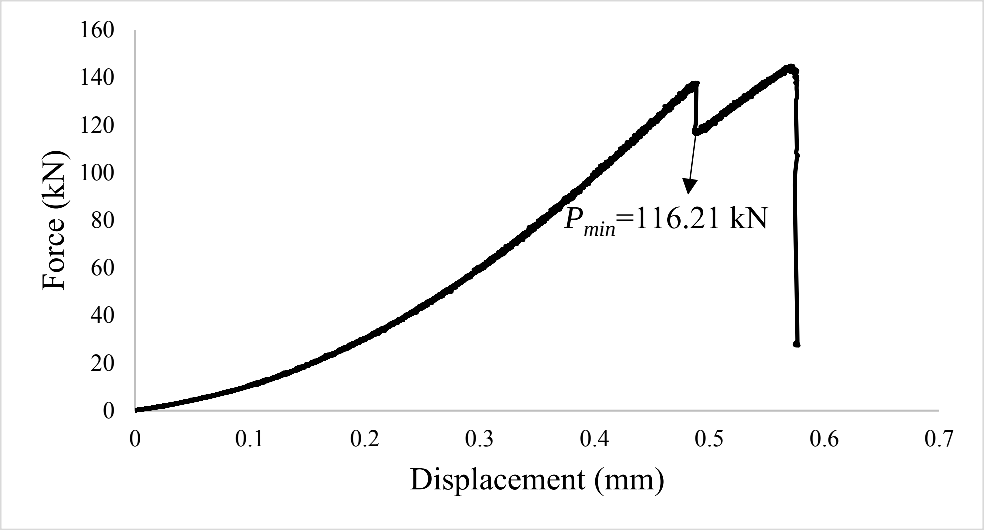

Figure A.44. Force versus displacement curve of A12528s2 specimen

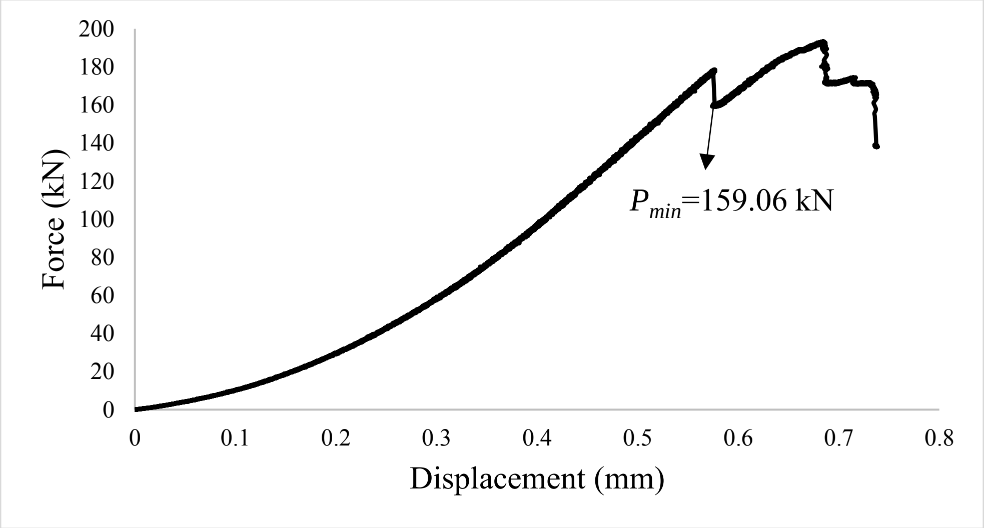

Figure A.45. Force versus displacement curve of A12534s1 specimen

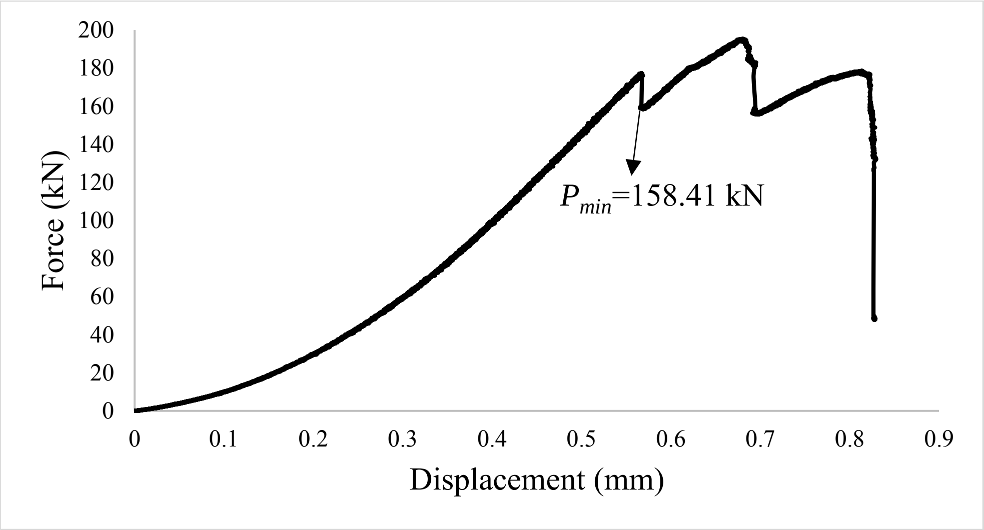

Figure A.46. Force versus displacement curve of A12534s2 specimen

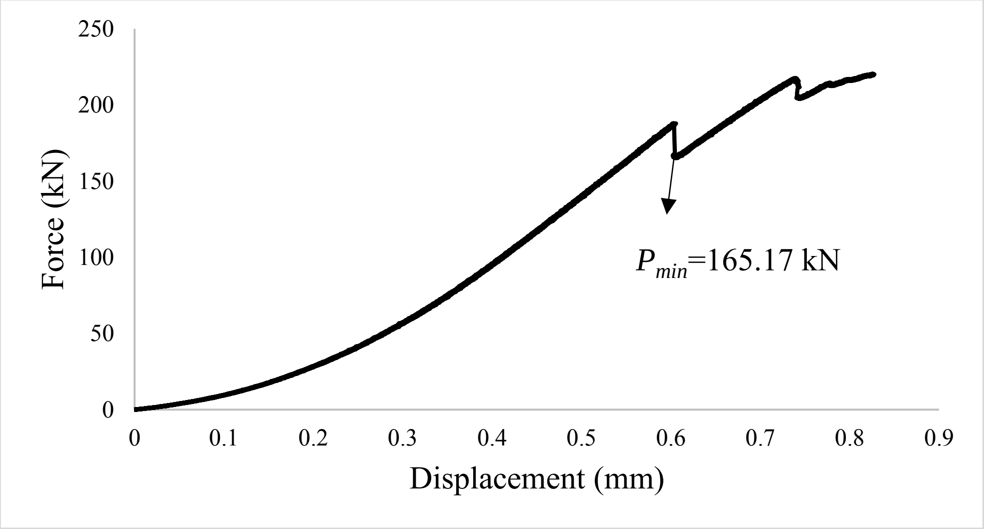

Figure A.47. Force versus displacement curve of A12536s1 specimen

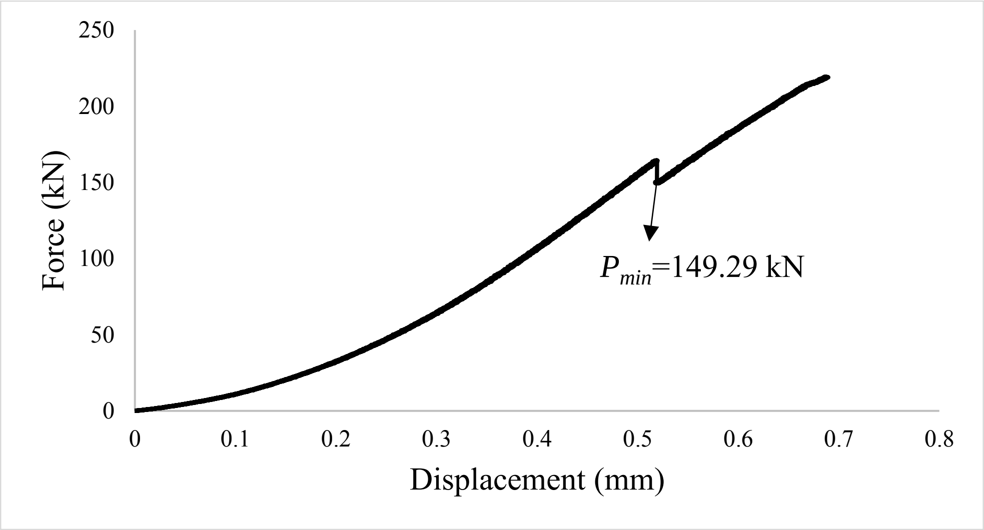

Figure A.48. Force versus displacement curve of A12538s1 specimen

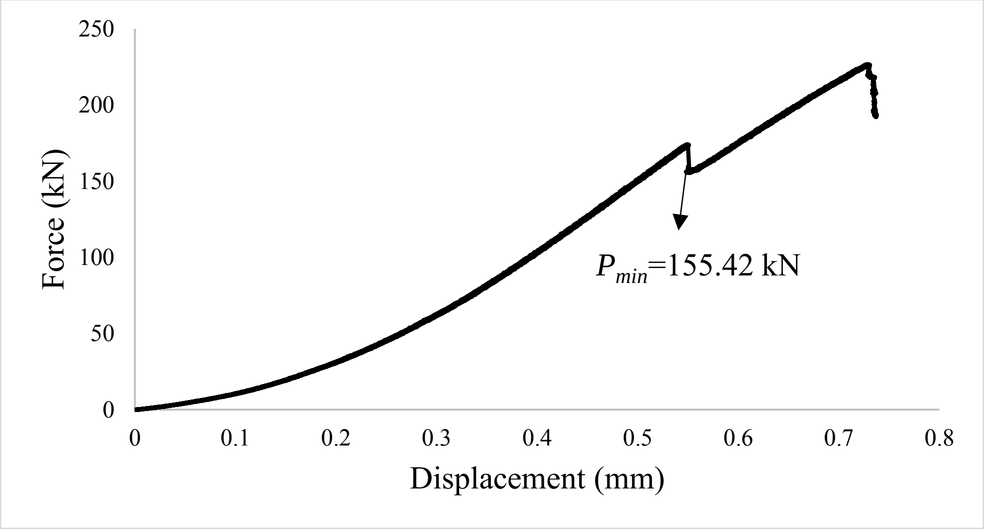

Figure A.49. Force versus displacement curve of A12538s2 specimen

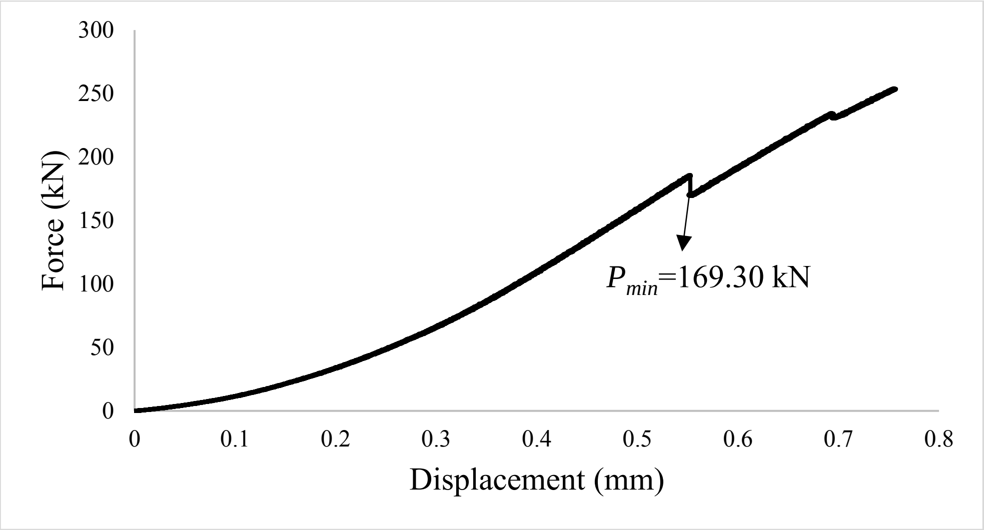

Figure A.50. Force versus displacement curve of A12542s1 specimen

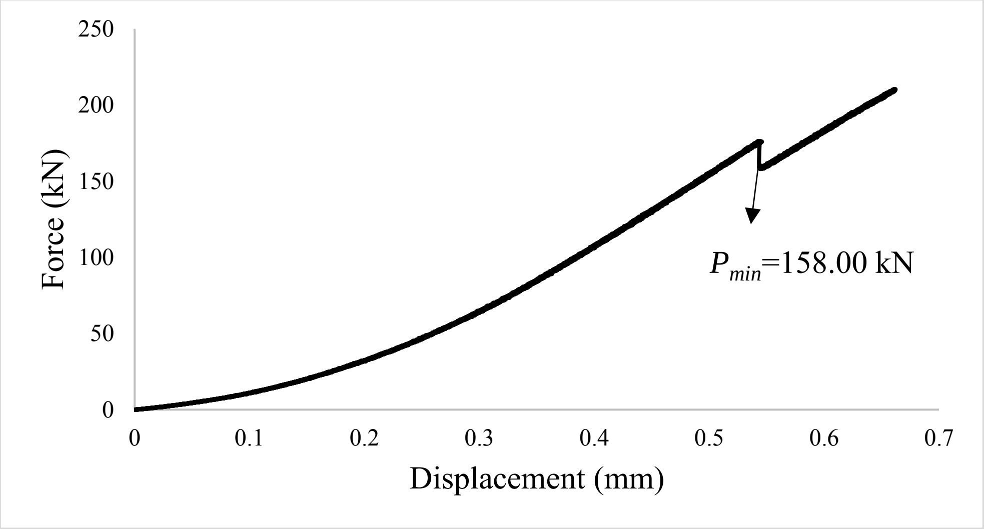

Figure A.51. Force versus displacement curve of A12542s2 specimen

B. EXPERIMENTALLY MEASURED CRITICAL CRACK LENGTHS OF TESTED SPECIMENS

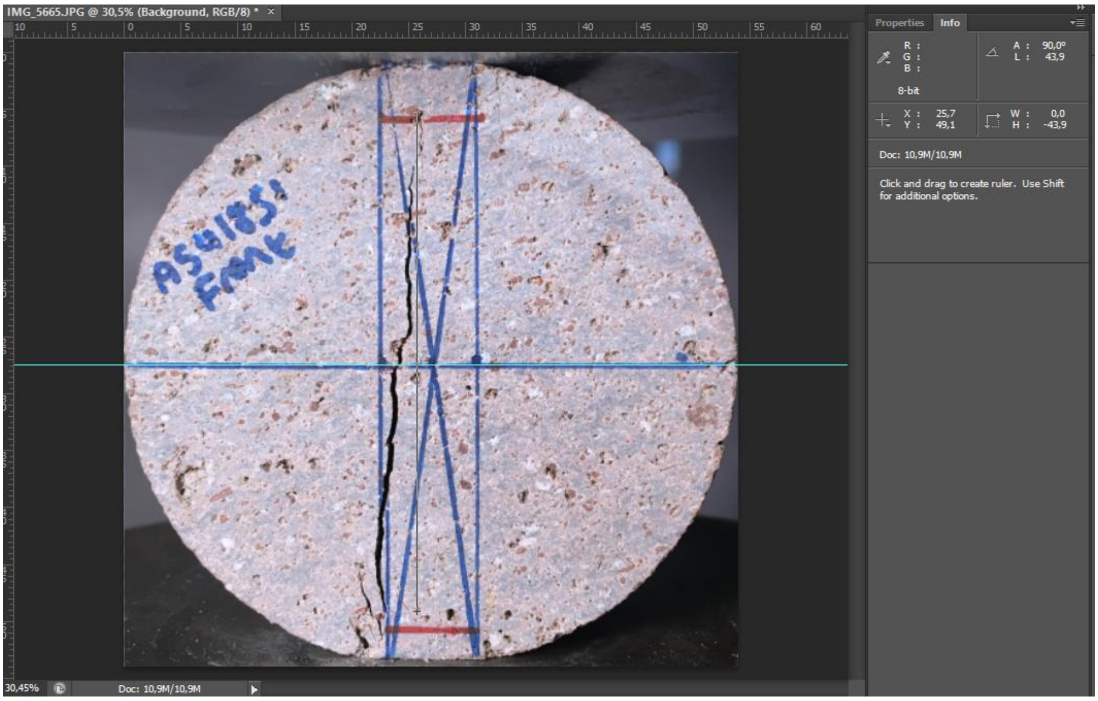

R :
G :
B :
8-bit
A : 90,0°
L : 43,9
X : 25,7
Y : 49,1
W : 0,0
H : -43,9
Doc: 10,9M/10,9M

Click and drag to create ruler. Use Shift for additional options.

Doc: 10,9M/10,9M

Figure B.1. Critical crack length measurement of A5418s1 coded specimen ($2a_{ce}$ =43.9 mm)

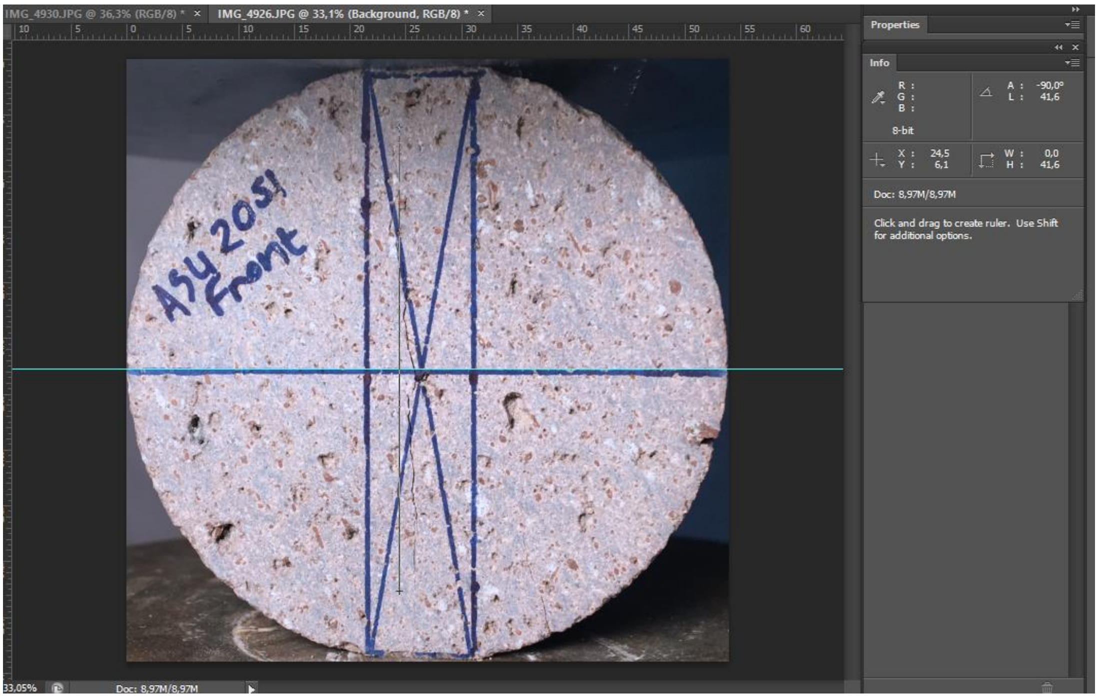

R :
G :
B :
8-bit

A : -90,0°
L : 41,6

X : 24,5
Y : 6,1

W : 0,0
H : 41,6

Doc: 8,97M/8,97M

Click and drag to create ruler. Use Shift for additional options.

Figure B.2. Critical crack length measurement of A5420s1 coded specimen ($2a_{ce}$ =41.6 mm)

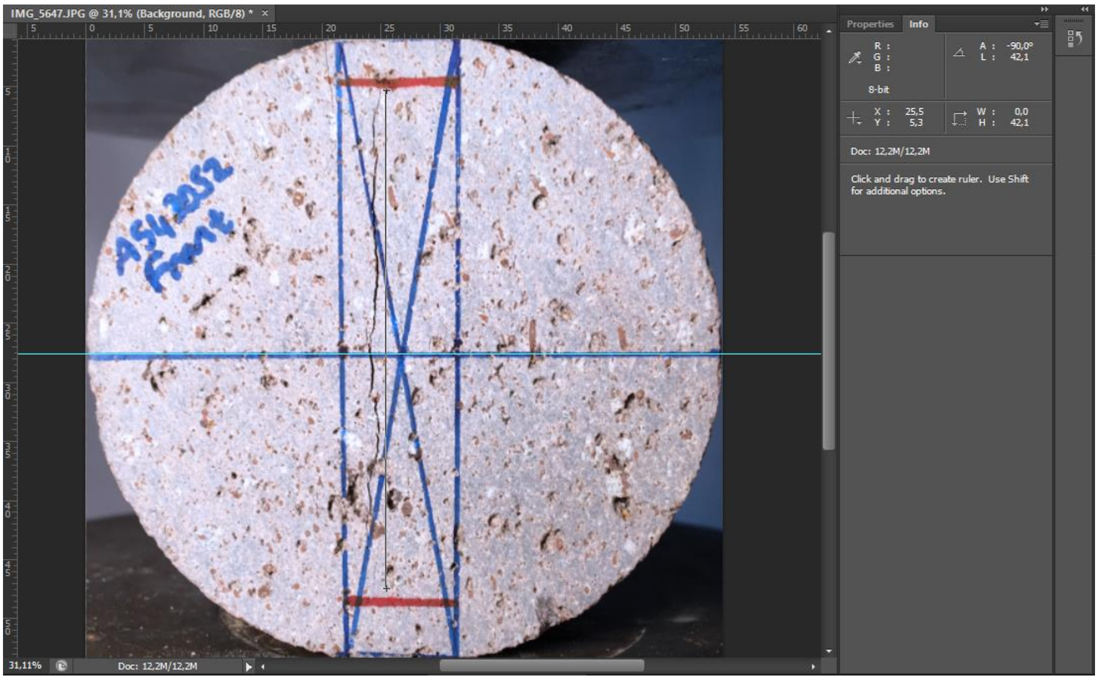

R :
G :
B :
8-bit

A : -90,0°
L : 42,1

X : 25,5
Y : 5,3

W : 0,0
H : 42,1

Doc: 12,2M/12,2M

Click and drag to create ruler. Use Shift for additional options.

Figure B.3. Critical crack length measurement of A5420s2 coded specimen ($2a_{ce}$ =42.1 mm)

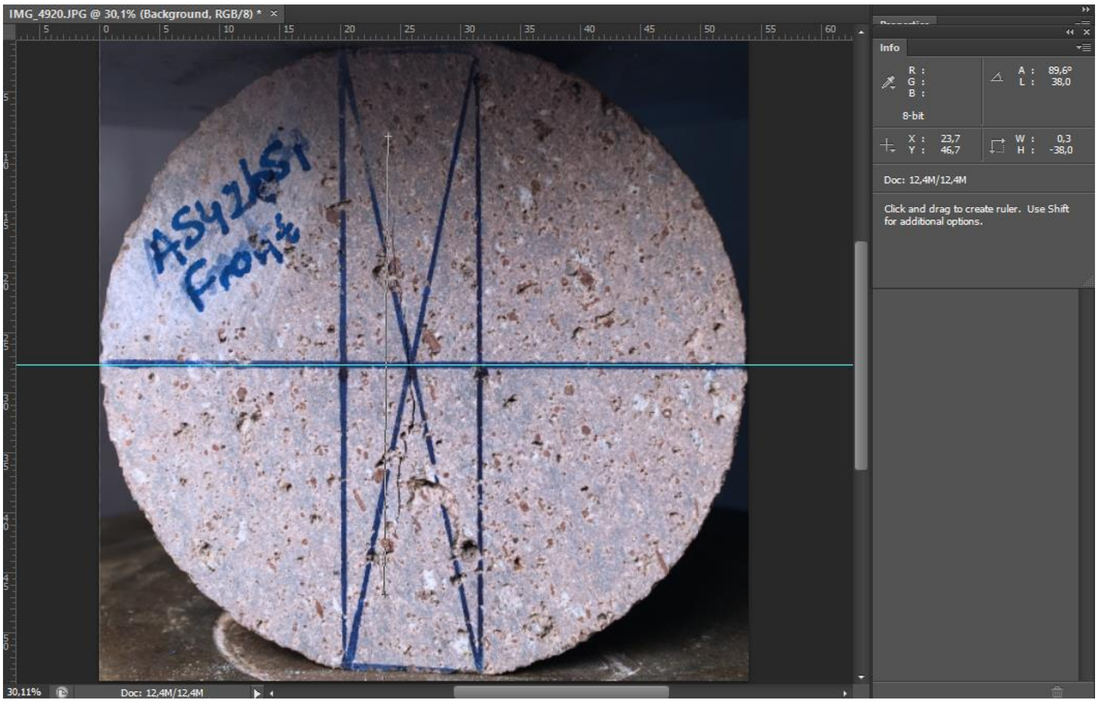
IMG_4920.JPG @ 30,1% (Background, RGB/8) *

Info

R :
G :
B :
8-bit

A : 89,6°
L : 38,0

X : 23,7
Y : 46,7

W : 0,3
H : -38,0

Doc: 12,4M/12,4M

Click and drag to create ruler. Use Shift for additional options.

30,11%

Figure B.4. Critical crack length measurement of A5426s1 coded specimen ($2a_{ce}$ =38.0 mm)

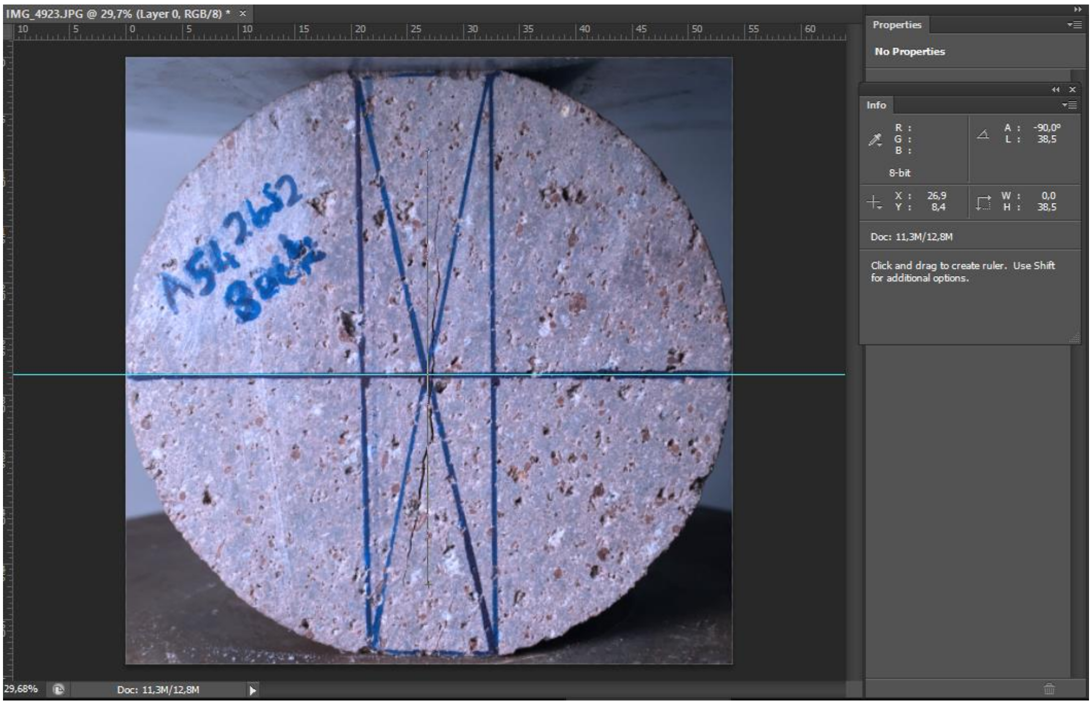
IMG_4923.JPG @ 29,7% (Layer 0, RGB/8) *

Properties

No Properties

Info

R :
G :
B :
8-bit

A : -90,0°
L : 38,5

X : 26,9
Y : 8,4

W : 0,0
H : 38,5

Doc: 11,3M/12,8M

Click and drag to create ruler. Use Shift for additional options.

29,68%

Figure B.5. Critical crack length measurement of A5426s2 coded specimen ($2a_{ce}$ =38.5 mm)

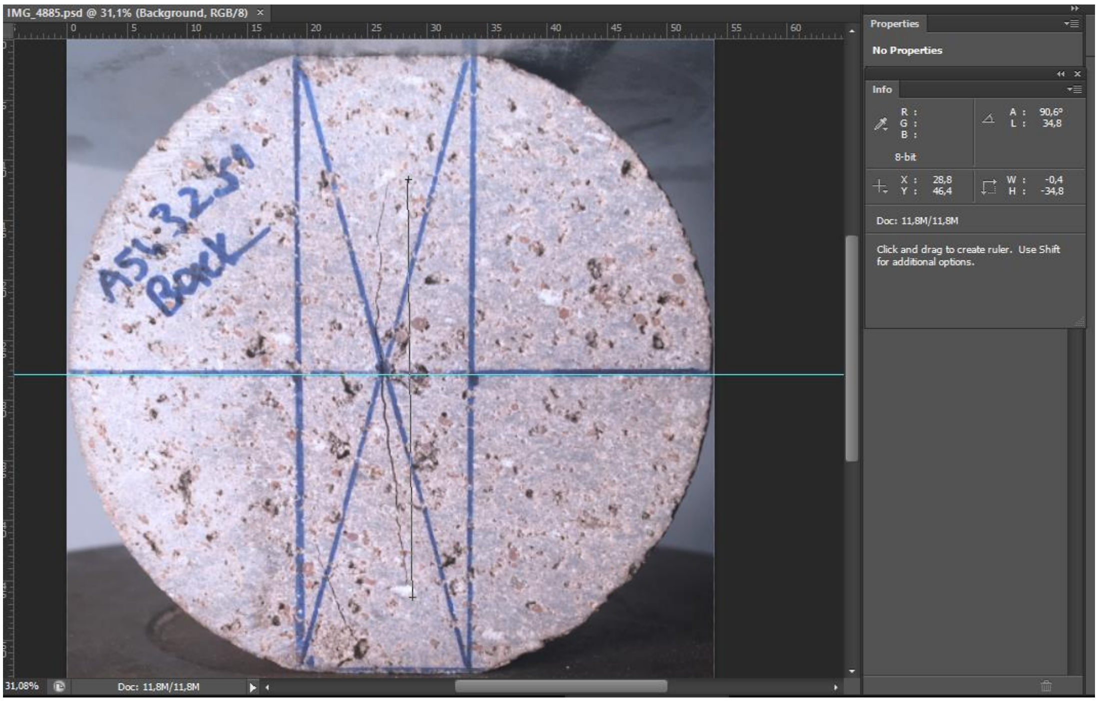

No Properties

R :
G :
B :
8-bit

A : 90,6°
L : 34,8

X : 28,8
Y : 46,4

W : -0,4
H : -34,8

Doc: 11,8M/11,8M

Click and drag to create ruler. Use Shift for additional options.

Figure B.6. Critical crack length measurement of A5432s1 coded specimen ($2a_{ce}$ =34.8 mm)

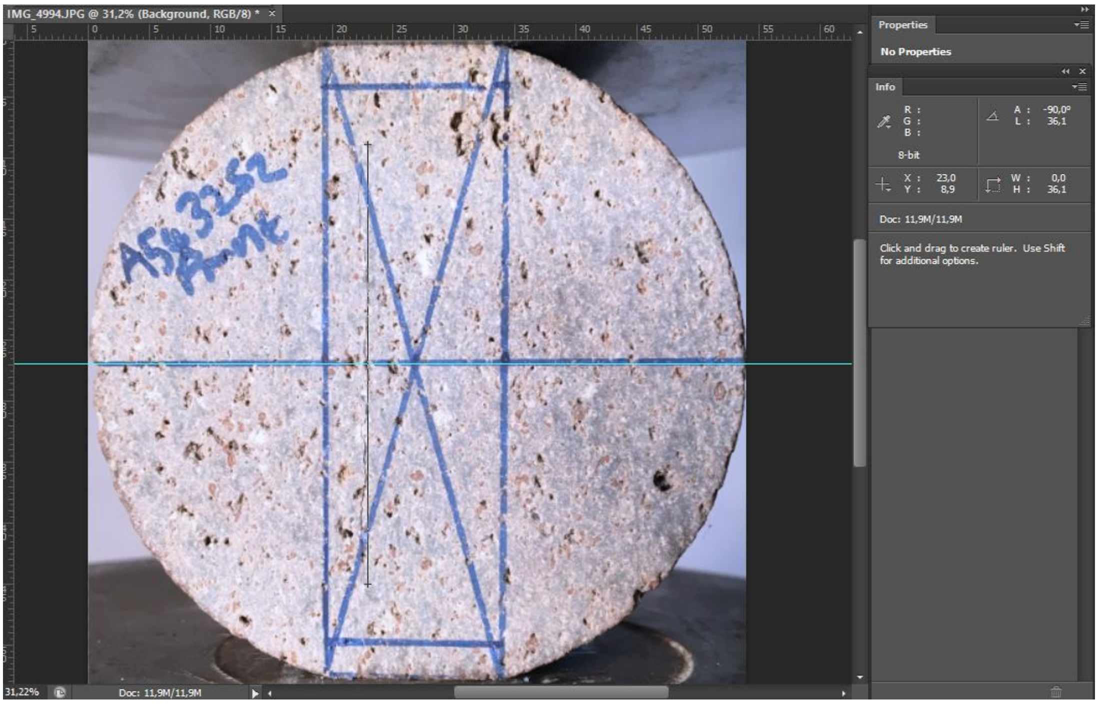

No Properties

R :
G :
B :
8-bit

A : -90,0°
L : 36,1

X : 23,0
Y : 8,9

W : 0,0
H : 36,1

Doc: 11,9M/11,9M

Click and drag to create ruler. Use Shift for additional options.

Figure B.7. Critical crack length measurement of A5432s2 coded specimen ($2a_{ce}$ =36.1 mm)

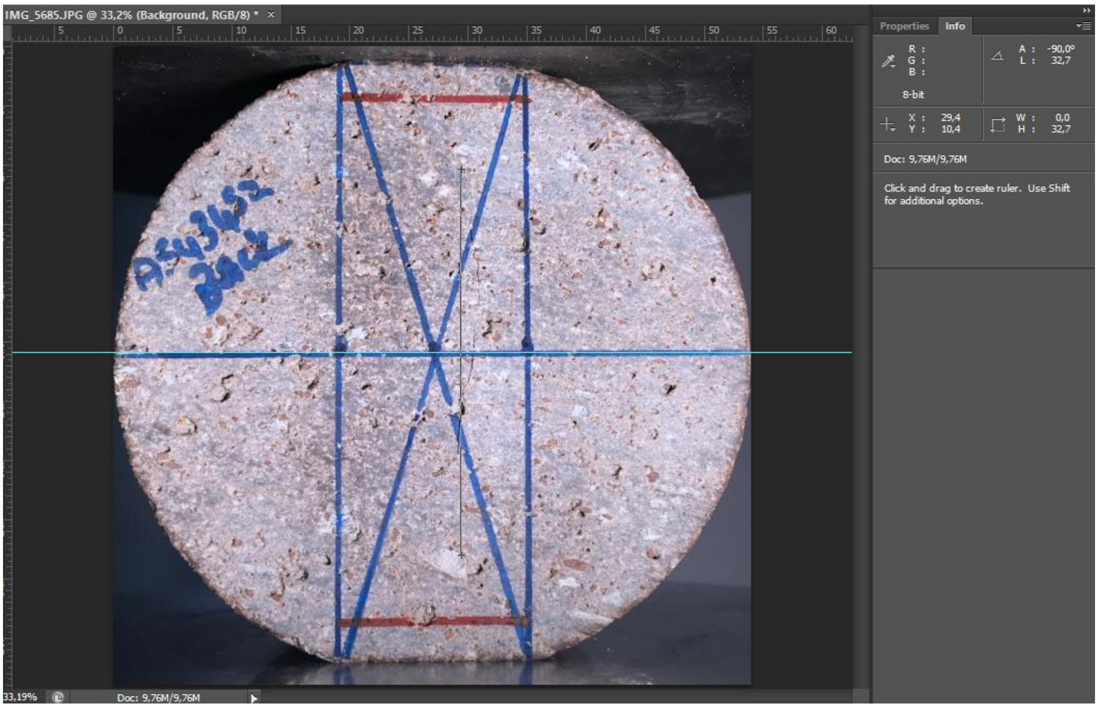

R :
G :
B :
8-bit
A : -90,0°
L : 32,7
X : 29,4
Y : 10,4
W : 0,0
H : 32,7
Doc: 9,76M/9,76M

Click and drag to create ruler. Use Shift for additional options.

Figure B.8. Critical crack length measurement of A5434s1 coded specimen ($2a_{ce}$ =32.7 mm)

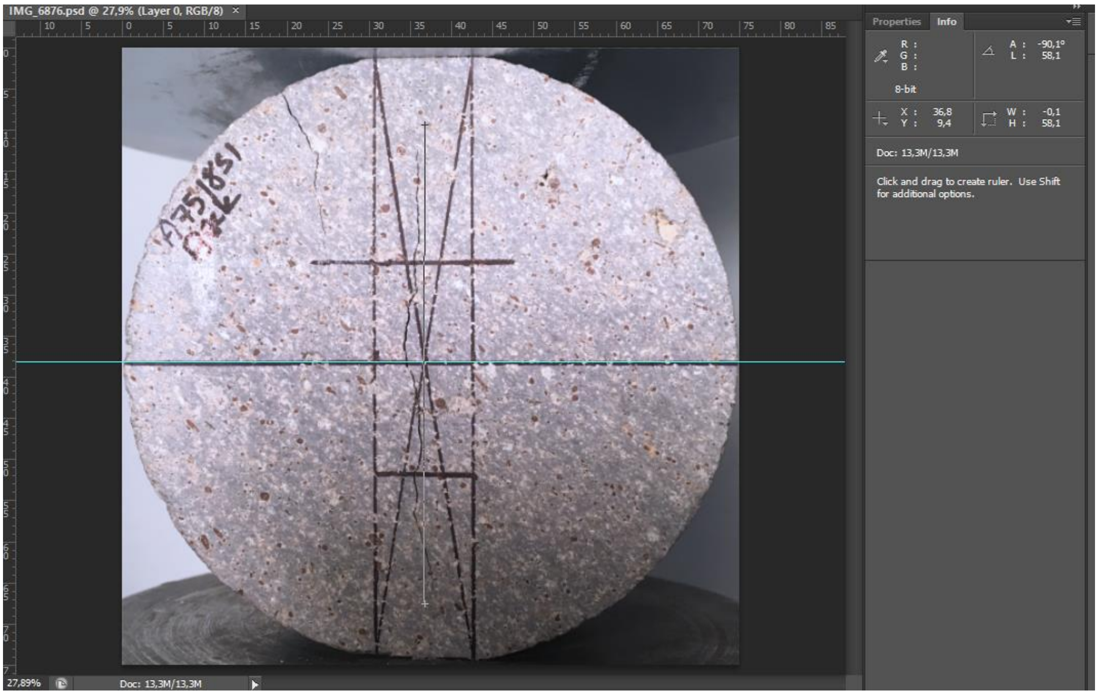

R :
G :
B :
8-bit
A : -90,1°
L : 58,1
X : 36,8
Y : 9,4
W : -0,1
H : 58,1
Doc: 13,3M/13,3M

Click and drag to create ruler. Use Shift for additional options.

Figure B.9. Critical crack length measurement of A7518s1 coded specimen $2a_{ce}$ =58.1 mm)

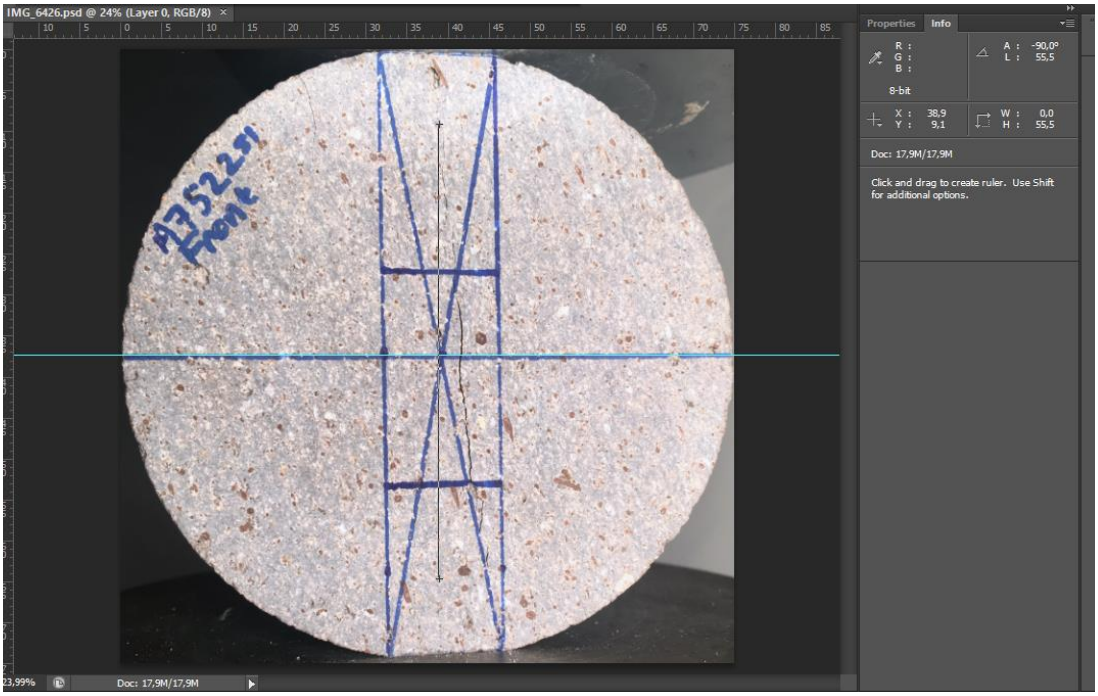

R :
G :
B :
8-bit

A : -90,0°
L : 55,5

X : 38,9
Y : 9,1

W : 0,0
H : 55,5

Doc: 17,9M/17,9M

Click and drag to create ruler. Use Shift for additional options.

Figure B.10. Critical crack length measurement of A7522s1 coded specimen ($2a_{ce}$ =55.5 mm)

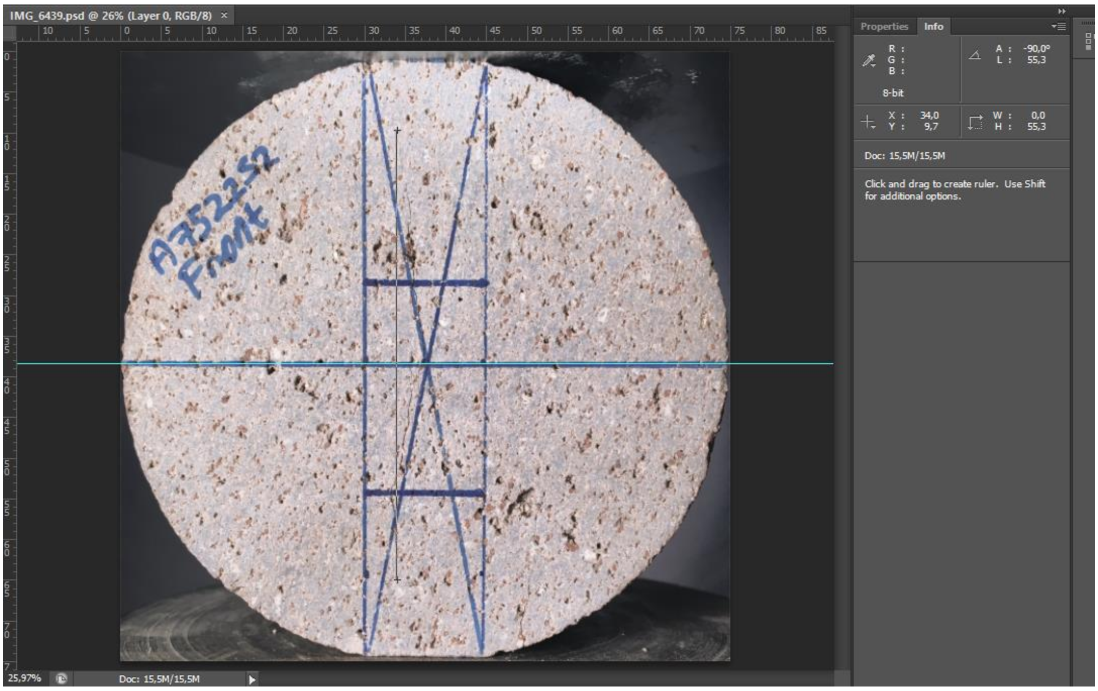

R :
G :
B :
8-bit

A : -90,0°
L : 55,3

X : 34,0
Y : 9,7

W : 0,0
H : 55,3

Doc: 15,5M/15,5M

Click and drag to create ruler. Use Shift for additional options.

Figure B.11. Critical crack length measurement of A7522s2 coded specimen ($2a_{ce}$ =55.3 mm)

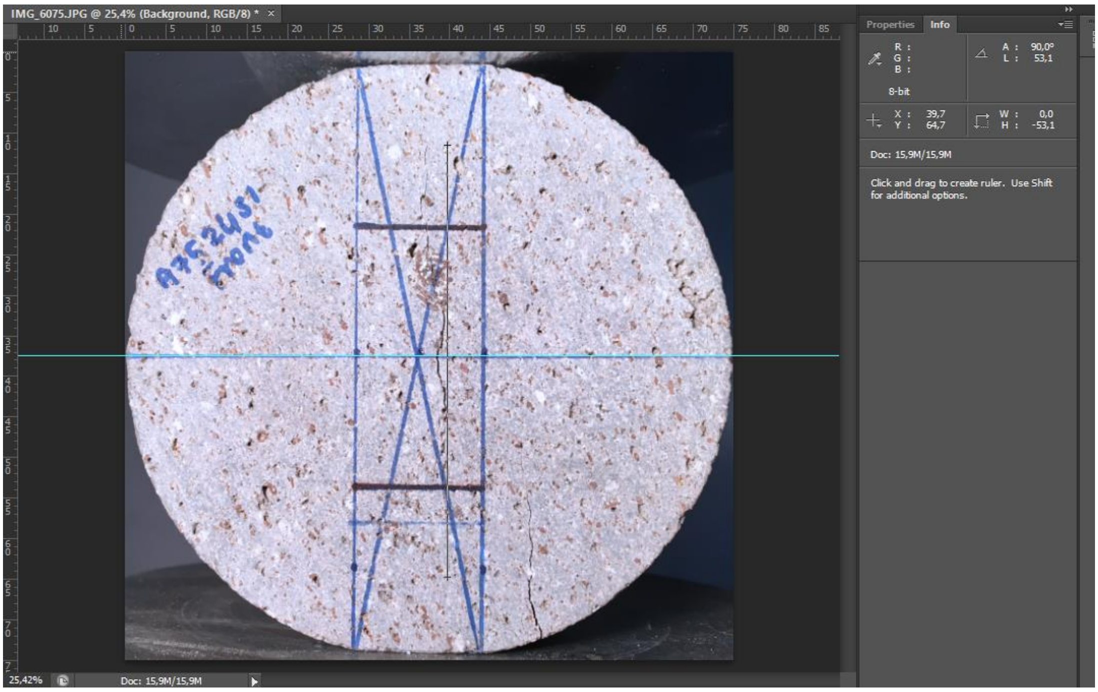

A : 90,0°
L : 53,1
8-bit
X : 39,7
Y : 64,7
W : 0,0
H : -53,1
Doc: 15,9M/15,9M

Click and drag to create ruler. Use Shift for additional options.

Figure B.12. Critical crack length measurement of A7524s1 coded specimen ($2a_{ce}$ =53.1 mm)

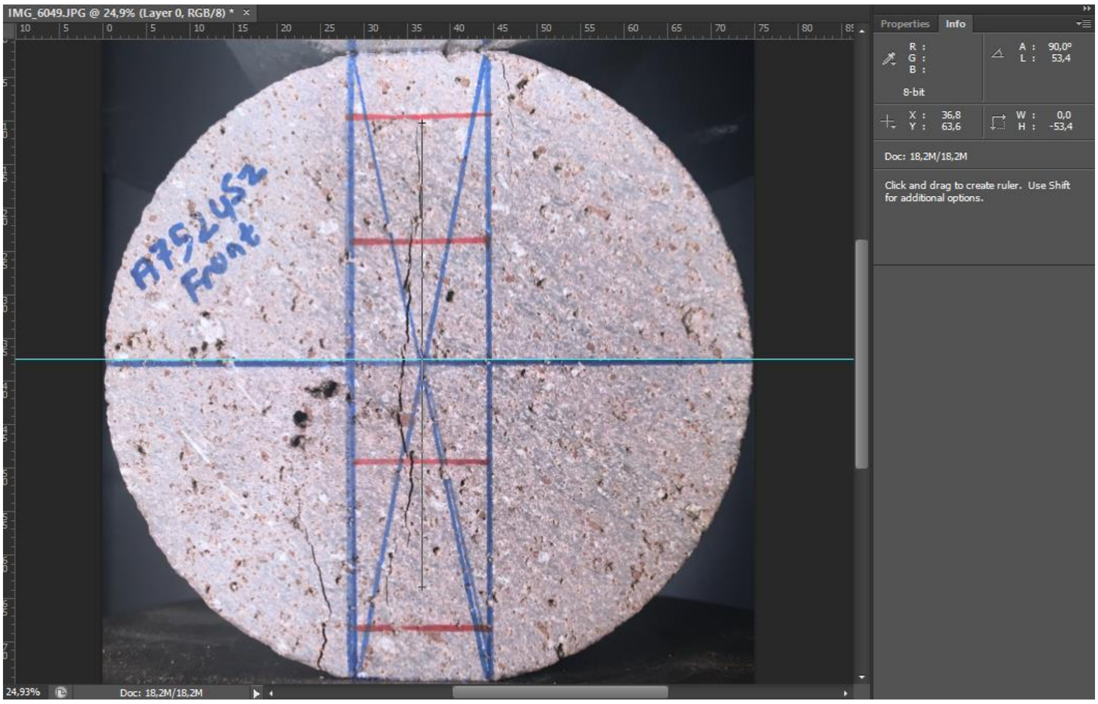

A : 90,0°
L : 53,4
8-bit
X : 36,8
Y : 63,6
W : 0,0
H : -53,4
Doc: 18,2M/18,2M

Click and drag to create ruler. Use Shift for additional options.

Figure B.13. Critical crack length measurement of A7524s2 coded specimen ($2a_{ce}$ =53.4 mm)

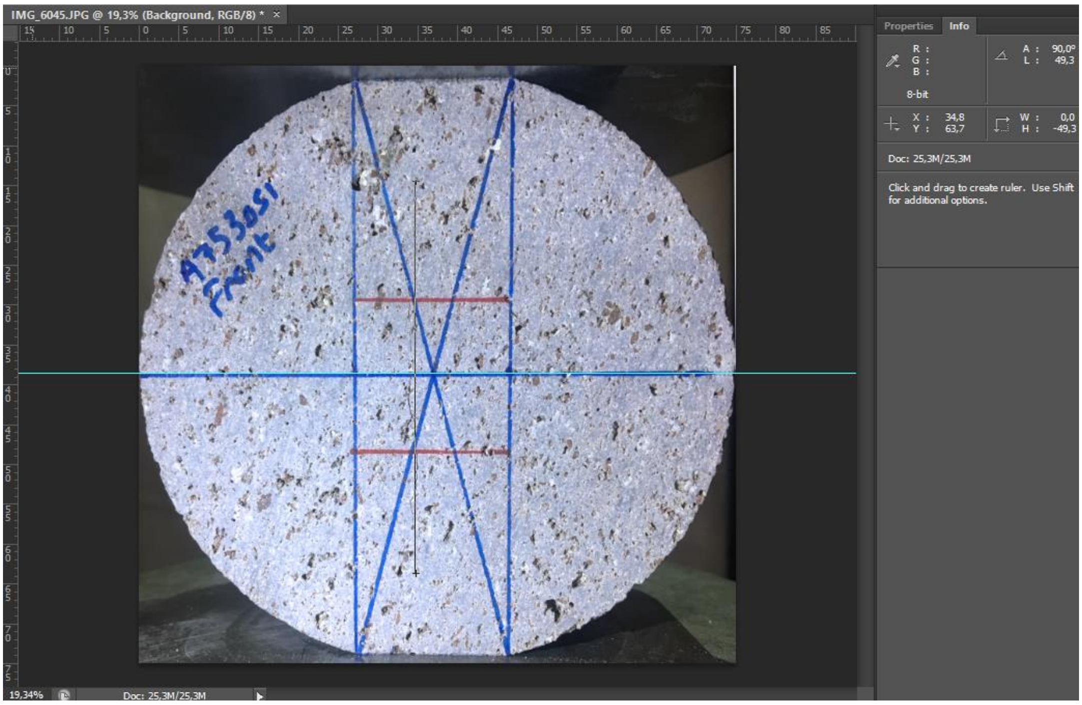

R :
G :
B :
8-bit

A : 90,0°
L : 49,3

X : 34,8
Y : 63,7

W : 0,0
H : -49,3

Doc: 25,3M/25,3M

Click and drag to create ruler. Use Shift for additional options.

Figure B.14. Critical crack length measurement of A7530s1 coded specimen ($2a_{ce}$ =49.3 mm)

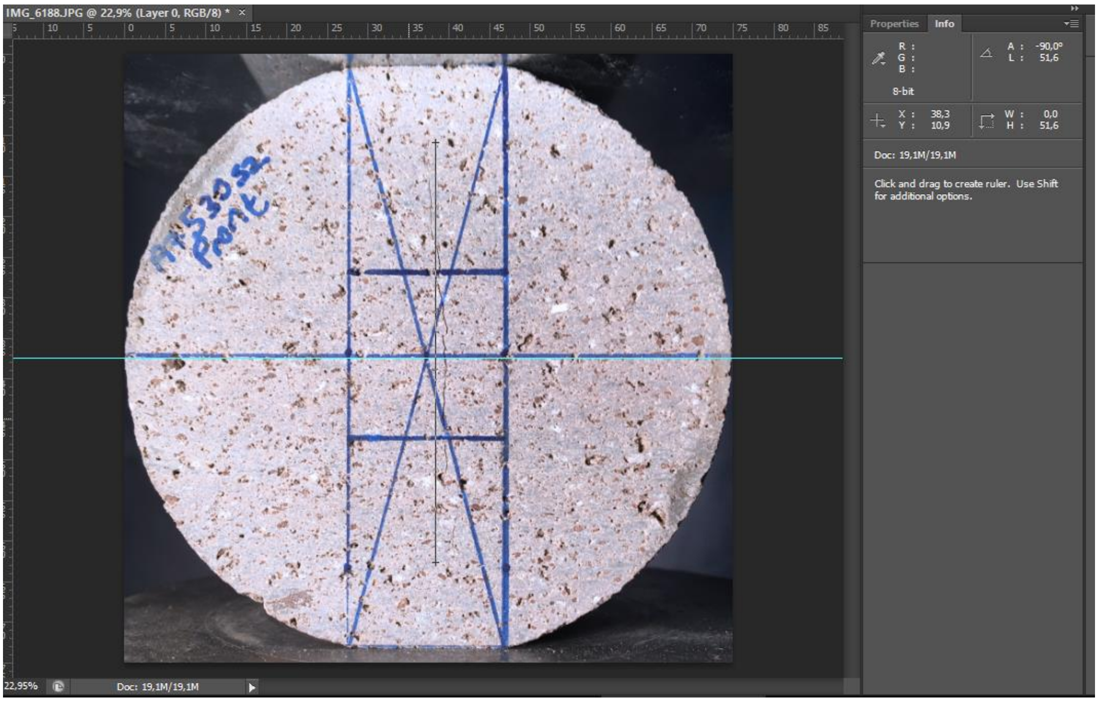

R :
G :
B :
8-bit

A : -90,0°
L : 51,6

X : 38,3
Y : 10,9

W : 0,0
H : 51,6

Doc: 19,1M/19,1M

Click and drag to create ruler. Use Shift for additional options.

Figure B.15. Critical crack length measurement of A7530s2 coded specimen ($2a_{ce}$ =51.6 mm)

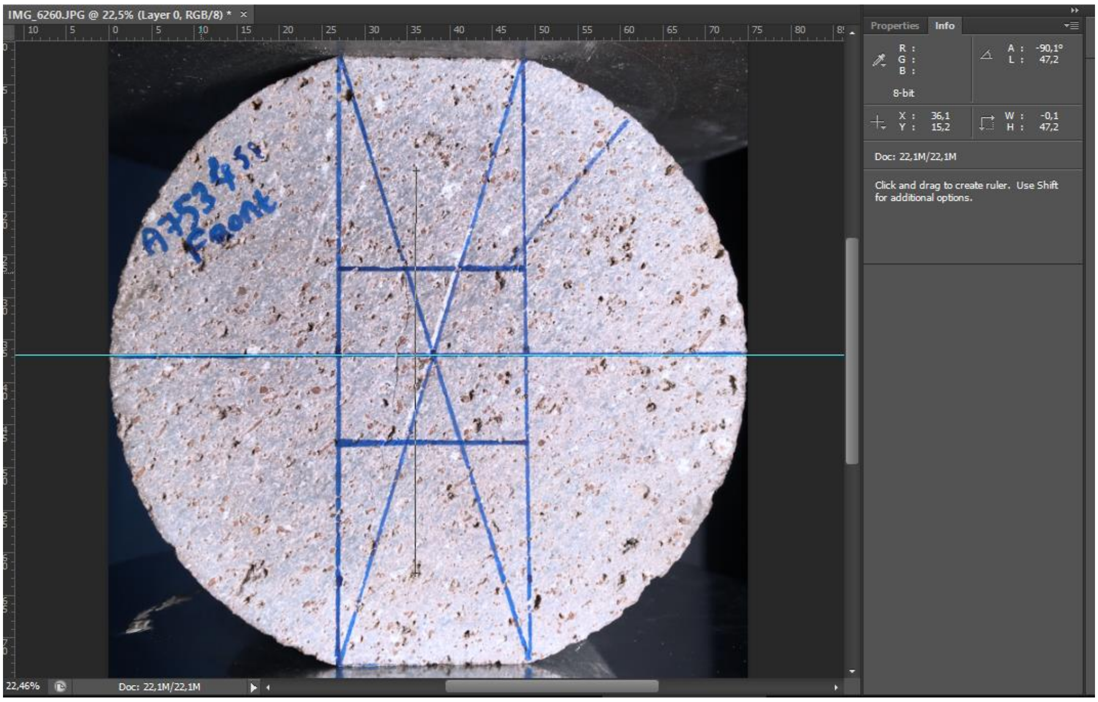

R :
G :
B :
8-bit
A : -90,1°
L : 47,2
X : 36,1
Y : 15,2
W : -0,1
H : 47,2
Doc: 22,1M/22,1M

Click and drag to create ruler. Use Shift for additional options.

Figure B.16. Critical crack length measurement of A7534s1 coded specimen ($2a_{ce}$ =47.2 mm)

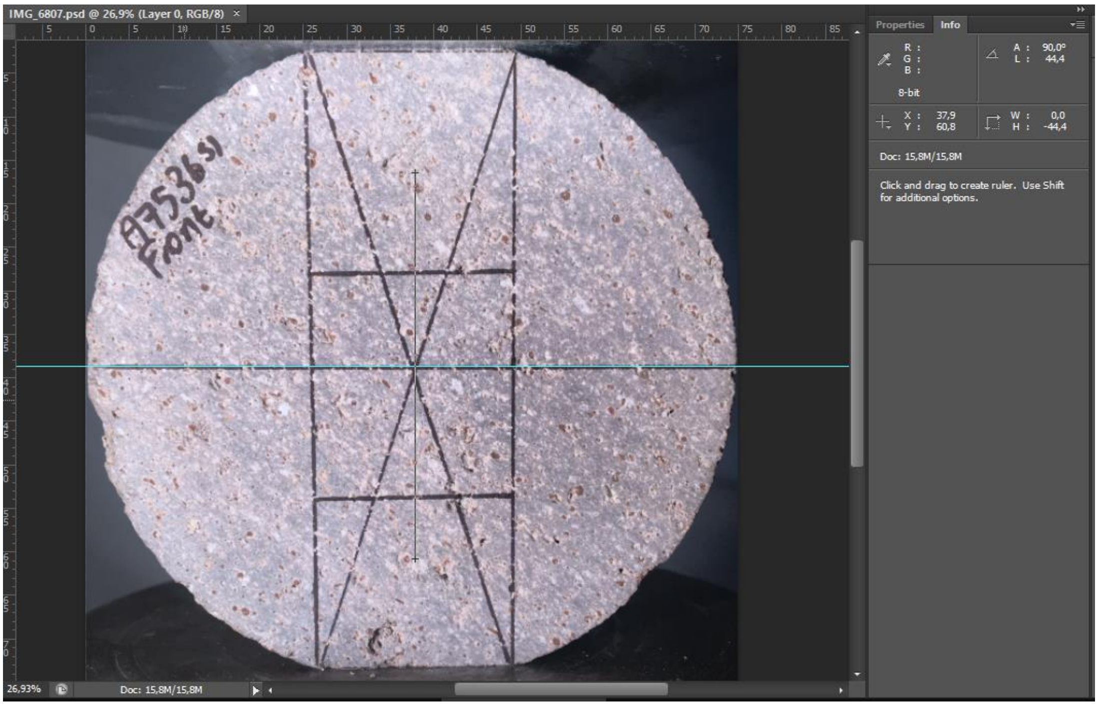

R :
G :
B :
8-bit
A : 90,0°
L : 44,4
X : 37,9
Y : 60,8
W : 0,0
H : -44,4
Doc: 15,8M/15,8M

Click and drag to create ruler. Use Shift for additional options.

Figure B.17. Critical crack length measurement of A7536s1 coded specimen ($2a_{ce}$ =44.4 mm)

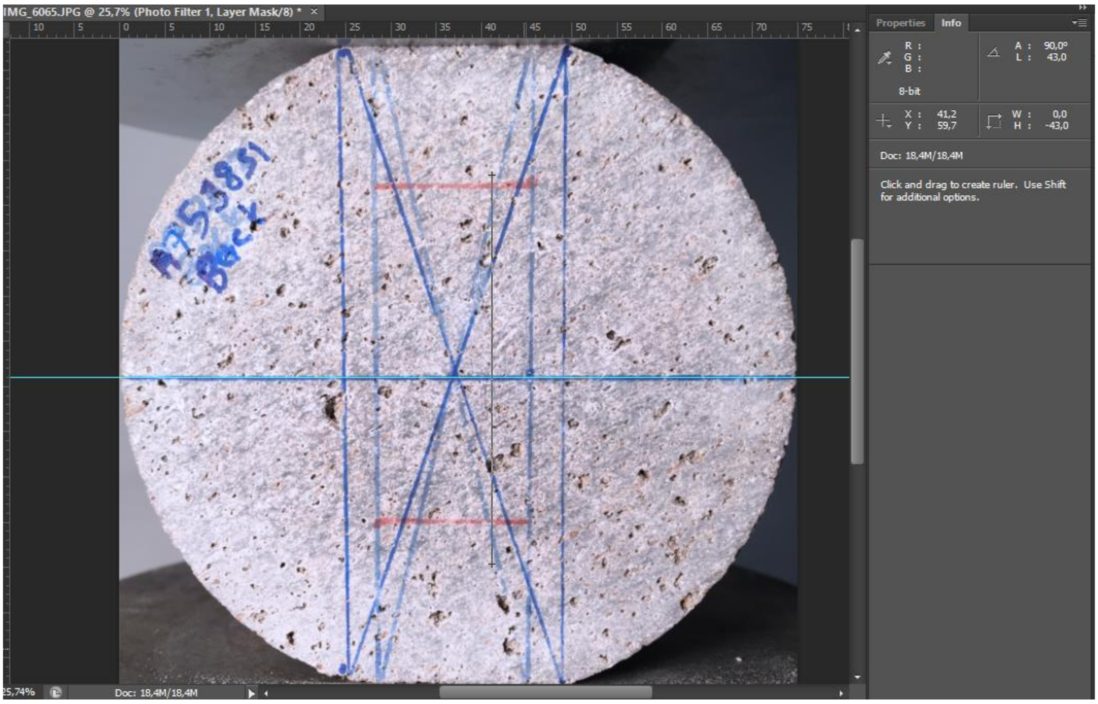

R :
G :
B :
8-bit

A : 90,0°
L : 43,0

X : 41,2
Y : 59,7

W : 0,0
H : -43,0

Doc: 18,4M/18,4M

Click and drag to create ruler. Use Shift for additional options.

Figure B.18. Critical crack length measurement of A7538s1 coded specimen ($2a_{ce}$ =43.0 mm)

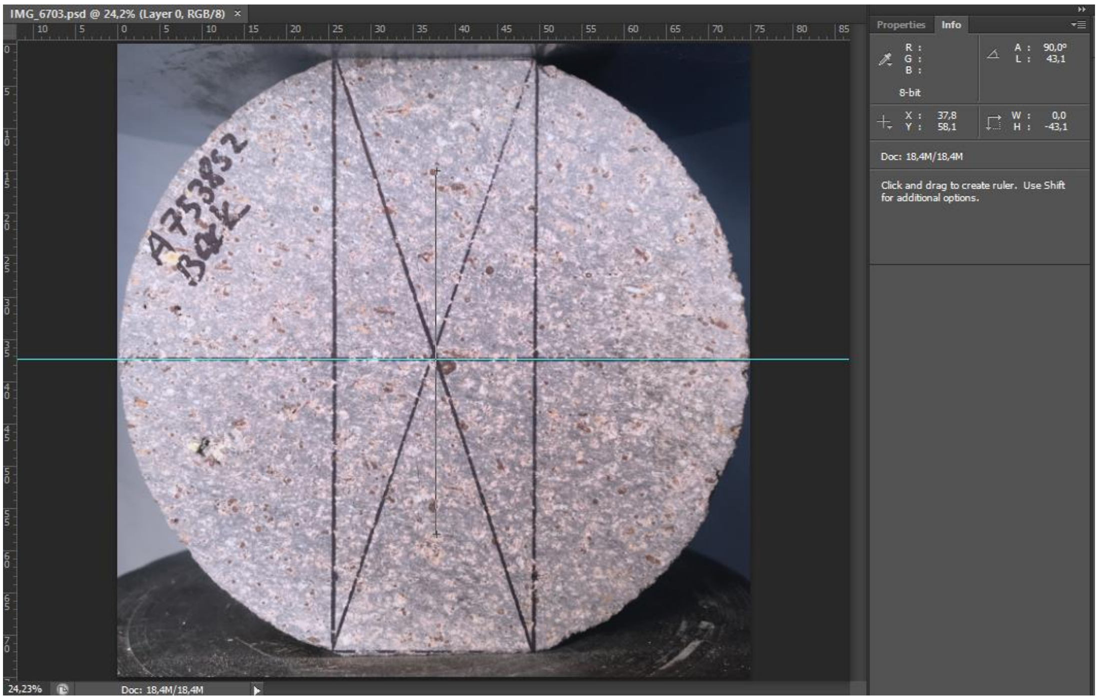

R :
G :
B :
8-bit

A : 90,0°
L : 43,1

X : 37,8
Y : 58,1

W : 0,0
H : -43,1

Doc: 18,4M/18,4M

Click and drag to create ruler. Use Shift for additional options.

Figure B.19. Critical crack length measurement of A7538s2 coded specimen ($2a_{ce}$ =43.1 mm)

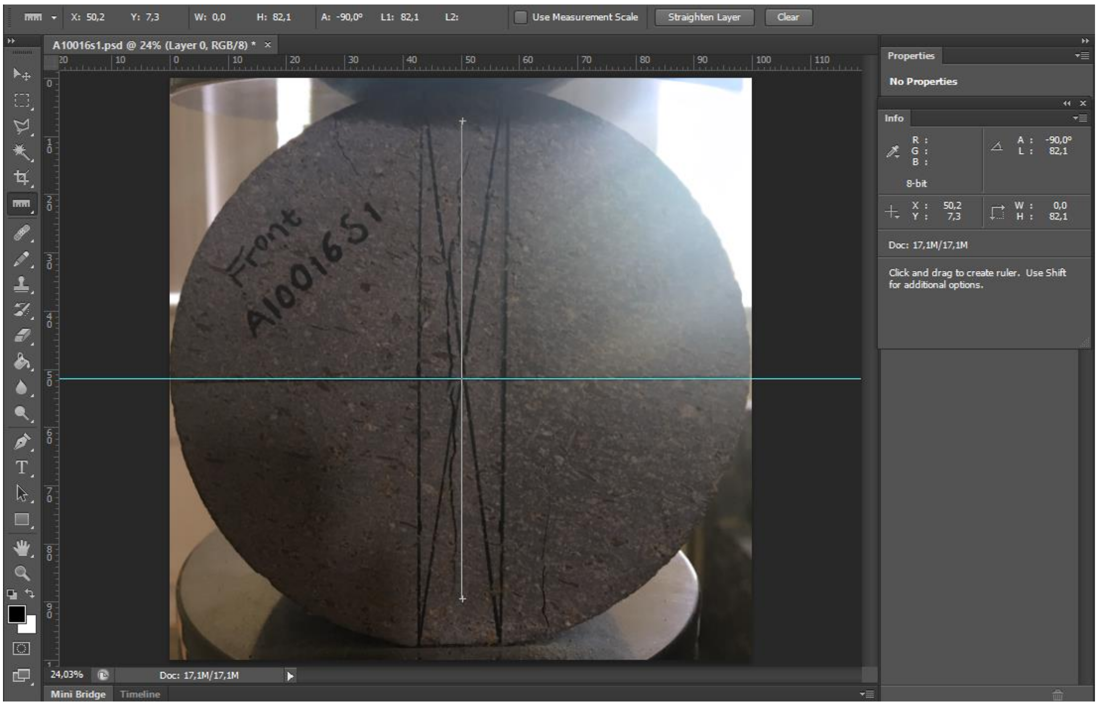

Figure B.20. Critical crack length measurement of A10016s1 coded specimen ($2a_{ce}$ =82.1 mm)

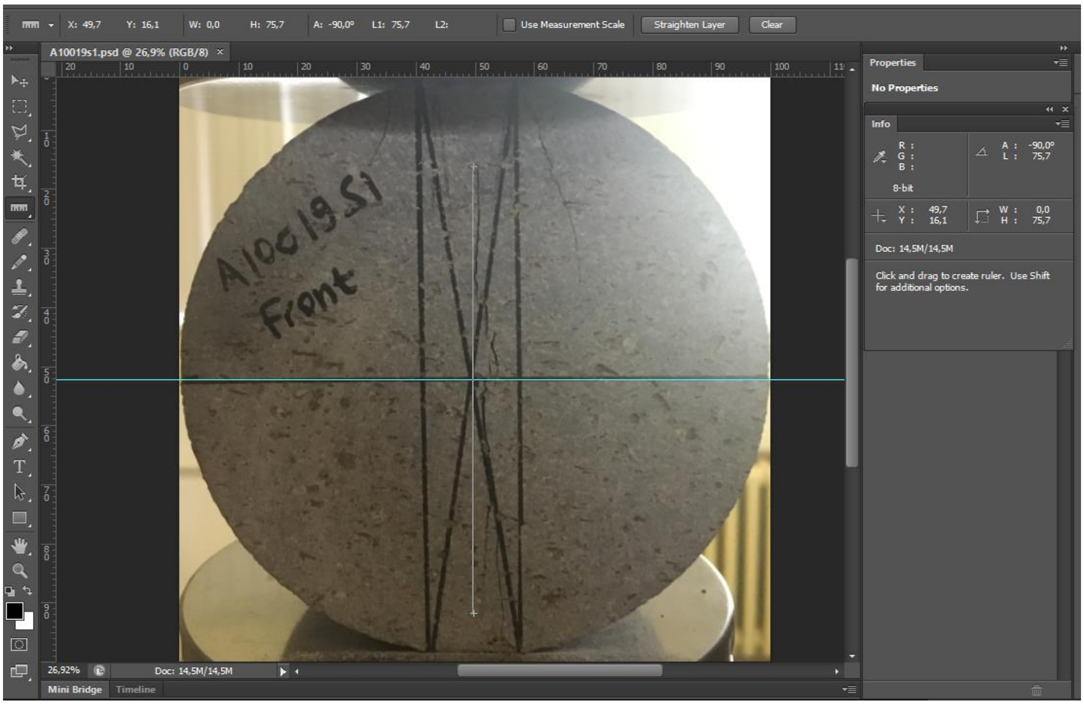

Figure B.21. Critical crack length measurement of A10019s1 coded specimen $2a_{ce}$ =75.7 mm)

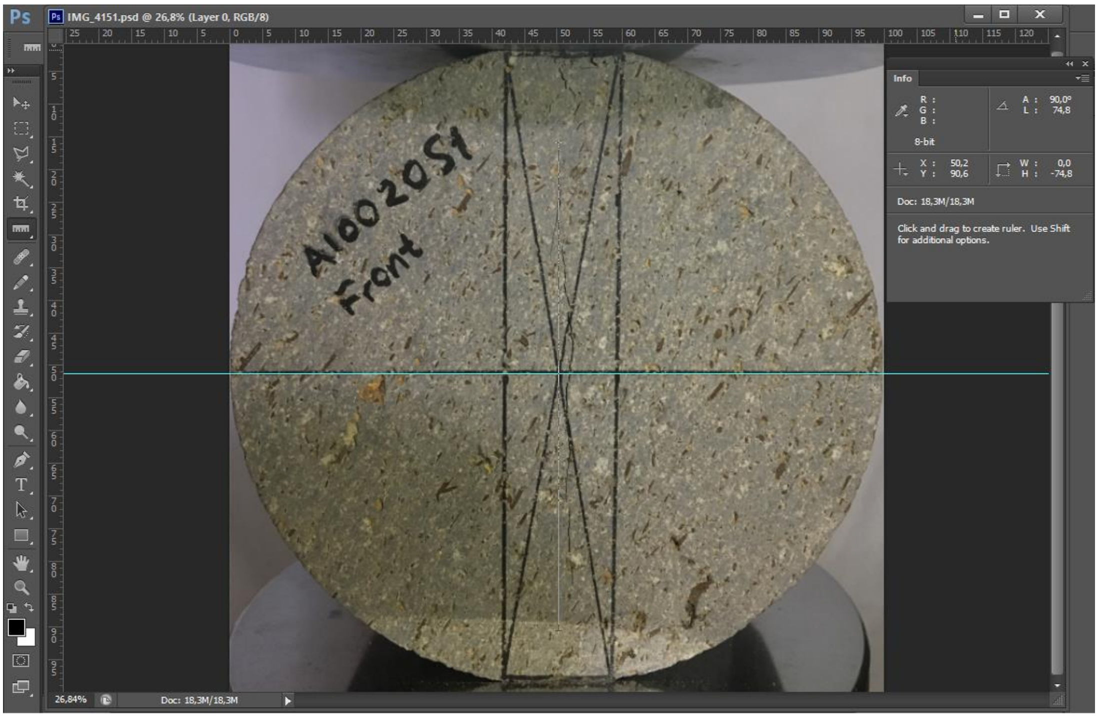

R :
G :
B :
8-bit
A : 90,0°
L : 74,8
X : 50,2
Y : 90,6
W : 0,0
H : -74,8
Doc: 18,3M/18,3M

Click and drag to create ruler. Use Shift for additional options.

Figure B.22. Critical crack length measurement of A10020s1 coded specimen ($2a_{ce}$ =74.8 mm)

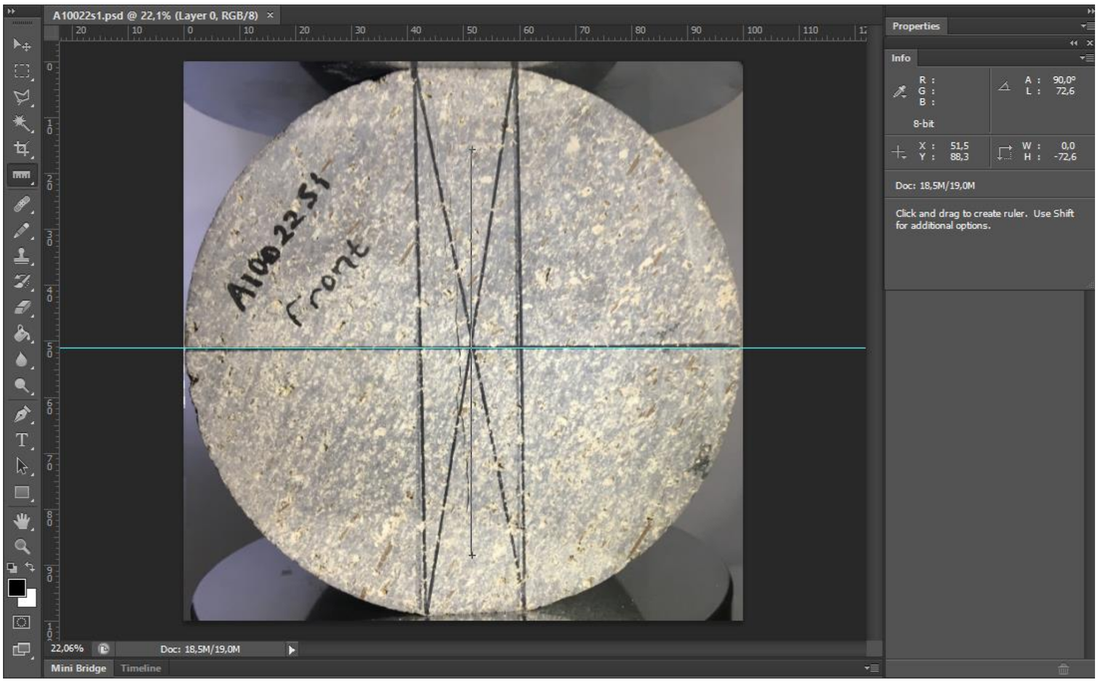

R :
G :
B :
8-bit
A : 90,0°
L : 72,6
X : 51,5
Y : 88,3
W : 0,0
H : -72,6
Doc: 18,5M/19,0M

Click and drag to create ruler. Use Shift for additional options.

Figure B.23. Critical crack length measurement of A10022s1 coded specimen ($2a_{ce}$ =72.6 mm)

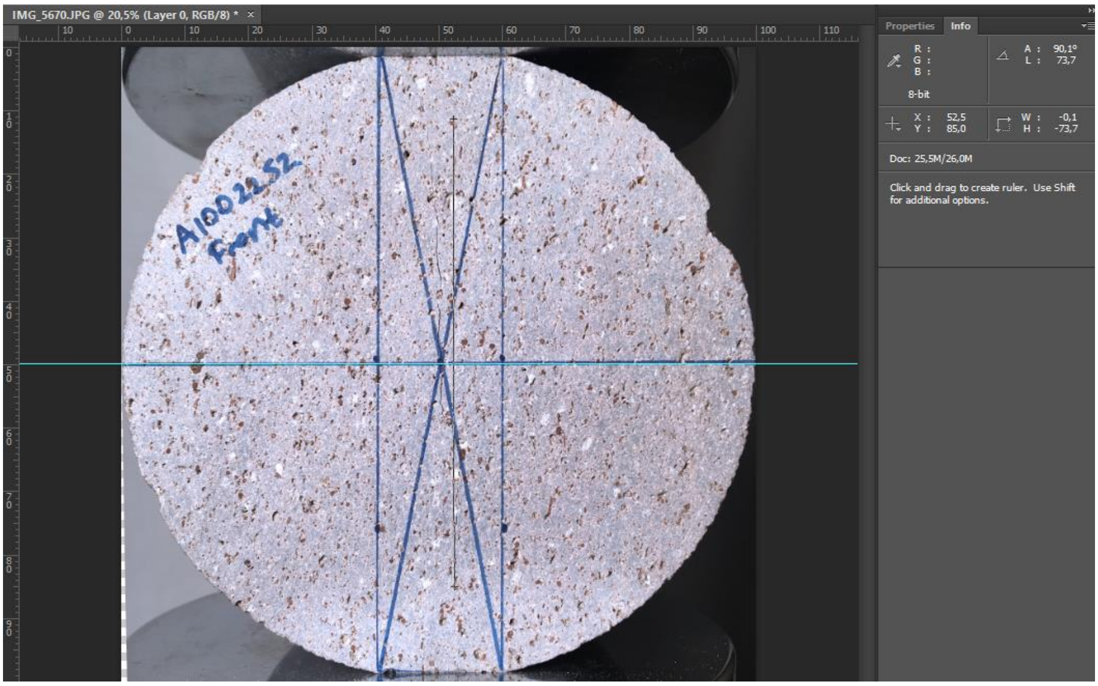

R :
G :
B :
8-bit
A : 90,1°
L : 73,7
X : 52,5
Y : 85,0
W : -0,1
H : -73,7
Doc: 25,5M/26,0M
Click and drag to create ruler. Use Shift for additional options.

Figure B.24. Critical crack length measurement of A10022s2 coded specimen ($2a_{ce}$ =73.7 mm)

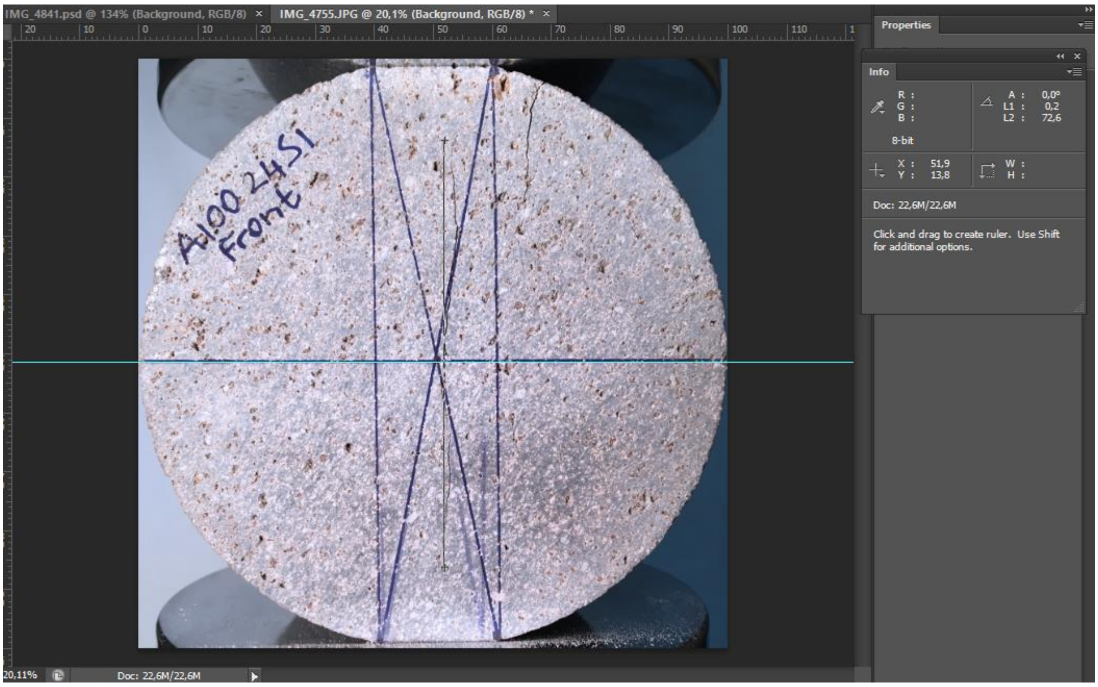

R :
G :
B :
8-bit
A : 0,0°
L1 : 0,2
L2 : 72,6
X : 51,9
Y : 13,8
W :
H :
Doc: 22,6M/22,6M
Click and drag to create ruler. Use Shift for additional options.

Figure B.25. Critical crack length measurement of A10024s1 coded specimen ($2a_{ce}$ =72.6 mm)

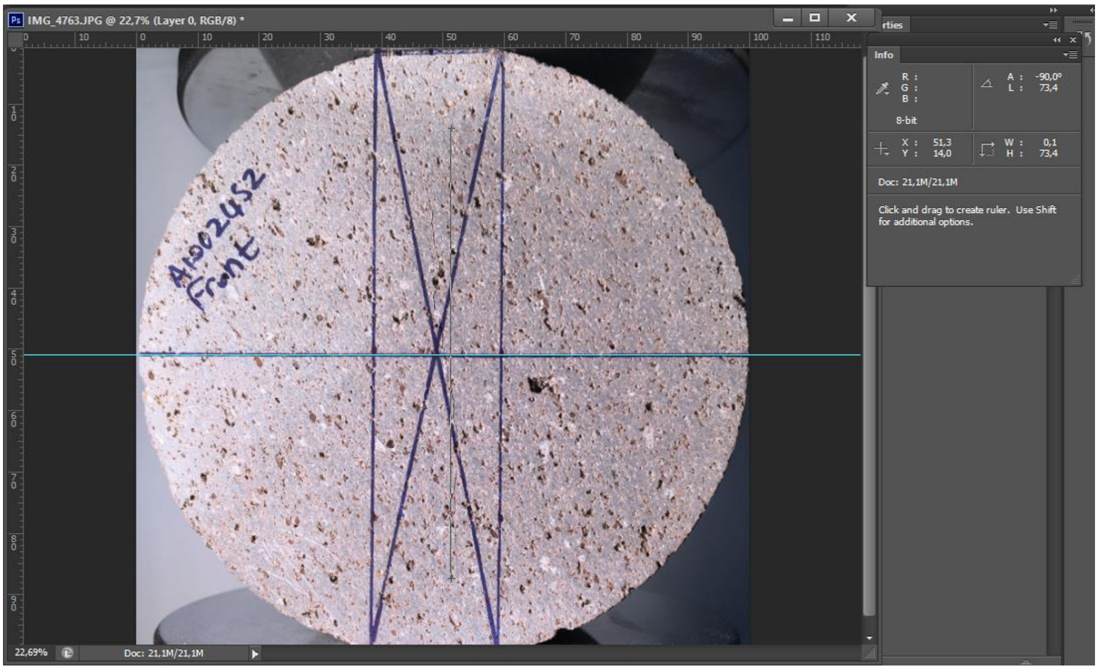

Info

R :
G :
B :
8-bit

A : -90,0°
L : 73,4

X : 51,3
Y : 14,0

W : 0,1
H : 73,4

Doc: 21,1M/21,1M

Click and drag to create ruler. Use Shift for additional options.

Figure B.26. Critical crack length measurement of A10024s2 coded specimen ($2a_{ce}$ =73.4 mm)

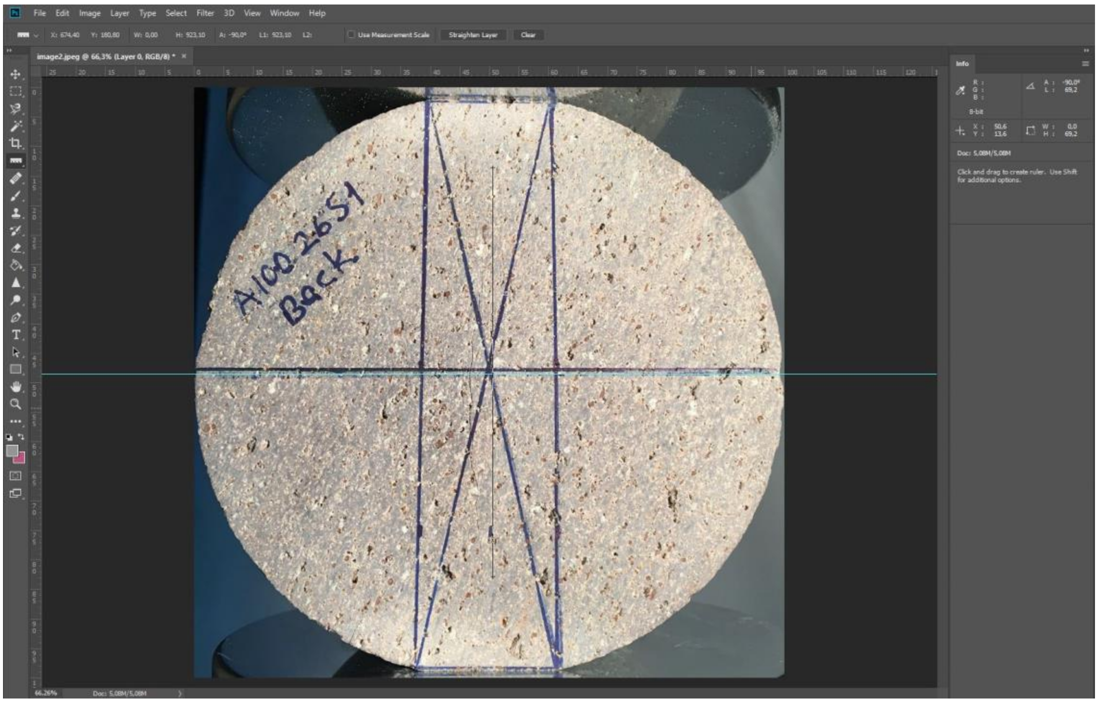

X: 674,40 Y: 180,80 W: 0,00 H: 923,10 A: -90,0° L1: 923,10 L2:

☐ Use Measurement Scale

Info

R :
G :
B :
8-bit

A : -90,0°
L : 69,2

X : 50,6
Y : 13,6

W : 0,0
H : 69,2

Doc: 5,08M/5,08M

Click and drag to create ruler. Use Shift for additional options.

Figure B.27. Critical crack length measurement of A10026s1 coded specimen ($2a_{ce}$ =69.2 mm)

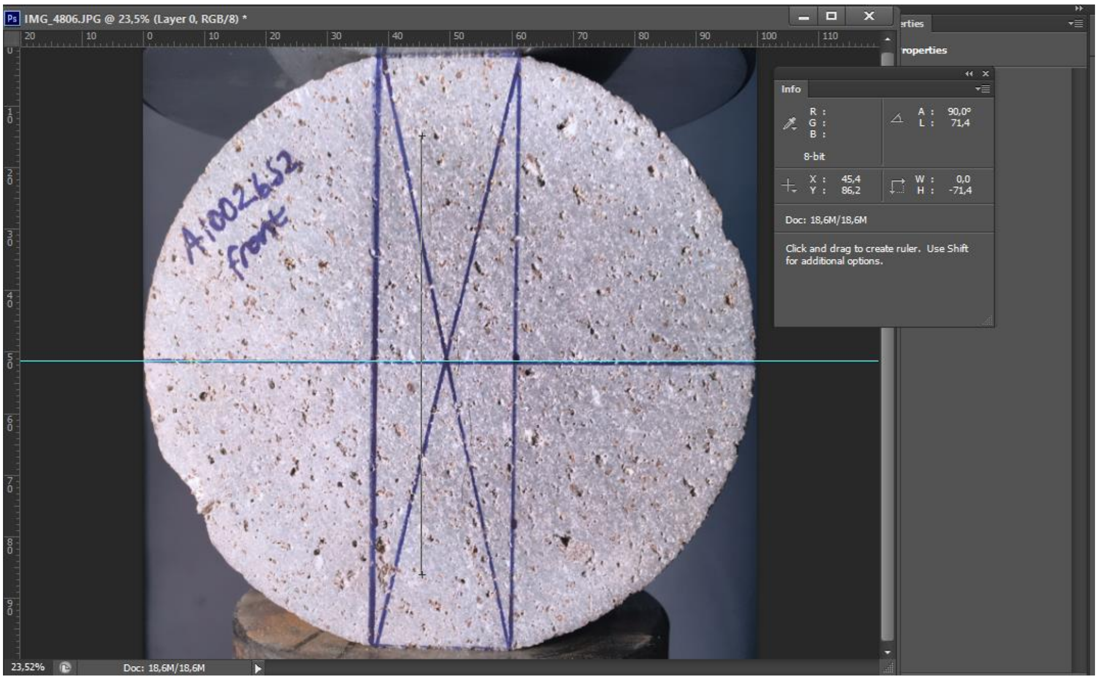

Figure B.28. Critical crack length measurement of A10026s2 coded specimen ($2a_{ce}$ =71.4 mm)

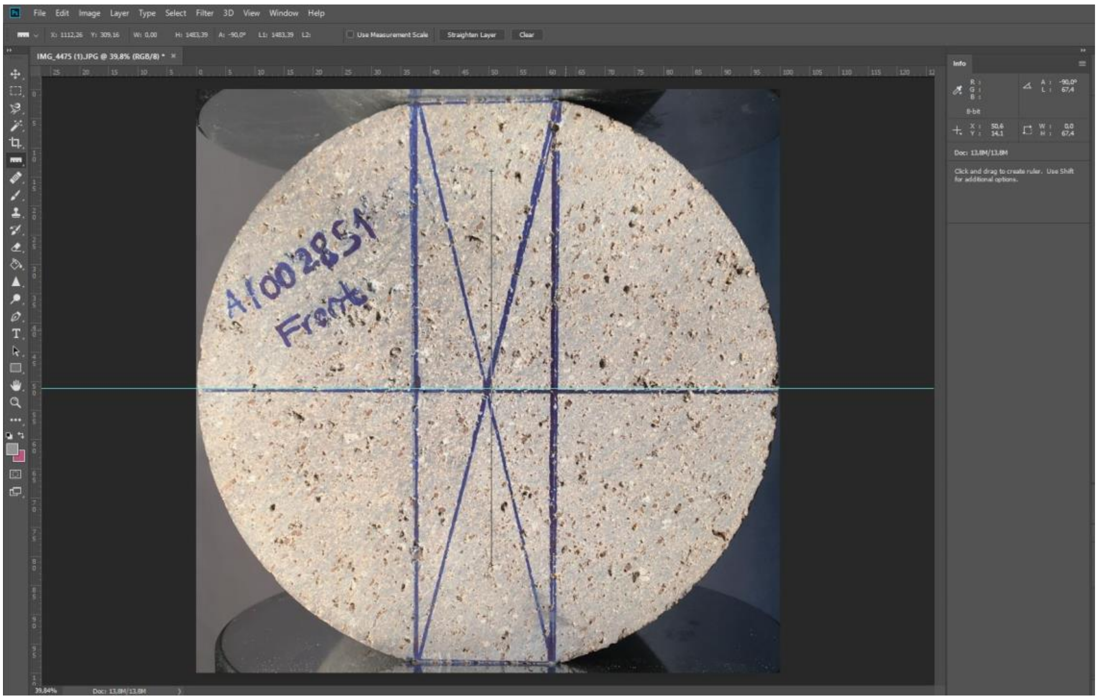

Figure B.29. Critical crack length measurement of A10028s1 coded specimen $2a_{ce}$ =67.4 mm)

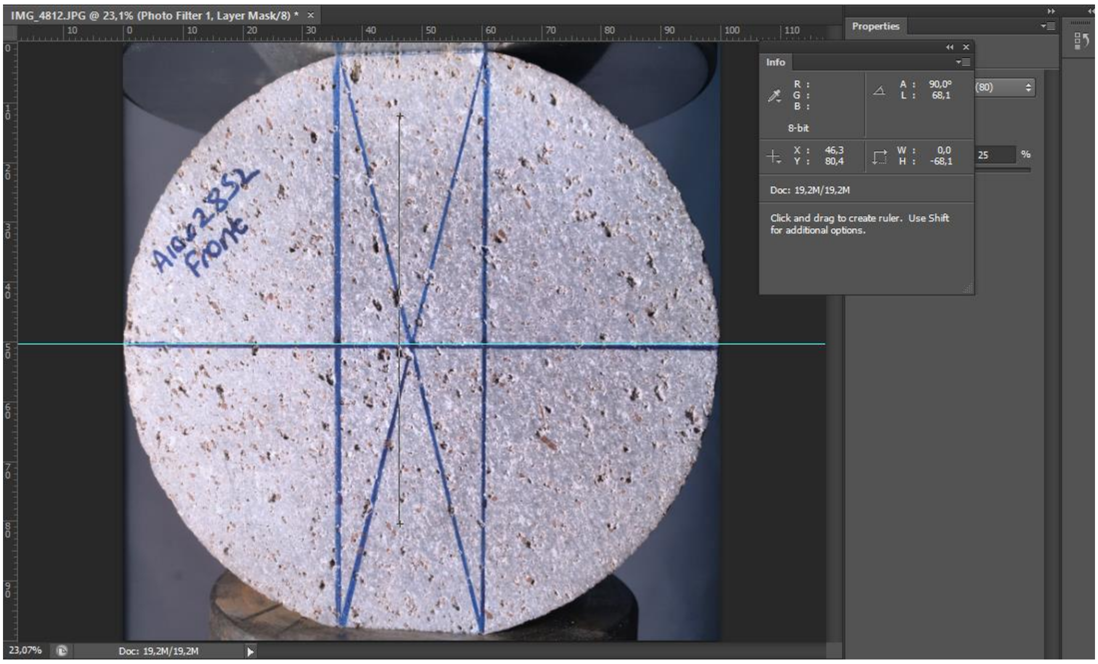
IMG_4812.JPG @ 23,1% (Photo Filter 1, Layer Mask/8) *

R :
G :
B :
8-bit
A : 90,0°
L : 68,1
X : 46,3
Y : 80,4
W : 0,0
H : -68,1
Doc: 19,2M/19,2M

Click and drag to create ruler. Use Shift for additional options.

23,07%
Doc: 19,2M/19,2M

Figure B.30. Critical crack length measurement of A10028s2 coded specimen ($2a_{ce}$ =68.1 mm)

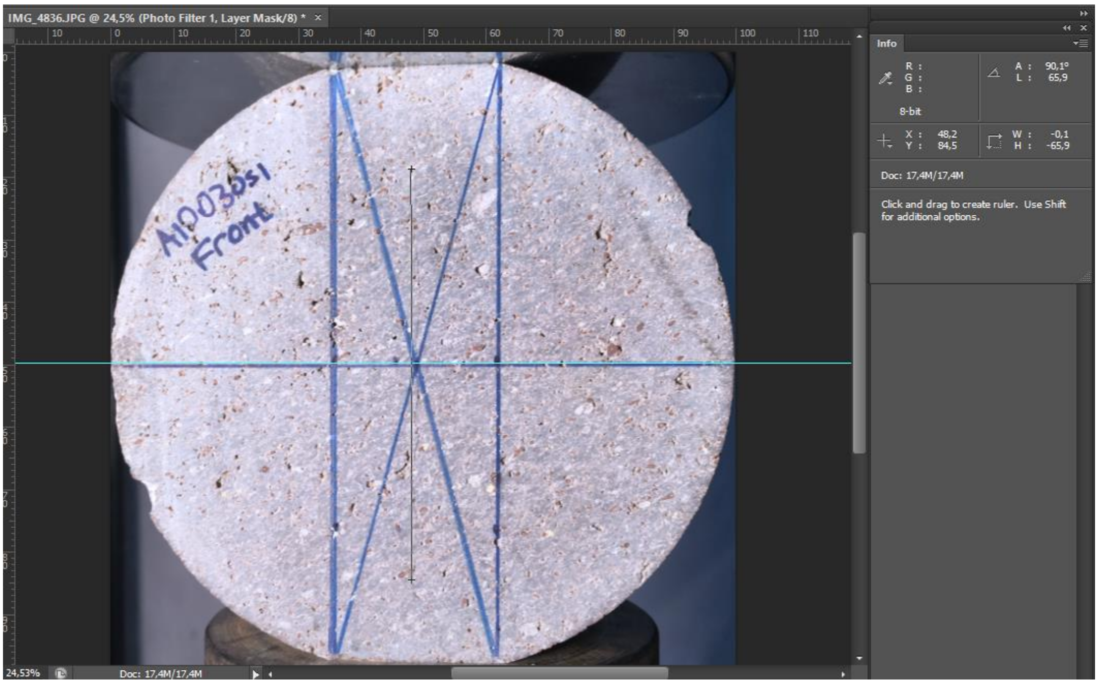
IMG_4836.JPG @ 24,5% (Photo Filter 1, Layer Mask/8) *

R :
G :
B :
8-bit
A : 90,1°
L : 65,9
X : 48,2
Y : 84,5
W : -0,1
H : -65,9
Doc: 17,4M/17,4M

Click and drag to create ruler. Use Shift for additional options.

24,53%
Doc: 17,4M/17,4M

Figure B.31. Critical crack length measurement of A10030s1 coded specimen ($2a_{ce}$ =65.9 mm)

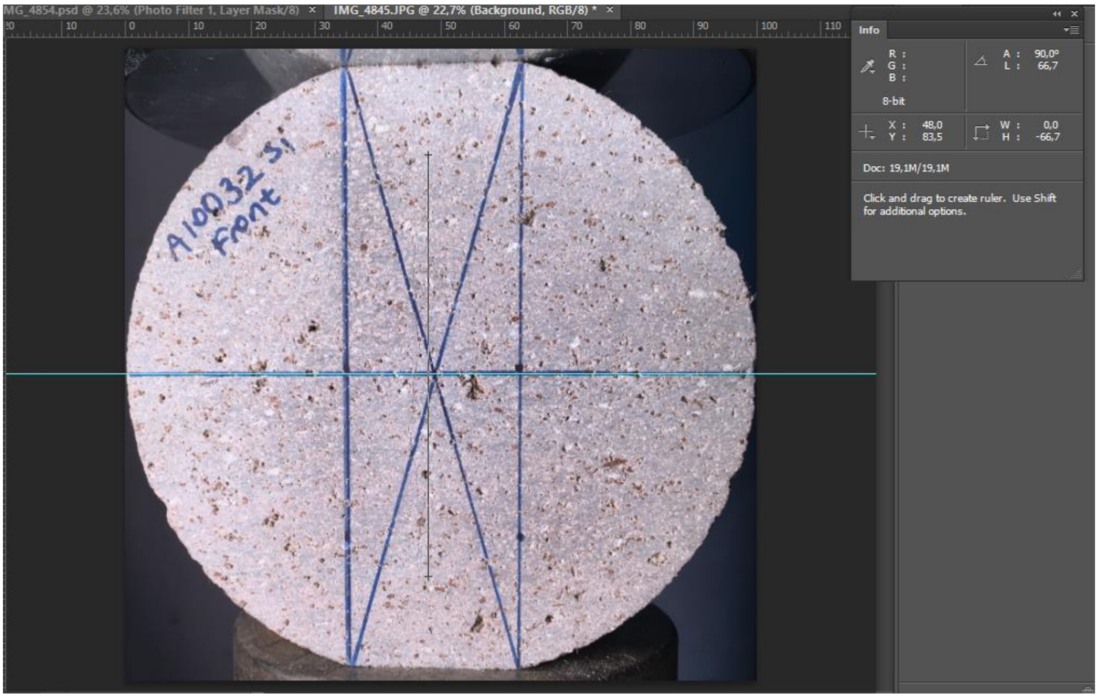

Figure B.32. Critical crack length measurement of A10032s1 coded specimen ($2a_{ce}$ =66.7 mm)

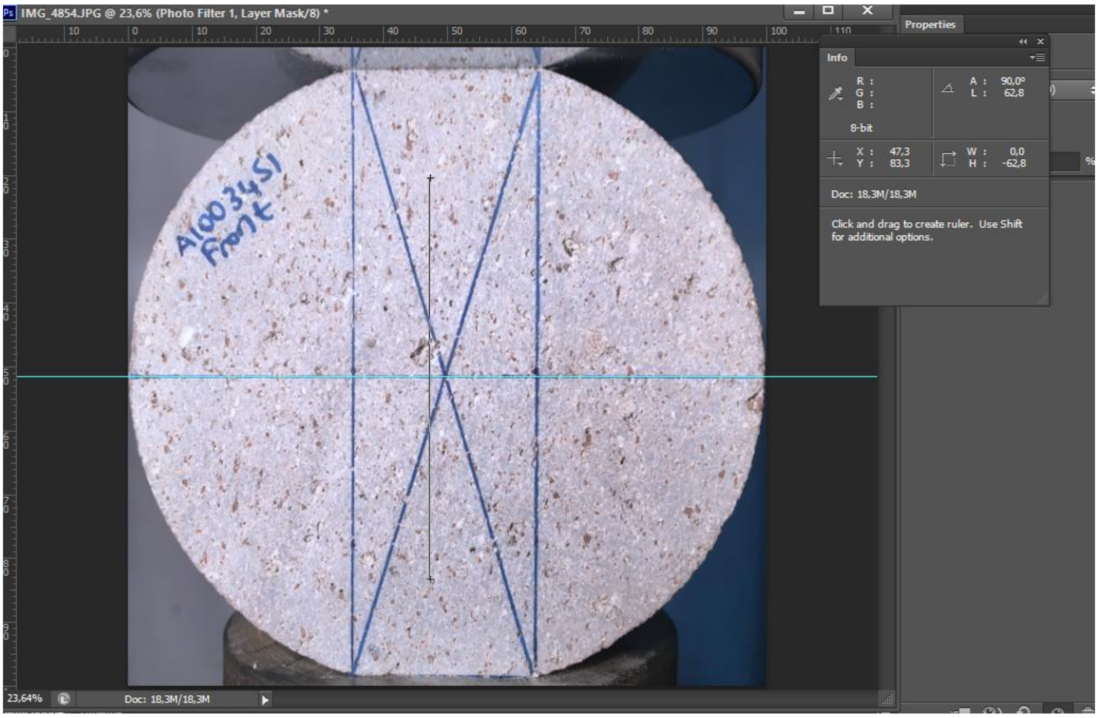

Figure B.33. Critical crack length measurement of A10034s1 coded specimen ($2a_{ce}$ =62.8 mm)

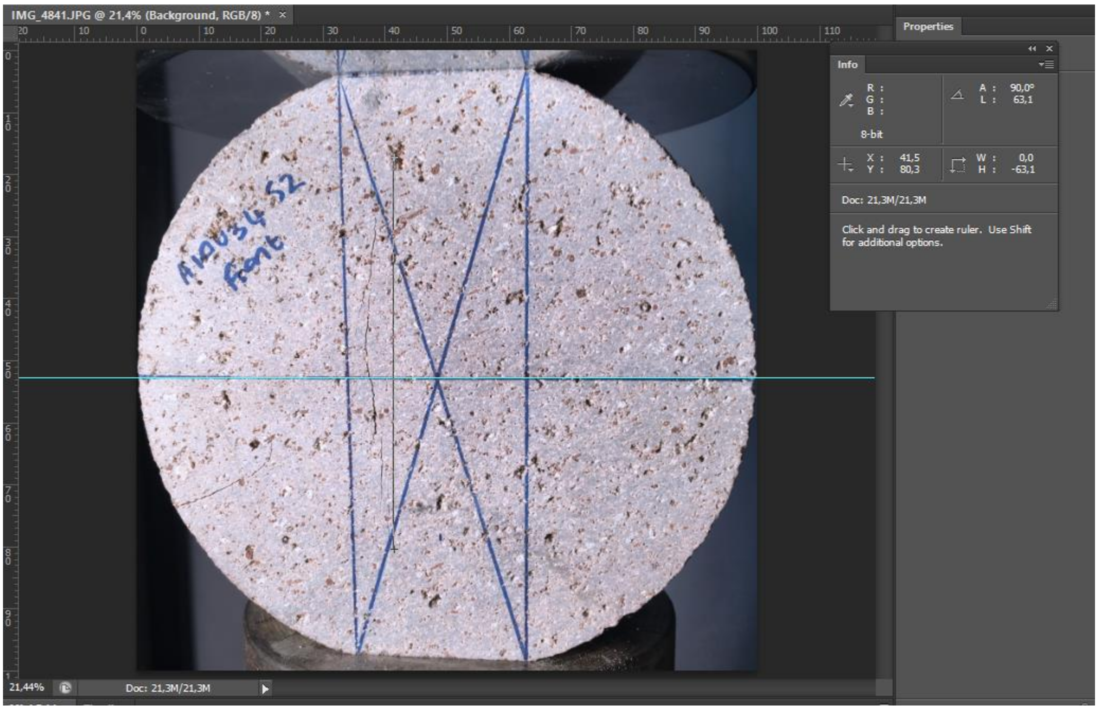

R :
G :
B :
8-bit

A : 90,0°
L : 63,1

X : 41,5
Y : 80,3

W : 0,0
H : -63,1

Doc: 21,3M/21,3M

Click and drag to create ruler. Use Shift for additional options.

Figure B.34. Critical crack length measurement of A10034s2 coded specimen ($2a_{ce}$ =63.1 mm)

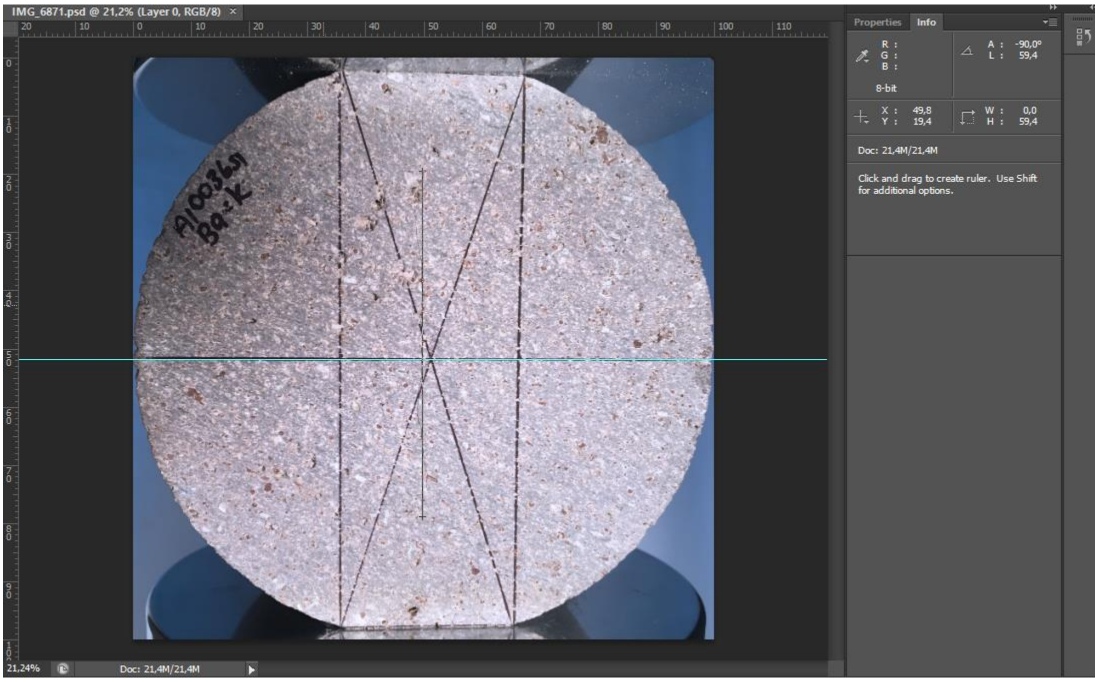

R :
G :
B :
8-bit

A : -90,0°
L : 59,4

X : 49,8
Y : 19,4

W : 0,0
H : 59,4

Doc: 21,4M/21,4M

Click and drag to create ruler. Use Shift for additional options.

Figure B.35. Critical crack length measurement of A10036s1 coded specimen ($2a_{ce}$ =59.4 mm)

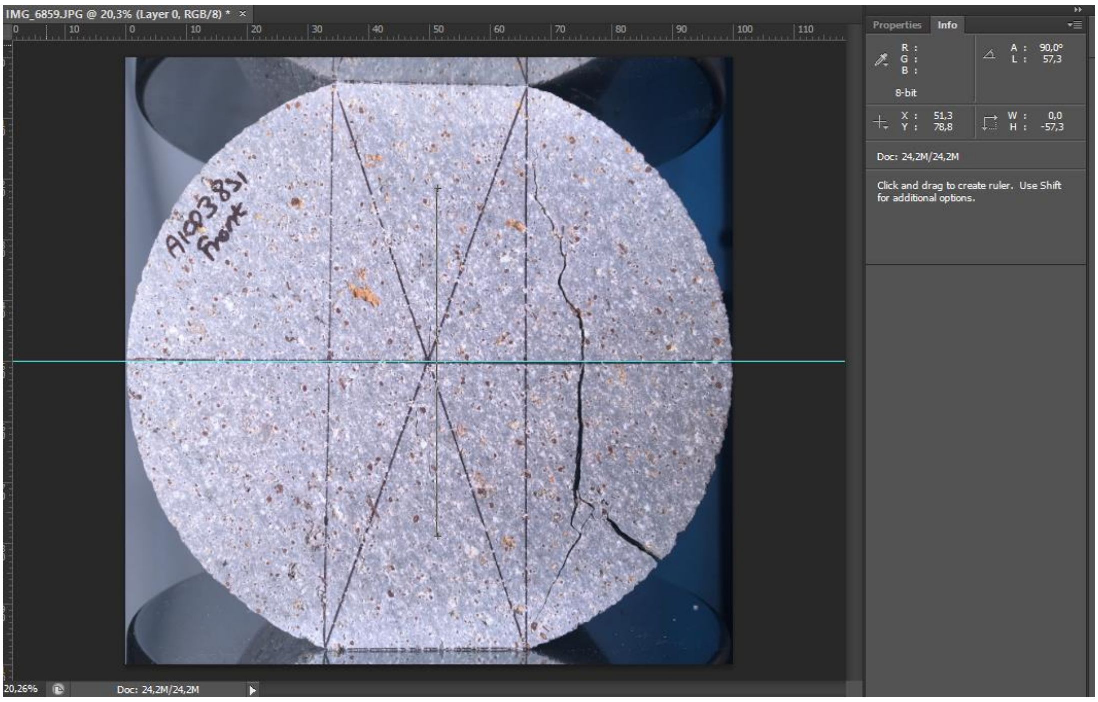
IMG_6859.JPG @ 20,3% (Layer 0, RGB/8) *

A : 90,0°
L : 57,3

X : 51,3
Y : 78,8

W : 0,0
H : -57,3

Doc: 24,2M/24,2M

Click and drag to create ruler. Use Shift for additional options.

20,26%

Doc: 24,2M/24,2M

Figure B.36. Critical crack length measurement of A10038s1 coded specimen ($2a_{ce}$ =57.3 mm)

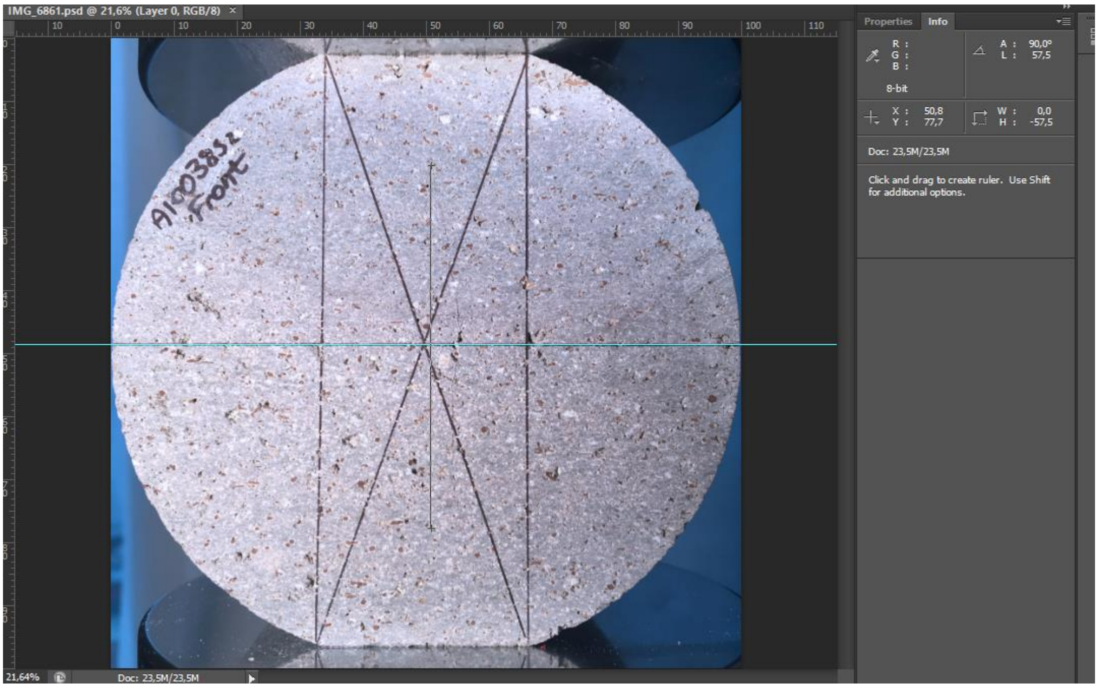
IMG_6861.psd @ 21,6% (Layer 0, RGB/8)

A : 90,0°
L : 57,5

X : 50,8
Y : 77,7

W : 0,0
H : -57,5

Doc: 23,5M/23,5M

Click and drag to create ruler. Use Shift for additional options.

21,64%

Doc: 23,5M/23,5M

Figure B.37. Critical crack length measurement of A10038s2 coded specimen ($2a_{ce}$ =57.5 mm)

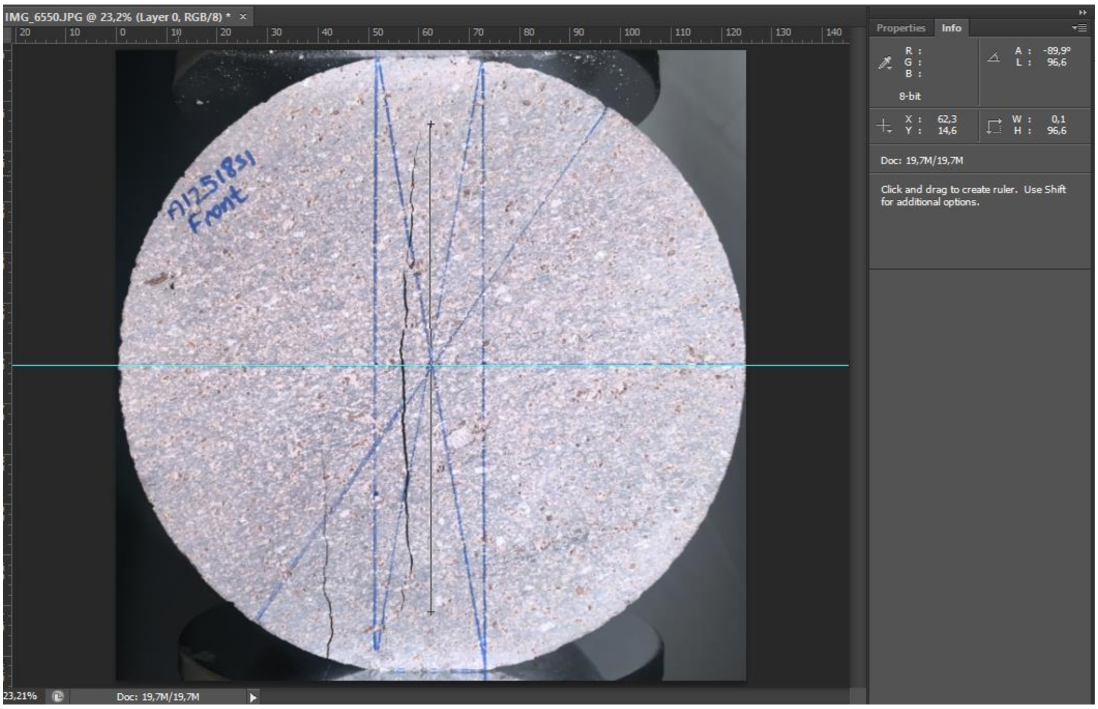

R :
G :
B :
A : -89,9°
L : 96,6
X : 62,3
Y : 14,6
W : 0,1
H : 96,6
Doc: 19,7M/19,7M

Click and drag to create ruler. Use Shift for additional options.

Figure B.38. Critical crack length measurement of A12518s1 coded specimen ($2a_{ce}$ =96.6 mm)

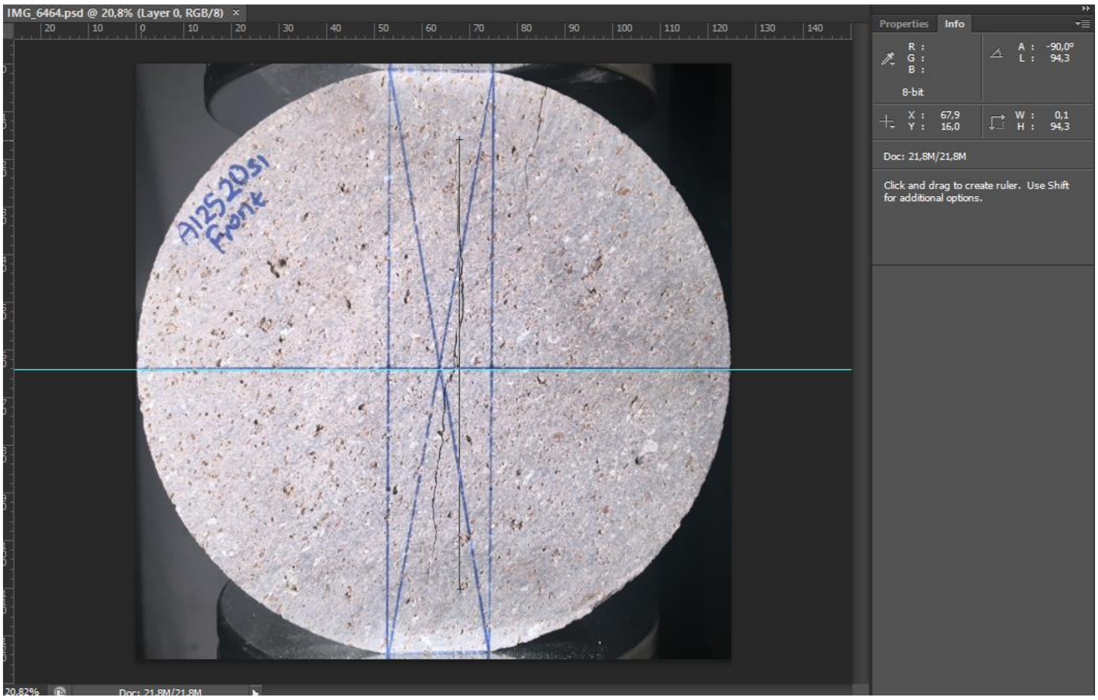

R :
G :
B :
A : -90,0°
L : 94,3
X : 67,9
Y : 16,0
W : 0,1
H : 94,3
Doc: 21,8M/21,8M

Click and drag to create ruler. Use Shift for additional options.

Figure B.39. Critical crack length measurement of A12520s1 coded specimen ($2a_{ce}$ =94.3 mm)

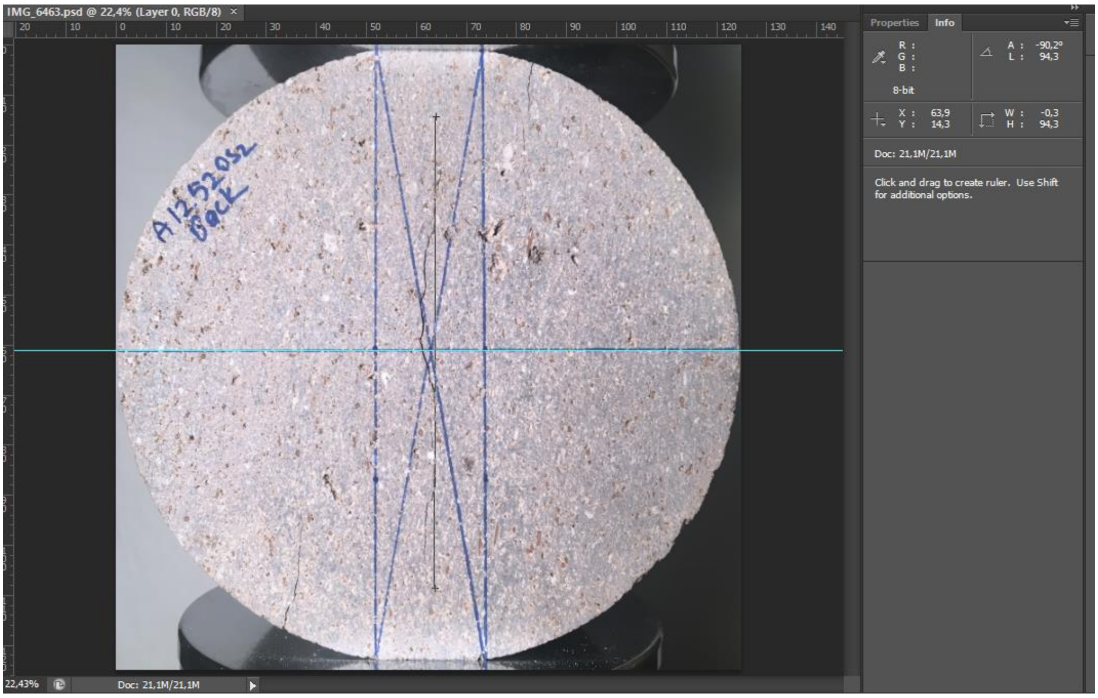

R :
G :
B :
8-bit

A : -90,2°
L : 94,3

X : 63,9
Y : 14,3

W : -0,3
H : 94,3

Doc: 21,1M/21,1M

Click and drag to create ruler. Use Shift for additional options.

Figure B.40. Critical crack length measurement of A12520s2 coded specimen ($2a_{ce}$ =94.3 mm)

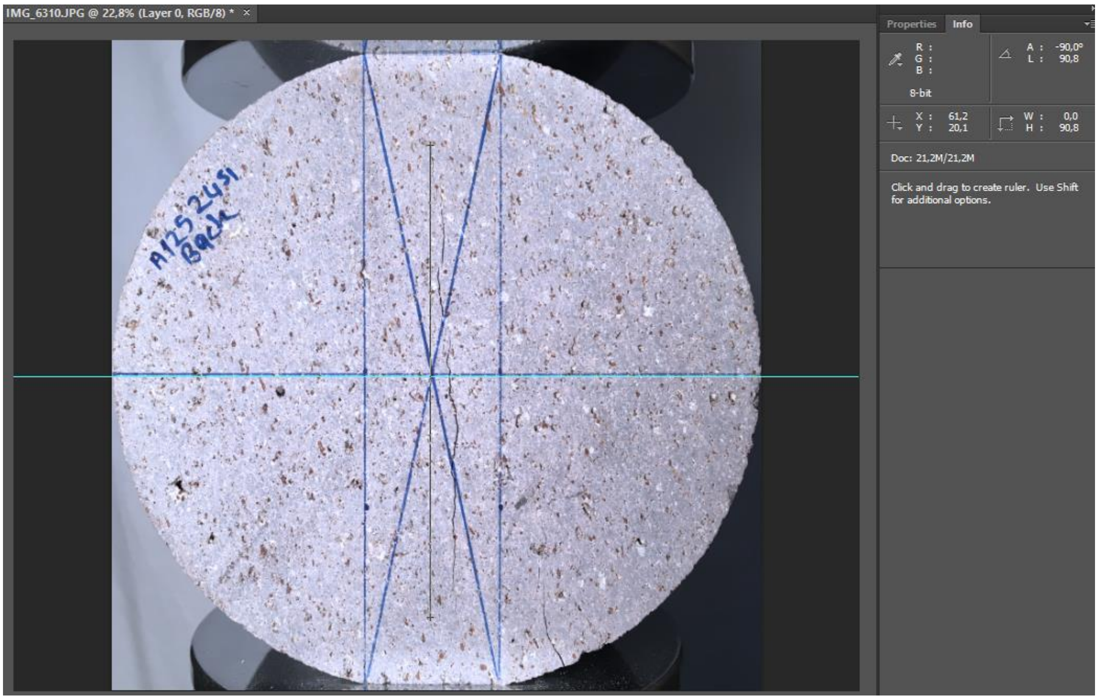

R :
G :
B :
8-bit

A : -90,0°
L : 90,8

X : 61,2
Y : 20,1

W : 0,0
H : 90,8

Doc: 21,2M/21,2M

Click and drag to create ruler. Use Shift for additional options.

Figure B.41. Critical crack length measurement of A12524s1 coded specimen ($2a_{ce}$ =90.8 mm)

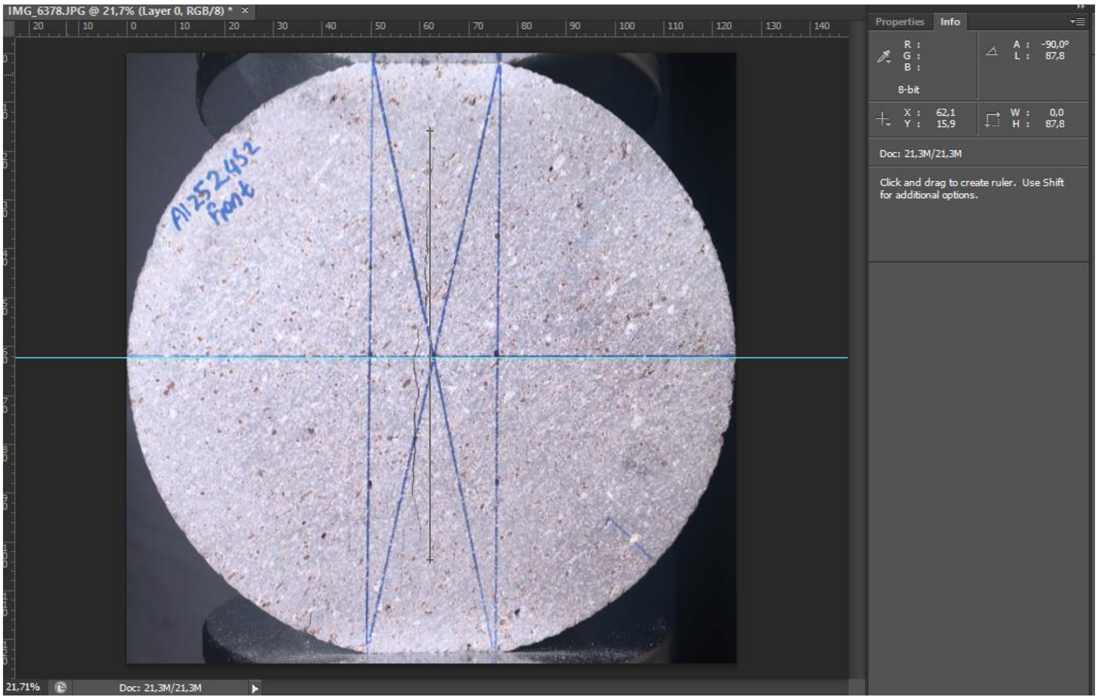

Click and drag to create ruler. Use Shift for additional options.

Figure B.42. Critical crack length measurement of A12524s2 coded specimen $2a_{ce}$ =87.8 mm)

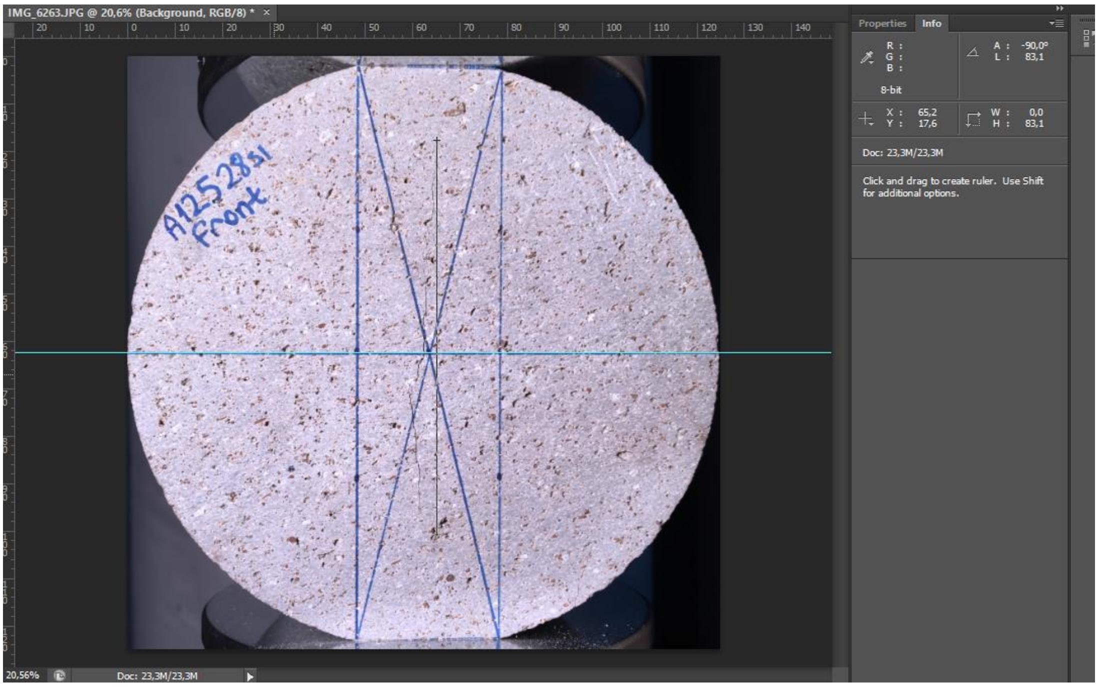

Click and drag to create ruler. Use Shift for additional options.

Figure B.43. Critical crack length measurement of A12528s1 coded specimen ($2a_{ce}$ =83.1 mm)

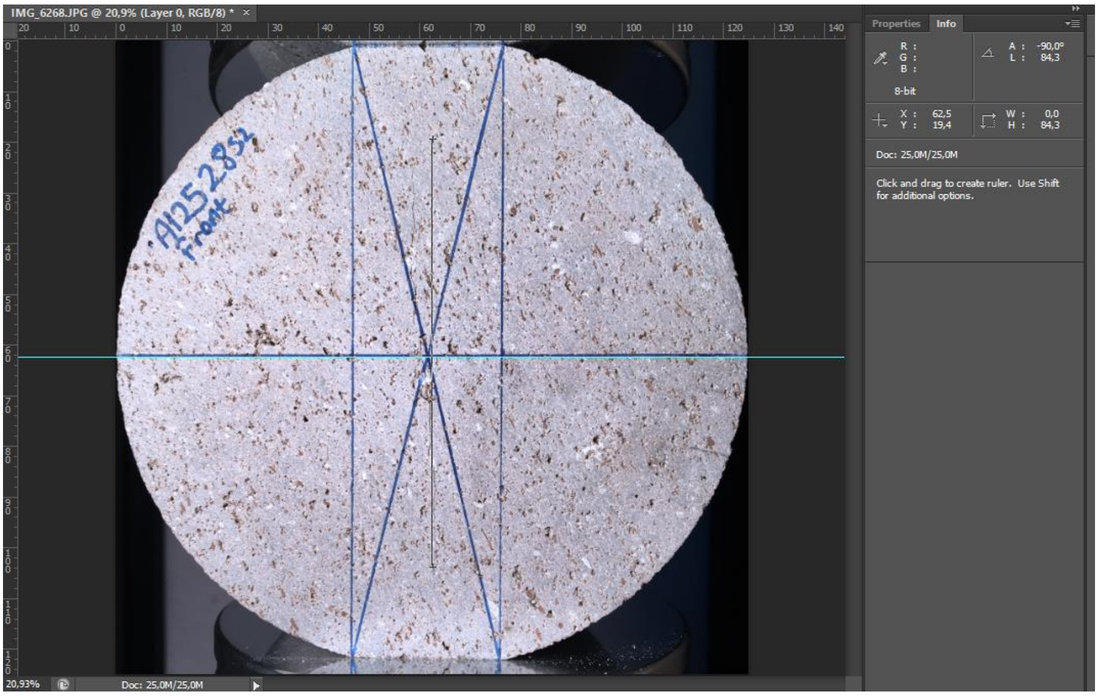

R :
G :
B :
8-bit
A : -90,0°
L : 84,3
X : 62,5
Y : 19,4
W : 0,0
H : 84,3
Doc: 25,0M/25,0M

Click and drag to create ruler. Use Shift for additional options.

Figure B.44. Critical crack length measurement of A12528s2 coded specimen ($2a_{ce}$ =84.3 mm)

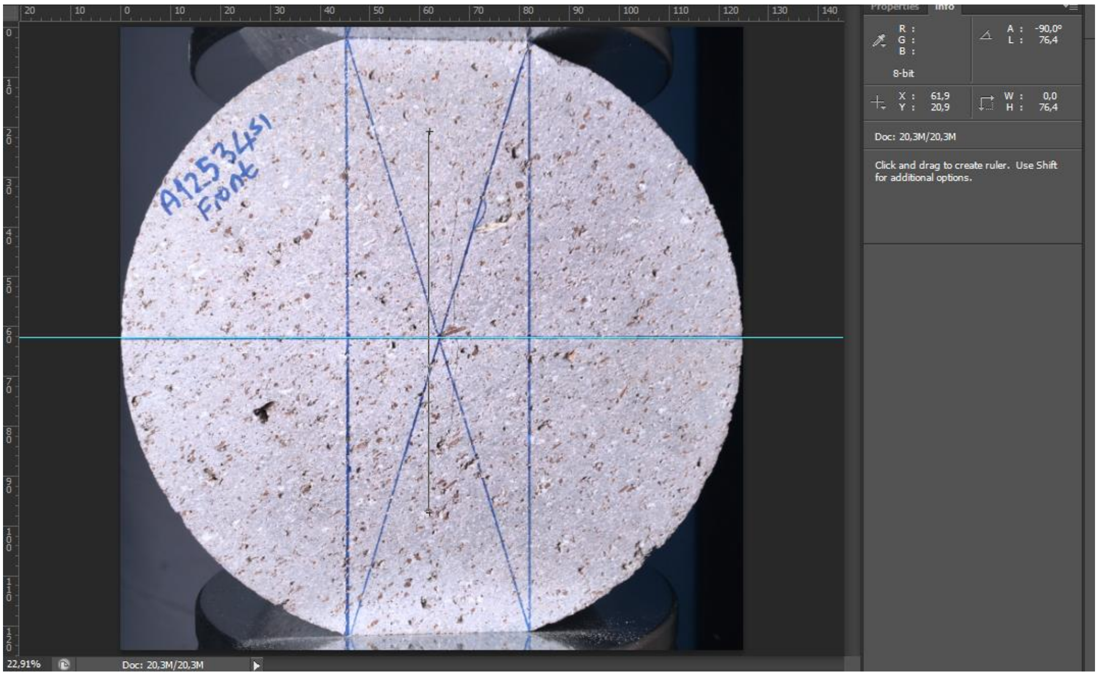

R :
G :
B :
8-bit
A : -90,0°
L : 76,4
X : 61,9
Y : 20,9
W : 0,0
H : 76,4
Doc: 20,3M/20,3M

Click and drag to create ruler. Use Shift for additional options.

Figure B.45. Critical crack length measurement of A12534s1 coded specimen ($2a_{ce}$ =76.4 mm)

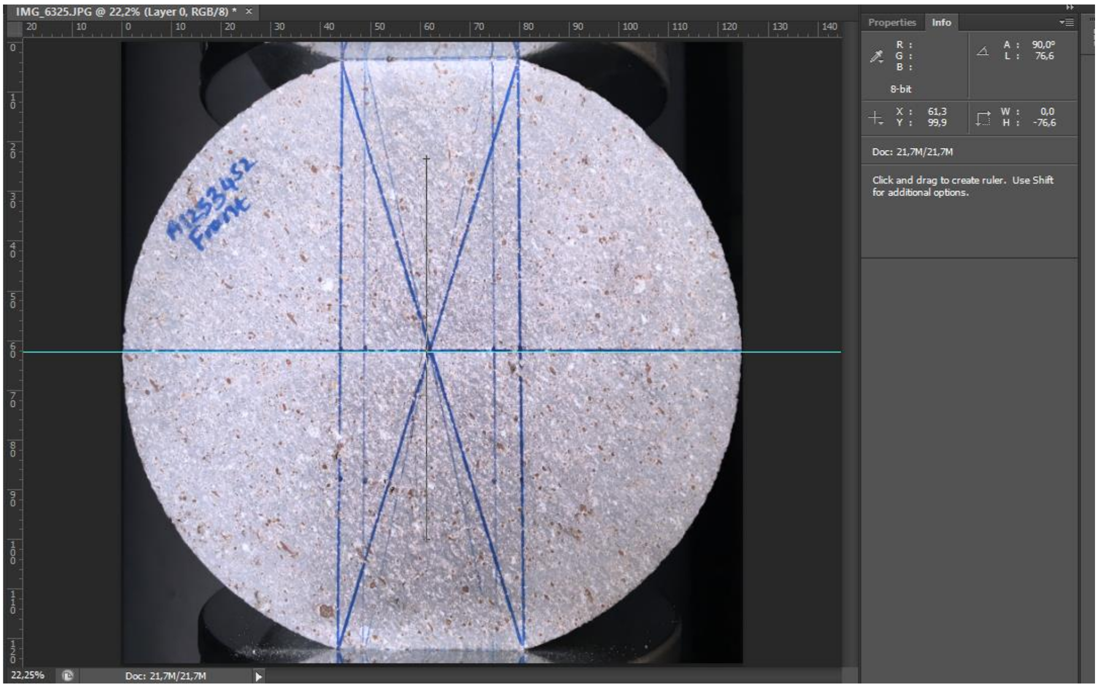

A : 90,0°
L : 76,6
X : 61,3
Y : 99,9
W : 0,0
H : -76,6
Doc: 21,7M/21,7M

Click and drag to create ruler. Use Shift for additional options.

Figure B.46. Critical crack length measurement of A12534s2 coded specimen ($2a_{ce}$ =76.6 mm)

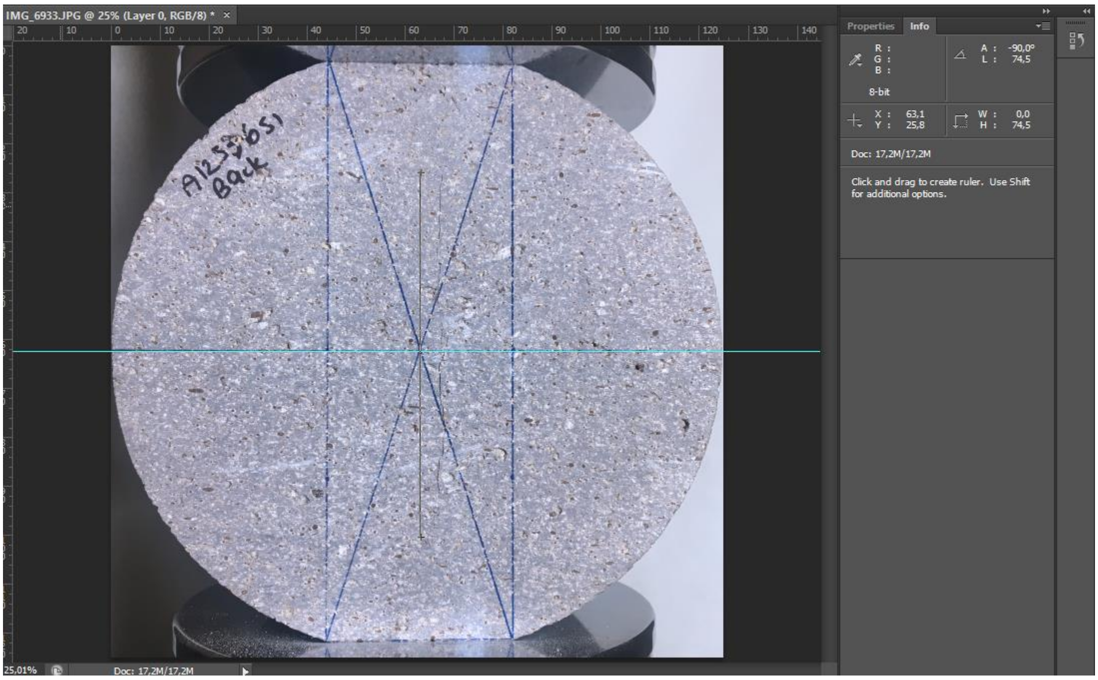

A : -90,0°
L : 74,5
X : 63,1
Y : 25,8
W : 0,0
H : 74,5
Doc: 17,2M/17,2M

Click and drag to create ruler. Use Shift for additional options.

Figure B.47. Critical crack length measurement of A12536s1 coded specimen ($2a_{ce}$ =74.5 mm)

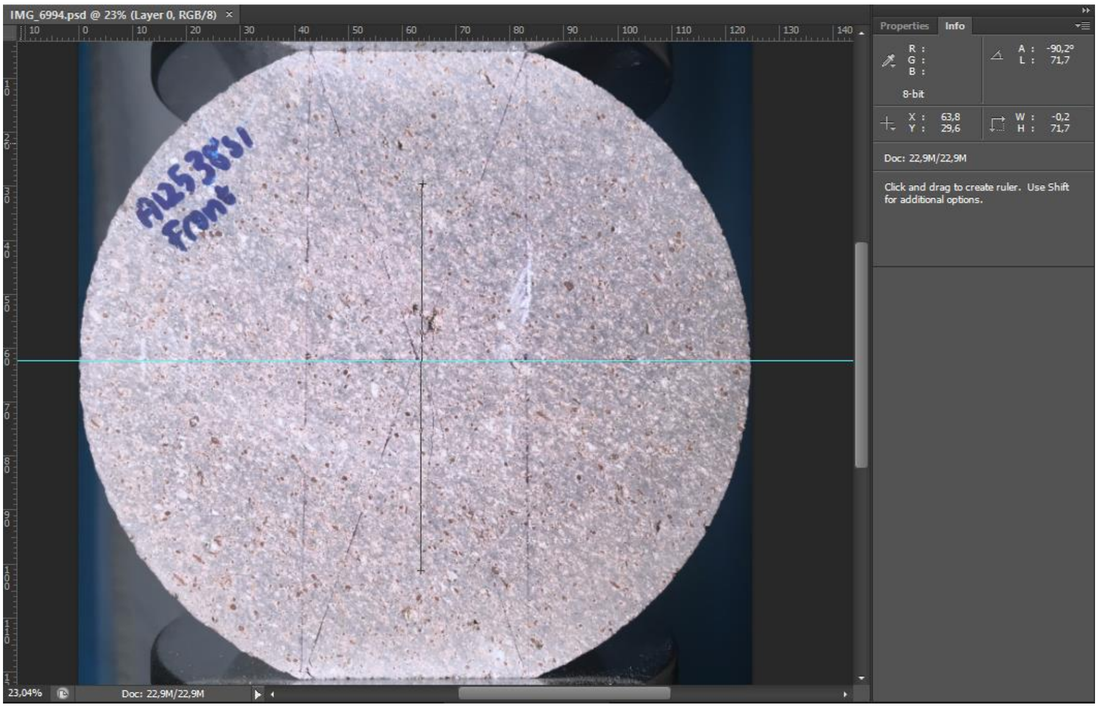

IMG_6994.psd @ 23% (Layer 0, RGB/8)

A : -90,2°
L : 71,7

8-bit

X : 63,8
Y : 29,6

W : -0,2
H : 71,7

Doc: 22,9M/22,9M

Click and drag to create ruler. Use Shift for additional options.

23,04%

Figure B.48. Critical crack length measurement of A12538s1 coded specimen ($2a_{ce}$ =71.7mm)

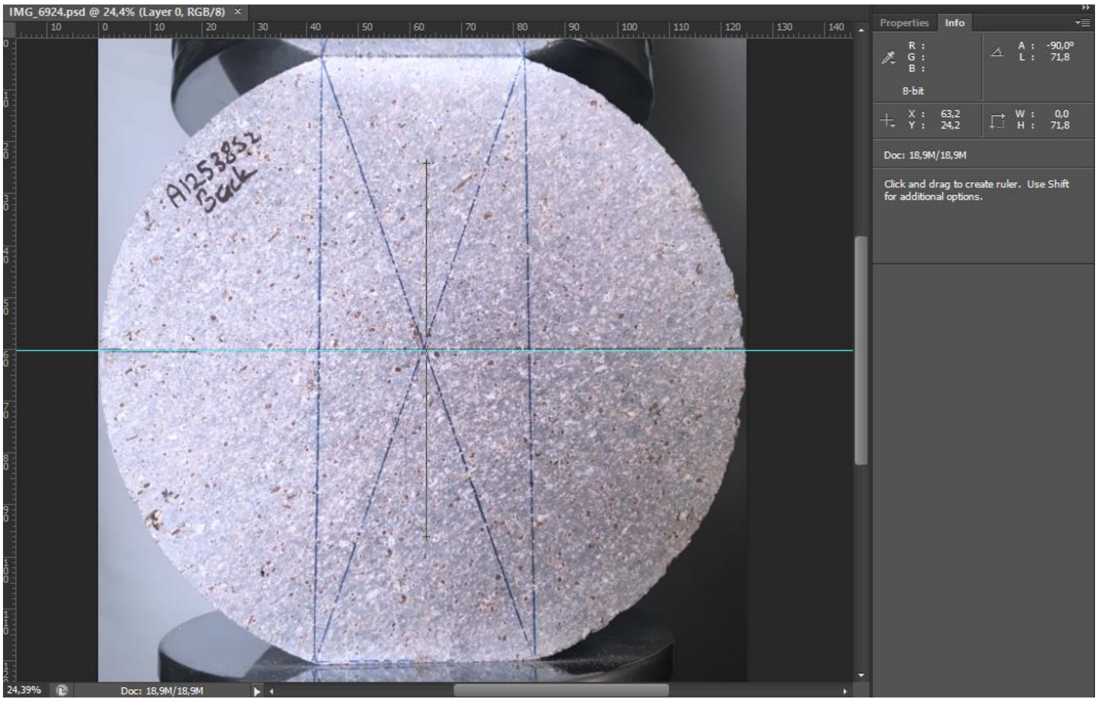

IMG_6924.psd @ 24,4% (Layer 0, RGB/8)

A : -90,0°
L : 71,8

8-bit

X : 63,2
Y : 24,2

W : 0,0
H : 71,8

Doc: 18,9M/18,9M

Click and drag to create ruler. Use Shift for additional options.

24,39%

Figure B.49. Critical crack length measurement of A12538s2 coded specimen ($2a_{ce}$ =71.8 mm)

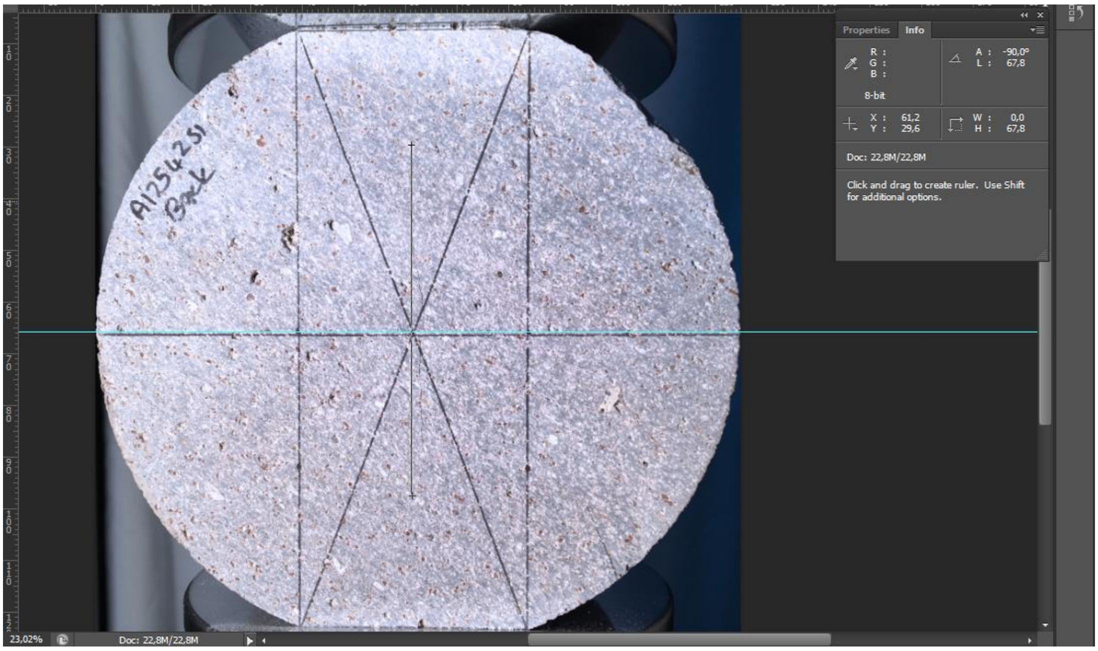

R :
G :
B :
8-bit
A : -90,0°
L : 67,8
X : 61,2
Y : 29,6
W : 0,0
H : 67,8
Doc: 22,8M/22,8M

Click and drag to create ruler. Use Shift for additional options.

23,02%
Doc: 22,8M/22,8M

Figure B.50. Critical crack length measurement of A12542s1 coded specimen ($2a_{ce}$ =67.8 mm)

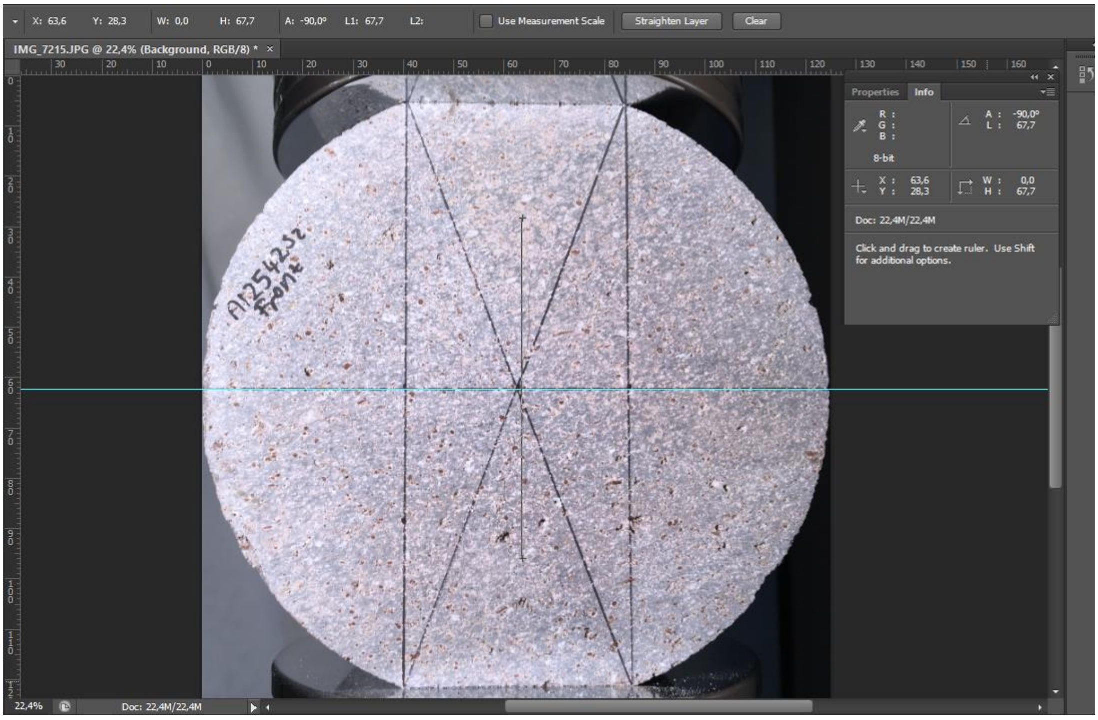

X: 63,6 Y: 28,3 W: 0,0 H: 67,7 A: -90,0° L1: 67,7 L2:

IMG_7215.JPG @ 22,4% (Background, RGB/8) *

R :
G :
B :
8-bit
A : -90,0°
L : 67,7
X : 63,6
Y : 28,3
W : 0,0
H : 67,7
Doc: 22,4M/22,4M

Click and drag to create ruler. Use Shift for additional options.

22,4%
Doc: 22,4M/22,4M

Figure B.51. Critical crack length measurement of A12542s2 coded specimen ($2a_{ce}$ =67.7 mm)